Searching for missing baryons through scintillation

Farhang Habibi

LAL 11-126
Juin 2011

THÈSE

Présentée le 15 juin 2011

par

Farhang HABIBI

pour obtenir le grade de

Docteur ès Sciences
de l'Université Paris XI, Orsay

Search for Missing Baryons through Scintillation

Soutenue devant la commission d'examen composée de :

M.	M.	Moniez	Directeur de thèse
M.	S.	Rahvar	Directeur de thèse
Mme	F.	Combes	Rapporteur
M.	J.	Rich	
M.	A.	Stocchi	Président
M.	R.	Mansouri	
M.	M.	Jalali	Rapporteur

Search for Missing Baryons through Scintillation

Farhang Habibi
Université Paris-SUD 11
Sharif University of Technology

Présentée le 15 juin 2011

Dedicated to my parents

Acknowledgments

This thesis would not have been possible without supervision of Marc Moniez. He is a great astronomer and teacher as well as a sincere friend of mine. I am grateful to Sohrab Rahvar the second supervisor of the thesis because of his guidances and helps during my stay in Tehran. I would like to show my gratitude to Reza Ansari who was as my third supervisor with his valuable scientific and computational assistances. I thank Guy Wormser and Achille Stocchi for supporting me as presidents of LAL during my stay in Orsay. I am thankful to Reza Mansouri for supporting me at School of Astronomy at IPM and Neda Sadoughi at Sahrif University. It is a pleasure to thank Jacques Haissinski for his encouraging attitude toward the students and Francois Couchot for his encouraging character as well as being a good tai chi opponent. I thank the administrative staff of LAL specially Genevieve Gilbert and Sylivie Prandt. I am grateful to my friends at LAL, Clement Filliard, Alexis Labavre, Sophie Blondel, Alexandra Abate, Joao Costa, Nancy Andari, Dimitris Varouchas, Karim Louedec, Marthe Teinturier, Jana Schaarschmidt, Aurélien Martens and Iro Koletsou. During my thesis I have passed good times in tai chi class with Denis and Herve Grasser and all people of the class. I am thankful to my friends at residence universitair la Pacaterie; Taj Muhammad Khan, Charlotte Weil, Mahdi Tekitek and Corina Elena. I also would like to thank all my Iranian friends and family in Iran and Europe. Finally, I thank Mr. Najjarian, my teacher at guidance school, who taught me what is appreciable is not being at top but being in progress.

خلاصه فارسی

مشاهدات اثر ریزهمگرایی نشان داده اند که مقدار ماده ی فشرده باریونی موجود در هاله ی راه کاهکشان به اندازه ای نیست که تمامی ماده ی باریونی گمشده ی کهکشان را توضیح دهد. از این رو ابرهای رقیق متشکل از مولکول سرد هیدروژن یکی از آخرین نامزدهای ماده ی تاریک باریونی هستند. از آنجایی که این ابر های مفروض نخستین، متعلق به زمان مهبانگ، دمایی کمتر از ۱۰ درجه کلوین دارند، تابش گرماییشان ناچیز و قابل صرف نظر کردن است. افزون بر این، قطبش پذیری ناچیز مولکول هیدروژن آن را از برهمکنش با موج الکترومغناطیس باز می دارد. تنها باندی که مولکول هیدروژن را تشدید می کند طول موج فرا بنفش است که برای ناظر زمینی قابل آشکارسازی نیست. تمامی این شرایط باعث شفاف بودن این ابر های مفروض برای ناظر زمینی می شود.

اندازه گیری منحنی نوری ستارگان واقع در پشت این محیط های گازی نامرئی و مشاهده ی اثر سوسوزنی می تواند راهی باشد برای آشکار سازی این محیط ها. اگر تلاطم موجود در این محیط ها قادر به ایجاد افت و خیز قابل ملاحظه در چگالی محیط باشد، جبهه ی موج نور ستاره ی زمینه را مختل می کند و اختلاف فاز به وجود می آورد. جبهه ی موج اعوجاج یافته مطابق قوانین پراش اپتیکی انتشار می یابد و شدت نور ستاره ی زمینه دچار افت و خیز می شود. به دلیل وجود سرعت نسبی بین چشمه، ابر و ناظر، طرح روشنایی (طرح پراش) صفحه ی ناظر را جارو می کند و ستاره ی زمینه سوسو می زند. بسته به فواصل نسبی بین چشمه، ابر و ناظر و همچنین شدت افت و خیز چگالی ابر، تباین قوی یا ضعیف شدت نور را در منحنی نوری چشمه شاهد خواهیم بود. همچنین، اثر سوسوزنی زمان های مشخصه ای دارد که تابعی از طول موج هستند. از این رو با رصد چشمه در باند های مختلف می توان اثر سوسوزنی را از سایر تغییرات دوره ای ذاتی چشمه متمایز کرد. با مشاهده ی تعداد زیادی ستاره که در پشت محیط متلاطم جای گرفته اند می توانیم بر شدت تلاطم موضعی (شعاع پخش) در راستای خط دید حد بگذاریم و از این راه ساختار های ظریف تر محیط را بررسی کنیم .

در این رساله، ما اثر سوسوزنی را شبیه سازی کرده ایم. ابتدا نشان داده شده که ابر بین ستاره ای را می توان به شکل صفحه ای ۲ بعدی تخمین زد. طیف ۲ بعدی اختلاف فاز را مطابق قانون کلموگرف به همراه شعاع پخش داده شده، در نظر گرفتیم و صفحه ی (اختلاف) فاز را بطور عددی تولید کردیم. در این کار تلاطم های نا کلموگرف هم بررسی شدند. همچنین نشان دادیم که محدودیت های محاسباتی چگونه صفحه ی فاز تولید شده را تحت تاثیر قرار می دهند. با محاسبه ی عددی انتگرال پراش هویگنس-فرنل، طرح پراش چشمه ی نور نقطه ای شبیه سازی شد. با در نظر گرفتن نمایه (پروفایل) ی روشنایی چشمه، طرح روشنایی برای چشمه ی نور گسترده بدست آمد و مشاهده کردیم که به ازای صفحه ی فاز و فواصل داده شده، چشمه های نور با اندازه ی زاویه ای بزرگتر طرح سوسوزنی کم افت و خیزتری درست می کنند. به کمک شبیه سازی رابطه ای بین پراکندگی شار منحنی های نوری سوسوزنی و نسبت شعاع تصویر شده چشمه به طول مشخصه ی سوسوزنی بدست آوردیم. از این رابطه برای ارتباط بین پراکندگی شار مشاهده شده ستاره و پارامترهای سوسوزنی (شعاع پخش، شعاع تصویر شده ی ستاره، طول موج و ...) استفاده می شود،. ما همچنین اثر همدوسی زمانی نور را بوسیله ی بر همنهش طرح های روشنایی ناشی از طول موج های مختلف بررسی کردیم.

با استفاده از دوربین فروسرخ تلسکوپ ان.ت.ت. چهار جهت مختلف را در طی دو شب رصد کردیم. سه تا از هدف ها سحابی های تاریک واقع در دیسک راه کاهکشان بودند تا انجام پذیری سوسوزنی را مورد آزمون قرار دهیم. هدف چهارم ابر ماژلانی کوچک بود تا بتوانیم ابر های شفاف احتمالی موجود در هاله را جستجو کنیم. پس از داده کاهی و داده پیرایی های لازم، منحنی های نوری را که بیشترین میزان تغییرات در شار داشتند، انتخاب کردیم. با استفاده از روش بکار گرفته شده توانستیم دو ستاره قیفاووسی در ابر ماژلانی کوچک و یک نامزد سوسوزنی در جهت سحابی بارنارد ۶۸ پیدا کنیم. با استفاده از نقشه ی جذب سحابی بارنارد ۶۸، سرخگرایی القا شده بر نور ستارگان پشت آن را تصحیح کردیم و با رسم نمودار رنگ-قدر، ستاره های رشته اصلی را از غول های سرخ تفکیک کردیم. با استفاده از داده های آزمایش اروس همین کار را برای ستاره های ابر ماژلانی کوچک انجام دادیم. با تخمین زدن نوع ستارگان و فواصلشان از ما توانستیم اندازه ی زاویه ای شان را تخمین بزنیم. با دانستن اندزه زاویه ای و پراکندگی شار هر ستاره، از رابطه ی بدست آمده از شبیه سازی استفاده کردیم و شعاع پخش هر راستای دید را برای هر چهار هدف تخمین زدیم. عمق نوری سوسوزنی بنابر تعریف احتمال مشاهده ی راستای دیدی است که شعاع پخش آن از مقداری داده شده کمتر باشد. ما حد بالای عمق نوری سوسوزنی را برای شعاع پخش های اندازه گیری شده در راستا های دید چهار هدف را محاسبه کردیم. مطابق مدل، عمق نوری سوسوزنی ابرها ی شفاف واقع در هاله برای شعاع های پخش بزرگتر از ۲۰ کیلومتر کمتر از یک درصد است. ما نشان دادیم که برای قبول یا رد این مدل به یک میلیون ستاره-ساعت رصد احتیاج است. با این مقدار رصد می توانیم مجموعه ی آماری فراگیرتری داشته باشیم و دقت بیشتری در اندزه گیری پراکندگی شار و در نتیجه شعاع پخش بدست آوریم.

روش بکار رفته در این رساله را می توان برای بررسی افت خیز موضعی چگالی در محیط بین ستاره ای بکار برد.

Résumé Français

Les expériences de recherche de microlentilles ont montré que les objets massifs compacts ne représentent pas une composante importante de la matière noire baryonique. Par conséquent, l'hydrogène moléculaire diffus et froid peut être l'un des candidats ultimes à la composante baryonique cachée de la Galaxie. De tels nuages moléculaires, supposés primordiaux, auraient une température inférieure à 10 K, et donc un rayonnement thermique insignifiant. Par ailleurs, compte tenu de la symétrie de la molécule d'hydrogène, elle ne peut interagir de manière résonante avec les ondes électromagnétiques qu'aux longueurs d'onde plus courtes que l'ultraviolet, ce qui ne peut être détecté par un observateur terrestre. Ces nuages doivent donc être considérés comme essentiellement transparents.Pour détecter cette matière gazeuse invisible, nous proposons de surveiller des étoiles d'arrière-plan avec une cadence élevée (de l'ordre d'une fois par minute) et d'analyser leurs courbes de lumière à la recherche de la signature d'effet de scintillation. Si la turbulence du milieu est suffisamment forte, elle peut produire des fluctuations de densité qui perturbent le front d'onde de la lumière d'une source d'arrière-plan. Le front d'onde, déformé par les retards de phase, se propage selon les lois de la diffraction optique, qui induisent des fluctuations d'intensité dans le plan d'un observateur. Etant donnés les mouvements relatifs entre le nuage et la ligne de visée, la figure de diffraction balaie le plan de l'observateur ce qui fait que la source en arrière-plan semble scintiller. Le contraste des variations lumineuses dépend des distances relatives entre la source, le nuage et l'observateur, et de l'importance des fluctuations de densité du nuage. Des échelles de temps caractéristiques régissent le phénomène, qui dépendent en particulier de la longueur d'onde. Il est alors possible de distinguer une source scintillante de toute autre variabilité intrinsèque (périodique ou non) par des observations à plusieurs longueurs d'onde.
En observant un grand nombre d'étoiles situées derrière un milieu turbulent, on peut établir des limites à l'intensité des turbulences locales (liée au rayon de diffusion) le long de la ligne de visée et sonder les structures les plus fines du milieu. Nous avons simulé numériquement l'effet de scintillation. En considérant les nuages comme des écrans

minces, nous avons utilisé le spectre de la fonction 2D qui décrit les retards de phase à partir de la loi de Kolmogorov, afin de simuler des écrans de phase. Nous avons étudié l'impact des limitations du calcul numérique sur la génération de la fonction de retard de phase. La figure de diffraction produite par une source ponctuelle sur le plan d'observation a été obtenue par le calcul de l'intégrale de diffraction de Huygens-Fresnel. Nous avons établi que la figure produite par une source étendue s'obtient par convolution avec le profil de cette source, et quantifié la perte de contraste due à cette limitation de la cohérence spatiale. Grâce à la simulation, nous avons dérivé une relation entre la modulation des courbes de lumière de scintillation et le rapport du rayon projeté de la source à la longueur caractéristique de scintillation. Cette relation peut être utilisée pour relier la dispersion de flux observée d'une étoile à des paramètres de scintillation (rayon de diffusion, rayon projeté de l'étoile). Nous avons également examiné l'effet de la cohérence temporelle de la lumière en superposant des figures de diffraction produites à des longueurs d'onde proches. Deux nuits d'observations ont été obtenues vers quatre directions avec le détecteur SOFI du NTT de l'ESO (en infrarouge proche). Trois des cibles étaient des nébuleuses sombres connues situées dans le disque galactique. Nous les avons utilisées pour tester la faisabilité de la détection de scintillation. La quatrième cible était le petit nuage de Magellan (SMC), choisi pour rechercher des structures turbulentes transparentes dans le halo de la Voie-lactée. Après réduction et nettoyage des données, nous avons sélectionné les courbes de lumière qui présentaient la plus grande variabilité (dispersion de flux). Grâce à notre méthode de sélection, nous avons (re)trouvé deux céphéides dans le SMC et un candidat à la scintillation vers la nébuleuse sombre Barnard 68. Après avoir corrigé les magnitudes des étoiles observées à partir de la carte d'absorption de Barnard 68, nous avons pu tracer leur diagramme couleur-magnitude (Ks-J), ce qui nous a permis de distinguer les étoiles de séquence principale (potentiellement plus fortement scintillantes) des géantes rouges. Le même travail a pu être mené pour les étoiles de SMC avec les bandes B et R, en utilisant de base de données de EROS. En estimant ainsi les types stellaires et les distances, nous avons calculé la taille angulaire des étoiles d'arrière-plan. A partir de cette taille apparente et de la dispersion des courbes de

lumière, nous avons pu déduire les limites inférieures des rayons diffusion du gaz le long de chaque ligne de visée.

Nous avons défini la profondeur optique de la scintillation comme la probabilité d'intercepter une structure turbulente avec un rayon de diffusion inférieur à une valeur donnée. Nous avons calculé la limite supérieure de cette profondeur optique en fonction d'un rayon de diffusion maximum selon chacune des directions étudiées. Un modèle de matière baryonique cachée sous forme de nuages moléculaires transparents prédit une profondeur optique de scintillation inférieure à un pour cent pour des rayons de diffusion supérieurs à ~20 km ; nous avons montré que l'observation de près d'un million d'étoiles x heures avec une précision photométrique meilleure que 1% est nécessaire pour confirmer ou exclure un tel modèle.Au delà de la recherche de matière baryonique cachée, la méthode que nous proposons peut aussi être utilisé comme un outil pour étudier les fluctuations de densité locale du milieu interstellaire.

Contents

Chapter 1

Missing Baryon Problem

About 80 years ago the mass discrepancy for the cosmic structures was revealed by observations. Although it is widely believed that the major part of the dark matter consists of Weakly Interacting Massive Particles (WIMPs, which are unknown non-baryonic matter), there is also hidden parts for the baryonic component of the Universe. Through this chapter, firstly we explain how observations point out the dark matter existence in section 1.1. In section 1.2, the standard Big Bang nucleosynthesis is discussed and the observation of the primordial light elements is given. Finally in section 1.3, the observed baryonic content of the cosmic structures is compared to the expectations from nucleosynthesis and CMB observations.

1.1 Evidences for Dark Matter

In this section, we review some essential works in mass measurements at cluster and galactic scales. Through these observations, we show that the dark matter is necessary in order to explain the significant discrepancy between the luminous mass and the dynamical mass obtained from rotation curves and velocity dispersions.

1.1.1 Dark Matter at Cluster Scale

The first astronomer who discovered the mass to light ratio discrepancy was F. Zwicky. In 1933, he determined the mass of the Coma cluster by measuring the radial velocity of the galaxies and using the Virial theorem. He compared this dynamical mass to the luminous mass of the galaxies using the stellar mass to light ratio and found the unexpected mass deficit of a factor of ~ 100 times compared to the luminous mass [Zwicky (1937)].

Virial Theorem

Consider a galaxy cluster of mass M with N galaxies of masses m_i. Choosing the centre of mass of the system as the origin of the reference frame, the total gravitational force

acting on mass m_i is:

$$\mathbf{F_i} \;=\; m_i \,\frac{d\mathbf{v_i}}{dt}, \tag{1.1}$$

where $\mathbf{v_i}$ is the galaxy velocity vector of galaxy i relative to the cluster centre of mass. Scalar multiplication of this equation with $\mathbf{r_i}$ gives:

$$\mathbf{r_i}.\mathbf{F_i} \;=\; \frac{1}{2}\,\frac{d^2}{dt^2}\,(m_i\, r_i^2) \;-\; m_i\, v_i^2, \tag{1.2}$$

where we have used $\mathbf{v_i} = \frac{d}{dt}\mathbf{r_i}$. The scalar variables r_i and v_i are the modulus of the distance and velocity vectors with respect to the mass centre. Summing this equation for N masses we obtain:

$$\frac{1}{2}\,\frac{d^2}{dt^2}\,I \;=\; \sum_i^N m_i\, v_i^2 \;+\; \sum_i^N \mathbf{r_i}.\mathbf{F_i}, \tag{1.3}$$

where $I = \sum m_i\, r_i^2$ is proportional to the system moment of inertia[1]. For the total kinetic energy we have:

$$K \;=\; \frac{1}{2}\sum_i^N m_i\, v_i^2 \;=\; \frac{1}{2}\,M\,\sigma_v^2, \tag{1.4}$$

where σ_v^2 is the velocity dispersion of the galaxies[2]. The total gravitational energy is:

$$U \;=\; \sum_i^N \mathbf{r_i}.\mathbf{F_i} \;=\; \sum_{\mathbf{i}} \sum_{\mathbf{j<i}} \mathbf{r_i}.\frac{\mathbf{G\,m_i\,m_j}}{|\mathbf{r_i}-\mathbf{r_j}|^{\mathbf{3}}}\,(\mathbf{r_i}-\mathbf{r_j}). \tag{1.5}$$

Considering two recent relations, the equation (1.3) can be re-written as:

$$\frac{1}{2}\,\frac{d^2}{dt^2}\,I \;=\; 2K \,+\, U, \tag{1.6}$$

For a gravitationally bound system, the moment of inertia changes within a lower and upper bands. Hence, for a sufficiently long time, τ (usually of the order of the time for a galaxy to cross the cluster) the variation of I is zero in average:

$$\frac{1}{2} \,<\, \frac{d^2}{dt^2}\, I \,>_\tau \;=\; 2 \,<\, K \,>_\tau \,+\, <\, U \,>_\tau, \tag{1.7}$$

and the Virial theorem is written as:

$$2 \,<\, K \,>_\tau \,+\, <\, U \,>_\tau \;=\; 0, \tag{1.8}$$

[1] It is exactly the moment of inertia, if (x, y, z) coordinates are chosen along the principal axis of the system.

[2] We recall that in mass centre frame the mean velocity is zero.

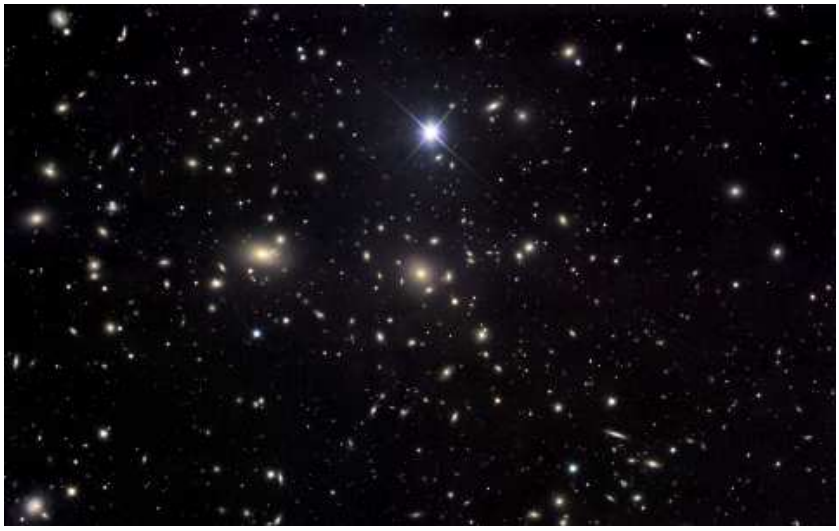

Figure 1.1: Coma cluster by Hubble space telescope.

Approximating a cluster with a homogeneous mass distributed in a sphere with radius R, the total potential energy is given by:

$$U = -\frac{5\,G\,M^2}{3\,R}. \tag{1.9}$$

Substituting this equation and equation (1.4) in relation(2.12), we obtain a relation between the cluster mass and its dispersion velocity $< \sigma_v^2 >$:

$$M = \frac{3\,R\,< \sigma_v^2 >}{5\,G}. \tag{1.10}$$

However, as shown in figure 1.1, Coma cluster is not exactly a uniform distribution of galaxies. Since the inhomogeneities reduce the potential energy compared to uniform mass distribution, Zwicky conservatively assumed a lower limit for potential gravity as:

$$U > -\frac{5\,G\,M^2}{R}, \tag{1.11}$$

and from the Virial theorem the lower limit of the cluster mass is obtained as:

$$M > \frac{R\,< \sigma_v^2 >}{5\,G}. \tag{1.12}$$

Zwiky observed the spectra of bright galaxies of Coma cluster and measured their radial velocity dispersion:

$$< \sigma_r^2 > = 5 \times 10^5\,\mathrm{km^2\,s^{-2}}. \tag{1.13}$$

For a velocity dispersion of spherical symmetry we have $< \sigma_v^2 > = 3 < \sigma_r^2 >$. The velocity dispersion is thus:

$$< \sigma_v^2 > \;=\; 1.5 \times 10^6 \,\mathrm{km^2\,s^{-2}}. \tag{1.14}$$

σ_v^2 is computed by averaging the square velocity of each galaxy regardless of their masses. It is not thus the exact weighted average computed from relation (1.4). This would not affect the order of magnitude of the calculated M since the observed bright galaxies have more or less all the same mass. Considering a size of $R \sim 1000$ kpc for Coma cluster, the minimum mass of the cluster through relation (1.12) is estimated as:

$$M > 4.5 \times 10^{13}\, M_\odot, \tag{1.15}$$

Zwicky had counted the number of galaxies as $N = 1000$. For a typical galaxy, he estimated a luminous mass of $M_g = 8.5 \times 10^7 M_\odot$ which gives the luminous mass of the cluster as $8.5 \times 10^{10} M_\odot$. Comparing this value to the mass computed in relation (1.15) and assuming that light traces the mass, the mass to light ratio of Coma cluster is:

$$\Gamma_* \;=\; 500\, \frac{M_\odot}{L_\odot}, \tag{1.16}$$

which is a quite large number compared with $\Gamma_* = (1\text{-}3)\, \frac{M_\odot}{L_\odot}$ observed in stellar systems.

This result is obtained by assuming that the cluster is a virialised system. This is a reasonable assumption since the cosmic structures are existing for billions of years in gravitationally bound systems. Assuming the usual stellar mass to light ratio for the cluster beside the observed dispersion velocity of ~ 1000 km s^{-1} leads to $K \gg -U$ and the galaxies would fly apart from each other. Therefore, the matter is missing by a factor of ~ 100 at cluster scale. It was the first evidence for existence of the dark matter.

1.1.2 Dark Matter at Galactic Scale

The mass discrepancy became more crucial when astronomers began measuring the rotational velocity of the galaxies. Consider a star located at the outer part of the luminous disk of a spiral galaxy, rotating in a circular Keplerian orbit about the galactic nucleus, the star rotation velocity V_c is given from Newton's law:

$$V_c \;=\; \sqrt{\frac{G\, M_R}{R}}, \tag{1.17}$$

where M_R is the galactic mass inside radius R and G is the gravitational constant. Through this relation, we expect that the rotation velocity decreases by $1/\sqrt{R}$ while we pass beyond the galactic luminous disk. As an unexpected result, the Keplerian decline was

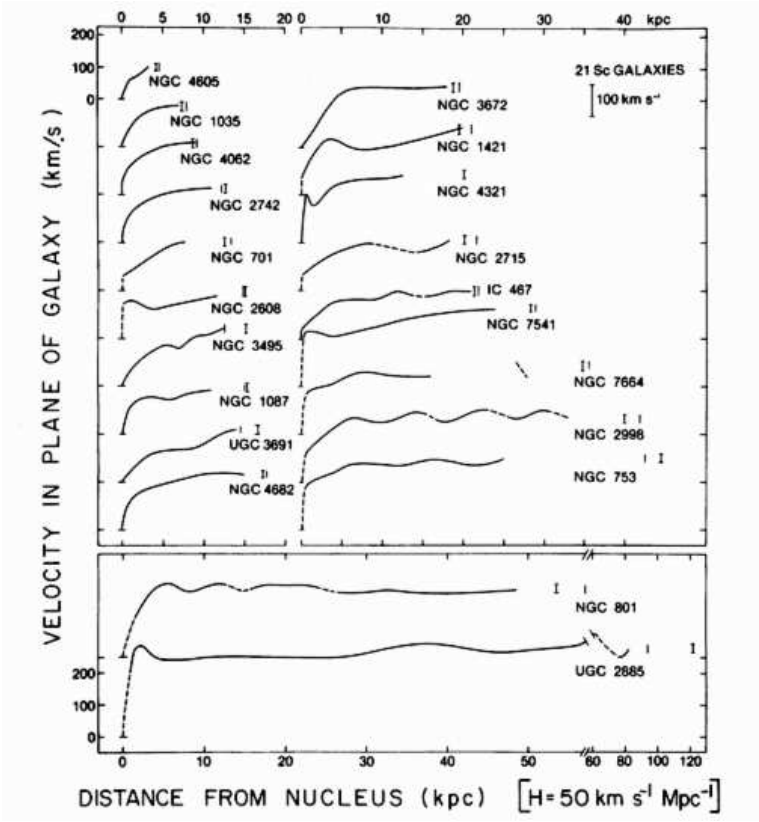

Figure 1.2: Rotation curves of 21 Sc galaxies within optical disk ordered by increasing size. Each curve is derived from mean velocities on both sides of the major axis. Dashed lines from the nucleus indicate regions where velocities are not available due to the small scale. Dashed lines at larger R indicate a velocity fall faster than Keplerian which is the evidence for galactic streams at galactic arms [Rubin et al. (1980)].

not confirmed by the observed rotation curves[3] for all disk galaxies. Instead, beyond the galactic central part, a relatively constant V_c was observed.

During 70's Rubin and her colleagues derived the rotation curves of some spiral galaxies. In one of their works [Rubin et al. (1980)], they studied the rotational properties of 21 Sc galaxies with luminosity range from 3×10^9 to 2×10^{11} $L_\odot$, masses from 10^{10} to 2×10^{12} $M_\odot$ and radii from 4 to 122 kpc. The selected galaxies had inclinations larger than 50^o to minimise the orbital velocity uncertainties. They determined the star velocities by detecting Hα (λ = 6548 Å) and [NII] (λ = 6583 Å) emission lines. The spectroscopy was done along the galactic plane by aligning the slit of the spectrograph with the galactic major axis. The velocities were estimated from the measured red-shift (or blue-shift) of

[3]The rotation curve is the rotation velocity of the galactic components versus their distance from the galactic centre.

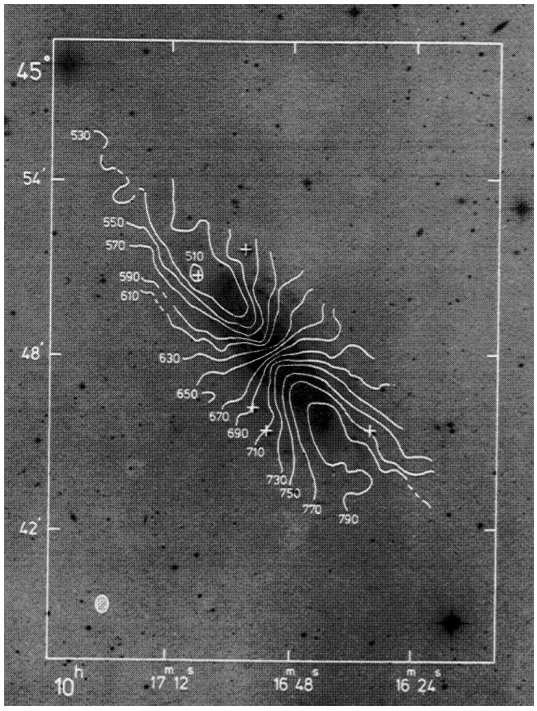

Figure 1.3: Radial velocity field in NGC 3198 superimposed on the optical image. The number for each contour indicates the heliocentric velocity in km s^{-1} [Bosma (1981)].

the emission lines through the relation: $V = c(\lambda - \lambda_0)/\lambda_0$ with accuracy of $\pm$ 3 km s^{-1}.

As illustrated in figure 1.2, no galaxy shows velocity which decreases significantly at large nuclei distance. Most galaxies exhibit rotational velocities which are increasing to the edge of the optical disk. It implies that rotation curves are still rising beyond the optical disk. The largest galaxies (e.g. UGC 2885) have flat rotation curves. All big and small galaxies show similar patterns of rotation curves. The velocity rise significantly within about 5 kpc and more slowly thereafter and the curve is flat at large R. Through these behaviours, Rubin and her colleagues concluded that the mass is not centrally condensed and significant mass is located at large R. The mass within the radius R should increase at least as fast as R since from relation (1.17) for flat V_c we should have $M \sim R$. The mass does not seem to be limited at the edge of the optical disk and consequently, non-luminous mass exists beyond the optical galaxy. The authors suggested that HI 21 cm observations[4] can clarify this point.

In 1981, A. Bosma published the detailed HI line maps of 25 spiral galaxies by using the Westbrok Synthesis Radio Telescope [Bosma (1981)]. The contours in figure 1.3 show regions with same velocities for NGC 3198. The spatial resolution is roughly 2 kpc. As it

[4]The interaction between nuclear and electronic spins of the atomic hydrogen produces 21 cm emission.

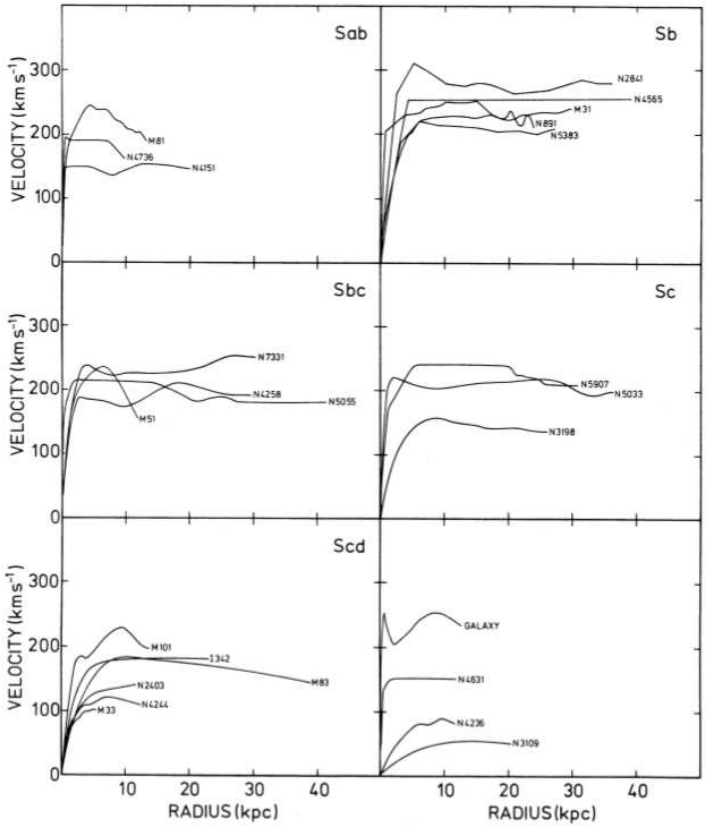

Figure 1.4: Rotation curves of 25 different spiral galaxies [Bosma (1981)].

is shown, the neutral hydrogen clouds are well distributed beyond the optical disk. Resolution depends on B/R ratio, where B is the telescope beam[5] and R is the scale of the observed region. If this ratio is larger than unity for inner parts the fast velocity change remains undetected. Therefore, to derive the rotation curves, Bosma used the available optical data for inner parts of the galaxies. It can be inferred from figure 1.4 that the observed rotation curves are flat or decline slowly and none of them become Keplerian in outer parts. The mass hence, does not converge to a final value at outermost observed distance from nucleus.

Since the stability of the disk is in question if all unseen matter is distributed in galactic plane, Ostriker, Peebles and Yahil proposed the existence of a massive hot halo, maximally extended up to 500 kpc, to stabilise the optical disk [Ostriker et al. (1974)]. In 1985, van Albada and his colleagues constructed a two-component mass model to fit the rotation curve of NGC 3198. The model consists of an exponential disk and a spherical

[5]Field of view.

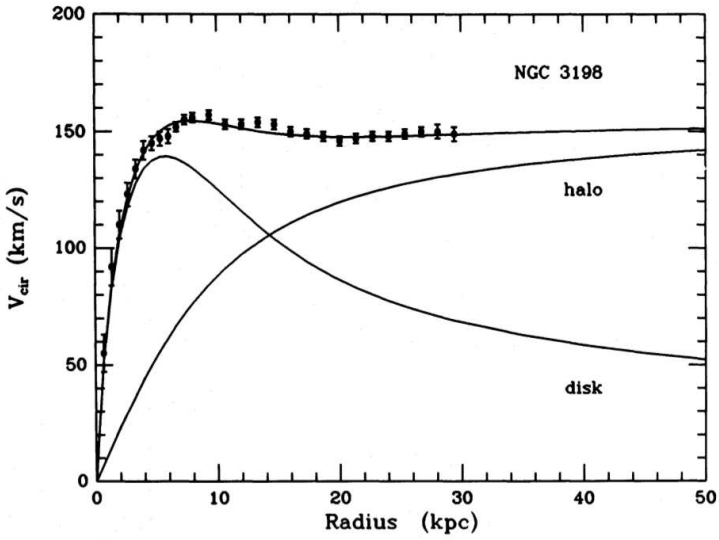

Figure 1.5: Contribution of the maximum disk and spherical halo model to the observed rotation curve of NGC 3198. The length scale of the disk is 2.68 kpc. The halo curve corresponds to a = 8.5 kpc and γ = 2.1 with $\rho(R_0)$ = 0.0040 $M_\odot$ pc^{-3}. The points represent the measured velocities including the error bars. Halo mass is $\sim$ 10 times the disk mass [van Albada et al. (1985)].

dark halo [van Albada et al. (1985)]. They consider an exponential law, $I(R) = I_0\, e^{-R/h}$, for the light distribution where h is the characteristic length scale of galaxies. For Hubble parameter H_0 = 75 km s^{-1} Mpc^{-1}, they found h = 2.68 kpc and measured the HI distribution to 11 scale lengths. For the disk contribution, they considered a model with largest disk mass (maximum disk considering the largest stellar mass to light ratio and 15% HI contribution to the disk mass) with an exponential density profile of same length scale as the light distribution. For density profile of the spherical dark halo they considered a model as:

$$\rho_{halo} \;=\; \rho_0\,[(\frac{a}{R_0})^\gamma \,+\, (\frac{R}{R_0})^\gamma]^{-1}, \tag{1.18}$$

where R_0 is chosen to be 8 kpc. a and γ are free parameters which are related to the halo core radius and density decreasing rate . The fit result is shown in figure 1.5. Within 30 kpc the measured mass (stars + HI) is 3.1 $\times$ 10^{10} $M_\odot$ computed from disk curve. The halo mass is 1.5 $\times$ 10^{11} $M_\odot$.

1.2 Standard Big Bang Nucleosynthesis

When the Universe was 10^{-11} second old, all four fundamental forces were already distinct. At this epoch, the temperature of the Universe was $\sim 10^{15}$K ($\sim$1000 GeV) and the

Universe was filled with a soup of quarks, leptons, photons, anti-quarks and anti-leptons. Such temperature is still too high to permit any stable baryon formation. By cooling the Universe, more massive types of quarks and leptons decay to their lighter counterparts. Matter and antimatter annihilate and at the end a small excess of matter left to form the baryons. The baryon formation starts effectively at $\sim 10^{-5}$s, when the temperature is $\sim 10^{12}$K ($\sim$1 GeV), by combining up and down quarks to create stable protons and neutrons. At this temperature protons and neutrons are in thermal equilibrium and convert to each other via weak interactions[6]:

$$\begin{aligned} n &\rightleftarrows p + e^- + \bar{\nu_e}, \\ p + \bar{\nu_e} &\rightleftarrows n + e^+, \\ n + \nu_e &\rightleftarrows p + e^-. \end{aligned} \tag{1.19}$$

The statistics of the baryons are given by the Boltzmann distribution:

$$n_b = 2(\frac{m_b k_B T}{2\pi\hbar^2})^{\frac{3}{2}} \exp(-\frac{m_b c^2}{k_B T}), \tag{1.20}$$

where, n_b, m_b and k_B are the baryon number density, the baryon mass and the Boltzmann's constant respectively. Hence, the ratio between number densities of neutrons and protons is given by the equation:

$$\begin{aligned} \frac{n_n}{n_p} &= (\frac{m_n}{m_p})^{\frac{3}{2}} exp(-\frac{Q}{k_B T}) \\ &\simeq exp(-\frac{1.5 \times 10^{10}\, K}{T}), \end{aligned} \tag{1.21}$$

where m_p = 938.3 MeV and m_n = 939.6 MeV are proton an neutron masses respectively; $Q = (m_n - m_p)c^2$ = 1.3 MeV $\equiv 1.5 \times 10^{10}$ K. Therefore, for temperatures $\gg 10^{10}$ K, there are approximately equal numbers of neutrons and protons. By expanding the Universe and reducing the temperature, the neutrons will more likely decay to protons than be created from them, thus, the number of protons start to increase slightly.

The reactions (1.19) are dominant as long as the weak interaction rate (Γ_{weak}) is greater than the expansion rate of the universe (H). In other words, when the characteristic time scale of the weak interaction becomes smaller than the Hubble time, the neutrinos decouple from the baryons and the thermal equilibrium is not hold anymore. The only reaction which remains is the β decay of the free neutrons: $n \longrightarrow p + e^- + \bar{\nu_e}$. The weak interaction rate is proportional to $G_F^2 T^5$, where G_F is Fermi's coupling constant. From Friedmann's equation for a flat universe $H^2 = \frac{8\pi G}{3}\rho$; during the radiative era ρ (total

[6]The general concepts and calculations of this section are gathered form [Coles & Lucchin (2002)], [Liddle (2003)] and [Palanque-Delabrouille (1997)].

density) is dominated by radiation and is proportional to $N_\nu T^4$, where N_ν is the number of neutrino species. Thus:

$$\begin{aligned} \frac{\Gamma_{weak}}{H} &\sim \frac{G_F^2 T^5}{T^2 N_\nu^{\frac{1}{2}}}, \\ \frac{\Gamma_{weak}}{H} &\simeq (\frac{k_B T}{0.8\text{MeV}})^3 = (\frac{T}{9.3\times 10^9 K})^3. \end{aligned} \tag{1.22}$$

At temperature $T_{d\nu} \sim 9.3 \times 10^9$ K, ($t \sim 1\, s$) the Universe expands faster than the weak interaction rate, which means it is cool enough to let neutrinos decouple from the baryons. From relation (1.21) the neutron to proton ratio freezes out at value:

$$(\frac{n_n}{n_p})_{freeze-out} \simeq 0.2. \tag{1.23}$$

1.2.1 Light Elements: Production

After neutrinos decoupling from baryons, synthesis of light elements (H, D, ^{3}He, ^{4}He, Li) begins by producing deuterium:

$$n + p \longrightarrow D + \gamma. \tag{1.24}$$

At a temperature lower than the binding energy of deuterium (B_D = 2.2 MeV), since baryon to photon ratio is low ($\eta = \frac{n_b}{n_\gamma} \sim 10^{-10}$), the energetic photons of the tail of Planck spectrum are sufficient to dissociate these " bottle-neck" deuteriums. The photo-dissociation of deuterium prevents the creation of more complex nucleus, but this destruction gets less and less important as the Universe expands and becomes cooler. Finally, at $T \sim 0.1$ MeV the production of light nucleus is effectively finished ($t \sim 1$ min.). During this epoch the density of the baryons is so low ($\sim 10^{-3}$ g cm^{-3}) that only two-body reactions are possible (three-body chain reactions occur inside the stars). These reactions include:

$$\begin{aligned} D + p &\longrightarrow {}^3He, \\ D + n &\longrightarrow {}^3H, \\ D + D &\longrightarrow {}^4He, \\ &\ldots \end{aligned} \tag{1.25}$$

From freeze-out time of weak interactions ($\sim$ 0.8 MeV) it takes about $\Delta t \sim 400$ s to the end of the nucleosynthesis[7]. Since the lifetime of a neutron is $\tau_n = 886s$, the β decay of neutrons is not negligible during the synthesis process. So, the neutron to proton ratio at $T \sim 0.1$ MeV ($t \sim 1$ min.)will be:

$$(\frac{n_n}{n_p}) = (\frac{n_n}{n_p})_{freeze-out} \times 2^{-\frac{\Delta t}{\tau_n}} \simeq 0.14. \tag{1.26}$$

[7] In radiative era $(\frac{t}{1s}) = \frac{2\times 10^{10} K}{T} = \frac{2MeV}{k_B T}$

We may also take into account the increase in number of protons because of the neutron decays but it is quite small fraction. The most abundant elements of the primordial nucleosynthesis are hydrogen and helium. Helium is formed because it is the most stable light element. Almost all neutrons combine with the same number of protons to produce He nucleons. The rest of protons remain as hydrogen nucleons since there are no more neutrons to bind with. The primordial helium content of the Universe is regarded as the ratio between the produced helium mass to the total baryonic mass:

$$Y_p = \frac{M_{He}}{M_b}, \tag{1.27}$$

where $M_b = (n_n + n_p)m_p$. Since He nucleus consists of two neutrons and two protons, half of the neutrons should bind with the same number of protons to form helium; so, $M_{He} = 4m_p \times \frac{1}{2}n_n$ where proton and neutron masses are taken to be equal. The corresponding helium fraction will be:

$$Y_p = \frac{2\frac{n_n}{n_p}}{1+\frac{n_n}{n_p}} = 0.25, \tag{1.28}$$

where $\frac{n_n}{n_p}$ is taken from relation (1.26). Therefore, about 25% of primordial baryons of the Universe are in form of helium and 75% remaining are essentially hydrogen. The fraction of produced helium slightly depends on η. Larger baryon to photon ratio results in less photo-dissociation of the bottle-neck deuteriums which gives shorter time to neutrons to decay. Therefore, the larger the amount of neutrons is, the larger the helium fraction will be.

It is worthy here to mention that N_ν (number of neutrinos species) affects the ultimate number of neutrons by changing the freeze-out temperature of the weak interactions. Higher N_ν means greater $T_{freeze-out}$ which gives higher $(\frac{n_n}{n_p})_{freeze-out}$. This would produce larger fraction of ^{4}He. Therefore, the observation of the primordial ^{4}He constrains the number of neutrinos species. One of the successes of the Big Bang nucleosynthesis is that $N_\nu = 3$ gives the best agreement between the observations and what standard Big Bang nucleosynthesis (hereafter SBBN) predicts.

Reaction chains of light element production during SBBN are sketched in figure 1.6. The traces of remained deuterium can be combined with the protons to produce ^{3}He. This element can be made also from the decay of ^{3}H which were formed from combination of the deuterium with the rarely survived neutrons. The abundance of deuterium and ^{3}He decrease when η increases since larger η gives more neutrons that are more likely to be incorporated in ^{4}He.

The last production of the SBBN is ^{7}Li which has a very small contribution to the primordial synthesised elements. The combination of the rare ^{3}He or ^{3}H with ^{4}He make

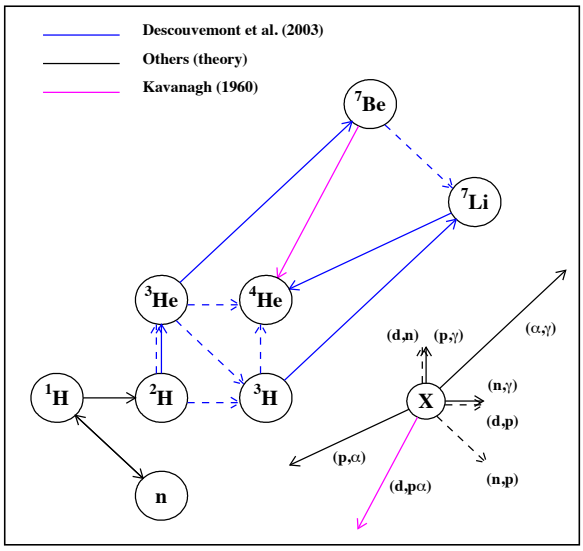

Figure 1.6: Reaction chain of the primordial light elements synthesis [Coc et al (2004)].

either ^{7}Li or ^{7}Be where the latter breaks to ^{7}Li and neutrino by capturing a neutron. ^{7}Li abundance varies differently with respect to η. For smaller baryon to photon ratio (low densities) ^{7}Li is produced mostly from ^{3}H and decreases with η; while in higher density it is formed from decay of ^{7}Be which were made from ^{3}He and increases with η.

No elements remain with mass number of 5 and 8 and the BBN effectively stops at ^{7}Li. This occurs because in one hand, ^{4}He is a tightly bound element and makes the heavier elements unstable:

$$\begin{aligned} {}^5Li &\longrightarrow {}^4He + p \quad (\tau \simeq 10^{-22}), \\ {}^5He &\longrightarrow {}^4He + n \quad (\tau \simeq 10^{-22}), \\ {}^8Be &\longrightarrow {}^4He + {}^4He \quad (\tau \simeq 10^{-16}). \end{aligned}$$

On the other hand, as mentioned before, because of low density of baryons the three-body reactions are negligible until the star formation begins.

1.2.2 Light Elements: Observations

According to the standard Big Bang nucleosynthesis, the primordial abundances only depend on the baryon to photon ratio η. These dependencies are shown in figure 1.7.

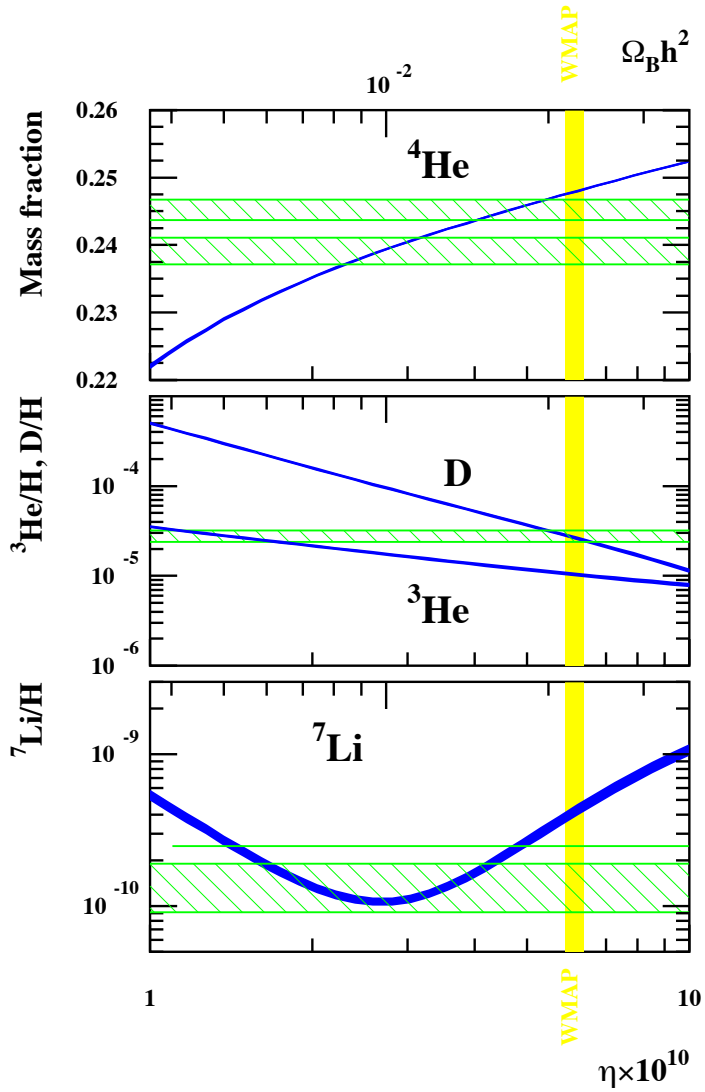

Figure 1.7: Numerical estimates of the primordial light element abundances as a function of the baryonic density, determined from SBBN model. The yellow strip is the observed range of η given from WMAP. The green lines come from direct observations of the primordial elements which are presented more precisely in the next figures.

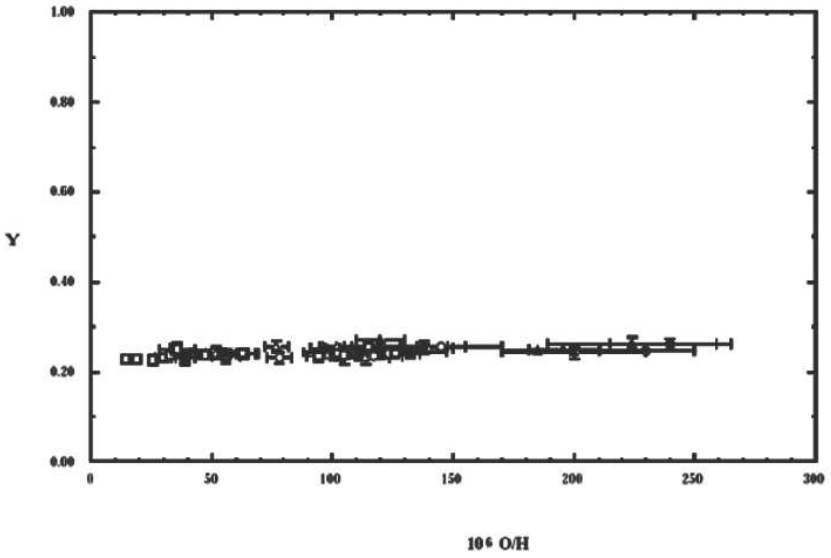

Figure 1.8: ^{4}He Mass fraction (Y) variations vs. metallicity in metal-poor regions of HII

Besides, determination of η value gives the current baryonic content of the Universe:

$$\begin{aligned} \Omega_b &= \frac{\rho_b^{(0)}}{\rho_c} = \frac{M_p n_b}{\rho_c} \\ &= \frac{M_p n_\gamma}{\rho_c}\eta, \end{aligned} \tag{1.29}$$

where M_p is the proton mass and ρ_c is the critical density of the Universe[8]. From observation of microwave background radiation the current number density of photons is [9] $n_\gamma \simeq 410.5$ cm^{-3}; so, equation(1.29) can be written as: ([Steigman (2006)]):

$$\eta_{10} = (273.9 \pm 0.3)\Omega_b h^2$$

where $\eta_{10} = \eta \times 10^{10}$. Therefore, measuring the primordial light elements provides a strong constraint on the baryonic content of the Universe.

Helium 4

After hydrogen, ^{4}He is the most abundant element among others but its abundance has the faintest dependency on η. The most accurate way to determine Y_p is to search heliums in extragalactic HII regions[10] with low metallicity contributions to avoid stellar effect on He

[8] $\rho_c = \frac{3H^2}{8\pi G} \simeq 1.8784 \times 10^{-29}$ gr cm^{-3}.

[9] Assuming no extra photons were produced after finishing the BBN.

[10] Hot clouds of hydrogen which is ionised because of the radiations from the newly born stars.

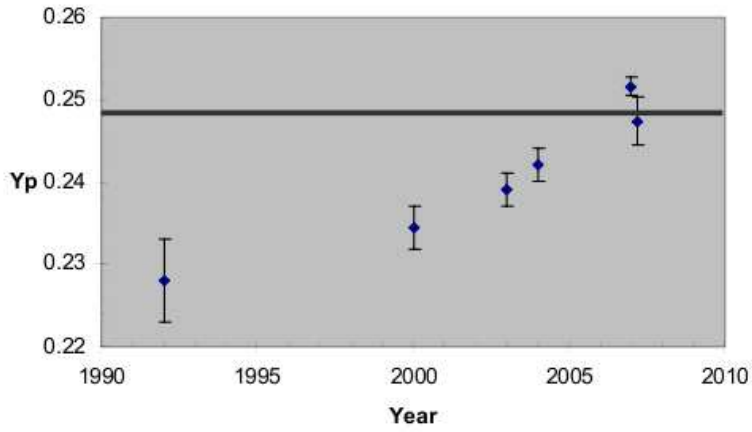

Figure 1.9: Determinations of primordial ^{4}He during recent years. These values are measured from metal-poor HII regions. The last point is measured by [Peimbert et al. (2007)] The horizontal solid line is the Y_p computed from SBBN+ WMAP ([Peimbert (2008)])

synthesis. Figure 1.8 shows the variation of ^{4}He vs. one of the metallicity indicators, O/H, in an extragalactic metal-poor HII region. O is the Oxygen abundance, the most common element used to quantify the metallicity since it is the most abundant heavy element[11] in the Universe and is easy to measure. As illustrated in the figure, the measured ^{4}He varies very slowly with the metallicity.

As explained by [Peimbert et al. (2007)], the measured value of Y_p has increased during recent years (Figure 1.9) due to the decrease in systematic errors. These systematics arise mainly from two sources. The first one is the limit on the precision of atomic data measuring the He I emission lines in HII regions. This means that observations with high spectral resolutions are needed; and the second is the uncertainties in thermal modelling of helium in HII regions. Considering these facts, Peimber et al. measured the following value for Y_p:

$$Y_p = 0.2477 \pm 0.0018 \pm 0.0023, \tag{1.30}$$

where the first error is due to the statistics and the second is the systematic error. For the interval $4 \leq \eta_{10} \leq 8$ or equivalently $0.2448 \leq Y_p \leq 0.2512$, we have the relation ([Steigman (2006)]):

$$Y_p = 0.2375 + \frac{\eta_{10}}{625}. \tag{1.31}$$

[11] About 53% of heavy elements in O-poor HII regions is Oxygen.

This relation is computed for $\tau_n = 886.7 \pm 0.8$. By remembering equation (1.30), Ω_b, according to the measured Y_p, will be:

$$\Omega_b h^2 = 0.02122 \pm 0.00663 \iff \eta_{10} = 5.813 \pm 1.81. \quad (1.32)$$

Deuterium

Preliminary searches for primordial deuterium began by observing absorption lines from the metal-rich ISM[12] toward the QSOs[13] [Rogerson et al. (1973)] and gave a limit on D/H value $\sim 10^{-5}$. On the one hand deuterium is a weakly bound nucleus which is easily destroyed and hardly created, on the other hand, it is highly probable that deuterium is depleted due to stellar nuclear activities in metal-rich regions, therefore, the observations give a lower limit on D/H value. Today, by using large telescopes and echelle spectrometers [14], D/H values are essentially measured from the metal-poor HI clouds which are minimally affected by stellar activity and located along the sightline of sufficiently bright QSOs. These clouds should have large column density of hydrogen ($N_{HI} \sim 10^{20}$ cm^{-2}) to give a significant column density ratio $\frac{N_{DI}}{N_{HI}}$ which measures D/H value. Moreover, these gaseous media should be quiescent enough that absorption lines of higher order HI and DI[15] Lyman series can be resolved [16]. These criteria make just about 1% of QSO sightlines suitable for D/H measurements.

Figure 1.10 shows an example of HI and DI absorption lines toward QSO SDSS1558-0031 at z$\sim$2.7 observed by [O'Meara et al. (2006)]. The hydrogen column density is large enough to produce a damped Lyα (DLA) system and shows damping wings, due to absorption, in the Lyman $\alpha - \gamma$ transitions (top panels). This feature makes it possible to fit the absorption profile and obtain a precise measurement of hydrogen column density. The best estimate for HI is $N_{HI} = 10^{20.67\pm0.05}$ cm^{-2} and the width of velocity distribution is 13.56 ± 1.0 km s^{-1}. DI column density is also large, so the transitions line are saturated within the core of the strong absorption lines, but the absorption lines due to transition from higher atomic levels show unsaturated DI absorption (from Lyγ through Lyman-13, lower panels) and are resolved. From this transition, DI column density was estimated to be $N_{DI} = 10^{16.20\pm0.04}$ cm^{-2}. These measurements imply a value of $D/H = 10^{-4.48\pm0.06}$.

The gold-standard set of D/H measurements from quasar absorption lines survey of high z metal-poor clouds, including the explained observations, is illustrated in figure 1.11. The horizontal solid line shows the value of weighted mean of the data, $D/H = 10^{-4.55\pm0.04}$.

[12] Inter Stellar Medium.
[13] Quasi-Stellar Object.
[14] high resolution spectrometers
[15] Neutral hydrogen and deuterium.
[16] Deuterium line has 82 km s^{-1} offset from hydrogen Lyman lines.

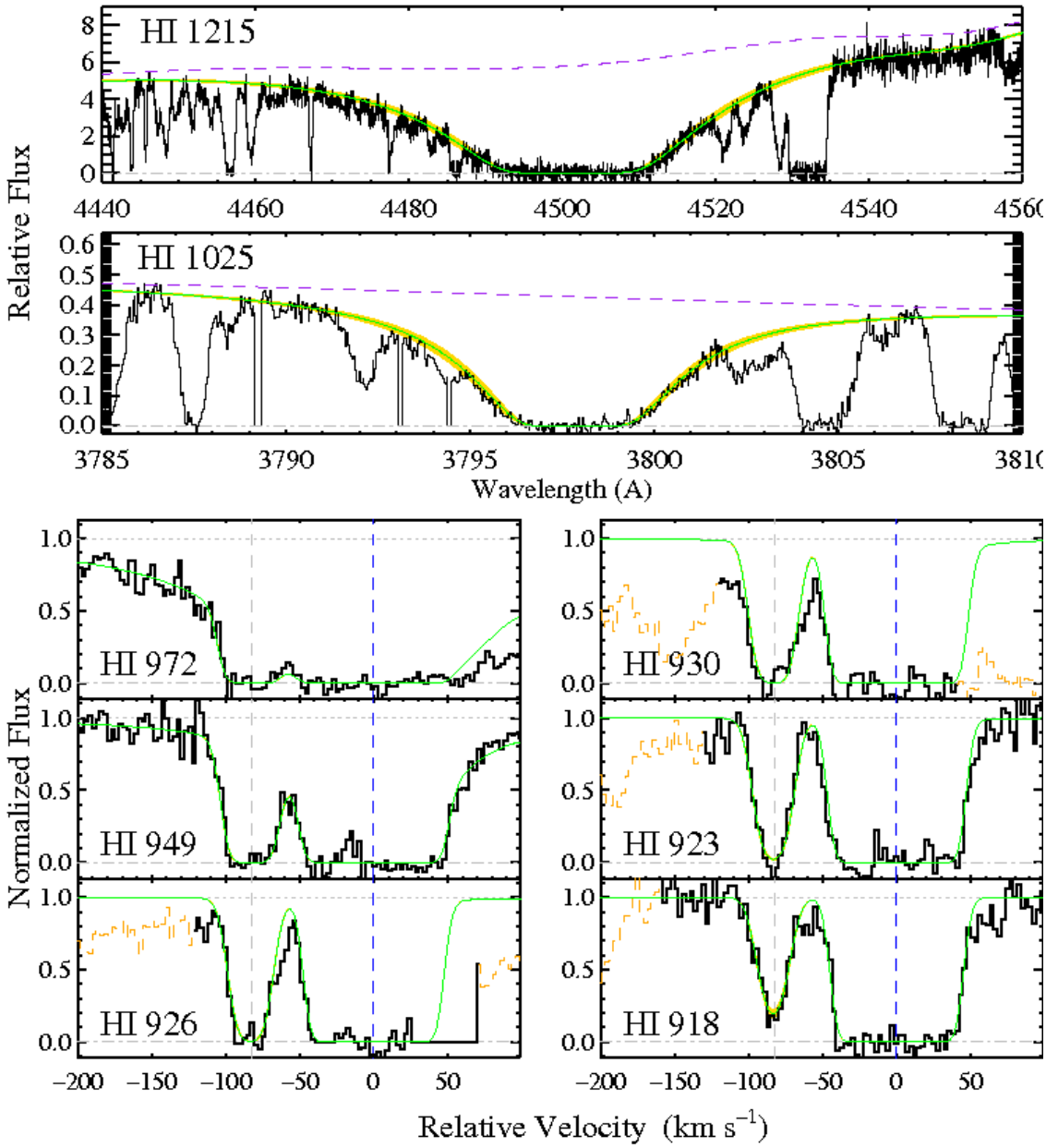

Figure 1.10: HI and DI Lyman series absorption at z = 2.70262, DLA toward SDSS1558-0031 (O'Meara et al. 2006). Lyα and Lyβ transitions are shown at two top panels and the higher transitions are shown in lower panels. The dashed line shows the estimate for the local continuum level. The solid green line shows the best single-component fit to DI and HI absorptions. N_{HI} is estimated from the damping wings present in Lyman $\alpha - \delta$ and N_{DI} from the unsaturated DI Lyman-11 ($\sim$ 918 Å wavelength in rest-frame). Lower panels show the details of the damped region. Absorption at $\sim$ 82 km s^{-1} belongs to DI.

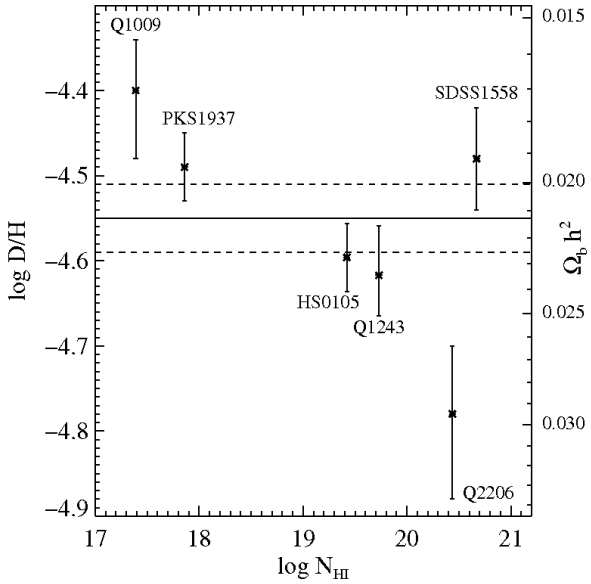

Figure 1.11: Six measurements of D/H vs. $\log N_{HI}$. The right hand axis shows the corresponding values of $\Omega_b h^2$. The solid horizontal line is the weighted mean of the measurements ([O'Meara et al. (2006)]) .

This value corresponds to:

$$\Omega_b\, h^2 \;=\; 0.0213 \pm 0.0013 \iff \eta_{10} = 5.8 \pm 0.7.$$

From WMAP five-year result combined with the distance measurements from the Type Ia supernovae (SN) and Baryonic Acoustic Oscillations (BAO), the baryonic content can be estimated as $\Omega_b h^2 = 0.02265 \pm 0.00059$ [Komatsu et al. (2009)], within the 1σ error of estimate from D/H measurements.

Lithium 7

[Spite & Spite (1982)] discovered that ^{7}Li abundances of very metal-poor ([Fe/H] < -1)[17] Pop II stars of the halo (old stars with effective temperatures T_{eff} > 6000 K) are independent of the temperature and metallicity. Since lithium has a fragile nucleus, it can be depleted inside the core of a star with low mass[18] which has a large convective zone. Thus, the abundance of Li, A_{Li} [19], decreases for lower temperatures. Figure 1.12 shows the variations of observed A_{Li} with respect to the temperature and metallicity. The figure reveals that stars with higher temperature do not suffer from such Li depletion and this explains the flat plateau either vs. metallicity or vs. temperature. It should be mentioned that the

[17] [Fe/H] = log(Fe/H) - log(Fe/H)$_\odot$.

[18] equivalently with lower surface temperature for main sequence stars.

[19] A_{Li}=12 + log(Li/H)

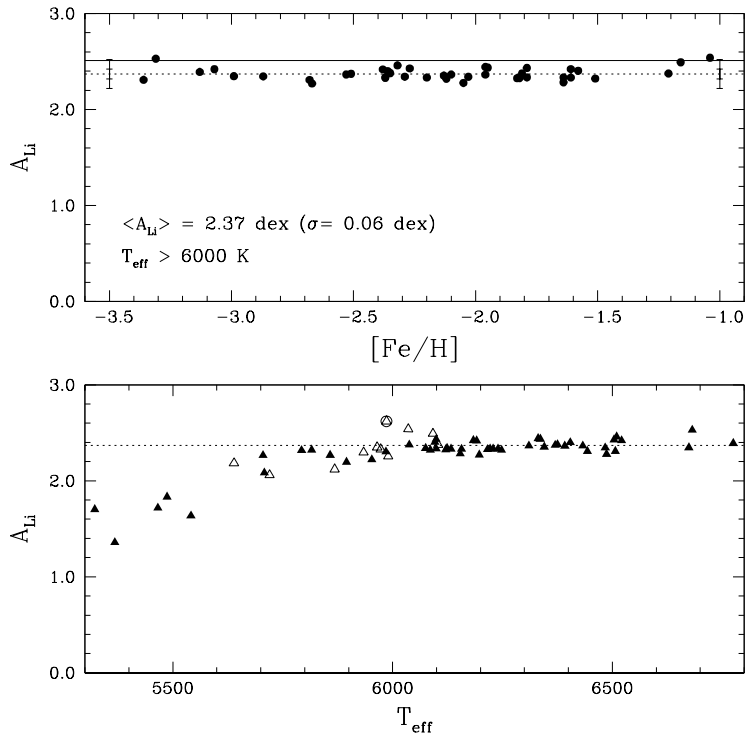

Figure 1.12: Top: Abundance of ^{7}Li in Spite plateau (T_{eff} > 6000 k). The dotted line shows the mean value of the observed abundances and the solid line indicates the predicted value by WMAP+SBBN. The error bars show 1 and 3 sigma dispersions where $\sigma = 0.05$ dex. Bottom: The same as a function of T_{eff}. The filled triangles are measurements of the metal-poor stars with [Fe/H] $\leq$ -1.5 and the open correspond to [Fe/H] > -1.5. The star (HD 106038) with highest Li abundance (open triangle inside the open circle at $t_{eff} \sim 6000$ K) is the star with peculiar abundances ([Nissen & Schuster (1997)])

amount of lithium increases for high metallicity stars (Pop I stars) due to cosmic ray processes and stellar productions. Determining the temperature of the star atmosphere is the most important parameter to obtain Li abundance. Since the metal-poor stars are very far, it is not possible to measure their radii and estimate their temperatures. So, an indirect method should be used. The uncertainties between the different methods cause different reports on A_{Li}. [Melendez & Ramirez (2004)] determined the lithium abundance in 62 halo dwarfs (Figure 1.12) by using the least model-dependent method of temperature measurement. They obtained A_{Li} = 2.37 dex or:

$$\frac{N_{Li}}{N_H} = 2.34 \times 10^{-10} \tag{1.33}$$

Comparing with the abundance derived from WMAP+SBBN, $\frac{N_{Li}}{N_H} = 4.26^{+0.49}_{-0.45} \times 10^{-10}$ [Coc et al (2004)], we see that each other disagree by a factor of about 2. Several possibilities are proposed to explain this discrepancy but none of them is fully successful.

One possibility is the existence of some unknown underestimated systematic errors, specially in the effective temperature estimate, or in the Li abundance measurements of the observed stars. Another possibility is the depletion of ^{7}Li in the plateau stars by diffusion to layers in which ^{7}Li can not be detected. This process needs some form of turbulence at the bottom of convective zone; but the detected ^{6}Li in the atmosphere of the plateau stars rules out such turbulence mechanism as it destroys ^{6}Li. It is also possible that the Galactic chemical evolution has destroyed ^{7}Li. Furthermore, we know that the systematic uncertainties of the nuclear cross sections computing in SBBN model have to be taken into account and also, some authors have proposed a non-standard model of nucleosynthesis[20].

1.3 Observed Baryonic Budget

As the observed light elements reveal a good agreement with the SBBN predictions, it is reasonable to expect the same agreement for the total observed baryonic budget of the Universe. In this section we summarise the observational measurements for the baryonic large structures from dwarf galaxies to galaxy clusters. This leads to the fact that the majority of baryons are hidden especially at galactic scales. At first, we explain how light traces mass for a galaxy embedded in a dark halo through Tully-Fisher relation. This will be followed by comparing the observed baryon fraction at different scales to the cosmic baryon fraction.

1.3.1 Baryonic Tully-Fisher Relation

In 1977, B. Tully and R. Fisher published a paper showing a tight correlation between the luminosity of ten nearby galaxies and their rotation curves at outer disks. Using a single-dish radio telescope, the velocity of the rotation curves were deduced from the width of HI 21 cm line profiles and the apparent inclination of the disks. By knowing the distance and the apparent magnitudes of the galaxies, they computed their absolute magnitudes in blue band [Tully & Fisher (1977)]. The variation of absolute magnitude versus logarithm of velocity is illustrated in figure 1.13. The correlation between the galactic luminosity L and the rotational velocity V_c is a power law:

$$L \propto V_c^b. \tag{1.34}$$

This empirical relation is known as the Tully-Fisher relation. They computed the scaling exponent as $b = 3.1$. Choosing appropriate mass-to-light ratio Γ_* for the observed galaxy stars, the Tully-Fisher relation can be expressed in terms of luminous mass of a galaxy:

$$\begin{aligned} M_\star &= \Gamma_\star L, \\ M_\star &= a_* V_c^b, \end{aligned} \tag{1.35}$$

[20]To find the references look at [Hosford et al. (2009)].

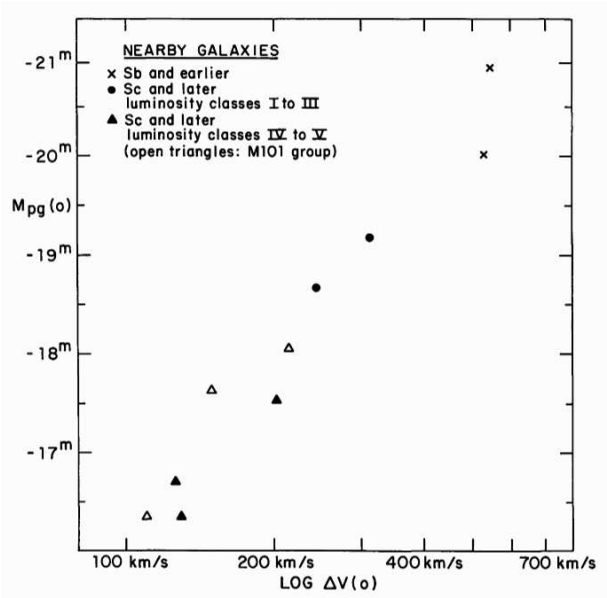

Figure 1.13: Linear correlation between absolute magnitude of nearby galaxies and logarithm of width of the 21 cm line. Crosses are M31 and M81, dots are M33 and NGC 2403, filled triangles are smaller systems in M81 group and open triangles are smaller systems in the M101 group [Tully & Fisher (1977)].

where a_* is a constant number. Γ_* is given in $M_\odot/L_\odot$ unit and is taken to be constant. It changes for different passbands. It is observed that the infrared wavelengths give the best correlation between star luminosity and mass.

In 2000, McGaugh and his colleagues extended the Tully-Fisher relation over five decades in stellar mass and one decade in rotation velocity [McGaugh et al. (2000)]. They used different samples of late-type rotation-supported galaxies observed in different wavelengths. They showed that for field galaxies with low surface brightness and $V_c \leq 90$ km/s the luminosity versus line width relation is systematically below the Tully-Fisher relation (figure 1.14a). Different colours stand for samples observed in different passbands; Blue: B band with $\Gamma_*^B = 1.4$, green: I band with $\Gamma_*^I = 1.7$, red: H band with $\Gamma_*^H = 1.0$, black: K' band with $\Gamma_*^{K'} = 0.8\ M_\odot/L_\odot$. Tthe field galaxies are faint but their gas content overweighs the stars in most of them for any plausible stellar mass-to-light ratio. The gas dominance allows us to determine the baryonic mass more precisely through HI 21 cm measurements. In figure 1.14b, the luminous mass M_* is replaced by the disk baryonic mass, $M_d = M_* + M_{gas}$. The mass in gas is taken from the observed HI mass with the standard correction for helium and metals: $M_{gas} = 1.4\ M_{HI}$. The authors assumed that the contribution of molecular clouds is negligible in late-type galaxies disks. Including the observed baryonic mass of the disk solves the discrepancy between the brighter and

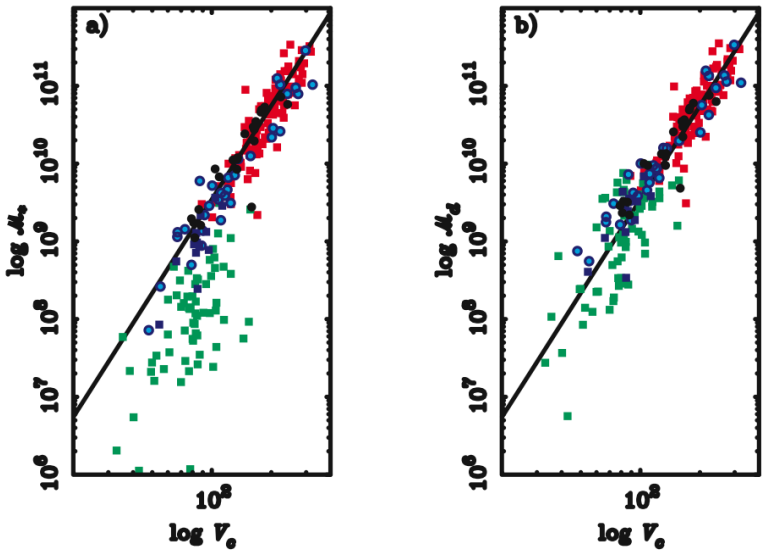

Figure 1.14: a: Luminous mass versus the rotational velocity in logarithmic scale for different galaxies. The Tully-Fisher power law breaks for $V_c \leq 90$ km/s. b: The mass deficit in (a) has been fixed by including the gas mass. The solid line is an unweighted fit to the red band data in (b) with slope of 4 [McGaugh et al. (2000)].

fainter galaxies. The baryonic Tully-Fisher relation hence is written as:

$$M_d \;=\; a\, V_c^b, \tag{1.36}$$

where a = 1.57 and b = 4. It shows steeper correlation between the mass and rotation velocity than the traditional relation (with b = 3.1). As one of the implications of this study on baryonic TF relation, the authors compared the mass disk content to the whole galactic baryon budget. The disk mass M_d can be expressed as a fraction of the total galactic mass (baryonic + non-baryonic) M_{tot}:

$$M_d \;=\; f_d\, f_b\, M_{tot}, \tag{1.37}$$

where $f_b = \frac{\Omega_b}{\Omega_m}$ is the baryon fraction and f_d is the detected baryon fraction associated to the galactic disk. McGaugh et al. assumed that $f_d \approx 1$ because on the one hand, different values of f_d would induce scatters on the mass-rotation velocity diagram whereas they are observed to be highly aligned. On the other hand, to have a constant (with negligible scatter) $f_d < 1$ for all galaxies, there need to be a fine tuning. They concluded there is no need to have baryonic dark matter.

In 2005, Pfenniger and Revaz [Pfenniger & Revaz (2005)] showed that galactic disks can contain dark baryons. Analysing the same sample used by McGaugh et al., Pfenniger and Revaz proposed that increasing M_{HI} by at least a factor of 3 would give better linear

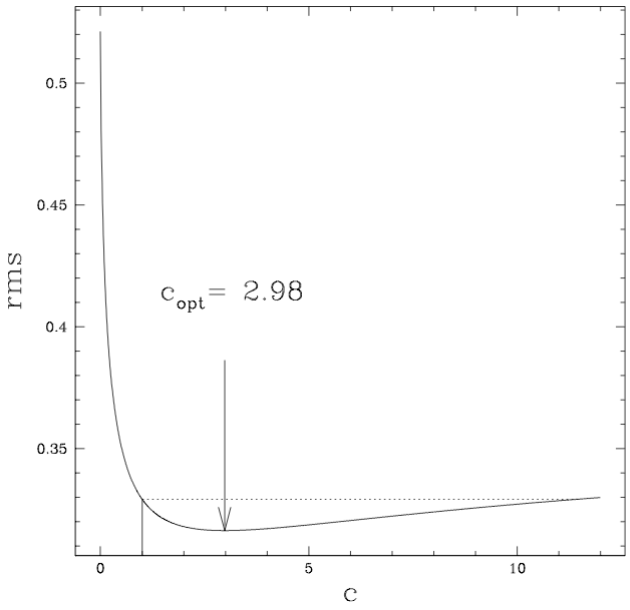

Figure 1.15: The best rms for linear least squares fit is obtained at $c \approx 3$. Dotted line mentions the rms of McGaugh et al. (c = 1) [Pfenniger & Revaz (2005)].

least-squares fit to mass-velocity distribution. It thus indicates that there can be some *unseen* baryonic gas within spiral galaxies. They redefined the Tully-Fisher relation as:

$$\log(M_* + c\, M_{HI}) \quad = \quad a + b \log V_c, \tag{1.38}$$

where M_{HI} is the observed galactic HI gas. They computed the least-squares fit to relation (1.38) for c in the range [0,15] and plotted the χ^2 rms against c value as illustrated in figure 1.15. From this figure they inferred that firstly, including the observed gas content of the galaxies decreases the rms by a factor of 1.6 from traditional TF relation (c = 0) to baryonic TF (c = 1). Secondly, the optimal c value having the least rms is not c = 1 (rms = 0.329) but is c = 2.98 (rms = 0.316). Furthermore, the rms is still smaller than 0.329 for c < 11.5. Obtaining smaller fit rms is not sufficient to prefer a 3-parameter model (equation (1.38)) to a 2-parameter one (equation (1.36)). Through three different statistical methods, Pfenniger and Revaz showed that data fits better expression (1.38) with fitted $c \approx 3$ than relation (1.36) (c = 1). There is a small probability (less than 0.01%) that the better χ^2 obtained for the 3-parameter model is due to the error fluctuations. The result of linear fit to equation (1.38) is shown in figure 1.16. They suggested that the dark component of the baryons essentially consists of cold molecular clouds.

1.3.2 Missing Baryons at Different Scales

The baryon fraction $f_b = \frac{\Omega_b}{\Omega_m}$ is the cosmic baryonic mass contribution to the total mass (CDM + baryons). From WMAP five-year results, $\Omega_b h^2$ = 0.02267 and $\Omega_m h^2$ = 0.1358

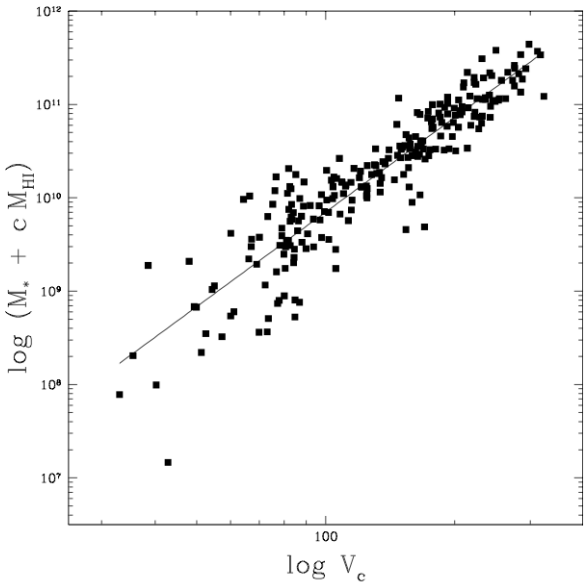

Figure 1.16: Least square fit to mass-rotation velocity curve including unseen gas with a = 3.11, b = 3.36 and c = 2.98 [Pfenniger & Revaz (2005)].

[Komatsu et al. (2009)] which give $f_b \approx 0.17$. In 2009, McGaugh and colleagues compared the observed baryonic budget $M_* + M_{gas}$ at different astronomical scales with the cosmic baryon fraction [McGaugh et al. (2010)]. As the early universe is supposed to be a homogeneous mix of cold dark matter and baryons, we expect to observe the same ratio for the cosmological structures.

The authors grouped the virialised systems into rotation-supported and pressure-supported systems. For rotating systems they distinguished between star dominant galaxies (early-type spiral galaxies with $M_* > M_{gas}$) and gas rich galaxies (late-type dim galaxies with $M_* < M_{gas}$). For the latter systems, the mass estimate is more accurate since the measurement is insensitive to mass-to-light ratio. The gas mass and velocity are estimated from HI 21 cm emission. Round symbols in figure 1.17 show the measured mass for rotating disks against rotation velocity. Dashed line is the baryonic Tully-Fisher relation (equation 1.36) which is observed for those systems and is generalised for larger mass and velocity scales. The rotation-supported[21] systems cover velocity range from 20 to 300 km/s.

Among the pressure-supported systems, the authors did not take into account the giant gas-free elliptical galaxies since the stars are not enough radially extended to measure the rotation velocity curve. On contrary, the small satellite galaxies (local group

[21] Like disk galaxy.

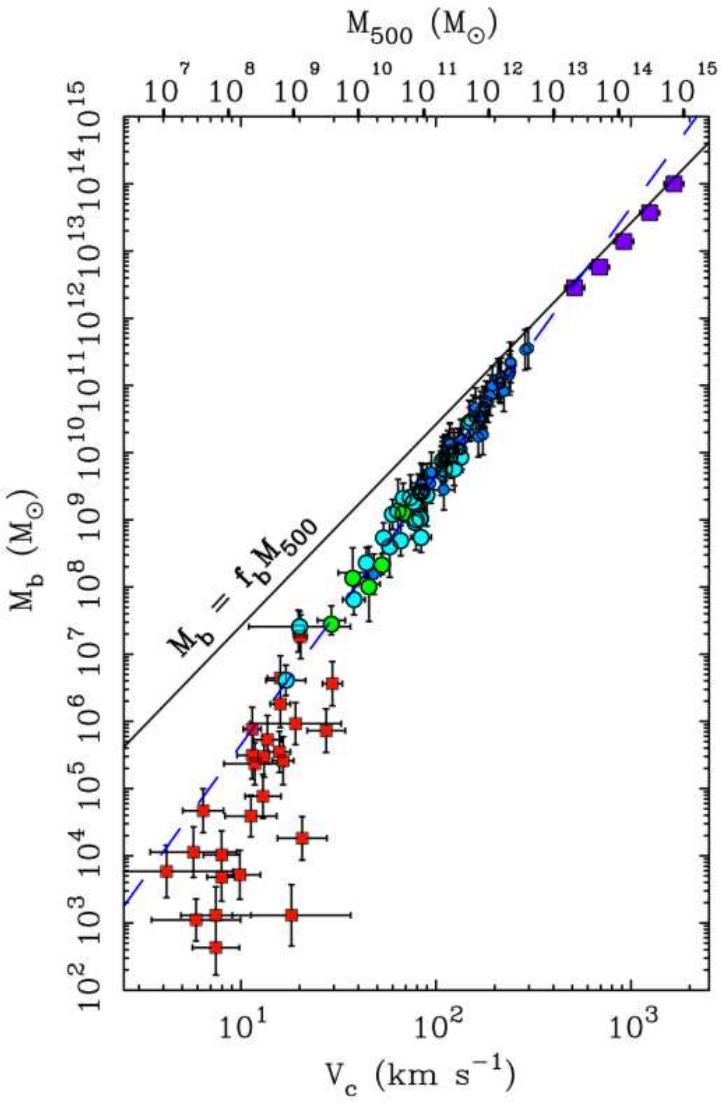

Figure 1.17: Relation between baryonic mass and rotation velocity. The sum of detected baryonic mass is plotted against the circular velocity of gravitationally bound extragalactic systems. Round symbols represent rotationally supported disks while square symbols represent pressure-supported systems. Larger symbols correspond to systems whose baryonic mass is dominated by gas and smaller symbols those dominated by stars. Dark blue circles are for star dominated spirals [McGaugh (2005)]. Light blue [Stark et al. (2009)] and green [Trachternach et al. (2009)] circles represent gas-dominated disks. Red squares represent Local Group dwarf satellites [Walker et al. (2009)]. Purple squares represent the mean of many galaxy clusters [Giodini et al. (2009)]. These pressure-supported systems fall close to, but systematically below the Baryonic Tully–Fisher relation defined by the disks (dashed line). The mass enclosed whithin an over-density of 500 times the critical density is shown by the upper abscissa assuming relation (1.39). If the structures baryonic fraction is the cosmic fraction (fb = 0.17), they would fall along the solid line [McGaugh et al. (2010)].

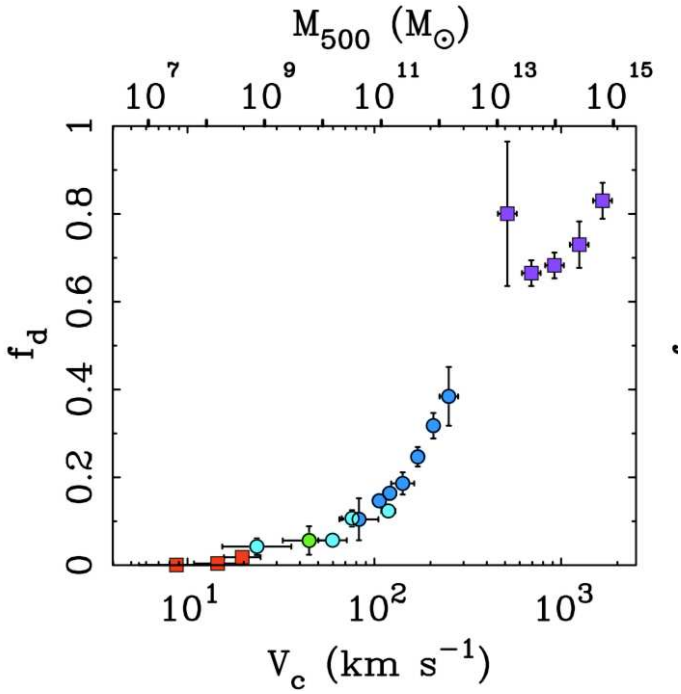

Figure 1.18: Detected baryon fraction versus rotation velocity. The colours represent the same as figure 1.17. Amount of undetected baryons increases significantly as the scale gets smaller [McGaugh et al. (2010)].

dwarfs, $M < 10^7 M_\odot$), with their quasi-spherical morphology, make it possible to estimate their stellar circular velocity from the observed sightline velocity dispersion. Red symbols show the local group dwarfs in figure 1.17. From star population studies, Γ_* = 1.3 $M_\odot/L_\odot$. At the scale of galaxy clusters, the baryonic mass is dominated by hot gas. The extension of a cluster is conventionally referred to its density contrast δ, with respect to the universe critical density ρ_c. Assuming a spherical mass distribution, the enclosed mass is derived as $M_\delta = 4/3\pi R_\delta^3 \delta \rho_c$. The cluster extension is referred to $\delta = 500$ [Giodini et al. (2009)]. With the definition of the critical density $\rho_c = 8\pi G/3H_0^2$ assuming circular velocity we obtain:

$$M_{500} \quad = \quad (204552\,\mathrm{km^{-3}s^3}M_\odot)\,V_{500}^3, \tag{1.39}$$

where H_0 = 72 km s^{-1} Mpc^{-1} [Freedman et al. (2001)]. Since the rotation curves are approximately flat within cluster halo, $V_c \approx V_{500}$. Violet squares in figure 1.17 represent the observed baryonic mass of clusters and their rotation velocities. The solid line is the plot of the baryonic mass at different scales assuming the cosmic baryon fraction and the gravitational mass computed through relation (1.39).

The pressure-supported systems deviate from the generalised Tully-Fisher relation. The

observed mass-velocity relation can be expressed as a broken power law with three different slopes at different scale ranges. While the slope slightly deviates from 4 for galaxy clusters, it is significantly steeper for dwarf galaxies. Moreover, the observed baryonic mass is always below the expectation from cosmic baryon fraction. From relation (1.39) gravitating mass scales as $M \sim V_c^3$ but the detected mass-velocity always has a steeper slope. Although the baryons approach their cosmic value at cluster scales, but there are missing mass at galactic scales. The mass deficit is more than 99% for dwarf galaxies. If f_d is the detected baryon fraction at any scale, we have:

$$f_d = \frac{M_b}{f_b M_{500}}, \tag{1.40}$$

where M_b is the observed baryonic mass. Figure 1.18 show f_d variation as a function of the rotation velocity. About 60% of baryons of our Galaxy are hidden. $f_d < 1$ at all scales and it gets smaller for smaller systems. Where these missing baryons reside is yet to be investigated. Also, the mechanism that gives a particular value of f_d with small scatter to a given scale is unknown. Since a dark halo consists of smaller sub-halos, it is not clear how sub-halos "know" to increase right amount of baryons to their parent halo to give the particular f_d and finally to approach the cosmic value at cluster scale.

Chapter 2

Cold Molecular Clouds

During the 90s, the microlensing searches done by EROS and MACHO collaborations revealed that there are not enough massive compact objects in the Galactic disk and halo to supply the dark matter content of the Galaxy. As shown in figure 2.1, the 95% C.L. exclusion limit of halo objects shows that less than 20% mass fraction of the halo can be made of dark massive compact objects with mass range within [10^{-7} $M_\odot$, 4 $M_\odot$]. This upper limit rules out MACHOs[1] as one of the most significant candidates of the Galaxy's baryonic dark matter [Lasserre et al. (2000)].

Matter in gaseous form is one of the ultimate candidates for hidden baryonic matter. In 1994, D. Pfenniger and F. Combes suggested the possibility of clouds made of cold molecular hydrogen (plus 25% He) located outside the optical disks of spiral galaxies or in their halos [Pfenniger & Combes (1994)]. These hypothesised clouds should be diffuse enough to survive from star formation activities, and be cold because warm and hot diffuse phases fill large space with too low density to contain large amount of baryonic matter. Since these clouds should be located in outer parts of the Galaxy, far from strong radiative sources, they can reach temperature < 10K. At such temperature and for certain conditions, the cloud pressure is larger than hydrogen sublimation pressure and the solid H_2 can form[2]. The solid hydrogen can be in thermal equilibrium with CMB at temperature of $\sim$ 3K through its black body absorption/emission [Pfenniger & Combes (1994)].

Unlike the atomic hydrogen, it is not possible to detect H_2 in 21 cm radio emission. When two hydrogen atoms combine, the spins of their electrons are coupled and cancel each other. For the same reason the degenerate vibrational and rotational states are not to be excited by external fields. However, H_2 absorbs photon in UV frequencies and excites to higher Vi-Ro levels. The UV can be either emitted by the high-mass star birth regions or the Active Galactic Nuclei (AGNs). Thus, in non-star formation clouds and far from the galactic centres there is no significant UV radiations to excite or dissociate molecular

[1] MAssive Compact Halo Objects

[2] For this task, condensation sites (such as dust) are needed.

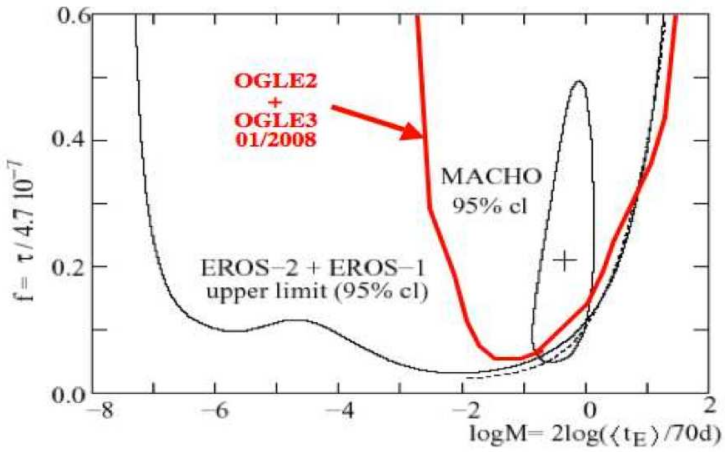

Figure 2.1: Published constraints on the fraction f of the standard spherical Galactic halo made of massive compact objects as a function of their mass M. The solid line labeled EROS shows the EROS upper limit based on the combination of the EROS1 results with the LMC EROS2 results. The dotted (incomplete) line takes into account the SMC search direction, conservatively assuming that the observed candidate belongs to the halo. The OGLE upper limit is shown with red line. The closed domain is the 95 % CL contour for the f value claimed by MACHO [Moniez (2008)].

hydrogen. Therefore, low temperature and low metallicity primordial clouds, far from UV sources, are transparent media and consequently invisible to the observer.

2.1 Cloud Model

In this section we explain the possibility of formation of self-similar molecular clouds and derive some of their physical properties. We start by discussing the turbulence which is one of the general observed properties of the ISM. Then, we briefly discuss the gas fragmentation and the fractal nature of the ISM.

2.1.1 Turbulence in the ISM

The motion of a fluid with velocity $\mathbf{v}(\mathbf{r},t)$ and kinematic viscosity ν is described by Navier-Stokes equations:

$$\frac{\partial}{\partial t}\mathbf{v}(\mathbf{r},t) \; + \; [\mathbf{v}(\mathbf{r},t)\,.\,\nabla]\,\mathbf{v}(\mathbf{r},t) \;\; = \;\; -\frac{1}{\rho}\,\nabla p + \nu\,\nabla^2\mathbf{v}(\mathbf{r},t). \tag{2.1}$$

Where ρ and p are fluid density and pressure. The energy dissipation is described in equation (2.1) by the Laplacian term and is proportional to the kinematic viscosity of the

molecules. It is believed that the Navier-Stokes equation describes the fluid behaviour in different regimes. In laminar regime, the fluid motion is dominated by viscosity term at the right side of the equation. For chaotic motions, viscosity looses its relevancy in favour of the non-linear term (at left side) which prevents us from obtaining analytical solutions. [Wheelon (2001)]

To give a qualitative description of a turbulent fluid motion [Tatarski (1961)], we consider a flow with characteristic kinematic viscosity ν and characteristic velocity v_L where the length L characterises the whole dimension of the flow given from the boundary conditions. The regime of the fluid motion is determined by the Reynolds number:

$$Re = \frac{L\, v_L}{\nu}.$$

A flow is in laminar regime if its Reynolds number is smaller that a critical value of Re_c[3]. As long as the Reynolds number is smaller than the critical value, the viscous dissipation is dominant. As Re increases beyond the critical value (e.g. by augmenting the velocity v_L), the contribution of non-linear term in equation (2.1) gets important and the instabilities in fluid motion arise.

We suppose that through a uniform velocity background, a velocity fluctuation Δv_l is produced in a region of characteristic size l. This fluctuation can be estimated to occur during a characteristic time scale $\tau = l/\Delta v_l$. It contains an energy per unit mass of $(\Delta v_l)^2$, and the energy per unit mass per unit time (power per unit mass) dissipated from the flow and injected to the velocity fluctuation can be estimated as $(\Delta v_l)^2/\tau \sim (\Delta v_l)^3/l$. Meanwhile, the velocity fluctuation induces a velocity gradient which dissipates the energy of flow into heat from the viscosity (the term at right in equation (2.1)). The energy dissipation per unit time per unit mass is of order of $\epsilon = \nu(\Delta v_l)^2/l^2$. Therefore, the velocity fluctuation can survive from transfering to heat if the energy injected from the flow is larger than the energy dissipated by viscosity:

$$\begin{aligned} (\Delta v_l)^3/l &> \nu(\Delta v_l)^2/l^2, \\ \frac{l\, v_l}{\nu} &> 1, \\ Re_l &> 1, \end{aligned}$$

where Re_l is the "inner" Reynolds number at scale l and velocity Δv_l. Since the computed relations only include the order of magnitudes and contain some unknown factors, the criterion obtained here should be re-written more precisely as $Re_l > Re_c$. In general, large scale velocity fluctuation, corresponding to large Re_l, would be easily excited, but if the largest Reynolds number ($Re = \frac{L\, v_L}{\nu}$) is smaller than the critical value Re_c the flow does not loose its stability and remains in laminar regime. As Re gets slightly larger than

[3] usually about 2000.

Re_c the fluid starts loosing its stability and enters the turbulent phase. In turbulent regime the velocity fluctuations are observed as eddies with the characteristic length l and "inner" Reynolds number Re_l. When the inner Reynolds number of an eddy with size l exceeds Re_c, the eddy becomes unstable and transfers its kinetic energy to the eddies with smaller sizes according to a cascade process. The energy cascades from larger eddies and is redistributed to eddies with smaller scales. The energy cascade occurs inertially because for very large Re (large kinetic energy per mass) the dissipation effect of viscosity is negligible since the non-linear term dominates the dissipative term. However, this process does not continue to infinitely small scales. At Kolmogorov micro-scale l_0 while the fluctuation has the characteristic velocity Δv_0, the magnitude of the energy dissipation rate by viscosity ϵ is of the same order of the injection rate of kinetic energy to the eddies and hence, the viscous forces are sufficiently strong to destroy them. The turbulence stops at this scale effectively. The micro-scale and the corresponding velocity depend only on energy dissipation rate and viscosity. Since at this scale $\epsilon = \nu(\Delta v_0)^2/l_0^2 \sim (\Delta v_0)^3/l_0$ we obtain:

$$\begin{aligned} l_0 &\sim (\frac{\nu^3}{\epsilon})^{1/4}, \\ \Delta v_0 &\sim (\nu\,\epsilon)^{1/4}. \end{aligned}$$

The length scales L and l_0 are usually mentioned as *outer* and *inner* scales of the turbulent flow. Within the interval between these two length scales, the energy cascades inertially and the fluid motion is highly non-linear with stochastic velocity field which consequently allows us to study the physics of the turbulence from a statistical point of view. ϵ is the constant power transferred per unit mass and is scale independent. Kolmogorov (1941) assumed that during the energy cascade process, the turbulence is locally isotropic. It is thus possible to derive a relation for the power spectrum of energy fluctuations as a function of the wave number ($q = 2\pi/l$) in Fourier space with dimensional analysis. The velocity fluctuation at scale l can be written as:

$$\Delta v_l \sim (\epsilon\, l)^{1/3}.$$

As mentioned before the energy fluctuations per unit mass of an eddy is proportional to Δv_l^2:

$$\begin{aligned} E_l &\sim (\epsilon\, l)^{2/3}, \\ E(q) &\sim \epsilon^{2/3}\, q^{-2/3}. \end{aligned}$$

The energy power spectrum in one dimensional Fourier space is:

$$P(q) = \frac{d}{dq}E(q) \sim \epsilon^{2/3}\, q^{-5/3}.$$

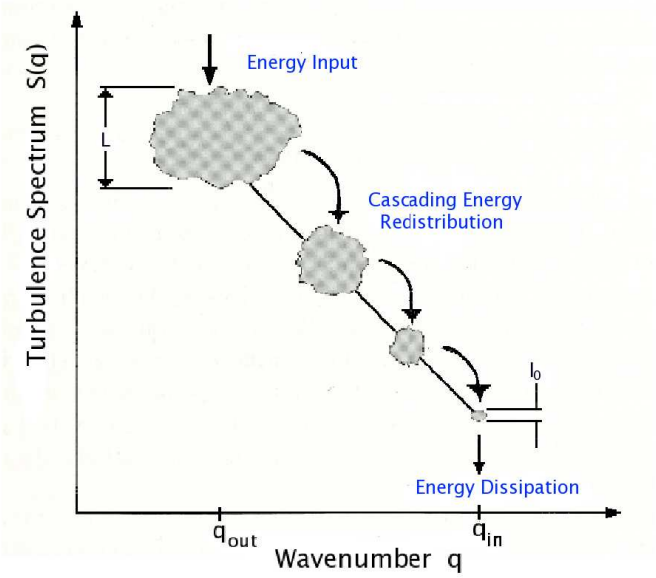

Figure 2.2: Spectral density of a turbulent flow. Energy cascades inertially from larger eddies to smaller ones between outer and inner scales $q_{out} = L^{-1}$ and $q_{in} = l_0^{-1}$. The invariance of the dissipation power per unit mass (ϵ) leads to a power law spectrum. [Wheelon (2001)]

Considering 3D isotropic turbulence, the volume element in Fourier space is $dq^3 = 4\pi q^2 dq$, and the energy power spectrum is computed as:

$$P(\mathbf{q}) \;=\; \frac{d^3}{dq^3}E(q) \;\sim\; q^{-2}\frac{dE(q)}{dq} \;\sim\; \epsilon^{2/3}\, q^{-11/3},$$

Therefore, the spectral density ($S(\mathbf{q}) = P(\mathbf{q})/V$, where V is the spatial volume) of the Kolmogorov turbulence can be written as:

$$S(\mathbf{q}) \;=\; C^2(\epsilon)\, q^{-11/3}, \tag{2.2}$$

where $C(\epsilon)$ is a constant, to be measured experimentally, which indicates the intensity of the turbulence power injection within a given scale interval, and $q = (q_x^2 + q_y^2 + q_z^2)^{1/2}$ is the wavenumber. A schematic sketch of the turbulence spectrum is presented in figure 2.2.

Turbulence usually exists in clouds with star formation and is also induced by shell expansion of supernovae. However, there are evidences which show there are cold gaseous regions, for example in outer disks, that would be strongly gravitationally unstable if they were not turbulent. This turbulence should be induced by engines other than star formation. These engines include thermal instability, magnetic instabilities, large self-

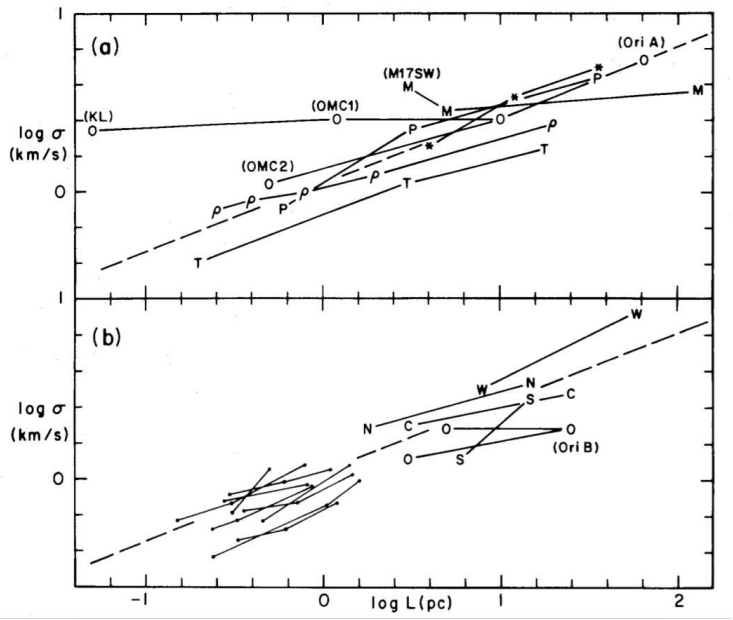

Figure 2.3: The velocity dispersion σ plotted versus region size L for clouds containing one or more sub-regions. Straight lines connect the symbols for each sub-region and the larger region or cloud of which it is a part. Dashed lines show $D = 1.76$ [Larson (1981)]
.

gravitational instabilities and unsteady spiral shocks [Ostriker (2007)]. Turbulence observed in the interstellar medium involves both atomic and molecular hydrogen clouds.

2.1.2 Fractal Nature

Cold gas structures are observed to be self-similar for some order of magnitude in size and density. Observations of nearby molecular clouds show their fractal nature in a range of at least 10^4 in scales and densities [Pfenniger & Combes (1994)]. Different sources such as self-gravity and turbulence may lead to cosmic fractal structures. Although the cold gas has a shorter cooling time[4] compared to its free fall time[5], which manifests its Jeans instability[6], the fractal nature of the cloud, as will be explained, prevents gravitational collapse and make the gaseous environment essentially a star non-formation medium as what is observed for outer disk gases.

In 1981, R. B. Larson measured the gas velocity dispersion σ_v at different scales r for some virialised clouds and also determined the gas mass M at each scale. Figure 2.3

[4]The cooling time is the time for a system to radiate all its thermal energy.
[5]The free fall time is the time for a gravitationally unstable structure to reach e^{-1} of its initial size.
[6]A structure is Jeans unstable when its gravitational energy exceeds twice its thermal energy.

shows the velocity dispersion he observed as a function of scale. He found the following scaling relations of the cloud mass, and of the velocity dispersion with the radius [Larson (1981)]:

$$\begin{aligned} M &\sim r^D, \\ \sigma_v^2 &\sim r^{D-1}, \end{aligned} \tag{2.3}$$

where D is the fractal dimension of the hierarchical cloud. From these relations, the observations indicate D to be between 1.6 and 2. There is no global fractal dimension for ISM in theory, but D varies with time since the cloud starts to fragment at $D = 3$ and the cloud does not arrive immediately to its final fractal form [Pfenniger & Combes (1994)].

As explained by F. Hoyle, a gaseous system with the cooling time shorter than the free fall time, can be considered as an isothermal medium. As an isothermal gas has a constant internal thermal energy, there is no energy dissipation. The short range molecular forces lead to equilibrium state at scales larger than molecules' mean free path and make the densities uniform. But a finite self-gravitating gas with no rotation can not remain in static equilibrium. Gravity is a long range force which acts at all scales longer than the molecular force range. The scale-free nature of the gravity leads to scale-free nature of the isothermal gas and the system starts to fragment into sub-clouds [Hoyle (1954)]. This property of gravity can not hold out continually to the smaller scales. At some small scale the free fall time equals the cooling time. The transition from isothermal to adiabatic conditions occurs and fragmentation stops. These smallest cloudlets are called *clumpuscules* which are the building blocks of the fractal cloud. The thermal transition allows them to have large temperature fluctuations. If the near isothermal condition, at clumpuscule scale, is not perturbed by star formation, a chaotic but weakly dissipative regime can occur.

2.2 Clumpuscules

In this section, we derive some physical characteristics of the clumpuscules. Through following sections, we show how the fractal dimension and the matter distribution at different fractal levels prevent the clumpuscules from gravitational collapse and keep them in statistical equilibrium through supersonic collisions.

We consider the free fall time t_{ff} and Kelvin-Helmholtz time t_{KH}, which is the time scale of thermal energy loss of the gas (cooling time) through black body radiation:

$$\begin{aligned} t_{ff} &= \frac{1}{\sqrt{\rho G}}, \\ t_{KH} &= \frac{3}{2}\frac{Mk_BT}{\mu m_p}\,\frac{1}{4\pi R^2 f\sigma T^4}. \end{aligned}$$

The denominator of the second equation is the Stephan-Boltzmann radiation where σ = 5.670 $\times$ 10^{-8} J s^{-1} m^{-2} K^4, f is the emissivity equals to one for an ideal black body radiation. The factor μ is the mean molecular weight[7], it equals 2.3 for combination of H_2 and He (3/4 molecular Hydrogen and 1/4 Helium) and equals to 0.63 for combination of ionised H and He. m_p is the proton mass. M and ρ are the mass and the density of the clumpuscule. Since $t_{ff} = t_{KH}$ for the clumpuscules, taking into account the mass-temperature relation for a virialised system $M = (3\,k_B\,T\,R)/(G\,\mu\,m_p)$, we can estimate some physical quantity of the clumpuscules as a function of temperature, mean molecular weight and emissivity:

$$\begin{aligned}
M_\bullet &\simeq 4\times10^{-3}\,T^{\frac{1}{4}}\mu^{-\frac{9}{4}}f^{-\frac{1}{2}}\ [M_\odot],\\
R_\bullet &\simeq 1.5\times10^{2}\,T^{-\frac{3}{4}}\mu^{-\frac{5}{4}}f^{-\frac{1}{2}}\ [AU],\\
L_\bullet &\simeq 9.2\times10^{-7}\,T^{\frac{5}{2}}\mu^{-\frac{5}{2}}\ [L_\odot],\\
\rho_\bullet &\simeq 1.1\times10^{8}\,T^{\frac{5}{2}}\mu^{\frac{3}{2}}f\ [\mathrm{H\,cm^{-3}}],\\
P_\bullet &\simeq 1.1\times10^{8}\,T^{\frac{7}{2}}\mu^{\frac{1}{2}}f\ [\mathrm{K\,cm^{-3}}],\\
\Sigma_\bullet &\simeq 3.2\times10^{23}\,T^{\frac{7}{4}}\mu^{\frac{1}{4}}f^{\frac{1}{2}}\ [\mathrm{H\,cm^{-2}}],\\
t_{ff,\bullet} &\simeq 9.2\times10^{3}\,T^{-\frac{5}{4}}\mu^{-\frac{3}{4}}f^{-\frac{1}{2}}\ [yr],
\end{aligned} \tag{2.4}$$

where $M_\bullet$ is the mass, $R_\bullet$ is the radius, $L_\bullet = 4\pi R^2 f\sigma T^4$ is the (virtual) black body luminosity, $\rho_\bullet$ is the average density, $P_\bullet$ is the average pressure, $\Sigma_\bullet$ is the average column density and $t_{ff,\bullet}$ is the free fall time of the clumpuscule. We comment below these quantities:

Mass: The typical mass of the clumpuscules weakly depend on the temperature. The fact that the cloudlet has Jupiter mass at low temperature and white dwarf mass at higher temperature does not imply that it evolves to a star or a giant planet. As temperature increases the cloudlet virial size ($R_\bullet$) decreases and a part of the mass evaporates to larger radii. This is similar to what happens for red giants and globular clusters. At high temperature ($T > 2\times10^3$), the molecular hydrogen becomes ionised and μ decreases, thus, the molecular weight decreases and the mass increases by a factor $(2.3/0.63)^{9/4} \simeq 18$.

Luminosity: The variation of the virtual luminosity ($L_\bullet$) with emissivity (f) is canceled due to R and T dependencies. The luminosity is virtual since the medium is nearly isothermal and it can be shown that $L_\bullet$ corresponds to gravitational power $\sim v^5/\mathrm{G}$ where v is the clumpuscules velocity. We will derive the gravitational power exchange later (see relation (2.21)).

Densities: The column density $\Sigma_\bullet$ corresponds to a few grams of H, H_2 and He in a square centimetre; so, at low temperature, the clumpuscule can be considered as almost

[7] $\mu^{-1} = \sum(x_i/A_i)$, where x_i is the specie fraction and A_i is the atomic (molecular) weight.

completely transparent in optical band if the gas is primordial. However, we expect the clumpuscules have inhomogeneities[8]. Therefore, $\rho_\bullet$ and $\Sigma_\bullet$, which are the average densities, are only rough estimators of the clumpuscule's opacity. Moreover, if a fraction of H_2 gas freezes to H_2 snows there is a possibility to have more opacity.

Time scales: Larger masses have shorter cooling time ($t_{KH} \sim M^{-5}$) and are Jeans unstable. They cool rapidly and fragment to smaller clumps. Small masses cool in longer time and, as will be diskussed, considering a fractal structure, clumpuscules survive from collapsing by colliding to each other supersonically at the same rate of their adiabatic contraction. They are never in a static state.

By computing the quantities given in expression (2.4) for molecular hydrogen at T = 3K and $0.1 \leq \mathrm{f} \leq 1$, we can estimate some physical properties of the clumpuscules:

$$\begin{aligned} M_\bullet &\sim 0.8 - 2.7 \times 10^{-3} \ [M_\odot], \\ R_\bullet &\sim 23 - 73 \ [AU], \\ L_\bullet &\sim 1.8 \times 10^{-6} \ [L_\odot], \\ \rho_\bullet &\sim 0.6 - 6 \times 10^{9} \ [\mathrm{H\,cm^2}{-}3], \\ P_\bullet &\sim 0.5 - 5 \times 10^{9} \ [\mathrm{K\,cm^{-3}}], \\ \Sigma_\bullet &\sim 0.8 - 2.7 \times 10^{24} \ [\mathrm{H\,cm^2}{-}2], \\ t_{ff,\bullet} &\sim 1.2 - 3.9 \times 10^{3} \ [yr]. \end{aligned} \tag{2.5}$$

Thus, the hypothesised clumpuscules have Jupiter mass and are spatially extended to a few tens of AU with column density of about 10^{24} H cm^{-2}.

2.3 Scaling Relations in Fractal Clouds

Since the fragmentation process occurs for Jeans unstable gravitational systems, it is a chaotic process and the produced clumps are not exactly self-similar. However we can expect them to have statistically self-similar properties which means that in average they fragment to sub-clumps according to a given probability distribution of number, mass and size of sub-clumps[9]. As a fractal structure, each clump at level L consists of N sub-clumps at level $L-1$ distributed according to a given probability density law. The recursive pattern continues until arriving to the 0th level in which the smallest mass unit appears. These smallest cloudlets are the building blocks of the fractal cloud: the clumpuscules.

[8] The idea of scintillation effect (explained in next chapter) is based on fluctuation of the column density due to such inhomogeneities.

[9] For the model being introduced here, the probability distribution is used only for density. Number and size of the sub-clumps are taken to be constants.

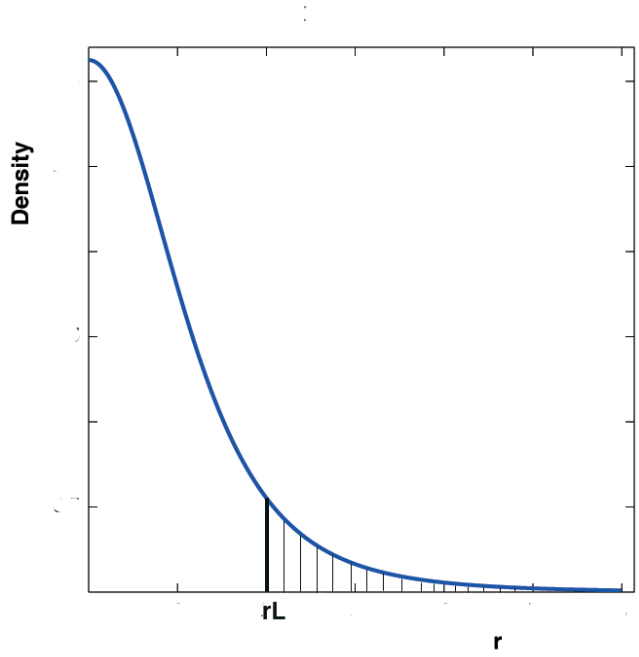

Figure 2.4: Plummer density distribution. The hatching zone corresponds to $r > r_L$ and contains $\eta = 12\%$ of the total mass.

A clump at level L in a fractal structure is defined with mass M_L not necessarily distributed in a limited volume but characterised by a length scale r_L following the density distribution $\rho(r, r_L)$. The mass within r_L, should be large enough to contain several sub-clumps at lower levels. Figure 2.4 shows the Plummer density distribution $\rho(r, r_L) = \rho_0/(r^2 + r_L^2)^{\frac{5}{2}}$. The mass within $r < r_L$ contributes for 88% of the total mass.

We consider a cloud of mass M with length scale r constructed from clumpuscules of masses M_0 with maximum of distribution around length scale r_0. As a fractal object, the whole cloud can be filled by $(r/r_0)^D$ clumpuscules where D is the fractal dimension. For a self-similar cloud the mass scaling relation is:

$$M/M_0 = (r/r_0)^D. \tag{2.6}$$

Therefore, the fractal dimension can be written as:

$$D = \frac{log(M/M_0)}{log(r/r_0)}. \tag{2.7}$$

By knowing the largest and the smallest length and mass scales, we can determine the fractal dimension D of the cloud.

The clump at level L contains N sub-clumps at level $L-1$ and $M_L = NM_{L-1}$. Following equation (2.6):

$$\begin{aligned} r_L^D &= N r_{L-1}^D \\ \alpha &\equiv \frac{r_{L-1}}{r_L} = N^{-D}. \end{aligned} \tag{2.8}$$

If the ratio of the consecutive levels is limited by a maximum value, α_{max}, the number of sub-clumps will have a minimum limit $N > \alpha_{max}^{-D}$.

The total number of sub-clumps up to level L is:

$$n_L = \prod_{i=1}^{L} N_i,$$

where N_i is the number of sub-clumps at each level lower than L. Through this model the numbers of sub-clumps are taken independent of the level $N_i = N$. The corresponding total mass is calculated as:

$$M_L = n_L\, M_0 \Longrightarrow \frac{r_L}{r_0} = (n_L)^{1/D}$$

The scaling of the average density of a cloud at level L, according to equation (2.6), is obtained as:

$$\frac{\langle \rho_L \rangle}{\langle \rho_0 \rangle} = \frac{M_L/r_L^3}{M_0/r_0^3} = (\frac{r_L}{r_0})^{(D-3)} \tag{2.9}$$

For $D < 3$, density increases at lower levels (scales). A similar relation can be derived for average column density at level L:

$$\frac{\langle \Sigma_L \rangle}{\langle \Sigma_0 \rangle} = \frac{M_L/r_L^2}{M_0/r_0^2} = (\frac{r_L}{r_0})^{(D-2)} \tag{2.10}$$

For $D > 2$, average column density is larger for larger clumps while for $D < 2$ it is the opposite. In the latter case, the probability that the clumps overlap through projection at a given scale decreases for larger scales. $\alpha^2 = (r_{L-1}/r_L)^2$ is the probability of having a sub-clump at a given position inside cloud if this probability does not depend on position (uniform probability). Probability of having n from N sub-clumps at the *same* position is $P(n)$ which is given by the binomial distribution:

$$\begin{aligned} P(n) &= \binom{N}{n} (\alpha^2)^n \, (1-\alpha^2)^{N-n} \\ &= \binom{N}{n} (N^{-2/D})^n \, (1-N^{-2/D})^{N-n} \end{aligned}$$

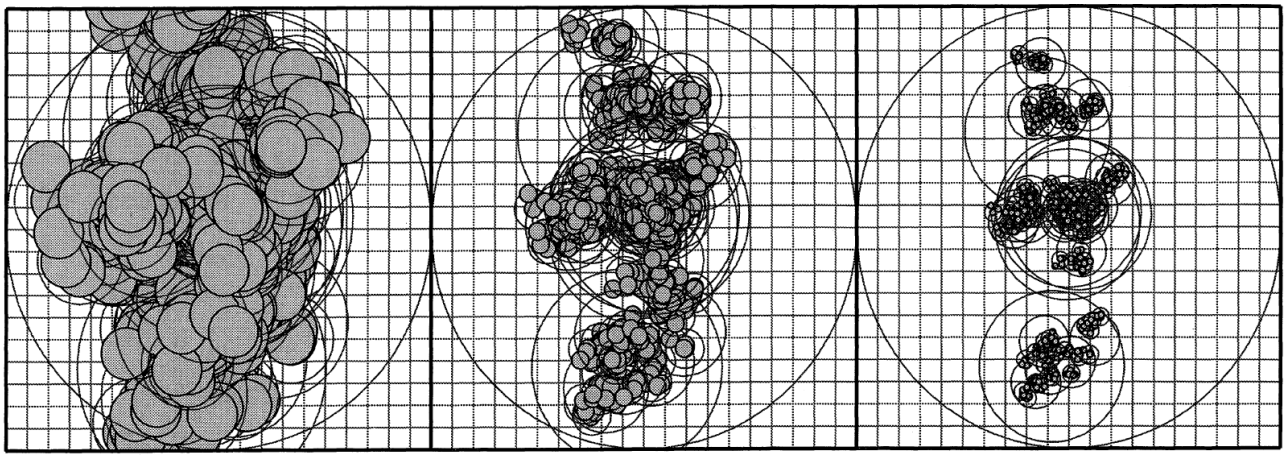

Figure 2.5: A fractal model with L = 4 levels and N = 5 clumps per level. From left to right D = 3, 2, and 1.5. The lowest level clumps are shown as opaque balls. The circles show the extensions of the higher level clumps. The background grid suggests a finite resolution device. Cloudlets are generated according to density law: $\rho(r, r_L) \sim \frac{1}{(r/r_l)^2}$ for $r < r_L$ and $\rho(r, r_L) \sim 0$ for $r > r_L$. [Pfenniger & Combes (1994)]

For larger D and N the probability approaches one. Thus, for smaller D, sub-clumps are less likely to be superimposed and are denser at lower levels. However this is not the realistic representation of sub-clumps' distribution, since in reality the coverage probability varies with the position in the parent cloud and the position of the sub-clumps are not independent but correlated. So, we are not allowed to use binomial probability to generate a hierarchical cloud. Figure 2.5 shows the hierarchical clouds for different fractal dimensions. In the generated clouds, the sub-clump existence probability decreases with distance from the centre. The sub-clumps in larger D are more superimposed than those of smaller dimensions. We can define a volume filling factor for a clump at level L as the ratio of the total volume of clumpuscules to the clump volume, assuming the clumpuscules have no overlap ($D \ll 3$):

$$f_L = \frac{n_L r_0^3}{r_L^3} \tag{2.11}$$

2.4 Properties of Virialised Fractal Clouds

If we approximate the total gravitational energy of a clump at level L as its own gravitational energy, neglecting gravitational effects from other clumps, the effect of residual gas located out of distance r_L and possible magnetic pressures, we can use the virial theorem to compute the velocities of clumps at level L:

$$v_L^2 = \frac{GM_L}{r_L} = v_0^2 (\frac{r_L}{r_0})^{D-1}, \tag{2.12}$$

where v_0 is the virial velocity of the clumpuscules. Therefore by measuring the velocities of the largest and the smallest clumps, we are able to compute the fractal dimension D:

$$D = 1 + 2\,\frac{\log(v_L/v_0)}{\log(r_L/r_0)} \tag{2.13}$$

From Larson's observations, equations (2.3) gives $v \sim r^k$, where the exponent k varies between 0.3 and 0.5 according to the observations [Elmegreen (1992)]. Therefore, from the relation (2.13) we get 1.6 < D < 2.

Approximating the fractal clouds as virialised systems is perhaps the most critical assumption since we neglect the outer clump gravitation and assume the gas contribution outside r_L is small. Furthermore, virial theorem is applied for bound systems where the second time-derivative of their inertia moments must vanish. This condition should be quite exceptional in a turbulent hierarchical cloud.

Dynamical (or crossing) time is defined as a time scale in which a clump at level L crosses a distance r_L with velocity v_L:

$$\tau_{dyn,L} = \frac{r_L}{v_L} = \tau_{dyn,0}(\frac{r_L}{r_0})^{\frac{3-D}{2}}, \tag{2.14}$$

for D < 3 the dynamical time decreases at lower levels.

Similarly, the mean collision time at level L is given as:

$$\tau_{col,L} = [\frac{N_L}{\frac{4}{3}\pi r_L^3}\ \pi(2r_{L-1})^2\ v_L]^{-1} = \frac{\tau_{dyn,L}}{3N_L}\ (\frac{r_L}{r_{L-1}})^2, \tag{2.15}$$

where $\pi(2r_{L-1})^2$ is the cross section of sub-clumps at level $L-1$. The system can survive from *internal* collisions if the ratio:

$$C_{int} = \frac{\tau_{col,L}}{\tau_{dyn,L}} = \frac{1}{3}N_L^{\frac{2}{D}-1} \tag{2.16}$$

is larger than one which is equivalent to D < 2. Otherwise, the rate of internal collisions would exceed the dynamical frequency and the sub-clumps would be dissolved. Using the same logic, we compare the collision time with the dynamical time of the next lower level to characterise the effect of *external* collisions on sub-clumps:

$$C_{ext} = \frac{\tau_{col,L}}{\tau_{dyn,L-1}} = \frac{1}{3}N_L^{\frac{7-3D}{2D}}, \tag{2.17}$$

for D < 2.33, C_{ext} is larger than one which prevents disruption of the fragments in sub-clumps from external collisions. If the sub-clumps collide frequently the new virial equilibrium is hard to be reached inside the sub-clumps. Figure 2.6 shows the ratios C_{int} and

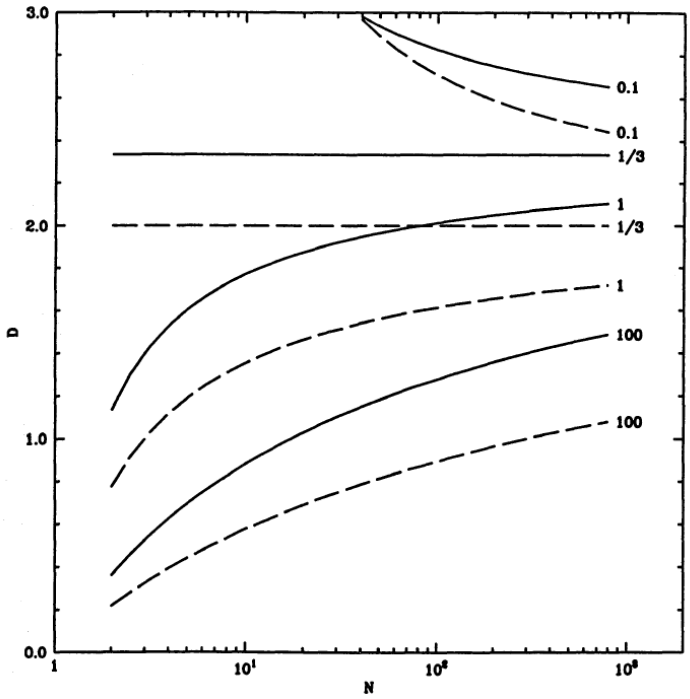

Figure 2.6: Ratios C_{int} (dash) and C_{ext} (solid) in the $N - D$ diagram for 2 < N < 10^3

C_{ext} in the D vs. N diagram. For D < 2 and large N, the system tends to be less collisional. At N < 10 and D > 1 the system is always collisional but much less collisional at $D \approx$ 1-2 than at D > 2.

The collision strength is characterised by the Mach number $\mathcal{M}_L$:

$$\mathcal{M}_L \;=\; \frac{v_L}{v_{L-1}} \;=\; (\frac{r_L}{r_{L-1}})^{\frac{D-1}{2}} \;=\; N_L^{\frac{1-1/D}{2}} \tag{2.18}$$

The collisions are supersonic at D > 1 since the collision speed is larger than internal sub-clumps' velocities. Hence, at D < 1 the collisions are subsonic. If 1 < D < 2 the collisions are slightly supersonic, $\mathcal{M}_L$ < 2 for N < 16. Let's consider the shock condition in the latter case. There are N_L clumps at level L with the mass essentially concentrated within the length-scale r_L. The residual gas (at $r > r_L$) is also supposed not to be a smooth gas but consist of sub-clumps. These sub-clumps interact supersonically with other clumps. We therefore expect shock production inside them. By applying shock condition to a gas with adiabatic index γ one can obtain the density ratio before and after the shock as:

$$\frac{\rho_{post}}{\rho_{pre}} \;=\; [\frac{2}{\gamma+1}\frac{1}{\mathcal{M}_L^2} + \frac{\gamma-1}{\gamma+1}]^{-1}. \tag{2.19}$$

Regarding relation (2.18), the ratio of densities depends on N_L, D and the adiabatic index of the gas. In transition from the inner part of the clump ($r < r_L$) to the outer part ($r > r_L$)

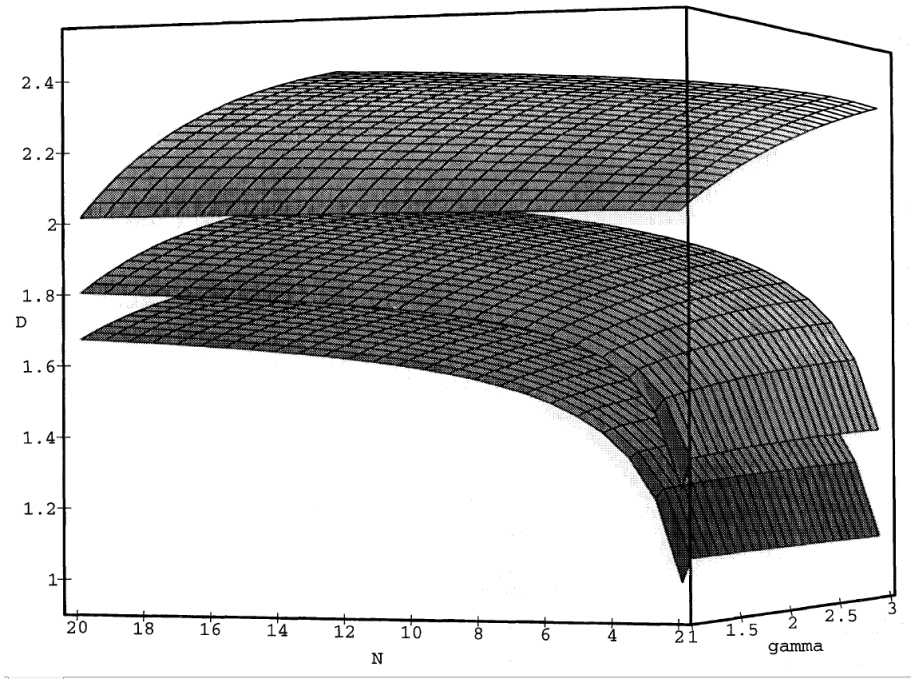

Figure 2.7: Real solutions for D of quartic equation (2.20) for η = 0.3 (bottom), 0.5 (middle) and 1 (top) in a $(N - \gamma - D)$ diagram. [Pfenniger & Combes (1994)]

the ratio between inner and outer densities is a fraction of the density contrast (relation (2.9)): $\eta \frac{<\rho_{L-1}>}{<\rho_L>}$, where η (< 1) is the fraction of gas distributed at $r > r_L$. We have:

$$\frac{\rho_{post}}{\rho_{pre}} = \eta \frac{< \rho_{L-1} >}{< \rho_L >}.$$

Substituting from relations (2.9) and (2.19) and for $x \equiv N^{1/D}$:

$$2x^4 + N(\gamma - 1)x^3 = \frac{N^2}{\eta}(\gamma + 1), \tag{2.20}$$

for $N \geq 2, \gamma \geq 1$ and $0 < \eta \leq 1$, only one of the four solutions is real. Figure 2.7 shows real solutions of the equation (2.20) for different η values. For plausible values of N and γ (for example, N = 10 and γ = 5/3) the fractal dimension D varies from 1.6 to 2 which is compatible with exponents derived from Larson's observations.

We can also compute the gravitational power exchange between the levels. Considering the virial equilibrium, the power is the gravitational energy (two times of the kinetic energy) divided by dynamical time:

$$P_L = M_L v_L^2 \frac{v_L}{r_L} = \frac{v_L^5}{G}, \tag{2.21}$$

where we have used relation (2.12) to compute the last term. Hence, the power ratio between a clump at level L and the clumpuscule is:

$$\frac{P_L}{P_0} = (\frac{v_L}{v_0})^5 = (\frac{r_L}{r_0})^{\frac{5}{2}(D-1)}, \tag{2.22}$$

for $D > 1$, this power decreases from higher levels to lower ones. This power is virtual since we have assumed the system to be virialised. If the equilibrium is perturbed, the power might be exchanged between the levels. The most interesting scaling relation is the scaling of the power per mass (ϵ) which is a crucial parameter in turbulence:

$$\epsilon_L = \frac{P_L}{M_L} = \frac{v_L^3}{r_L},$$

using relation (2.12):

$$\frac{\epsilon_L}{\epsilon_0} = (\frac{r_L}{r_0})^{(3D-5)/2}. \tag{2.23}$$

For $D > 5/3$, the power per mass in larger at larger scales and the inverse for $D < 5/3$. When $D = 5/3$ (Kolmogorov turbulence), the power per mass is constant at all scales.

2.5 Stability, Turbulence and Star Non-Formation Conditions

Stability

From equation (2.15), for $D > 1.5$ and with small N, clumps collide frequently at all levels. Although the collisions happen supersonically (relation (2.18)), they should not make strong gaseous shocks within the higher level clumps since the clumps encounters are mainly gravitational. Two clumps attract each other gravitationally, they collide when their spatial positions overlap and the collision continue through sub-clump scales. According to virial theorem, the collision of two clumps should lead to cooling of the final clump after some τ_{dyn}. This happens because after the collision, in order to restore the new virial equilibrium, the gravitational potential energy must be two times of the kinetic energy excess produced by clump collision. This causes the expansion of the final clump and temperature decrese.

At level of clumpuscules, the hydrodynamical regime changes to be smooth with adiabatic condition. The heat produced by the shock travels with the same velocity of clumpuscule expansion because $\tau_{dyn,0} = \tau_{ff} = \tau_{KH}$. The shocks are not hypersonic since for $2 < N < 20$ and $1 < D < 2$ the Mach number is always smaller than 2.12 (relation (2.18)) which leads to a temperature increase by a factor smaller than 3 ([Elmegreen (1992)]). Moreover, the near isothermal condition and the expansion of the clumpuscules added to the virial

condition, which transfers the produced kinetic energy to potential energy, prevents gas from loosing much energy by radiating it away. Collisions of clumpuscules in a fractal structure follow a loop of gaining (through shocks) and loosing (by radiation) the energy which let them to expand, re-fragment and reform eternally if the rate of energy radiated by shocks is equal to the energy gained by clumpuscules. Thus, the fractal gas can stay in statistical equilibrium.

Turbulence

Suppose r_L is the largest scale where energy can be transferred from the general galactic differential rotation to the cloud by means of turbulence. The power per mass of the turbulence produced from galactic rotation with angular velocity Ω at distance R from galactic centre is computed as [Landau & Lifshitz (1971)]:

$$\begin{aligned} \epsilon_g &\approx v_L r_L \, (R\frac{d\Omega}{dR})^2 \\ \epsilon_g &\approx v_L r_L \, (\frac{v_c}{R})^2 \;=\; v_L r_L \Omega^2 \end{aligned} \tag{2.24}$$

where $v_c \;=\; R\,\Omega$ is the constant rotation velocity at distance R from the galactic centre. Equating ϵ_g to ϵ_L (the power per mass exchange at level L) in equation (2.23) we obtain:

$$\frac{r_L}{r_0} \;=\; (\frac{v_0}{v_c}\,\frac{R}{r_0})^{2/(3-D)} \tag{2.25}$$

The fractal dimension can be again computed from some typical values of R = 15 kpc, r_L = 1.5 kpc (outer scale of the turbulence), $r_0 = R_\bullet$ (relation (2.6)), $v_0 = \sqrt{3kT/\mu m_p}$ and v_c = 200 km s^{-1}. Using these values we get D = 1.60. Including relation (2.14), the energy dissipation time can be computed as:

$$\tau_{diss} \;=\; \frac{1}{2}\frac{v_c^2}{\epsilon_g} \;=\; \frac{1}{2}\tau_{dyn,0}\,(\frac{R}{r_L})^2\,(\frac{r_L}{r_0})^{(3-D)/2} \tag{2.26}$$

For the same values of parameters given above, we have τ_{diss} = 3.7 Gyr showing that these fractal objects can live for cosmological times.

Clumpuscules dissipate the turbulence energy through black body radiation to reach their final bound state. The energy per mass which is dissipated is the kinetic energy per mass $\sim \frac{1}{2}$ (200 km s^{-1})^2 = 2 $\times$ 10^{14} erg g^{-1} quite larger than the energy released by H_2 formation process $\sim$ 2.2 eV/m_H = 2 $\times$10^{12} erg g^{-1}. Thus, considering the corresponding values of $L_\bullet$ and $M_\bullet$ for the clumpuscules we get the dissipation time scale as:

$$\tau_{200} \;=\; \frac{\frac{1}{2}(200\text{ km s}^{-1})^2}{L_\bullet/M_\bullet} \;=\; 16\,T^{-9/4}\,\mu^{1/4}\,f^{1/2}\;\text{[Gyr]} \tag{2.27}$$

For T = 3 k, μ = 2.3 and f = 1 we get τ_{200} = 1.2 Gyr. So, after about a Gyr the clumpuscules are bound and take their observed rotation velocities. The computed τ_{200} is the lower bound of the dissipation time scale. Near isothermal condition provides a weakly dissipative regime with a low energy dissipation by turbulence . Also, energy sources like CMB decrease the dissipation rate.

Star Non-Formation

From relations (2.4) the increase in temperature makes the clumpuscules smaller and the dynamical (free fall) time shorter which in turn, from relation (2.15), decreases the collision rate. As an example, consider a cloud with mass of 10^6 $M_\odot$ and radius of 30 pc. By substituting these values, from relation (2.4) to relation (2.7) we calculate the fractal dimension as a function of μ and T with f = 1:

$$D(\mu, T) = \frac{77.2 - ln\, T + 9\, ln\, \mu}{42.5 + 3\, lnT + 5\, ln\, \mu} \tag{2.28}$$

Figure 2.8 at top shows the variation of D with the temperature for μ = 2.3 and 0.63. The fractal dimension falls as temperature increases. At bottom we have the ratio of clumpuscules collision time to their free fall time (relation (2.17)) for N = 10 and 100. $\tau_{col,1}/\tau_{dyn,0}$ grows rapidly when the temperature increases specially for large values of N. As the temperature augments the collision rate decreases and the clumpuscules remain longer in adiabatic regime, they contract and get denser. Moreover, at T > 3000 K we have D < 1 and the collisions will be subsonic, which is a circumstance favourable to clumpuscules contraction. These conditions increase the possibility of the star formation process. If there is any nearby effect such as supernova explosion or large scale galactic disturbances then the increase in clumpuscules' temperature with T > 3000 K is possible and the stars may form.

2.6 Conclusion

The fact that outer disk cold clouds can survive for $\gg 10^8$ yr despite of their short cooling time $\ll 10^6$ yr can be explained by taking into account the fractal form of the clouds which is shaped essentially from gravitational interactions. From the scenario explained in this chapter, the turbulence energy, originated from galactic rotation, cascades through hierarchy until the last level and dissipate there through black body radiation at T < 10 K. The time scale of radiation due to dissipation is of order of Gyr. If this slow energy transfer from galactic rotation along the hierarchy occurs in a steady state then the power per mass is constant and the fractal dimension will be D = 1.67 (equation (2.23)) corresponding to Kolmogorov turbulence. The fragmentation stops at a scale where the transition between

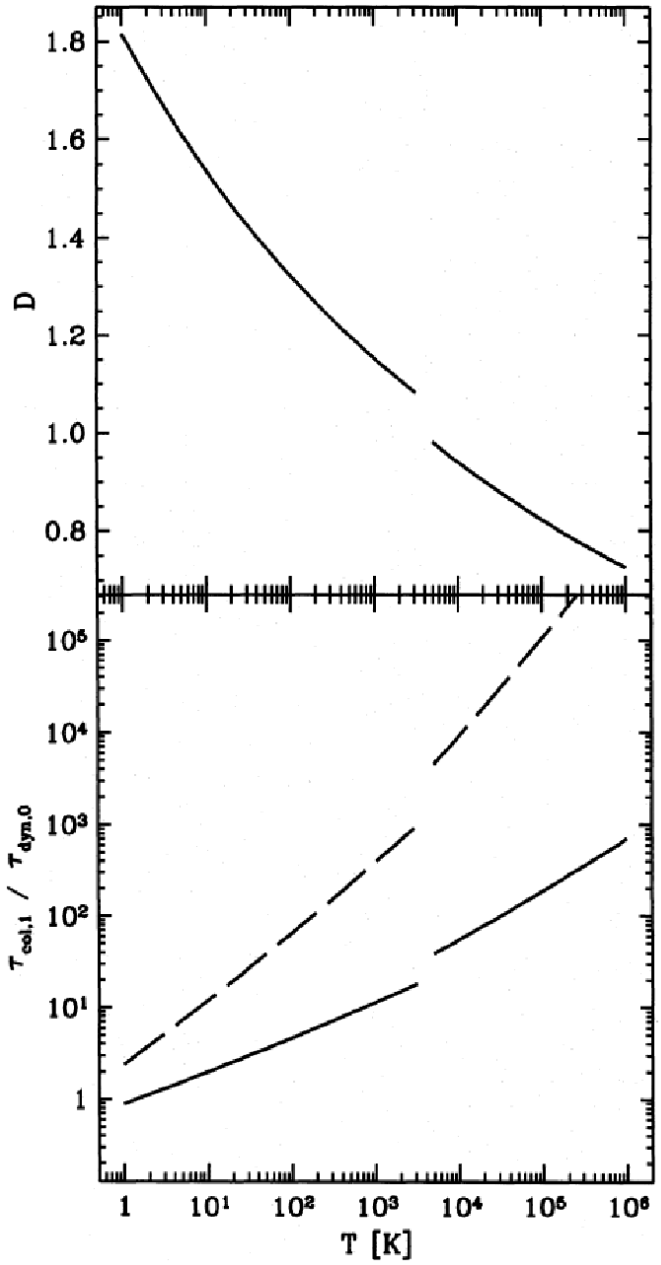

Figure 2.8: Top: dependence of the fractal dimension D as a function of T for a cloud with $M = 10^6$ $M_\odot$ and a radius of 30 pc. At $T < 3000$ K, $\mu = 2.3$ and at $T > 5000$ K, $\mu = 0.63$. Bottom: variation of the ratio $\tau_{col,1}/\tau_{dyn,0}$ with the temperature for the same condition, for $N = 10$ (solid) and $N = 100$ (dash) [Pfenniger & Combes (1994)].

isothermal contraction and adiabatic contraction happens. These tiniest scales contain the clumpuscules which are the building blocks of the fractal clouds. They contain objects of Jupiter mass with size of $\sim$ 30 AU and a column density $\sim 10^{24}$ H cm^{-2}. In a proper range of fractal dimension, 1.5 < D < 2, and $N \sim 10$, clumpuscules can experience frequent supersonic collisions. The collision time is comparable to the time scale of the adiabatic contraction (τ_{ff} or $\tau_{dyn,0}$). By colliding supersonically, the clumpuscules merge and expand due to reheating caused by shocks. The process of coalescence, fragmentation and disruption of clumpuscules continues in a statistical equilibrium. Far enough from any external heating sources and energetics, the cloud can be assumed to be in thermal equilibrium with cosmic background radiation and no star formation process take part. Hence, the clumpuscules consist of hydrogen gas mainly in molecular phase.

Chapter 3

Scintillation Effect

We propose to use the refractive properties of the medium to detect the transparent clouds. If turbulence occurs, the molecular density fluctuates stochastically causing refraction index fluctuations. Thus, a crossing wavefront experience variable optical path depending on the location, which induce a stochastic phase delay to the wavefront. The propagation of the distorted wave produces an interference (illumination) pattern on the observer plane. The relative motion between the pattern and the observer produces the apparent scintillation of the background source.

3.1 Wave Propagation in a Dielectric Medium

We briefly review the propagation of the electromagnetic waves in a homogeneous, polarisable and magnetizable medium with electrical permittivity ϵ, magnetic permeability μ and electrical conductivity σ. The propagation of electromagnetic waves is described by Maxwell's equations. Assuming the medium contains no free charge, the equations can be written as[1]:

$$\begin{aligned} \operatorname{div} \mathbf{E} &= 0, \\ \operatorname{curl} \mathbf{E} &= -\frac{\mu}{c}\frac{\partial \mathbf{H}}{\partial t}, \\ \operatorname{curl} \mathbf{H} &= \frac{\epsilon}{c}\frac{\partial \mathbf{E}}{\partial t} + \frac{4\pi\sigma}{c}\mathbf{E}, \\ \operatorname{div} \mathbf{H} &= 0, \end{aligned} \tag{3.1}$$

where $\mathbf{E}$ and $\mathbf{H}$ are electric and magnetising fields[2] respectively. c is the light speed in vacuum. Computing the curl of the two middle equations of relations (3.1) and substituting other two equations, we obtain the following equations for electric and magnetising

[1] CGS system is used.

[2] For magnetic field $\mathbf{B}$, we have $\mathbf{B} = \mu\,\mathbf{H}$.

fields:

$$\begin{aligned} \nabla^2 \mathbf{E} &= \frac{\epsilon\mu}{c^2}\frac{\partial^2 \mathbf{E}}{\partial^2 t} + \frac{4\pi\mu\sigma}{c^2}\frac{\partial \mathbf{E}}{\partial t}, \\ \nabla^2 \mathbf{H} &= \frac{\epsilon\mu}{c^2}\frac{\partial^2 \mathbf{H}}{\partial^2 t} + \frac{4\pi\mu\sigma}{c^2}\frac{\partial \mathbf{H}}{\partial t}. \end{aligned} \tag{3.2}$$

As we are interested in a medium made of H_2 molecules (which is an electrical insulator), $\sigma = 0$ and relations (3.2) reduce to an ordinary wave equations. Since the wave is propagating in a dense medium, the wave velocity is no longer the vacuum light velocity and has the value c':

$$c' = \frac{c}{\sqrt{\mu\epsilon}}.$$

Therefore, the optical refraction index, n_r, of the medium is:

$$n_r = \frac{c}{c'} = \sqrt{\mu\epsilon}.$$

Assuming no magnetisation in the medium $\mu \approx 1$:

$$n_r = \sqrt{\epsilon}. \tag{3.3}$$

This has been verified in radio and infra-red frequencies as well as for the optical part of the electromagnetic spectrum for molecular hydrogen.

3.1.1 Dielectric Polarization

The external *macrophysical field strength* **E** causes the negative and positive charges of the medium to be separated from each other making electric dipoles. This effect is called polarisation. The dipole moment density per unit volume **P** is proportional to **E**:

$$\mathbf{P} = \frac{\epsilon - 1}{4\pi}\mathbf{E}. \tag{3.4}$$

If the medium is gaseous with negligible intermolecular interactions and assuming there is no permanent dipole moment[3], the external field, **E**, will be the only *effective field* seen by the molecules. Therefore, the dipole moment induced from electric field is written as:

$$\mathbf{p} = \alpha\mathbf{E},$$

where α is the *polarizability* of the molecule. Assuming the molecular number density per unit volume is n, the dipole moment density is given as:

$$\mathbf{P} = n\,\alpha\mathbf{E}. \tag{3.5}$$

Since, in general, molecules can be considered as long stretched structures which are not isotropic, molecule's polarisability differs by its different spatial orientation with respect to the external field. Far from UV frequencies (resonance frequencies of H_2), the mean polarisability of H_2 is $\overline{\alpha} = 0.8032 \times 10^{-30}$ m^3 [CRC (1998-99)].

[3]Which is true for H_2.

3.1.2 Phase Delay due to Refraction

From relations (3.4) and (3.5) we compute the permittivity of the medium:

$$\epsilon \;=\; 1 + 4\pi\, n\, \alpha$$

Using equation (3.3)] ($n\,\alpha \ll 1$):

$$n_r \approx 1 + 2\pi\, n\, \alpha. \tag{3.6}$$

The variation of the refraction index is proportional to the density fluctuation of the medium. The excess of optical path, δ, with respect to vacuum along the wave propagation direction, z, is:

$$\delta(x,y) \;=\; \int_0^{L_z} (n_r - 1)\, dz \;=\; 2\pi\, \alpha \int_0^{L_z} n(x,y,z)\, dz \;=\; 2\pi\, \alpha N_l(x,y). \tag{3.7}$$

Where N_l is the column number density of the gaseous medium. One can calculate the 2D phase delay from equation (3.7):

$$\phi(x,y) \;=\; \frac{2\pi}{\lambda}\, \delta(x,y) \;=\; \frac{(2\pi)^2\, \alpha}{\lambda}\, N_l(x,y) \tag{3.8}$$

Considering a turbulent interstellar cloud, the 3D density is distributed stochastically and inhomogeneously through various scales and this creates random fluctuations of the 2D phase delay. The relation between the spectrum of the 3D density fluctuations and the phase spectrum will be discussed in section 3.3.

3.2 Thin Screen Approximation

In addition to the phase delay produced by the fluctuations of the refraction index, there is another source of phase delay due to the wave scattering from the inhomogeneities inside the turbulent medium. In contrast to the phase delay induced by refraction, this latter case is purely geometrical and the phase delay is produced by excess in (geometrical) optical path. This effect can be neglected if the geometrical phase delay is negligible compared to the refractive phase delay. This is the case if the deviation of the light trajectory from the line of sight -due to scattering- is small and the medium can be considered as a *thin screen*.

Figure 3.1 shows the ray trajectory through a turbulent medium deviated from a straight line by the consecutive scatterings from inhomogeneities with size of l. The size l spans the inner to the outer scales of the turbulent medium. For simplicity, we have chosen a 2D picture with transversal x and radial z coordinates. The wavefront enters the medium along the z direction and scatters in x direction through its propagation inside the medium.

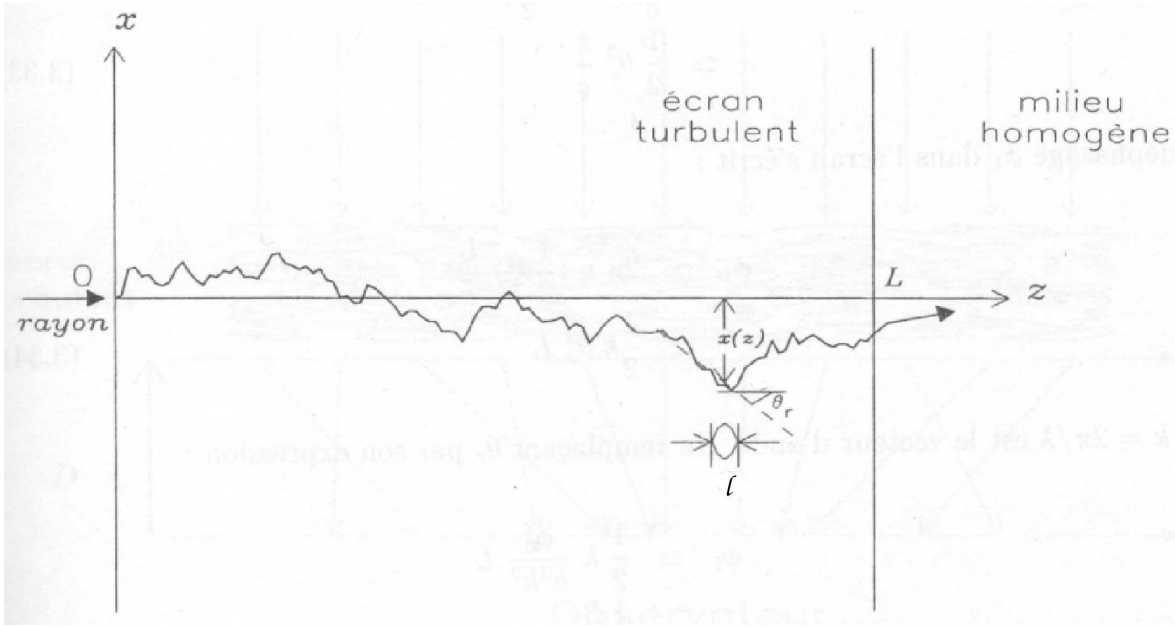

Figure 3.1: Inside a turbulent cloud, an entering wave from z direction is scattered from inhomogeneities with typical size of l along the transversal direction x. The cloud can be considered to as a thin screen when the translation along x is smaller than size of inhomogeneities [Hamidouche (2003)].

While the ray moves from z to $z + \Delta z$ and scatters from inhomogeneity of size l, it gets a transversal deviation of $x(z + \Delta z)$ - $x(z)$. The thin screen approximation is valid if each of the transversal displacements is much smaller than l:

$$x(z + \Delta z) - x(z) \ll l \implies \Delta z\, \theta_r \ll l, \tag{3.9}$$

where θ_r is the scattering angle at given z (see figure 3.1). According to figure 3.2, light scatters from an inhomogeneity with size l. Considering a maximum phase delay ϕ_0 induced on wavefront by the inhomogeneity, at first order the scattering angle is estimated as:

$$\theta_r \simeq \frac{\phi_0}{kl} \simeq \frac{l}{2f}, \tag{3.10}$$

where $k = 2\pi/\lambda$ is the wavenumber and f is the *focal length* of the inhogeneity. From relations (3.9) and (3.10) we have:

$$\Delta z \ll \frac{k\, l^2}{\phi_0} = 2f, \tag{3.11}$$

—— crossing the total thickness of the cloud we should have $\Delta z = L_z$ (larger than the outer scale of the turbulence L_{out} meaning that l is always < L_z). Therefore, the screens

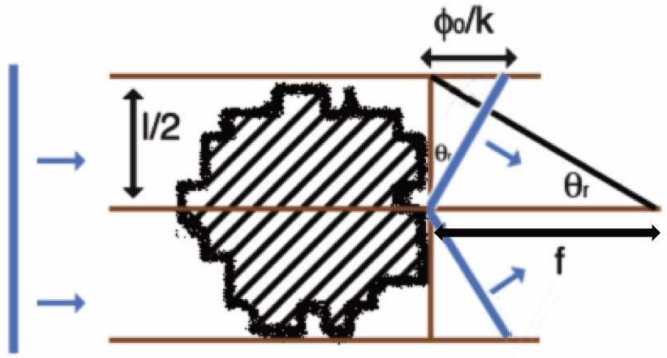

Figure 3.2: Schematic view of light scattering from an inhomogeneity with size l.

satisfies the thin screen approximation if:

$$L_{out} \;<\; L_z \;\ll\; 2f. \tag{3.12}$$

To compute the total optical path excess δ_s due to scattering, we consider that for an infinitesimal radial displacement dz there is a transversal translation $dx = \theta_r\, dz$:

$$ds \;=\; \sqrt{dx^2 + dz^2} \;=\; \sqrt{1+\theta_r^2}\, dz. \tag{3.13}$$

To hold the approximation, θ_r should be a small angle:

$$ds \;=\; (1+\frac{1}{2}\theta_r^2)\, dz \;\Longrightarrow\; s \;=\; L_z + \frac{1}{2} L_z\, \theta_r^2, \tag{3.14}$$

where we have integrated for z from 0 to L_z to compute the total distance s traveled by the ray. The optical path excess is:

$$\delta_s \;=\; s - L_z \;=\; \frac{1}{2} L_z \theta_r^2. \tag{3.15}$$

The total phase delay ϕ_s produced by scattering is given as:

$$\phi_s \;=\; k\,\delta_s \;=\; \frac{1}{2} L_z \frac{\phi_0^2}{k\, l^2} \;=\; \frac{1}{4}\frac{L_z}{f}\phi_0. \tag{3.16}$$

From inequality (3.12), we get:

$$\phi_s \ll \phi_0. \tag{3.17}$$

For instance, an inhomogeneity inside a clumpuscule with size $l < L_z = 30$ A.U. can be considered at first order as a spherical (biconvex) lens. Using the focal length relation[4] and refraction index from equation (3.6), we compute $f < 10^{26}$ m and always $f \gg L_z$.

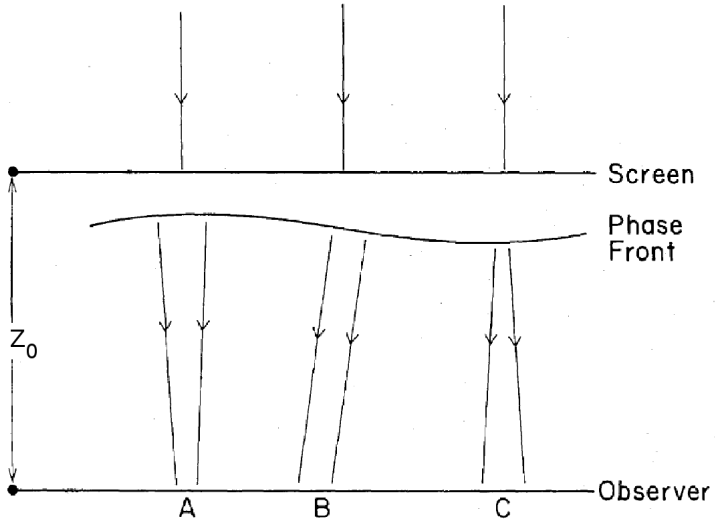

Figure 3.3: Schematic view of refractive scintillation. The monochromatic plane wave enters the turbulent screen. The phase is distorted after crossing the screen and shows converging and diverging configurations. On the observer plane, the light intensity is maximal at A, varies rapidly at B and is minimal at C. When there is a relative motion between the screen and the earth, fluctuations in light intensity (scintillation) will be observed from the earth. [Romani et al. (1986)]

Therefore, thin screen approximation is valid for clumpuscules.

By using the thin screen approximation, we consider a physical condition in which the phase delay due to the geometrical increase of the scattered path is negligible compared to the phase delay induced by the column density fluctuations. We can therefore describe the cloud as a 2D screen where the distortions induced to the wavefront are mainly due to fluctuations of the column density. The optical behaviour of such a screen is described by a *phase screen* given by equation (3.8).

Figure 3.3 gives a general idea of the scintillation effect in refractive mode (see section 3.5.3). The wavefront is distorted after crossing the screen. Depending on the shape of the distorted wavefront, light converges or diverges causing focusing/defocusing effects. Scintillation of a background star happens when the observer and the screen are in relative motion. Here we have assumed that the observed flux fluctuations are produced essentially from the screen-observer relative motion and not by the evolution of the screen's structures (the *frozen* screen approximation). The typical relative velocity of screen-observer is $\sim$ 100 km/s for the halo objects while the typical turbulence speed

[4] $f^{-1} = (n_r - 1)(\frac{2}{R} + \frac{2(n_r-1)d}{n_r R^2})$ where R (= l/2) is the radius of the lens curvature and d (= l) is the thickness of the lens.

inside the cloud is ~ 0.1 km/s.

3.3 Spectral Density of the Screen Phase

In the simulation chapter, we generate realisations of the phase screen from the spectral density of the phase fluctuations, $S_\phi(q_x, q_y)$. As shown by R.V.E Lovelace (1970), this spectrum is related to the three dimensional spectrum of the number density fluctuations of the molecules, S_{3n}. The Fourier transform of number density fluctuations, $n(x, y, z)$ is:

$$F_{3n}(q_x, q_y, q_z) = \iiint_{-\infty}^{\infty} n(x, y, z)\, e^{-2\pi i(xq_x+yq_y+zq_z)}\, dx\, dy\, dz,$$

where q_x, q_y, q_z are the coordinates in Fourier space. Now, we compute the Fourier integral for $q_z = 0$:

$$\begin{aligned} F_{3n}(q_x, q_y, q_z = 0) &= \iiint_{-\infty}^{\infty} n(x, y, z)\, e^{-2\pi i(xq_x+yq_y)}\, dx\, dy\, dz \\ &= \iint_{-\infty}^{\infty} \Big[\int_{-\infty}^{\infty} n(x, y, z)\, dz \Big]\, e^{-2\pi i(xq_x+yq_y)}\, dx\, dy \\ &= \iint_{-\infty}^{\infty} N_l(x, y)\, e^{-2\pi i(xq_x+yq_y)}\, dx\, dy \\ &= F_{N_l}(q_x, q_y), \end{aligned} \tag{3.18}$$

which is the Fourier transform of column density fluctuations. From equation (3.8), the Fourier transform of phase screen is $F_\phi = \frac{(2\pi)^2\alpha}{\lambda}\, F_{N_l}$. By substituting this relation in equation (3.18):

$$F_\phi(q_x, q_y) = \frac{(2\pi)^2\alpha}{\lambda}\, F_{3n}(q_x, q_y, q_z = 0).$$

Here, we will consider the average properties of a statistical set of screen realisations from a given power spectrum $\langle |F_{3n}|^2 \rangle$. The spectra are related as follows:

$$\langle |F_\phi(q_x, q_y)|^2 \rangle = (\frac{(2\pi)^2\alpha}{\lambda})^2\, \langle |F_{3n}(q_x, q_y, q_z = 0)|^2 \rangle, \tag{3.19}$$

where $\langle\, \rangle$ shows ensemble averaging over all realisations of the 2D phase Fourier components. Equation (3.19) can be re-written as:

$$L_x\, L_y\, S_\phi(q_x, q_y) = (\frac{(2\pi)^2\alpha}{\lambda})^2\, L_x\, L_y\, L_z\, S_{3n}(q_x, q_y, q_z = 0).$$

L_x, L_y and L_z are the dimensions of the box enclosing the cloud. The line of sight is assumed to be along the z direction. The spectral density of the phase screen will be:

$$S_\phi(q_x, q_y) = (\frac{(2\pi)^2\alpha}{\lambda})^2\, L_z\, S_{3n}(q_x, q_y, q_z = 0). \tag{3.20}$$

S_{3n} is a power law within inertial scale range of $L_{out}^{-1} < q < L_{in}^{-1}$ (see section 2.1.1):

$$S_{3n}(q_x, q_y, q_z) \;=\; C_n^2 \; q^{-\beta}, \tag{3.21}$$

by substituting it in to equation (3.20), we obtain:

$$S_{\phi}(q_x, q_y) \;=\; (\frac{(2\pi)^2\alpha}{\lambda})^2 \, L_z \, C_n^2 \, q^{-\beta}. \tag{3.22}$$

C_n^2 is a constant giving the strength of the turbulence spectrum, $q = \sqrt{q_x^2 + q_y^2 + (q_z = 0)^2}$ and β is the exponent of the power law spectrum (β = 11/3 for Kolmogorov turbulence).

3.4 Diffusion Radius

We can study the statistical properties of the phase screen also in the configuration space. The phase structure function:

$$D_{\phi}(x, y) \;=\; \langle [\phi(x + x', y + y') - \phi(x', y')]^2 \rangle, \tag{3.23}$$

gives the rms of the phase screen for different transversal separations (x, y). Assuming an isotropic medium, D_{ϕ} depends only on transversal length and not on the direction. Hence, $D_{\phi} = D_{\phi}(r)$ where $r = \sqrt{x^2 + y^2}$. The *difusion radius* is defined as the transversal separation for which the rms of the phase is 1 radian:

$$D_{\phi}(R_{diff}) \;=\; 1 \text{ radian}. \tag{3.24}$$

The diffusion radius gives a general view of the turbulence strength. As R_{diff} gets smaller the fluctuation in phase (and consequently the fluctuation in column density) gets larger for a given transverse scale. This means that more power is injected to the flow. In contrast, larger R_{diff} happens while the variation of the column density is slower and there is less power injection to the turbulent flow.

Considering an isotropic turbulence with a given β within its inertial cascade, the phase structure function can be written as:

$$D_{\phi}(r) \propto r^{\beta-2}, \tag{3.25}$$

and from the definition of R_{diff} we have [Narayan (1992)]:

$$D_{\phi}(r) \;=\; (\frac{r}{R_{diff}})^{\beta-2}. \tag{3.26}$$

We derive the diffusion radius as a function of the cloud turbulence and the geometrical parameters:

$$\begin{aligned} D_\phi(x,y) &= \langle[\phi(x+x',y+y')-\phi(x',y')]^2\rangle \\ &= \langle[(\phi(x+x',y+y')-\langle\phi\rangle)-(\phi(x',y')-\langle\phi\rangle)]^2\rangle \\ &= 2\left[(\langle\phi^2(x',y')\rangle-\langle\phi\rangle^2)-\langle(\phi(x'+x,y'+y)-\langle\phi\rangle)(\phi(x',y')\rangle-\langle\phi\rangle)\right] \\ &= 2\left[\zeta_\phi(0,0)-\zeta_\phi(x,y)\right], \end{aligned} \tag{3.27}$$

where $\zeta_\phi(x,y)$ is the 2D auto-correlation function of the phase screen. Here, we should mention that the average of the phase fluctuations is zero ($\langle\phi\rangle = 0$). The auto-correlation is the inverse Fourier transform of the phase spectral density:

$$\zeta_\phi(x,y) = \iint_{-\infty}^{\infty} S_\phi(q_x,q_y)e^{2\pi i(xq_x+yq_y)}dq_xdq_y. \tag{3.28}$$

Substituting equation (3.28) in equation (3.27) we obtain:

$$D_\phi(x,y) = 2\iint_{-\infty}^{\infty} S_\phi(q_x,q_y)(1-e^{2\pi i(xq_x+yq_y)})dq_xdq_y. \tag{3.29}$$

By substituting equation (3.22) in equation (3.29), we compute the phase structure function in polar coordinates:

$$D_\phi(r) = 2C_n^2L_z\left[\frac{(2\pi)^2\alpha}{\lambda}\right]^2\int_0^\infty\int_0^{2\pi} q^{-\beta}(1-e^{2\pi i\, r\, q\, cos\theta})d\theta q dq, \tag{3.30}$$

here $q=\sqrt{q_x^2+q_y^2}$ and $r=\sqrt{x^2+y^2}$. By integrating on θ:

$$D_\phi(r) = 2C_n^2(2\pi)L_z\big[\frac{(2\pi)^2\alpha}{\lambda}\big]^2\int_0^\infty q^{1-\beta}(1-J_0(2\pi rq))dq, \tag{3.31}$$

where J_0 is the Bessel function of the first kind of rank zero. Computing the integral for q:

$$D_\phi(r) = 2C_n^2(2\pi)^{\beta-1}f(\beta)L_z\big[\frac{(2\pi)^2\alpha}{\lambda}\big]^2r^{\beta-2}, \tag{3.32}$$

where

$$f(\beta) = \int_0^\infty s^{1-\beta}(1-J_0(s))ds = \frac{2^{-\beta}\,\beta\,\Gamma(-\beta/2)}{\Gamma(\beta/2)}. \tag{3.33}$$

For Kolmogorov turbulence $f(\beta=11/3)\sim 1.118$. By definition of R_{diff} from relation (3.24) and using equation (3.32), we obtain:

$$R_{diff} = [2C_n^2(2\pi)^{\beta+3}f(\beta)L_z\alpha^2\lambda^{-2}]^{1/(2-\beta)}. \tag{3.34}$$

From Parseval's theorem the integration of the spectrum in Fourier space is equal to the total dispersion. Therefore, we can link the constant C_n^2 to the cloud's parameters by integrating the spectral density of the volume number density fluctuations:

$$\begin{aligned} \sigma_{3n}^2 &= \int_{L_{out}^{-1}}^{L_{in}^{-1}} S_{3n}(q_x, q_y, q_z)\, dq_x\, dq_y\, dq_z \\ &= \int_{L_{out}^{-1}}^{L_{in}^{-1}} C_n^2 q^{-\beta} (4\pi) q^2 dq \;=\; \frac{4\pi C_n^2}{\beta - 3}(L_{out}^{\beta-3} - L_{in}^{\beta-3}), \end{aligned} \tag{3.35}$$

where σ_{3n} is the dispersion of the density fluctuations. Considering the fact that $L_{out} \gg L_{in}$ we estimate C_n^2 for β = 11/3:

$$C_n^2 = \frac{\sigma_{3n}^2}{6\pi L_{out}^{2/3}}. \tag{3.36}$$

If we assume that the outer scale of the turbulence is the same as the cloud size $L_z = L_{out}$,

$$C_n^2 = \frac{\sigma_{3n}^2}{6\pi L_z^{2/3}}. \tag{3.37}$$

Using equations (3.34) and (3.37), R_{diff} can be expressed as a function of the cloud's parameters and the wavelength:

$$R_{diff} = 789\,\mathrm{km} \left[\frac{\lambda}{1\mu\mathrm{m}}\right]^{\frac{6}{5}} \left[\frac{L_z}{10\mathrm{A.U.}}\right]^{-\frac{1}{5}} \left[\frac{\sigma_{3n}}{10^9\mathrm{cm}^{-3}}\right]^{-\frac{6}{5}}. \tag{3.38}$$

For any existing *local* turbulence with outer scale smaller than the cloud size, we substitute relation (3.36) in equation (3.34):

$$R_{diff} = 744\,\mathrm{km} \left[\frac{\lambda}{1\mu\mathrm{m}}\right]^{\frac{6}{5}} \left[\frac{L_z}{10\mathrm{A.U.}}\right]^{-\frac{3}{5}} \left[\frac{L_{out}}{10\ \mathrm{A.U.}}\right]^{\frac{2}{5}} \left[\frac{\sigma_{3n}}{10^9\mathrm{cm}^{-3}}\right]^{-\frac{6}{5}}. \tag{3.39}$$

(The constants of the two latter equations are different since they depend on different numbers of parameters). The phase spectral density can be expressed as a function of the diffusion radius by combining equations (3.22) and (3.34):

$$S_\phi(q_x, q_y) = \frac{R_{diff}^2}{2\,(2\pi)^{\beta-1}\, f(\beta)}\,(R_{diff}\, q)^{-\beta}. \tag{3.40}$$

3.5 Fresnel Diffraction and Scintillation Regimes

So far, we have discussed one of the optical aspects of the turbulent cloud by studying the statistical properties of the phase screen. Now, we consider the propagation of the

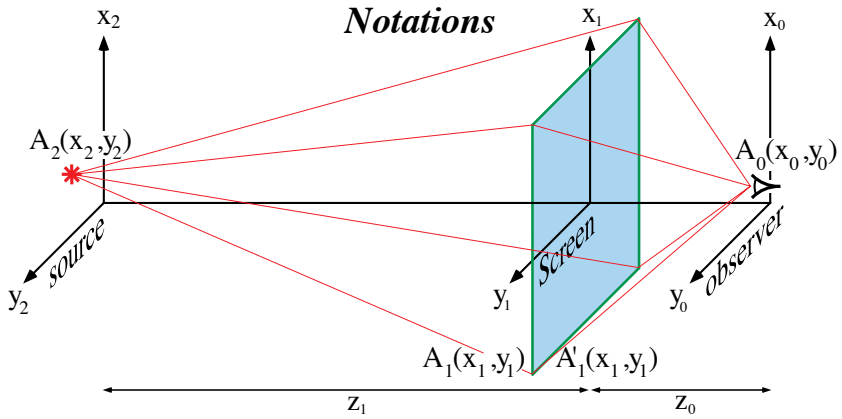

Figure 3.4: Notations: The source is located in the (x_2, y_2) plane, the screen contains the diffusive structure, and the observer is located in the (x_0, y_0) plane. $A_1(x_1, y_1)$ and $A'_1(x_1, y_1)$ are the amplitudes before and after screen crossing. [Moniez (2003)]

distorted wavefront and compute the corresponding *illumination pattern* on the observer plane. The formation of dark/luminous regions on the observer plane is due to optical diffraction as explained below.

Let $A_2(x_2, y_2)$ be the luminous (complex) amplitude produced on the source plane as shown in Figure 3.4. For a monochromatic point-like source with wavelength λ and amplitude A located at (x_2, y_2) on the source plane, omitting the time periodic factor $e^{-i\omega t}$, the amplitude just before entering the screen is given by the spherical wave equation:

$$A_1(x_1, y_1) \;=\; Ae^{ikr_{12}}/r_{12} \simeq Ae^{ikz_1}/z_1, \tag{3.41}$$

where $k = 2\pi/\lambda$ is the wave number, and

$$r_{12} \;=\; \sqrt{z_1^2 + (x_1 - x_2)^2 + (y_1 - y_2)^2} \tag{3.42}$$

$$\;=\; z_1\sqrt{1 + (\frac{x_1 - x_2}{z_1})^2 + (\frac{y_1 - y_2}{z_1})^2}, \tag{3.43}$$

r_{12} can be approximated by z_1 in the denominator of the relation (3.41) as we will always be in the situation where $z_1 \gg x_1$ and y_1 which means the distance of the background sources is much larger than the cloud size. For the same reason, the phase kr_{12} can be estimated by kz_1. We can thus consider the waves entering the medium as *plane waves*. The effect of the screen on the wave after crossing the screen can be represented by a phase delay that depends only on x_1 and y_1:

$$A'_1(x_1, y_1) \;=\; \frac{Ae^{iz_1}}{z_1} e^{i\phi(x_1, y_1)}, \tag{3.44}$$

where $\phi(x_1, y_1)$ is the phase screen discussed in section 3.1.2. After subsequent propagation in vacuum the amplitude on the observer plane $A_0(x_0, y_0)$ is given by the diffraction integral using Huygens-Fresnel diffraction principle:

$$A_0(x_0, y_0) = \iint_{-\infty}^{+\infty} A'_1(x_1, y_1)\, \frac{e^{ikr_{01}}}{i\lambda r_{01}}\, \cos\theta\, dx_1 dy_1, \tag{3.45}$$

where

$$r_{01} = z_0 \sqrt{1 + (\frac{x_0 - x_1}{z_0})^2 + (\frac{y_0 - y_1}{z_0})^2}. \tag{3.46}$$

$\cos\theta = z_0/r_{01}$, hence, θ is the angle of the direction defined by (x_0,y_0) on the observer plane and (x_1,y_1) on the screen with respect to the normal. We use the *stationary phase approximation* which states that the main contribution to integral (3.45) comes from the regions in which the exponential argument is extremum ($x_1 = x_0$ and $y_1 = y_0$). Indeed, r_{01} varies very fast as soon as $\sqrt{(x_0 - x_1)^2 + (y_0 - y_1)^2}$ is larger than a few Fresnel radii and the contribution of the corresponding (x_1, y_1) regions is cancelled by the fast oscillations of the term $e^{ikr_{01}}$.

Another approximation applicable to the diffraction integral is the *Fresnel approximation*. Let $\rho^2 = (x_1 - x_0)^2 + (y_1 - y_0)^2$; equation (3.46) can be expanded in Taylor series:

$$r_{01} \;=\; z_0\,(1 + (\frac{\rho}{z_0})^2)^{\frac{1}{2}} \;=\; z_0 + \frac{\rho^2}{2z_0} - \frac{\rho^4}{8z_0^3} + ... \tag{3.47}$$

Fresnel approximation consists in keeping only the two first terms of the expansion (3.47). It is sufficient if the third term is such that $k\,\frac{\rho^4}{8z_0^3} \ll 2\pi$ or equivalently, $\frac{\rho^4}{8z_0^3\lambda} \ll 1$. This is the usual condition of our observations. As an example, for a nearby nebula at $z_0 \sim 1$ kpc, $\rho_{max} \sim 30$ A.U. and at infrared wavelength: $\frac{\rho^4}{8z_0^3\lambda} \sim 10^{-2}$. Thus, we approximate the relation (3.46) as:

$$r_{01} \simeq z_0 \left[1 + \frac{1}{2}(\frac{x_0 - x_1}{z_0})^2 + \frac{1}{2}(\frac{y_0 - y_1}{z_0})^2\right]. \tag{3.48}$$

Since $e^{ikz_0\left[1+\frac{1}{2}(\frac{x_0-x_1}{z_0})^2+\frac{1}{2}(\frac{y_0-y_1}{z_0})^2\right]}$ oscillates very fast when (x_1, y_1) is far from (x_0, y_0), we can keep this expression for r_{01} up to infinite without changing the integral, thanks to the stationary phase approximation. Moreover, as z_0 is much larger than the screen size, we can estimate $\cos\theta \simeq 1$ and $r_{01} \simeq z_0$ on the denominator of integral (3.45). Applying these approximations to equation (3.45), light amplitude on the observer plane is obtained as:

$$\begin{aligned} A_0(x_0, y_0) &= \frac{e^{ikz_0}}{i\lambda z_0} \iint_{-\infty}^{+\infty} A'_1(x_1, y_1) e^{\frac{ik}{2z_0}[(x_0-x_1)^2+(y_0-y_1)^2]} dx_1 dy_1 \\ &= \frac{e^{ikz_0}}{2i\pi R_F^2} \iint_{-\infty}^{+\infty} A'_1(x_1, y_1) e^{i\frac{(x_0-x_1)^2+(y_0-y_1)^2}{2R_F^2}} dx_1 dy_1, \end{aligned} \tag{3.49}$$

where $R_F = \sqrt{z_0/k} = \sqrt{\lambda z_0/2\pi}$ is the *Fresnel radius*. R_F is of order of 1500 km to 15,000 km at λ = 500 nm, for a screen located between 1 kpc to 100 kpc from us. This length scale characterises the (x_1, y_1) domain that effectively contributes to the integral for a given (x_0, y_0). When $\sqrt{(x_0 - x_1)^2 + (y_0 - y_1)^2)}$ is larger than a few Fresnel radii, the contribution to the integral vanishes due to the fast oscillation of the phase term.

Whether the diffraction type is Fresnel or Fraunhofer depends on the ratio of the screen size and the Fresnel radius. In our case, the cloud size is some tens of A.U. and R_F is some thousands of kilometers. As $\frac{L_z}{R_F}$ is always > 1, we are in Fresnel diffraction mode.

By substituting $A'_1(x_1, y_1)$ from equation (3.44) to equation (3.49):

$$A_0(x_0, y_0) \;=\; \frac{e^{ikz_0}}{2i\pi R_F^2}\,\frac{e^{ikr_{12}}}{z_1} A \iint_{-\infty}^{+\infty} e^{i\phi(x_1,y_1)} e^{i\frac{(x_0-x_1)^2+(y_0-y_1)^2}{2R_F^2}}\, dx_1 dy_1 \quad (3.50)$$

Relation (3.50) formulates the illumination pattern produced for a point-like source as observed on the observer plane. As mentioned before, the illumination pattern sweeps the observer plane if there is a relative transverse motion between the observer and the screen. This induces a variation of the light from the source with the time, called scintillation.

3.5.1 Extended Source and Spatial Coherence

A star can be considered as an *extended source* made of incoherent point-like sources distributed in a limb profile. The observed intensity from a point-like source, $I_0(x_0, y_0)$, is:

$$I_0(x_0, y_0) \;=\; |A_0(x_0, y_0)|^2 \;=\; \frac{L_s}{z_1^2}\, h(x_0, y_0), \quad (3.51)$$

where $L_s = |A|^2$ is the luminosity of the source and

$$h(x_0, y_0) \;=\; \left|\frac{1}{2\pi R_F^2} \iint_{-\infty}^{+\infty} e^{i\phi(x_1,y_1)} e^{i\frac{(x_0-x_1)^2+(y_0-y_1)^2}{2R_F^2}}\, dx_1 dy_1\right|^2. \quad (3.52)$$

Let $I_0(x_0, y_0)$ be the illumination pattern of a point-like source located at (0,0) on the source plane; if the source is translated to point (x_2,y_2) the intensity at (x_0,y_0) on the observer plane will be $I(x_0, y_0) = I_0(x_0 - x_2 z_0/z_1\,,\; y_0 - y_2 z_0/z_1)$. This means that by changing the position of the point-like source on the source plane, the illumination pattern just translates on the observer plane.

As a combination of incoherent point-like sources, the total intensity $I_{ext}(x_0, y_0)$ is the

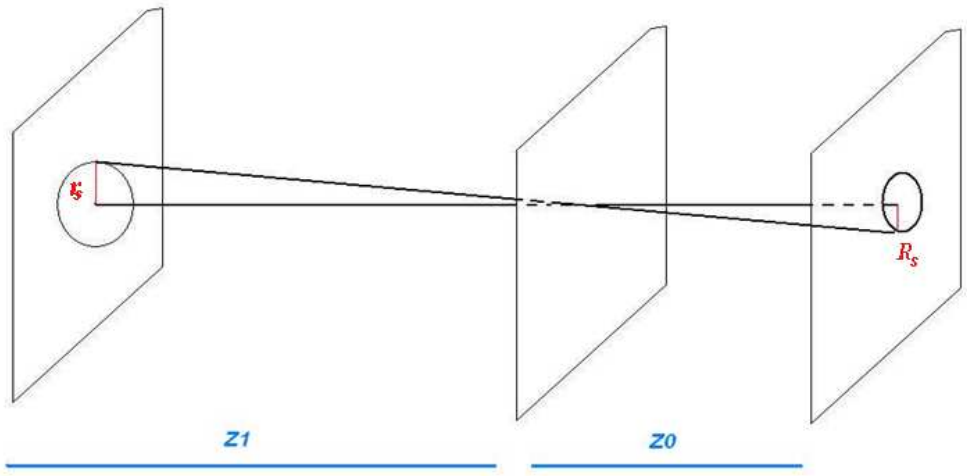

Figure 3.5: An extended source with radius r_s (left plane) has a projected radius R_s = $(z_0/z_1)\, r_s$ on the observer plane (right plane).

sum of intensities produced by each element of the extended source:

$$\begin{aligned} dI_{ext}(x_0, y_0) &= \frac{1}{z_1^2}\, h(x_0 - x_2\frac{z_0}{z_1},\, y_0 - y_2\frac{z_0}{z_1})\, dL_s(x_2, y_2) \\ &= \frac{L_s}{z_1^2}\, h(x_0 - x_2\frac{z_0}{z_1}\,,\, y_0 - y_2\frac{z_0}{z_1})\, p(x_2, y_2)\, dx_2\, dy_2, \\ I_{ext}(x_0, y_0) &= \frac{L_s}{z_1^2} \iint\limits_{S.P.} h(x_0 - x_2\frac{z_0}{z_1}\,,\, y_0 - y_2\frac{z_0}{z_1})\, p(x_2, y_2)\, dx_2\, dy_2, \end{aligned} \tag{3.53}$$

where $p(x_2, y_2)$ is the limb profile of the extended source, $\iint p(x_2, y_2)\, dx_2\, dy_2 = 1$ and L_s is the total luminosity. $S.P.$, the "Source Profile" is the integration domain limited by the surface covered by the source profile on the source plane. By changing the variables X_0 = $x_2 z_0/z_1$ and $Y_0 = y_2 z_0/z_1$, we have:

$$I_{ext}(x_0, y_0) = \frac{L_s}{z_1^2} \iint (\frac{z_1}{z_0})^2\, h(x_0 - X_0\,,\, y_0 - Y_0)\, p(\frac{z_1}{z_0}X_0\,,\, \frac{z_1}{z_0}Y_0)\, dX_0\, dY_0 \tag{3.54}$$

We define the projected luminosity profile of the extended source $P_r(X_0, Y_0) = p(\frac{z_1}{z_0}X_0\ ,\ \frac{z_1}{z_0}Y_0)$. The illumination pattern of an extended source is obtained as:

$$\begin{aligned} I_{ext}(x_0, y_0) &= \frac{L_s}{z_0^2} \iint_{P.S.P.} h(x_0 - X_0\ ,\ y_0 - Y_0)\, P_r(X_0, Y_0)\, dX_0\, dY_0 \\ &= \frac{L_s}{z_0^2}\, P_r * h \\ &= (\frac{z_1}{z_0})^2\, P_r * I_0, \end{aligned} \tag{3.55}$$

where $P.S.P.$ (stands for "Projected Source Profile") is the integration domain (the projected surface of the source profile on the observer plane, see figure 4.10). The final result is that the illumination from an extended source is given by the convolution between the illumination pattern of the point-like source, $h(x_0, y_0)$, and the projected profile of the extend source on the observer plane, $P_r(x_0, y_0)$. Therefore, the illumination pattern of an extended source is *smoother* than the pattern produced by a point-like source. The projected radius of the source R_s acts as a low-passband spatial filter, and variations with length scale smaller than R_s are washed out. We will discuss this point again in the next chapter.

3.5.2 Weak Scattering Regime: $R_{diff} \gg R_F$

The diffusion radius R_{diff} is the length scale which characterises the transverse variations of the phase screen. If $R_{diff} \gg R_F$ the phase does not change noticeably within a few Fresnel zones, $D_\phi(R_F) \ll 1$ and the wave front is only mildly perturbed.

For a constant phase, $\phi(x_1, y_1) = const.$, the point-like source illumination pattern $h(x_0, y_0)$ = 1. In weak scattering regime, there are small phase fluctuations and $h(x_0, y_0)$ is weakly perturbed from unity. If the phase screen is focusing in the first Fresnel zone around (x_0, y_0) the propagation term $\frac{(x_0-x_1)^2+(y_0-y_1)^2}{2R_F^2}$ is partly compensated by the variation of $\phi(x_1, y_1)$ and $h(x_0, y_0) > 1$. The inverse result is obtained when the phase screen is defocusing. The propagation term acts as a spatial low-passband filter with length scale R_F. Therefore, for a point-like source, in weak scattering regime, the flux variations on the observer plane depend on the scale R_F [Narayan (1992)].

The effect of the source extension on the illumination pattern in this regime depends on the projected radius of the source R_s, compared to Fresnel radius. If $R_F > R_s$ the Fresnel radius remains as the characteristic length of the scintillation, if not, the variations of intensity are filtered by R_s. From observational view point, the Fresnel radius is usually of order of hundreds of kilometers while the projected radius is ten thousands of kilometers wide. Usually, the scintillation in weak scattering regime is washed out by the source profile.

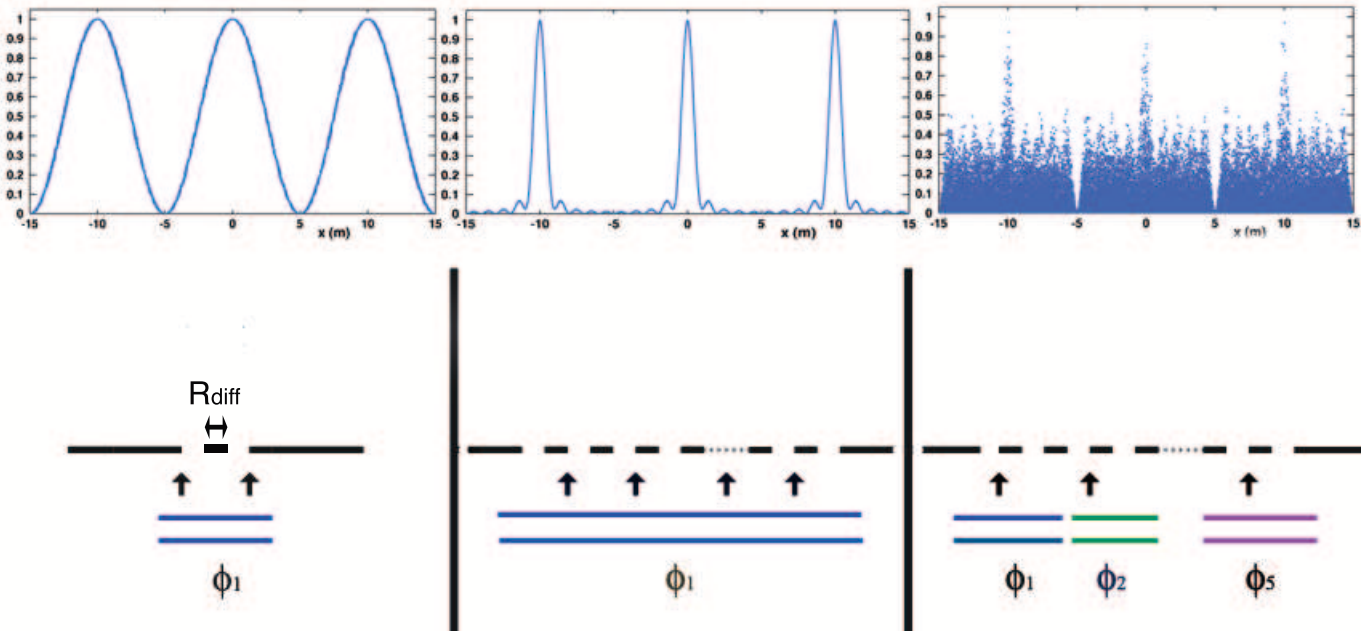

Figure 3.6: 1D Young Experiment. Vertical axes show the relative intensity. Left: Diffraction pattern by a slit-pair scattering. Waves have the same phase ϕ_1 while crossing the slits. dark/luminous regions have the typical size of 10 m. Middle: Diffraction pattern by five slit-pairs scattering. The light from the slit-pairs are at the same phase ϕ_1. All scattered waves interfere constructively at the same maxima as the double-slit (left panel) experiment with narrower luminous distribution. Right: Same as the middle panel but the phase of light varies stochastically from pair to pair. Here also the typical size of dark/luminous regions are 10 m. An extra phenomenon is the speckles with typical separation of ~ 0.1 m.

3.5.3 Strong Scattering Regime: $R_{diff} \ll R_F$

Strong scattering happens when $R_{diff} \ll R_F$. The phase screen varies by many radians within a Fresnel radius since $D_\phi(R_F) \gg 1$. R_F is not anymore the length scale of scintillation because R_{diff} is the characteristic size of the (x_1, y_1) domain which contribute coherently to integral (3.50) around (x_0, y_0). The contribution is assumed to be coherent because the phase screen can be considered as sufficiently constant (within a radian) in scale R_{diff} to contribute to the integral. We can consider the screen as a 2D plane made of many patches with size R_{diff} located at distance R_{diff} from each other. The phase is nearly constant (within a radian) in each patch and varies stochastically from patch to patch. To understand the physics of strong scattering regime we compare it to Young experiment with multiple slits (see figure 3.6) [Narayan (1992)]. Here, each patch is similar to a pair of slits with slits separated by distance of R_{diff} from each other and emitting light with the *same* phase ϕ_1. Each pair is located at distance R_{diff} from the next pairs. Figures 3.6 compare Young experiments with multiple slits. Slits are at successive dis-

tance R_{diff} = 0.1 m, λ = 1 μm and the pattern is shaped at z_0 = 1000 km. Left panel of figure 3.6 shows the diffraction pattern of a double-slit scatterer. The initial phase of the wave before crossing each slit is the same. As the light scatters from a patch with R_{diff} size, the angle between successive dark/luminous regions on the observer plane from the screen is:

$$\theta_{scatt} = \frac{\lambda}{R_{diff}}. \tag{3.56}$$

The corresponding distance on the observer plane is $z_0\theta_{scatt} = z_0\lambda/R_{diff}$ = 10 m. We define the *refractive radius* R_{ref}, to be the typical size between dark/luminous regions:

$$R_{ref} \;=\; \frac{z_0\lambda}{R_{diff}} \;=\; 2\pi\frac{R_F^2}{R_{diff}}, \tag{3.57}$$

in our example R_{ref} = 10 m.

In the middle panel, the number of slit-pairs (coherent patches) is five. All patches have the same initial phase ϕ_1. Since the light is scattered within angle θ_{scatt} from each patch, each point on the observer plane receives light from all patches located inside angle θ_{scatt} on the screen. This is called *multipath propagation*. The luminosity maxima remain at the same positions as for the double-slit experiment, but the width of luminous regions are narrower showing the dominance of destructive interferences between the maxima. The right panel of figure 3.6 is the same as the middle one but the initial phases of the slit-pairs vary stochastically from pair to pair (with corresponding phases ϕ_1 to ϕ_5). This is similar to what happens in our turbulent phase screen. According to the figure, there is a random diffraction pattern with two modes of intensity variations. The first one is a global variation mode with length scale of R_{ref}. The randomness of the initial phases decreases the global contrast. This is called *refractive scintillation*. Within these large structures, a highly frequent fluctuation of intensity produces the *speckles*. These random speckles are due to multi-path propagation of light and have a characteristic separation $\sim \lambda/\theta_{scatt} = R_{diff}$, producing the second type of scintillation called *diffractive scintillation* [Narayan (1992)].

The equation (3.57) can be re-written as:

$$R_{ref}(\lambda) = \frac{\lambda z_0}{R_{diff}} \sim 30,860\,\text{km}\left[\frac{\lambda}{1\mu\text{m}}\right]\left[\frac{z_0}{1\,\text{kpc}}\right]\left[\frac{R_{diff}(\lambda)}{1000\,\text{km}}\right]^{-1}. \tag{3.58}$$

Taking into account the relative motion between the screen and the observer plane characterised by V_T, there are two time scales for the strong regime of scattering, $t_{ref} = R_{ref}/V_T$ and $t_{diff} = R_{diff}/V_T$:

$$t_{ref}(\lambda) \;\simeq\; 5.2\,\text{min.}\left[\frac{\lambda}{1\mu\text{m}}\right]\left[\frac{z_0}{1\,\text{kpc}}\right]\left[\frac{R_{diff}(\lambda)}{1000\,\text{km}}\right]^{-1}\left[\frac{V_T}{100\,\text{km/s}}\right]^{-1}, \tag{3.59}$$

considering equation (3.39):

$$t_{diff}(\lambda) = 7.4\,\mathrm{s}\left[\frac{\lambda}{1\mu\mathrm{m}}\right]^{\frac{6}{5}}\left[\frac{L_z}{10\mathrm{A.U.}}\right]^{-\frac{3}{5}}\left[\frac{L_{out}}{10\mathrm{A.U.}}\right]^{\frac{2}{5}}\left[\frac{\sigma_{3n}}{10^9\mathrm{cm}^{-3}}\right]^{-\frac{6}{5}}\left[\frac{V_T}{100\,\mathrm{km/s}}\right]^{-1} \quad (3.60)$$

These are the characteristic times of the light curve for a *point-like source*. As discussed before, the extension of the source has a crucial impact on the intensity variations of the light curve and always tends to smooth the fluctuations. As we will see in the next chapter, the projected star radius R_s is such that the speckles of the diffractive scintillation are alway washed out since usually $R_s > R_{diff}$. Thus, the refractive scintillation if $R_{ref} > R_s$ is the only fluctuation mode observed from the strong regime.

Chapter 4

Simulation

The simulation of the scintillation effect allows us to link the observables -measured from the light curves- to the physical properties of the turbulent medium. Through simulation we can study the behaviour of a variety of generated light curves due to different values of the scintillation parameters. We start with the simulation of a phase screen in section 4.1. The accuracy of the phase screen is checked by re-computation of R_{diff} from the generated phase. In section 4.2, we calculate the illumination pattern due to the propagation of the wave surface after crossing the screen. The images of the illumination patterns of a point-like and an extended source are produced. We discuss the sensitivity of the illumination patterns to the sampling of the phase screen. The effect of the time coherence of the source on the illumination patterns are also studied. In section 4.3, we statistically link the modulation index to the geometrical parameters of the scintillation effect. The light curves are extracted from the 2D illumination pattern. We have also considered turbulence types other than the Kolmogorov one and compare their statistical properties. After concluding, in section 4.4 we discuss the next steps for the future work.

4.1 Simulation of the Phase Screen

The two dimensional phase screen $\phi(x, y)$ can be simulated as a realisation of the phase power spectrum $P_\phi(q) = L_x\, L_y\, S_\phi(q)$ where L_x and L_y are the length and width of the screen, q is the spatial frequency and the spectral density $S_\phi(q)$ is given by relation 3.40. We begin by generating the 2D Fourier component of the phase screen ($F_\phi(q_x, q_y)$) from the spectrum $P_\phi(q)$ through a stochastic process. Then, by computing inverse Fourier transform, the 2D phase screen is calculated:

$$\phi(x, y) \;=\; \iint F_\phi(q_x, q_y)\, e^{2\pi i\,(xq_x + yq_y)}\, dq_x\, dq_y. \tag{4.1}$$

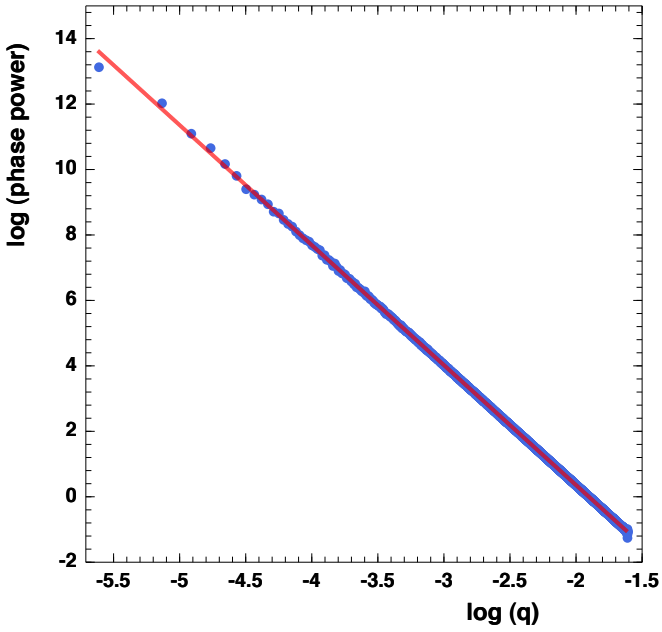

Figure 4.1: Red line: Initial phase spectrum. Blue points: Reconstructed spectrum from a realisation of a screen generated from the initial spectrum.

4.1.1 Generating the Fourier Component of the Phase Screen

The phase power spectrum is the ensemble average of the square module of different realisations of the phase Fourier components:

$$P_\phi(q) \quad = \quad \langle |F_\phi(q_x, q_y)|^2 \rangle_{q=\sqrt{q_x^2+q_y^2}}. \tag{4.2}$$

The fact that P_ϕ only depends on q comes from the isotropy of the turbulence. By assuming the ergodicity of the process, one can generate a single realisation $F_\phi(q_x, q_y)$ by selecting it stochastically from a Gaussian distribution with $\sigma^2 = P_\phi(q)$. Through this generation, the mean square of the generated $F_\phi(q_x, q_y)$ over the radius $q = \sqrt{q_x^2 + q_y^2}$ is $P_\phi(q)$.

A discrete phase screen with size $L_x = L_y = L$ is produced as a $N \times N$ matrix with pixel size Δ_1 ($L = N\Delta_1$)[1]. The corresponding Fourier space is also discrete with frequencies:

$$\begin{aligned} q_x &= \frac{n_x}{N\Delta_1}, \\ q_y &= \frac{n_y}{N\Delta_1}, \end{aligned} \tag{4.3}$$

[1] In general, the screen and the pixels need not to be necessarily square.

where n_x and n_y are integers spanning 0 to $N-1$. As we use FFT[2] technique, we should keep in mind that the Fourier components of positive frequencies are located in matrix elements with $n_{x,y} = 0$ to $N/2$ and the other elements belong to negative frequencies. By using a double loop on n_x and n_y, we explore the (q_x, q_y) domain, we compute q values for each pair of (q_x, q_y) and generate a value $F_\phi(q_x, q_y)$ from $P_\phi(q)$ as follows: $F_\phi(q_x, q_y)$ is a random realisation of parameter f_ϕ takesn from the Gaussian distribution $\frac{1}{\sqrt{2\pi P_\phi(q)}}\, e^{-f_\phi^2/(2P_\phi(q))}$. Both real and imaginary parts of $F_\phi(q_x, q_y)$ are generated from this distribution and the final value is divided by $\sqrt{2}$. Figure 4.1 shows the initial phase spectrum and the spectrum reconstructed from $F_\phi(q_x, q_y)$. The effect of the pixel size (sampling noise) will be discussed in section 4.2.3.

4.1.2 The Phase Screen

After generating $F_\phi(q_x, q_y)$, the phase screen is computed from relation (4.1) by FFT. Figure 4.2 shows an example of the simulated phase screen in grey scale. The dark and bright structures correspond to regions with large and small column density. $\phi(x, y)$ is generated in a 10000 $\times$ 10000 matrix with pixel size $\Delta_1 = 32.6$km. The original power spectrum is assumed to be Kolmogorov with a diffusion radius R_{diff} = 100 km. A horizontal section of the screen is plotted in Figure 4.3 which shows the phase variations as a function of the position along a transversal section of the screen. The larger structures are clearly visible since the spectrum contains more power at large scales. The average phase fluctuation should be one radian for transverse separation of R_{diff} on the screen (bottom of the figure). We discuss the accuracy of the reconstructed structure function in the following sub-section.

Check of the Structure Function Reconstruction

To check the quality of the simulated phase screen, we reconstructed the phase structure function from the simulated screen and re-calculated R_{diff}. In this purpose, we computed the reconstructed phase spectrum, $S_\phi^{rec}(q)$, from the generated $F_\phi(q_x, q_y)$:

$$S_\phi^{rec}(q) \;=\; \frac{\langle |F_\phi(q_x, q_y)|^2 \rangle_{q=\sqrt{q_x^2+q_y^2}}}{L_x\, L_y}, \tag{4.4}$$

[2]Fast Fourier Transform.

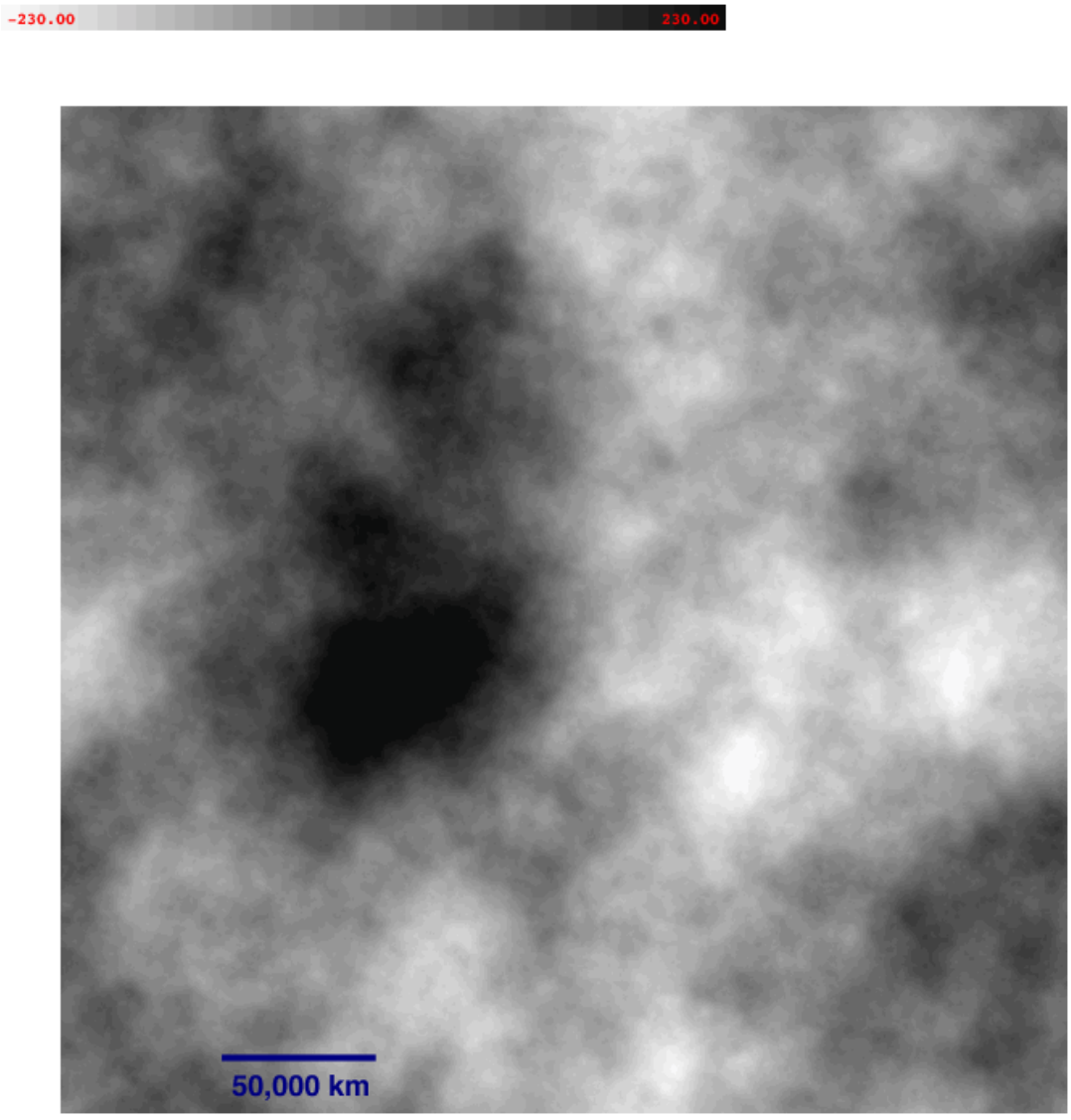

Figure 4.2: Simulated fluctuations of the phase screen with N = 10,000, Δ_1 = 32.6 km and R_{diff} =100 km. Phase fluctuations are given in radian (grey scales in radian).

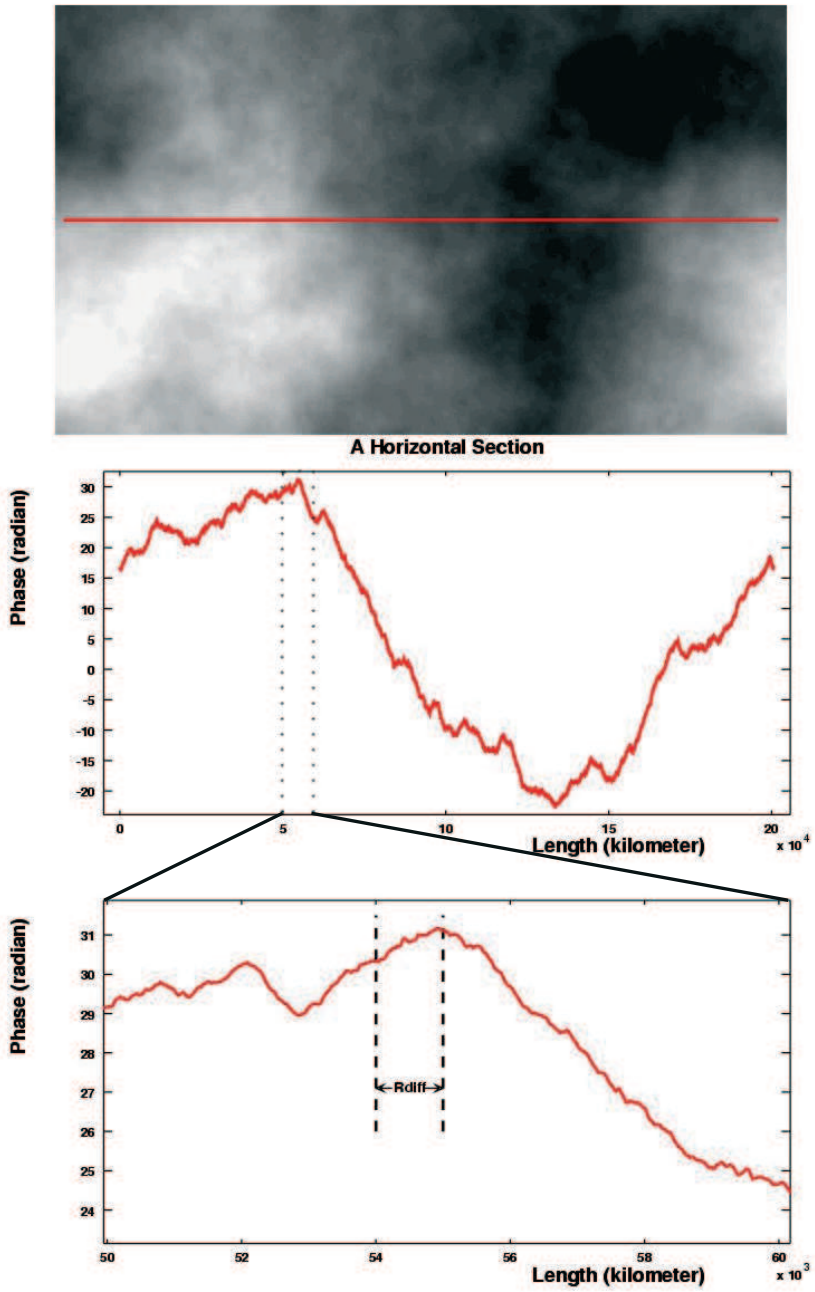

Figure 4.3: Top: A horizontal section of the phase screen. Middle: Phase variations as a function of position along the section. Bottom: Detailed phase variation within the diffusion radius is about one radian (should be one on average, by definition).

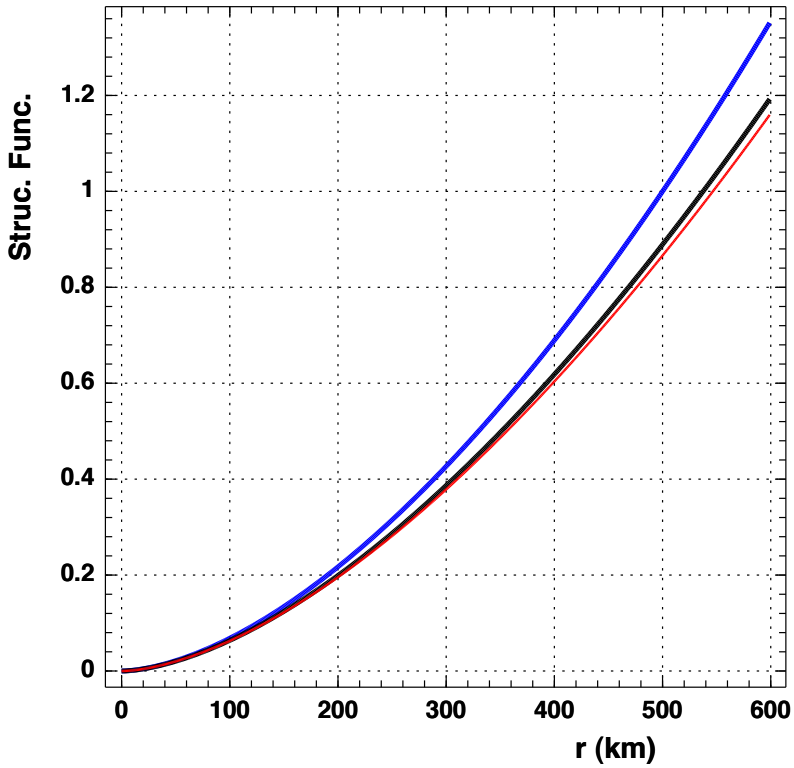

Figure 4.4: Phase structure function vs. transverse distance r with R_{diff} = 500 km. Blue line is the initial structure function. Red line is what we obtain from one of the realisations of the phase screen through simulation. The black curve is the numerical computation of the structure function from the phase spectrum with the same sampling used in simulation.

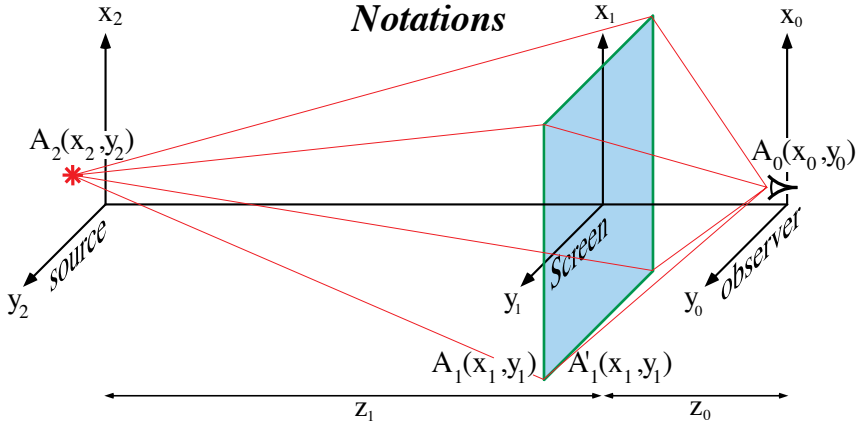

Figure 4.5: Coordinates on the screen and the observer plane are (x_1, y_1) and (x_0, y_0) respectively.

where the average is made on $|F_\phi(q_x, q_y)|^2$ with the same $q = \sqrt{q_x^2 + q_y^2}$. The reconstructed phase auto-correlation function is given by Fourier transform:

$$\begin{aligned} \xi^{rec}(\mathbf{r}) &= \iint S_\phi^{rec}(\mathbf{q})\, e^{2\pi i\, \mathbf{q}.\mathbf{r}} d\mathbf{q}, \\ \xi^{rec}(r) &= \int_{q_{min}}^{q_{max}} \int_0^{2\pi} q\, S_\phi^{rec}(q) e^{2\pi i\, qr cos\theta} d\theta\, dq \\ &= \int_{q_{min}}^{q_{max}} 2\pi q\, S_\phi^{rec}(q)\, J_0(2\pi qr)\, dq, \end{aligned} \tag{4.5}$$

where J_0 is the Bessel function. The reconstructed structure function is given by $D_\phi^{rec}(r)$ = 2($\xi^{rec}(0) - \xi^{rec}(r)$). In figure 4.4, we show the initial phase structure function of a medium with R_{diff} = 500 km by the blue curve, for which $D_\phi(500\,\text{km})$ = 1 radian by definition. The red curve represents the reconstructed function from one of the realisations of the screen. The reconstructed function equals one radian at $r \approx$ 540 km. To find the origin of the difference, we replaced $S_\phi^{rec}(q)$ by the initial spectrum $S_\phi(q)$ in equation (4.5). Then, we computed the integral numerically with the same sampling (number of pixels $N \sim$ 14,000 with Δ_1 = 28.85 km) and the same integration limits (q_{min}, q_{max}) [3] as the simulation. The black curve shows the integration result which differs by a few percent from the result of simulation (red curve). We showed that the black curve approaches the blue curve when $q_{min} \to 0$ and $q_{max} \to \infty$. This means that sampling affects the integration domain.

As a conclusion, since we are restricted by a finite number of pixels, we loose the contributions of the large and small scales in the reconstructed R_{diff}. The solution to avoid this limitation is to generate larger screens (bigger N) with higher resolutions (smaller Δ_1) to cover wider interval of frequencies which in return need to use computers with higher computational capacities.

4.2 Illumination Pattern

After the plane wave crosses the screen, light propagation is described by the Huygens-Fresnel principle which leads to the computation of the diffraction integral. The geometry of the diffraction is shown in figure 4.5. This Integral -that enters the calculation of the intensity on the observer plane $I(x_0, y_0) = I_0 h(x_0, y_0)$- can be considered as a Fourier transform by re-writing equation (3.52) as:

$$h(x_0, y_0) = |\, \frac{1}{2\pi i R_F^2} \int_{-\infty}^{+\infty} \int_{-\infty}^{+\infty} e^{i\,(\phi(x_1,y_1) + \frac{x_1^2+y_1^2}{2R_F^2})}\, e^{-2\pi i\,(\frac{x_0}{2\pi R_F^2} x_1 + \frac{y_0}{2\pi R_F^2} y_1)}\, dx_1 dy_1\, |^2,$$

[3] in 1D: $q_{min} = \frac{1}{N\Delta_1}$ and $q_{max} = \frac{1}{2\Delta_1}$.

$$h(x_0, y_0) = |\frac{1}{2\pi R_F^2} \quad FT(e^{i(\phi(x_1,y_1)+\frac{x_1^2+y_1^2}{2R_F^2})})|^2 \quad _{(f_x=x_0/2\pi R_F^2,\, f_y=y_0/2\pi R_F^2)}. \tag{4.6}$$

Here, (x_1, y_1) are the screen's coordinates. Fourier transform is taken on exponential of $\phi(x_1, y_1)$ (the generated phase screen) plus a quadratic term $\frac{x_1^2+y_1^2}{2R_F^2}$. The integrand of the Fourier transform is:

$$G(x_1, y_1) = e^{i(\phi(x_1,y_1)+\frac{x_1^2+y_1^2}{2R_F^2})}. \tag{4.7}$$

Since we sample $G(x_1, y_1)$ with N points separated by Δ_1, the Fourier integral is a Fourier series of a function with period $L = N\Delta_1$[4]. (x_1, y_1) coordinates take discrete values:

$$\begin{aligned} x_1 &= j_x\,\Delta_1, \\ y_1 &= j_y\,\Delta_1, \end{aligned} \tag{4.8}$$

where j_x and j_y are integers spanning interval $[0, N-1]$. The corresponding frequency variables and domain are:

$$\begin{aligned} f_x &= \frac{k_x}{N\Delta_1}, \\ f_y &= \frac{k_y}{N\Delta_1}, \end{aligned} \tag{4.9}$$

where k_x and k_y are integer values spaning interval $(-N/2, N/2]$. The relation between (x_0, y_0) and (k_x, k_y) is given by:

$$\begin{aligned} x_0 &= k_x\,\frac{2\pi R_F^2}{N\Delta_1}, \\ y_0 &= k_y\,\frac{2\pi R_F^2}{N\Delta_1}. \end{aligned} \tag{4.10}$$

The pixel size of the illumination pattern, Δ_0, corresponding to $k_x = 1$ in relation (4.10), is given by $\frac{2\pi R_F^2}{N\Delta_1}$ satisfying the relation:

$$N\Delta_1\Delta_0 = 2\pi R_F^2. \tag{4.11}$$

The optimum corresponds to the condition $\Delta_1 = \Delta_0$. In this case, the total size of the pattern corresponds to the geometrical shadow imprint of the screen. This equation implies that if we decide to increase the resolution on the screen we loose the resolution on the illumination pattern. This effect can be compensated by increasing the number of pixels, N, but it is restricted by computational capacity.

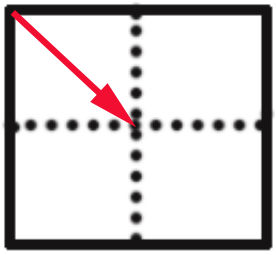

Figure 4.6: The coordinate is shifted from the corner of the pixel to the centre.

The Quadratic Term

The term $\frac{x_1^2+y_1^2}{2R_F^2}$ is the consequence of the propagation of spherical waves after crossing the screen in the Fresnel diffraction. The quadratic term completely depends on the spatial coordinates (x_1, y_1) . Technically, since we are dealing with discrete coordinates (j_x, j_y) the program assigns these coordinates to the top left corner of each pixel, and we need to convert them with respect to the geometrical centre of the pixels (see figure 4.6). This correction is needed as we will compare the illumination patterns of a screen with different pixel sizes through image subtraction. We use therefore the following coordinate transform:

$$j_x \to j_x + \frac{\Delta_1}{2} \quad , \quad j_y \to j_y + \frac{\Delta_1}{2}.$$

Image Centre

FFT puts the components with positive (f_x, f_y) at top left part of the result matrix. Therefore, the origin of (x_0, y_0) is at the corner instead of the centre of the image (see equation (4.6)). Suppose $g_{k_x k_y}$ is the Fourier series of discrete $G(x_1, y_1)$:

$$g_{k_x k_y} = \sum_{j_x=0}^{N-1} \sum_{j_y=0}^{N-1} G_{j_x j_y} \, e^{2\pi i \, (j_x k_x + j_y k_y)/N}, \tag{4.12}$$

where N (number of pixels at each axes) is the period of the series. To centre the origin on the observer plane, we shift the frequencies by: $k_x \to k_x + N/2$ and $k_y \to k_y + N/2$. The centred $g^c_{k_x k_y}$ is given as:

$$g^c_{k_x k_y} = \sum_{j_x=0}^{N-1} \sum_{j_y=0}^{N-1} (-1)^{(j_x+j_y)} G_{j_x j_y} \, e^{2\pi i \, (j_x k_x + j_y k_y)/N} \tag{4.13}$$

[4]The integral limits are no more infinite.

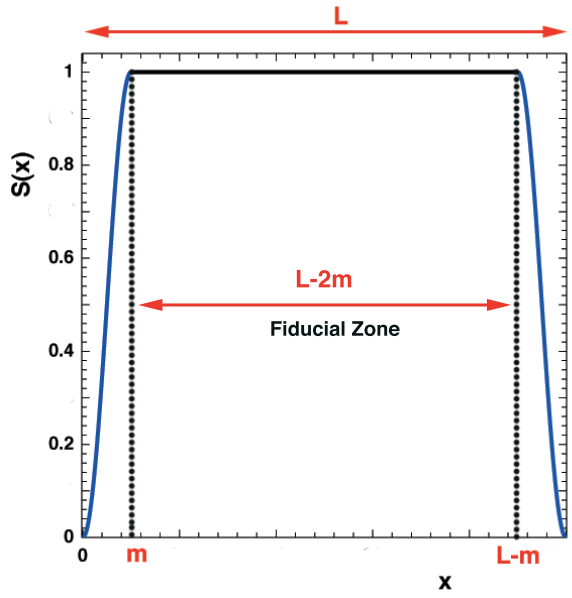

Figure 4.7: Smoothing function $S(x)$. L is the screen size. m is the length of the margin from the screen borders.

This frequency shift does not affect the intensity computation since it is just a half period shift in Fourier space. It just changes the frequency order of $g_{k_x k_y}$. We therefore multiply $G_{j_x j_y}$ by $(-1)^{(j_x+j_y)}$ factor before applying FFT.

Smoothing

Computing the integral (4.6) numerically limits the integration domain of (x_1, y_1) from $-\frac{N\Delta_1}{2}$ to $+\frac{N\Delta_1}{2}$ rather than infinite limits. This is physically equivalent to compute the Fresnel integral within a diaphragm with the size of the screen. In this case, we face an extra effect: The light diffraction from the edges of the diaphragm. This effect causes rapid intensity variations at the borders of the observer's plane. To attenuate this effect and remove the rapid oscillations, we used the smoothing function $S(x)$:

$$S(x) = \begin{cases} \frac{1}{2}(\sin(\frac{3\pi}{2} - \frac{\pi x}{m}) + 1) & 0 \leq x \leq m, \\ 1 & m < x < L - m, \\ \frac{1}{2}(\sin(\frac{3\pi}{2} - \pi(1 + \frac{x-L+m}{m})) + 1) & L - m \leq x \leq L, \\ 0 & \text{otherwise}, \end{cases}$$

where m is the length of the margin from the borders of the screen with size L. This function is shown in figure 4.7. We multiplied the function $G(x_1, y_1)$ with $S(x_1) \times S(y_1)$.

To illustrate the smoothing effect, we compute the diffraction integral for an aperture with

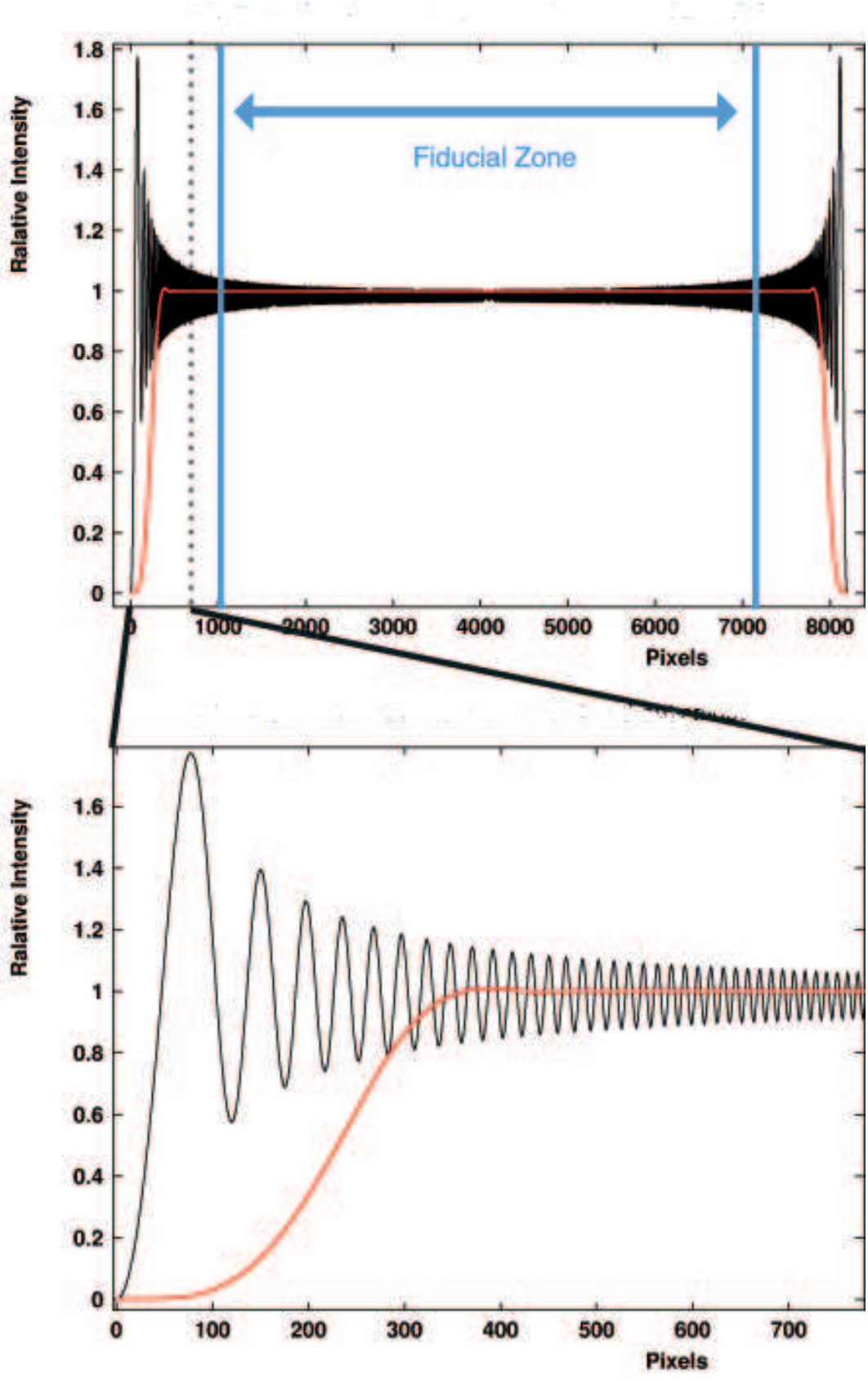

Figure 4.8: A horizontal section of the illumination pattern in the absence of the cloud (uniform phase screen). The red and the black curves are the results with and without smoothing respectively. The lower panel shows a zoom of the upper one.

size L and a constant phase function $\phi(x_1, y_1) = 0$. The black curve in figure 4.8 shows a section of the diffraction pattern computed without smoothing. If we were integrating over an infinite (x_1, y_1) domain (no aperture), we would expect a uniform intensity on the observer plane ($h(x_0, y_0) = 1$). By smoothing, this uniformity is achieved in a given region on the observer plane called Fiducial zone (Red curve in figure 4.8). We have chosen $m = 10R_F$ and added another $10R_F$ to the margins on the observer plane to avoid any perturbing effects on the estimated intensity. The final Fiducial zone is then a square with distance of

$$d = 2m = 20R_F \tag{4.14}$$

from the borders of the observer plane (see figure 4.9).

4.2.1 Point-Like Source

Figure 4.9 shows the pattern produced by a turbulent medium with R_{diff} = 100 km located at 160 pc far from the earth at wavelength λ = 2.162 μm. The corresponding Fresnel radius is R_F = 1300 km which is larger than the diffusion radius and hence we are in strong scintillation regime. The hot speckles (of typical size R_{diff} = 100 km) can be distinguished from the larger dark/luminous structures which have a typical size $R_{ref} = \frac{2\pi R_F^2}{R_{diff}} \simeq$ 100,000 km.

4.2.2 Extended Source

As discussed in section 3.5.1, the extension of the source has a crucial impact on the illumination pattern. From relation (3.55), the illumination pattern of an extended source of luminosity L_s is the pattern of a point-like source convoluted by the projected limb profile of the source $P_r(x_0, y_0)$:

$$I_{ext} = \frac{L_s}{z_0^2} P_r * h. \tag{4.15}$$

We have approximated the limb profile as a uniform disk with sharp edges:

$$P_r(X_0, Y_0) = \begin{cases} 1/\pi R_s^2 & \sqrt{X_0^2 + Y_0^2} \leq R_s \\ 0 & \text{otherwise} \end{cases}$$

where $R_s = \frac{z_0}{z_1} r_s$ is the projected source radius on the observer plane. Inserting this profile in equation (3.55) gives:

$$I_{ext}(x_0, y_0) = \int_{y_0 - R_{proj}}^{y_0 + R_{proj}} \int_{x_0 - \sqrt{R_{proj}^2 - (y_0 - Y_0)^2}}^{x_0 + \sqrt{R_{proj}^2 - (y_0 - Y_0)^2}} I(x_0 - X_0, y_0 - Y_0)\, dX_0\, dY_0 \tag{4.16}$$

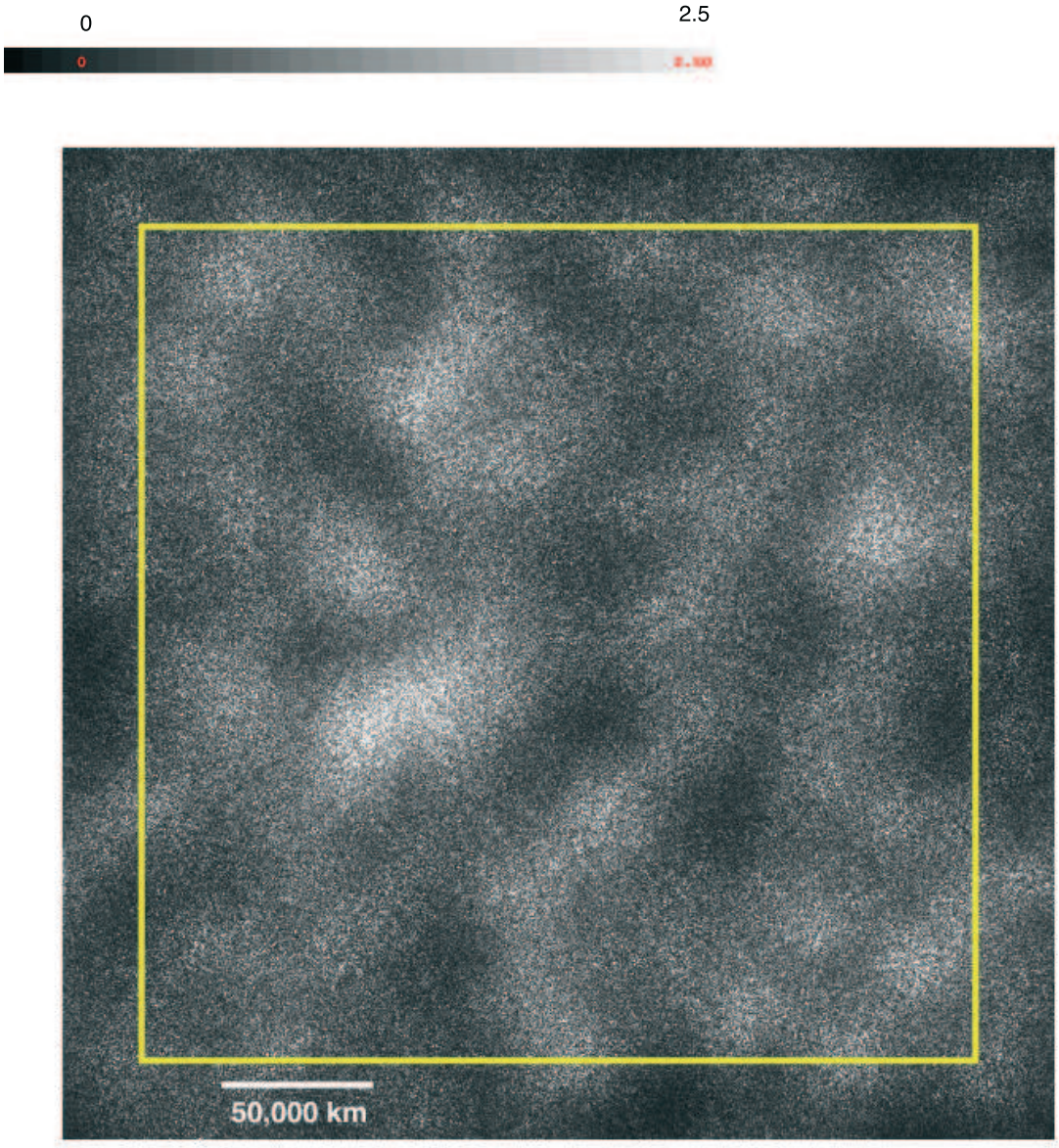

Figure 4.9: Typical illumination pattern of a point-like source: R_{diff} =100 km, R_F= 1300 km, R_{ref} = 106500 km. The typical length scale of hot speckles is R_{diff} and the scale of the larger structures is R_{ref}. The Yellow square shows the fiducial zone. Grey scale shows the relative intensity fluctuations.

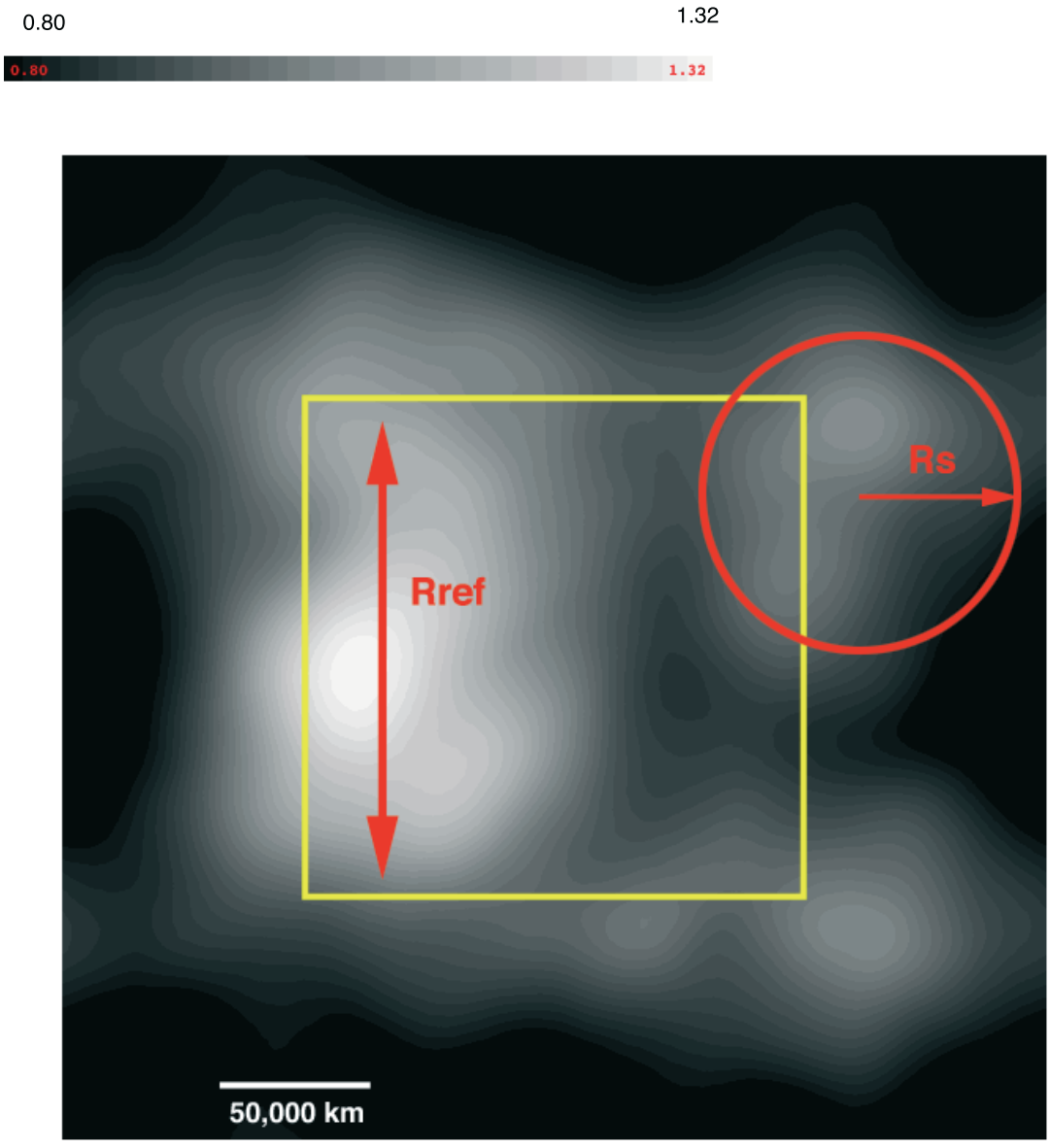

Figure 4.10: Typical illumination pattern of an extended source with $r_s = 0.5\ R_\odot$ ($R_s \simeq$ 54,000 km). The hot speckles are washed out and only the larger scales survive. The yellow square shows the new Fiducial zone. Grey scale shows the relative intensity fluctuations.

The convolution integral (4.15) is computed in Fourier space instead of configuration space:

$$FT(P_r * h) = FT(P_r) \, . \, FT(h) \tag{4.17}$$

Figure 4.10 shows the convolution of the pattern shown in figure 4.9 with a projected profile of a star with r_s = 0.5$R_\odot$ located at 8 kpc (R_s = 54,600 km). The geometrical configuration is the same as figure 4.9. High frequency fluctuations of the speckles disappear and the pattern looses contrast. The variations at scales larger than R_s remain since $R_{ref} > R_s$.

As the convolution involves a disk of radius R_s, we can perform the calculation it only at a distance larger than R_s from the borders. We therefore define a new Fiducial zone by including a margin of 20R_F + R_s from the initial borders. Any statistical analysis should be made within this zone to be safe from any borer effect perturbation.

4.2.3 Effect of Sampling

In general, the screen should be sufficiently sampled to avoid the aliasing effects. Aliasing happens when $G(x_1, y_1)$ contains frequencies higher than the Nyquist frequency f_{Nyq} = $1/(2\Delta_1)$. From relation (4.7), G contains two length scales, the diffusion and Fresnel radii.

R_{diff} is the characteristic length of the phase screen $\phi(x_1, y_1)$. It is at least necessary that $R_{diff} > 2\Delta_1$ to sample phase variations within the diffusion radius. R_F appears in the quadratic term $exp(i\,(\frac{x_1^2+y_1^2}{2R_F^2}))$. This term oscillates faster as x_1 and y_1 increase. Aliasing occurs if the distance between two consecutive peaks is smaller than $2\Delta_1$. In one dimension we expect aliasing if:

$$\frac{(x_1 + 2\Delta_1)^2 - x_1^2}{2R_F^2} > 2\pi,$$
$$x_1 > \Delta_1(\pi(\frac{R_F}{\Delta_1})^2 - 1). \tag{4.18}$$

In terms of number of pixels $n_1 = x_1/\Delta_1$:

$$n_1 > \pi(\frac{R_F}{\Delta_1})^2 - 1. \tag{4.19}$$

The condition $R_F = 2\Delta_1$ is obviously insufficient since after $\sim$ 11 pixel ($\sqrt{x_1^2 + y_1^2} > 11$ pixel) the quadratic term is under-sampled. In practice, at infrared wavelengths and for a screen located at $\sim$ 100 pc, the Fresnel radius is $\sim$ 1000 km. By choosing $\Delta_1 \sim 15$ km, the aliasing starts at $n_1 \sim$ 13,900 pixels from the centre of the image and hence, for

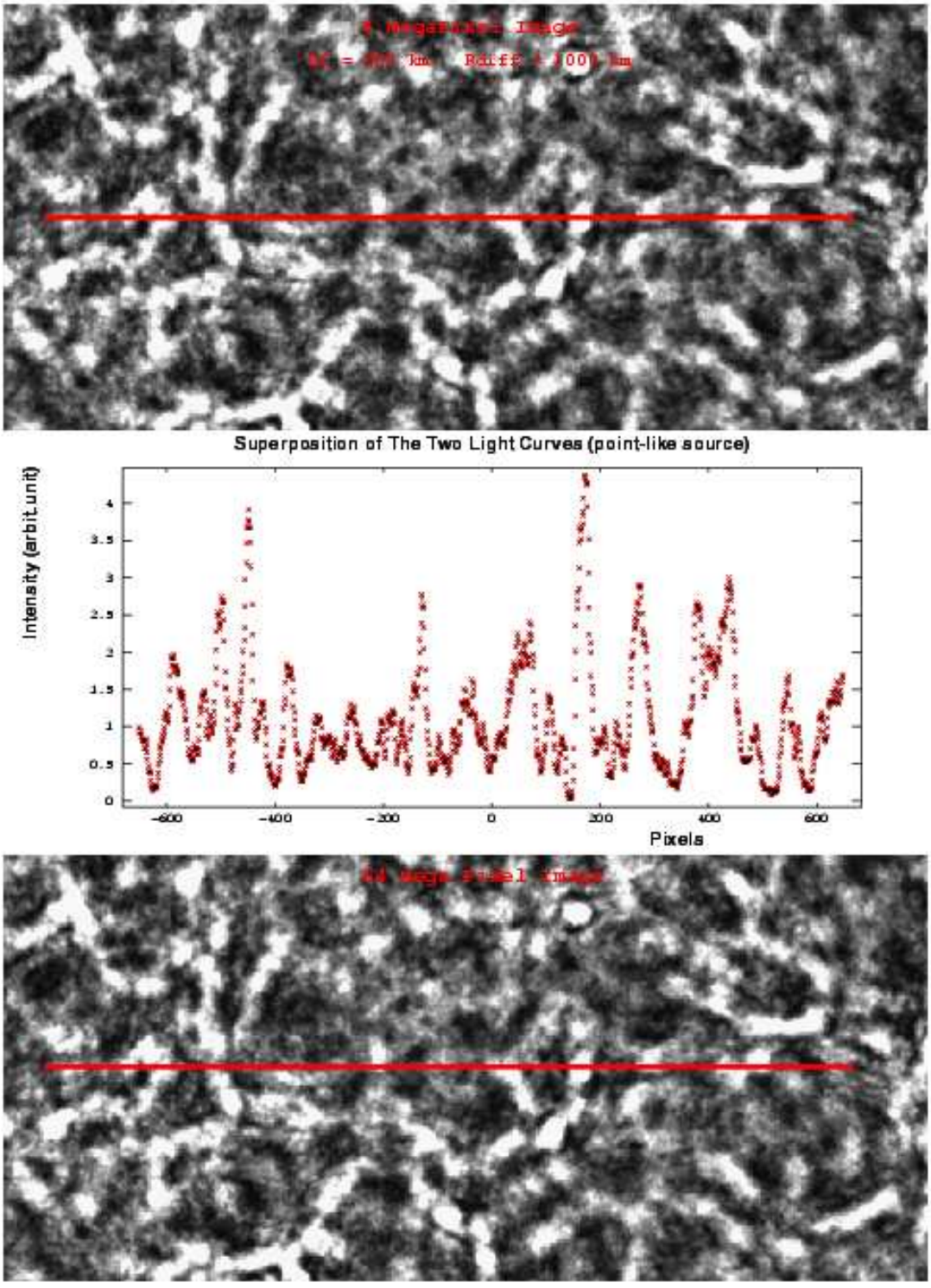

Figure 4.11: Diffraction patterns of a point-like source with two different screen samplings: Δ_1 = 48 km (top) and Δ_1 = 12 km (bottom). Middle: Superposition of two horizontal sections (red lines) of the patterns shown by red points and black crosses.

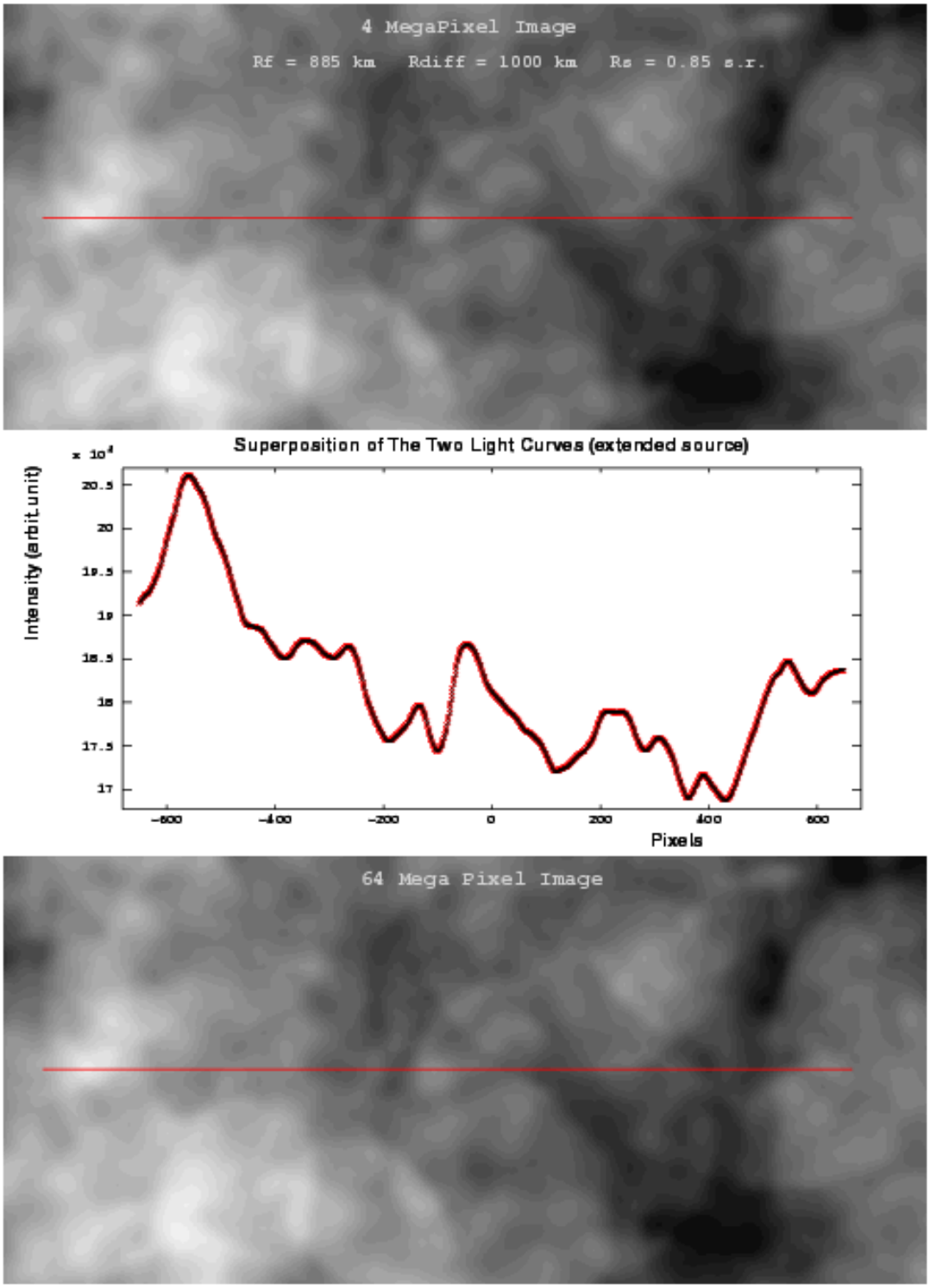

Figure 4.12: Convolution of figure (4.11) with an extended source profile. Superposition of two sections of the corresponding regions are shown by red and black curves on the middle panel.

a simulation with N < 20,000, aliasing effect is usually avoided.

To check the numerical stability of the illumination pattern, we investigate the effect of sampling of the screen on the computed illumination pattern. We consider a screen with a given size and diffusion radius and also a given geometrical configuration. The screen is sampled with two different pixel sizes Δ_1 and we compare the corresponding illumination patterns.

To compare the two patterns, we need to do a pixel by pixel comparison. On the one hand, we change the pixel size of the screen to obtain a different sampling and on the other hand, the screen size $L_{screen} = N\Delta_1$ should be left unchanged. We proceed the resampling and comparision process through the following steps:

- Change the screen sampling by h(> 1) factor: $\Delta_1 \rightarrow h\Delta_1$
- $N(= L_{screen}/\Delta_1) \rightarrow N/h$
- From equation (4.11): Δ_0 is unchanged
- Image size $L_{pattern}(= N\Delta_0) \rightarrow L_{pattern}/h$
- Extract the central region of the initial pattern and compare it with that of the re-sampled one.

For instance, we produce a screen with $R_{diff} = 1000$ km , $R_F = 886$ km and $R_s = 0.85R_\odot$ in a $N \times N$ matrix with N = 8192 and Δ_1 = 12 km. The corresponding illumination patterns of point-like and extended sources are shown on top of figures 4.11 and 4.12. We re-sample the generated screen by attributing the average phase of each 4×4 neighbour pixels in a new larger pixel. Thus, a new sampled phase screen is constructed in a 2048 $\times$ 2048 matrix with Δ_1 = 48 km[5]. The corresponding illumination patterns are shown at the bottom of the figures 4.11 and 4.12. We superimpose the same horizontal section of the illumination patterns (the middle panel of the figures). They vary quite similarly.

To compare images in similar zones we subtract them from each other. Figure 4.13 shows the subtraction of two illumination patterns of a point-like source with different screen samplings. A horizontal section of the subtracted pattern is shown at the middle and the distribution of the pixel differences is shown at the bottom. This distribution has a dispersion smaller than 1 percent. Figure 4.14 shows the same plots for an extended source. The dispersion is smaller than 10^{-4} percent which is quite small. The subtraction distribution is not Gaussian. We did not investigate the origin of this non-Gaussianity and felt satisfied to obtain a small difference between patterns with different samplings.

[5]We also checked for 4096 $\times$ 4096 matrix with Δ_1 = 24 km.

The average values of both distributions are negative. Although the total flux power is the same for both patterns (they are generated from the same power spectrum), on average the power per pixel for pattern with N = 8192 is smaller than the pattern with N = 2048. We have subtracted the central region of the larger pattern from the smaller one and hence, the difference is negative on average.

4.2.4 Polychromatic Source

So far, the illumination pattern is computed for a monochromatic source (fixed λ). But observations are done through filters with non-zero passbands. To take into account the contributions of different wavelengths to the pattern, we superimpose the illumination patterns obtained with the same diffusive structure (the same column density fluctuations) at different wavelengths.

Scaling Laws

Since the Fresnel radius $R_F = \sqrt{\frac{z_0\lambda}{2\pi}}$ depends on wavelength, according to equation (4.11) the pixel size Δ_0 of the pattern is proportional to λ. Therefore, for a given screen size, the longer the wavelength is, the larger the illumination pattern will be. Wavelength variation not only changes the Fresnel radius but also changes the diffusion radius. From definition of Fresnel radius:

$$R_F(\lambda) \;=\; \sqrt{\frac{\lambda}{\lambda'}} R_F(\lambda'). \tag{4.20}$$

A given screen is described by a column density, $N_l(x_1, y_1)$, which produces a phase delay $\phi_\lambda(x_1, y_1)$ that depends on λ. Therefore it comes from equation (3.34):

$$R_{diff}(\lambda) \;=\; (\frac{\lambda}{\lambda'})^{6/5}\, R_{diff}(\lambda'), \tag{4.21}$$

and for the refraction radius, $R_{ref} = \frac{2\pi R_F^2}{R_{diff}}$, we get:

$$R_{ref}(\lambda) \;=\; (\frac{\lambda}{\lambda'})^{-1/5} R_{ref}(\lambda'). \tag{4.22}$$

According to equation (3.8), the phase delays satisfy:

$$\phi_\lambda \;=\; (\frac{\lambda}{\lambda'})^{-1}\, \phi_{\lambda'}. \tag{4.23}$$

To produce illumination patterns with various λ, we firstly generate a phase screen for the shortest wavelength (λ'). Then, by multiplying all phase pixels by λ/λ', a new phase screen corresponding to wavelength λ is produced. The quadratic term of $G(x_1, y_1)$is also re-calculated by multiplying $R_F(\lambda')$ by $\sqrt{\lambda/\lambda'}$. Taking into account these modifications, integral (4.6) is computed for different λ values. The final illumination pattern is obtained by co-adding the different images.

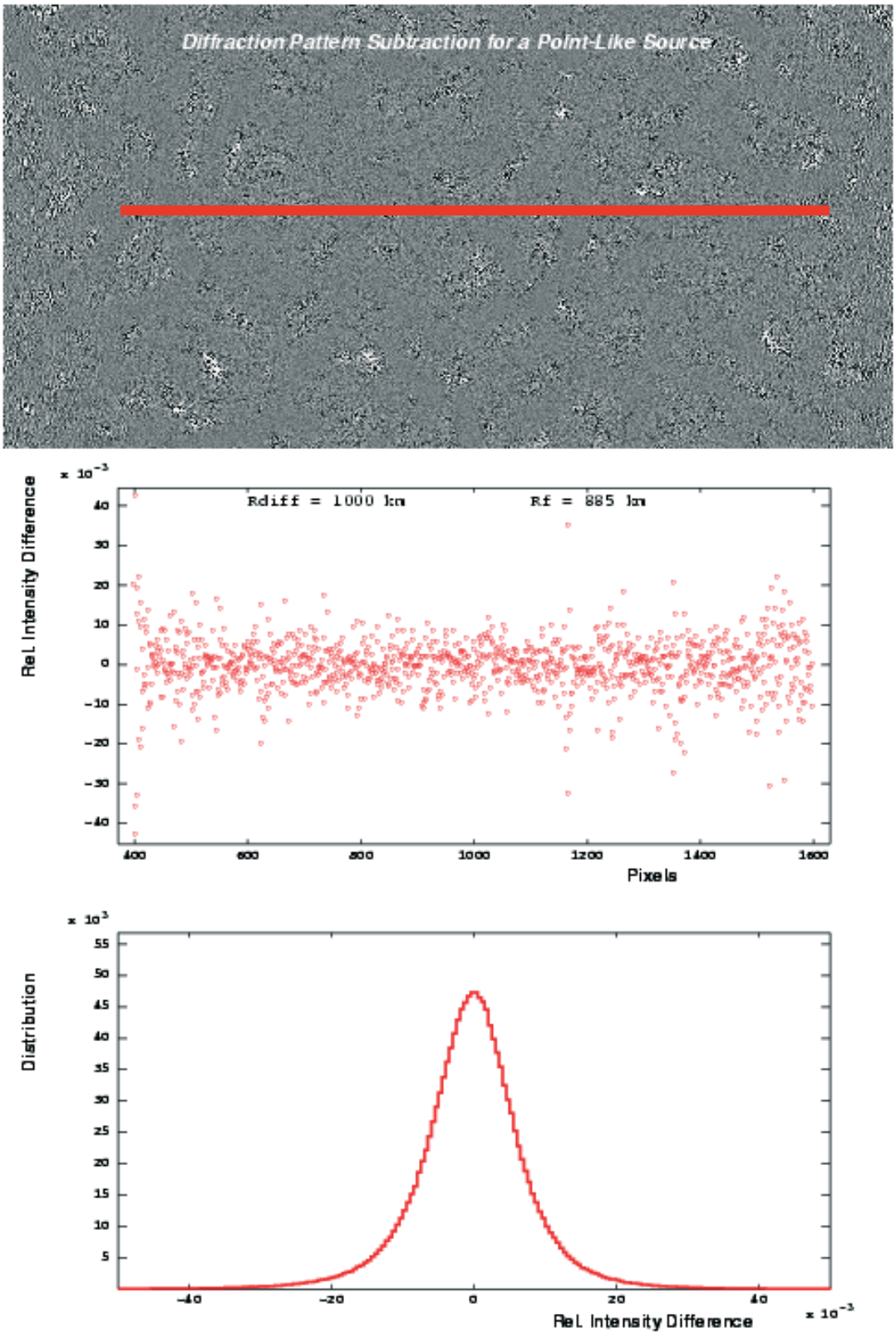

Figure 4.13: Top: subtraction of diffraction patterns for a point-like source with two different screen samplings. Middle: the light curve along the red horizontal section of the subtracted pattern. Bottom: pixel distribution of the relative intensity differences with average of order of 10^{-4}. Relative dispersion is less than 1%.

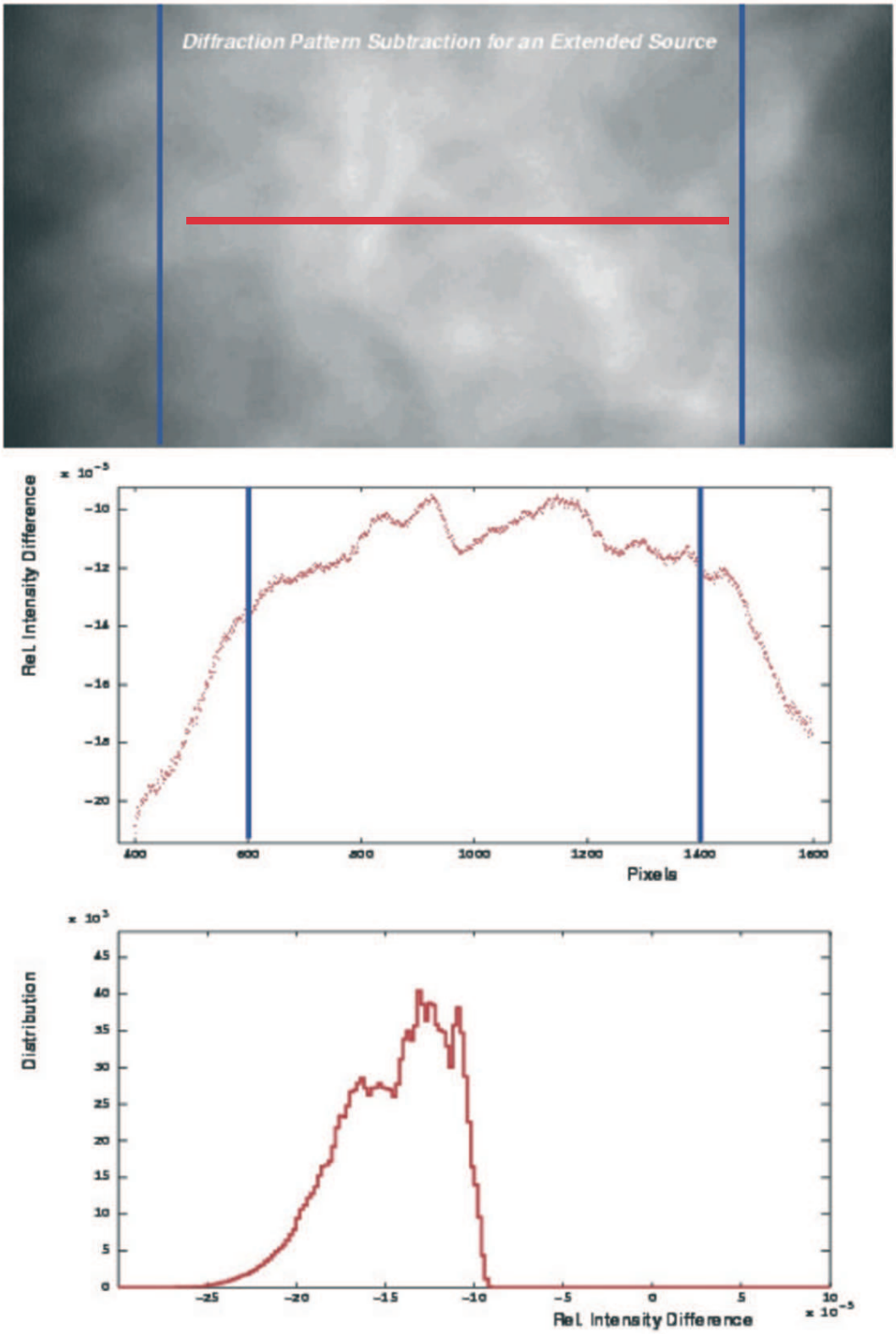

Figure 4.14: The same as figure 4.13 but for an extended source. Relative variations are of order of 10^{-4}. Blue lines shows the Fiducial zone.

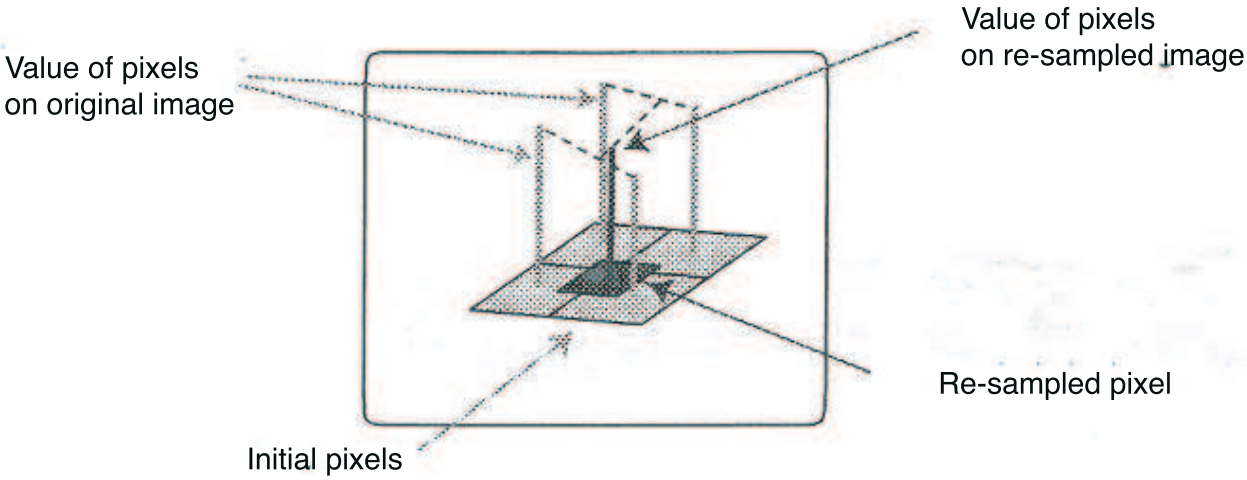

Figure 4.15: The value of the re-sampled pixel is given by bilinear interpolation of the first four initial pixels.

Co-addition

To co-add the patterns we re-sample all images (hereafter current images) to the pixel grid of the smallest image produced by the shortest wavelength.

Let the pixel size of the smallest image be $\Delta_0^{'}$ and the one for any current image be Δ_0. We define the homothetic coefficient as: $h_c = \frac{\Delta_0^{'}}{\Delta_0}$. From equation (4.11), considering the same screen pixel size and number (i.e. the same *physical* screen), h has to satisfy:

$$h_c = \frac{\Delta_0^{'}}{\Delta_0} = \frac{R_F^{'2}}{R_F^2} = \frac{\lambda'}{\lambda}, \tag{4.24}$$

and the image has therefore a different sampling (and consequently a different extension, since N is not changed). To co-add the images obtained at different wavelengths, we resample them according to the scheme illustrated in figure 4.15. The content of a re-sampled pixel is calculated by bi-linear interpolation of its four neighbour pixels.

Simulation of a Wide Passband Image

The standard UBVRI filter system has passbands that all satisfy $\Delta\lambda/\lambda \leq 0.1$. The relative variations of the characteristic lengths within the filter passband are: $\Delta R_F/R_F \leq 0.05$, $\Delta R_{diff}/R_{diff} \leq 0.12$ and $\Delta R_{ref}/R_{ref} \leq 0.02$.

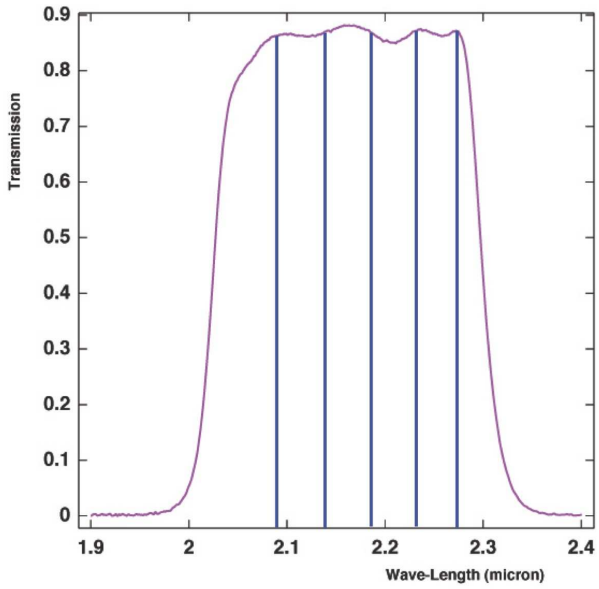

Figure 4.16: Passband filter of SOFI camera in K_s band. We approximate this passband with the superimposition of five wavelengths Dirac distributions within the band and co-add the corresponding illumination patterns with equal weights.

In the simulation, we have used the passband of SOFI camera in K_s band. Figure 4.16 shows the shape of this passband. We approximate it as a rectangular function over transmitted wavelengths with central value of 2.162 μm and width of 0.275 μm. Five different wavelengths were selected from the interval [2.09 , 2.28] μm to compute their corresponding illumination patterns.

Figure 4.17 shows a comparison between a monochromatic and a polychromatic illumination patterns of a point-like source. The pattern looses its clarity and contrast when the light time coherence is reduced. The speckles are diluted and less contrasted. This can be understood by the fact that the size of the superimposed speckles varies by $\sim 12\%$. On contrary, the structures of size of R_{ref} are less sensitive to the variations of λ ($\sim 2\%$). Hence, there is no significant difference between monochromatic and polychromatic patterns for an *extended* source. The time coherence limitations affect the speckles but not the large dark/luminous scales and for an extended source, the speckles disappear and only the larger scales remain visible.

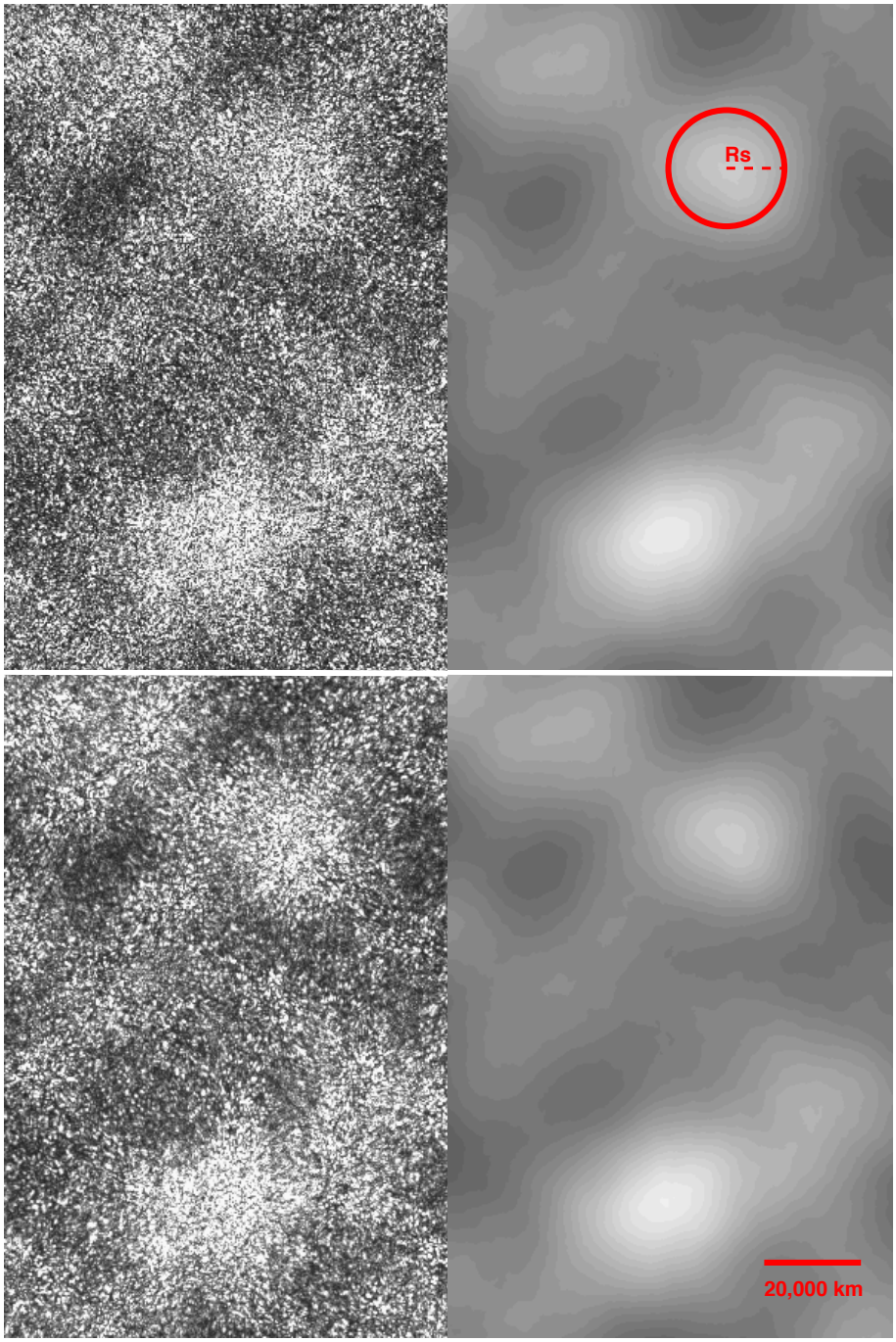

Figure 4.17: Top left: Illumination pattern produced by a point-like monochromatic source. The contrast is 100%. Top right: The same from an extended source with 46% contrast. Bottom left: The illumination pattern of a point-like polychromatic source. The contrast is 75%. Bottom right: The same for an extended source with 46% contrast. The passband width does not induce a major deviation from illumination pattern of a monochromatic extended source.

4.3 Illumination Pattern and Observables

The main observable parameter of scintillation which we used in our data analysis is the *modulation index*. It is defined as the flux dispersion, σ_I, divided by the mean flux, $\bar{I}$: $m = \sigma_I/\bar{I}$. We explain how it is possible to relate this observed modulation index to the geometrical parameters (R_{diff}, λ, R_s etc.) through simulation. The time scale of the variations -derived through the spectrum of the illumination pattern- is the other observable for the simulation process. This spectrum is related to the properties of the screen (R_{diff}). Furthermore, we discuss the extraction of the light curves from the simulated illumination pattern and the way they represent the statistics of the original 2D pattern. At last, expectations from scintillation with turbulence laws other than Kolmogorv are discussed.

4.3.1 Modulation Index

For a point-like source in the strong scintillation regime the modulation index $m_{point} \approx 1$ [Narayan (1992)]. For an extended source in the same regime, we have always $m_{extend} < 1$. In the latter case, R_s/R_{ref} seems to intuitively be the natural parameter to drive the modulation index. When the projected star radius R_s is much smaller than R_{ref}, variations at scale > R_{ref} are not affected by the convolution with the source profile. As R_s increases relatively to R_{ref}, the long scale variations will be smoothed and modulation decreases. $x = R_s/R_{ref}$ parameter can be expressed as a function of the diffusion radius of the cloud and other geometrical parameters as follows:

$$x = \frac{R_S}{R_{ref}(\lambda)} = \frac{r_s R_{diff}(\lambda)}{\lambda z_1} \sim 2.25 \left[\frac{\lambda}{1\mu m}\right]^{-1} \left[\frac{r_s/z_1}{R_\odot/10\,kpc}\right] \left[\frac{R_{diff}(\lambda)}{1000\,km}\right]. \qquad (4.25)$$

To quantify the decrease of m_{extend} with the ratio $x = R_s/R_{ref}$, we performed series of simulations with different phase screens and stellar types. We generated series of screens with R_{diff} = 50 km to 500 km by steps of 50 km. For each screen, we considered different sources -at the same geometrical distances- with radii from $0.25R_\odot$ to $1.5R_\odot$ by steps of $0.25R_\odot$ and computed the illumination patterns. The modulation indices were calculated within the fiducial zone of each 2D illumination pattern. Top panel of figure 4.18 shows the estimated m_{extend} for each generated pattern. The modulation is relatively large-scattered for each x. This is due to the fact that the Fiducial zone is not large enough and contains a limited number of regions with size of R_{ref} or R_s. In some cases there are very few two dark/luminous regions (see figure 4.10). The number of large scales fluctuations within the Fiducial domain is $N_F \sim \frac{d^2}{\pi \max(R_{ref},R_s)^2}$ where d is the size of the Fiducial zone.

After discarding the cases with N_F < 4, we established the red and green curves at lower panel of figure 4.18 which represent the limits of the modulation indices. By measuring

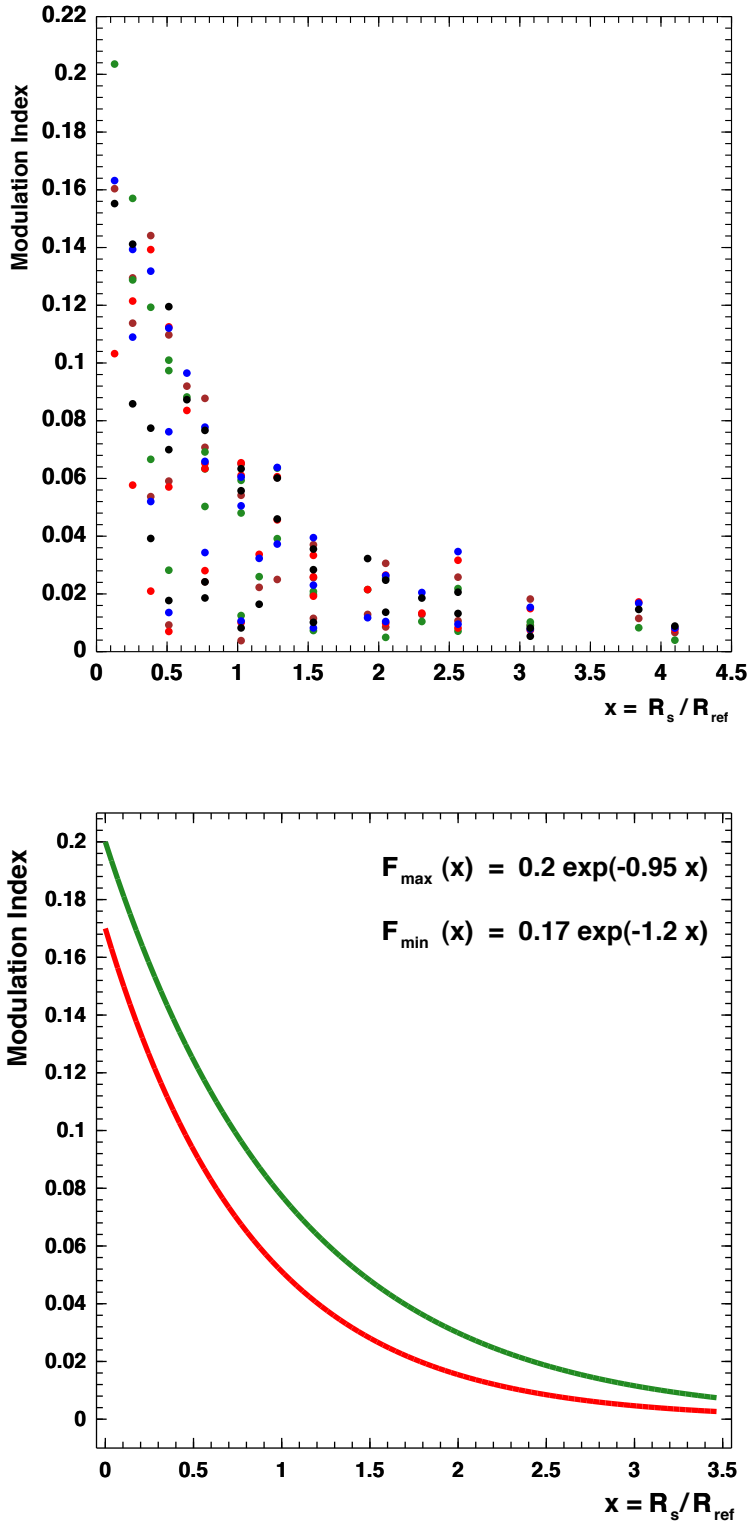

Figure 4.18: The expected intensity modulation index $m = \sigma_I/\bar{I}$ for simulated scintillating stellar illumination patterns as a function of R_S/R_{ref}. Top: Five realisations for each R_{diff} are shown with different colours. Bottom: the modulation indices are essentially contained between the curves represented by functions $F_{min}(x)$ and $F_{max}(x)$. These functions allow one to constrain x when we know constraints on m.

m value from an observed light curve and with an estimate of star type and distance, we can constrain R_{diff} from equation (4.25) by using these curves.

4.3.2 Light Curves

What we observe with a single telescope is not the 2D illumination pattern but a light curve. Because of the relative motions, the telescope scans a 1D section of the pattern. We simulated light curves by extracting straight lines from the 2D pattern. If a light curve is sufficiently long (or equivalently if the observation time is long enough) its series of light measurements represents an unbiased sub-sample of the 2D pattern.

For instance, the left panels of figure 4.19 represent the illumination pattern of a point-like source and three associated light curves. Here, $R_{ref} \approx$ 28000 km and m_{point} = 1.18. The light curves are extracted from three horizontal parallel lines with length of $\sim 3.5 \times 10^5$ km. The corresponding time scale depends on the relative transverse velocity. They are selected far from each other in order not to be affected by the fluctuations of the same regions. Modulation indices along the light curves differ from the 2D's by less than 5%. As long as modulation is characterised by R_{ref} and R_{diff} it implies that a light curve that spans $\sim$ tens of refraction radii gives a good approximation of the scintillation modulation index for a point-like source.

The right panels in the same figure show the 2D pattern for an extended source with $R_s \approx$ 41000 km and hence, $R_s > R_{ref}$. Flux fluctuations are smoothed and characterised by the length scale R_s giving m_{extend} = 0.04. The light curves are extracted in the same way as the point-like source within the corresponding restricted fiducial zone (see figure 4.10). They span $\sim 2.5 \times 10^5$ km and therefore statistically include less than 10 R_s-scale variations. Because of this statistically short length, the light curve to light curve estimates of m_{extend} fluctuate typically $\sim 1/\sqrt{10} \approx 30\%$. The fluctuations on m_{extend} can be lowered with longer light curves.

For a known cloud distance, to get precision of 5% on m_{extend} with $R_s < R_{ref}$, the light curve should be as long as $\sim$ 400 R_{ref}. If we observe through a turbulent core with $R_{diff} \sim$ 200 km in B68 nebula located at 80 pc at λ = 2.16 μm, and assuming $V_T \sim 20$ km/s, an observing period of $\sim$ 28 hours is needed to measure the modulation index with this precision. When searching for unseen turbulent media located at unknown distances from us, diffusion and refraction radii are unknown and we can only obtain a probability distribution of the observation time for a requested precision on modulation index.

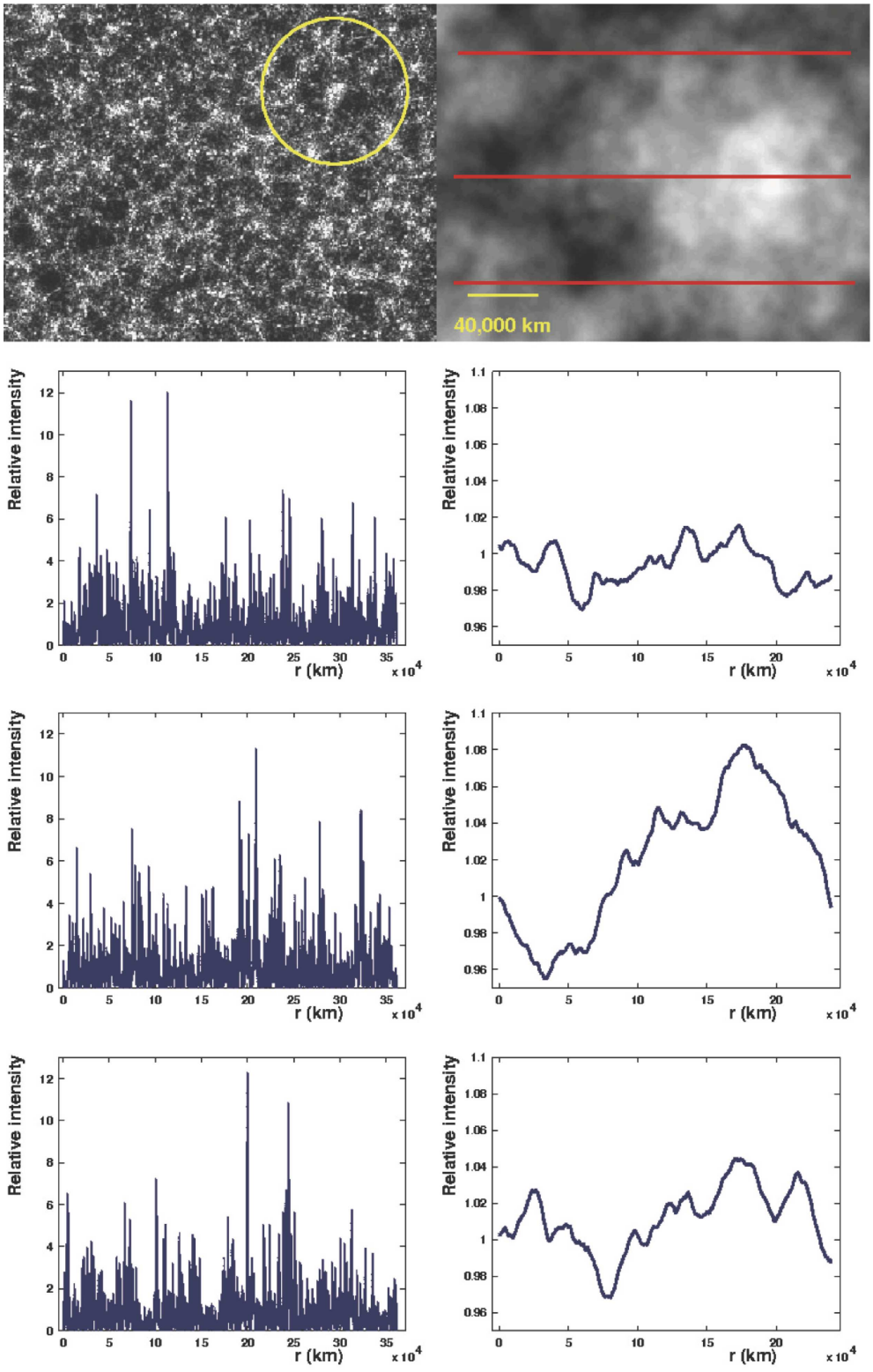

Figure 4.19: Light curves extracted along the red lines for both illumination patterns. Left column: 2D pattern of a point-like source in K_s band with R_{diff} = 300 km and $R_{ref} \approx$ 28000 km. Modulation indices of the three light curves fluctuate by less than 5% from the 2D pattern modulation index. Right column: the same illumination pattern for the extended source with r_s = 0.5 $R_\odot$ ($R_s \approx$ 41000 km). The modulation indices fluctuate by more than 30% around the 2D pattern index implying the necessity of longer light curves for a better statistical representativity. The distance scale is common for both patterns. The circle shows the projected star radius. The luminosity scales (grey levels) are not the same for the two patterns.

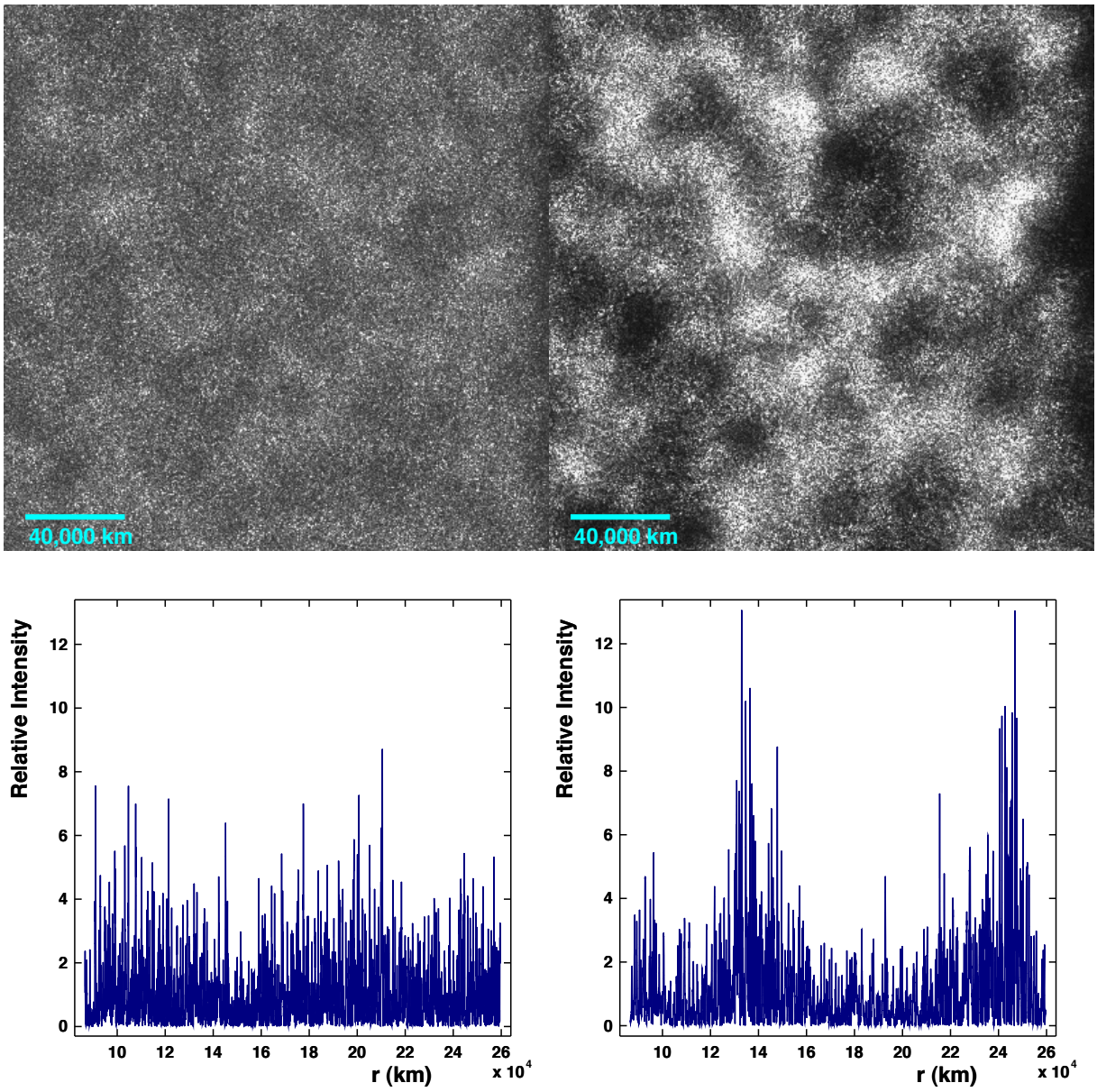

Figure 4.20: Scintillation of a point-like source with different non-Kolmogorov turbulences. Left: Illumination pattern and typical light curve produced by a medium with R_{diff} = 100 km ($R_{ref} \approx 8 \times 10^4$ km) and β = 3.1. Most fluctuations arise at small scales $\sim R_{diff}$. Right: β = 3.9. Fluctuations contain more power at larger scale $\sim R_{ref}$. The patterns are represented with the same grey scale.

4.3.3 Non-Kolmogorov Scintillation

We have investigated a possible deviation from the Kolmogorov turbulence law[6]. Using relation (3.40), we chose two different phase spectra with β = 3.1 and β = 3.9. To study the scintillations, firstly we generated two phase screens according to the corresponding spectra and computed the illumination pattern of a point-like source for each of them. Figure 4.20 illustrates the illumination pattern produced by β = 3.1 (left) and β = 3.9 (right). For both images R_{diff} = 100 km, R_F = 1151 km and $R_{ref} \approx 8 \times 10^4$ km. As can be seen from visual aspect, on the one hand turbulence with larger exponent produces stronger contrast at large scales compared to the other one (β = 3.1). On the other hand, the pattern with β = 3.1 shows larger fluctuations at small scales than for β = 3.9. This can be seen quantitatively from the light curves shown on the same figure. For larger exponent, large variations at scale $\sim R_{ref}$ produce modulation $m_{point}(3.9)$ = 1.16. While the light curve for smaller exponent behaves smoother at large scales, the large fluctuations at scale $\sim R_{diff}$ produces $m_{point}(3.1)$ = 1 which is already smaller than the modulation index of the other light curve.

We further study the differences of illumination patterns by convoluting the point-like source patterns with the profile of an extended source with $r_s = 0.25 R_\odot$ ($R_s \sim 0.36$ R_{ref}). The patterns with the light curves are represented in figure 4.21. As expected the speckles have disappeared from the images. The pattern with β = 3.1 has a modulation $m_{extend}(3.1)$ = 0.04. Since the modulation is mainly induced by the large scale fluctuations, the pattern with β = 3.9 has a larger modulation index $m_{extend}(3.9)$ = 0.22.

To understand the origin of the difference, we compare the two phase spectra at top of figure 4.22. At smaller length scales the spectrum with gentler slope contains more power than the steeper one. It causes larger intensity fluctuations in small scales for the scintillation pattern of the smaller exponent. Inversely, the steeper spectrum has more power for fluctuations at large scales and less for smaller scales. Moreover, by computing the total power distributed from R_{ref} to R_{diff} (by integrating equation (3.40)) we find for β = 3.9 about an order of magnitude power excess compared to the other one (β = 3.1). Therefore, the larger the β exponent is the stronger flux fluctuations are produced. As a conclusion, for turbulences with steeper slopes in spectrum, the detection of the scintillation should be easier due to larger modulation index expectation. This fact is shown at bottom of the figure 4.22. We plot the modulation index against the x factor for three different β including the Kolmogorov case (blue points). By increasing β, we gain modulation specially for smaller x values.

[6]For the observed super sonic turbulence (with β > 11/3) look at [Larson (1981)].

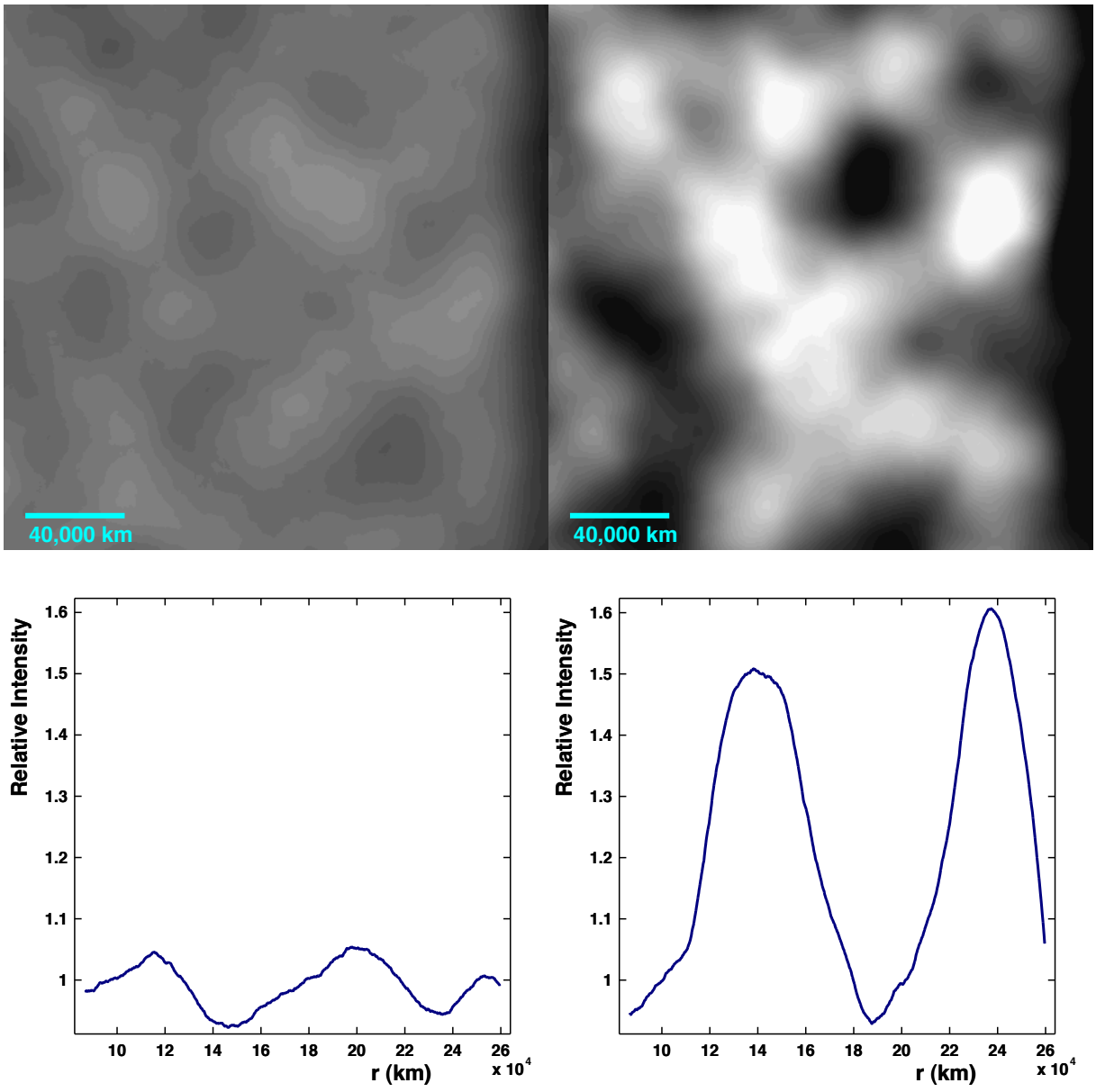

Figure 4.21: Scintillation of an extended source in non-Kolmogorov turbulences. The patterns are the ones of figure 4.20 convoluted by the projection of a star with radius $r_s = 0.25 R_\odot$ ($R_s \sim 0.36\ R_{ref}$). The modulation index is more reduced for the pattern produced by smaller turbulence index.

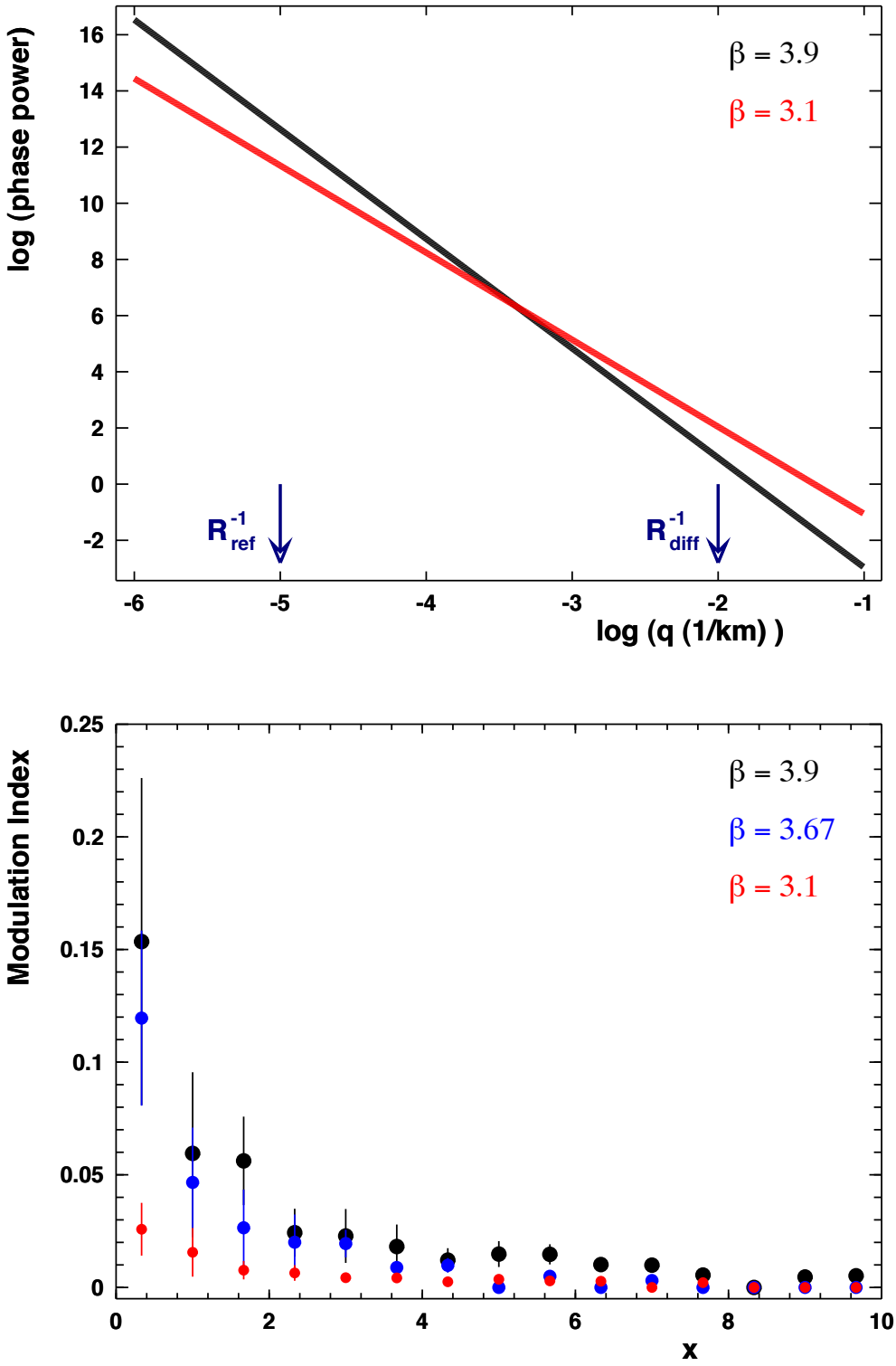

Figure 4.22: Top: Two different phase screen power laws. Bottom: Modulation index as a function of $x = R_{ref}/R_s$ for different turbulence power laws. As the power law gets steeper, a larger modulation is produced. Blue circles show the Kolmogorov turbulence.

4.4 Conclusion and Future Studies

Through this work, we have simulated the phase delay induced by a turbulent medium on the wave front. We faced computational limitations to sample the phase spectrum between sufficiently large and small outer and inner scales. We have established the connection between the modulation index and the geometrical parameters of the source and the turbulent medium. Furthermore, we showed that if the spectral index of the turbulence is larger, it is more probable to detect scintillating light curves.

Determining the refraction radius R_{ref} is another way to estimate the diffusion radius of the cloud. Time scales like $T_{ref} = R_{ref}/V_T$ and $T_s = R_s/V_T$ (where V_T is the relative velocity between the cloud and the line of sight) are observables that we have not yet studied. Extraction of these observables needs time spectral analysis of the light curves. Although in weak regime of scintillation and in strong regime with $T_s > T_{ref}$, the modulation index is small but R_s remains a characteristic length scale which may leave some signature on the time spectra of the light curves.

Chapter 5

Feasibility Studies

As a preliminary investigation to detect the scintillation effect induced by the ISM, we observed during two nights in near infrared bands with SOFI camera of ESO-NTT in June 2006. Telescope time was attributed to the OSER[1] project by the ESO committee through the standard observing time application[2]. IR observation was preferred for two main reasons. Firstly, for a feasibility test for scintillation process, we chosed to observe fields which are already known to contain large amounts of gas. In this purpose dark (dusty) nebulae have been selected and observations in IR band allowed us to monitor the stars behind the gas. Secondly, as rapid scintillation with time scales of a few minutes are expected, their detection need a fast read-out detector. At the epoch of observations, IR detectors with 5 seconds of read-out time were the fastest among other types of detectors.

5.1 The Targets

Considering the probable small optical depth of the scintillation process, all our selected fields contain large numbers of background stars. From the four selected targets (figure 5.1), the SMC[3] direction probes the hypothesis of halo transparent clouds, while the others point toward known visible dark nebulae located in the Galactic disk. These dark nebulae were chosen by considering the following requirements:

- Maximising the gas column density to benefit from a large phase delay. Data from 2MASS were used to select the clouds that induce the larger reddening of the background stars, pointing toward the thickest clouds.

- We selected the nebulae which are strongly structured (from visual inspection), and favoured those ones with small spatial structures to increase the chances of having large column density fluctuations (with small diffusion radius R_{diff}).

[1] Optical Scintillation by Extraterrestrial Refractors.
[2] Request ref: 077.c-0613
[3] Small Magellanic Cloud

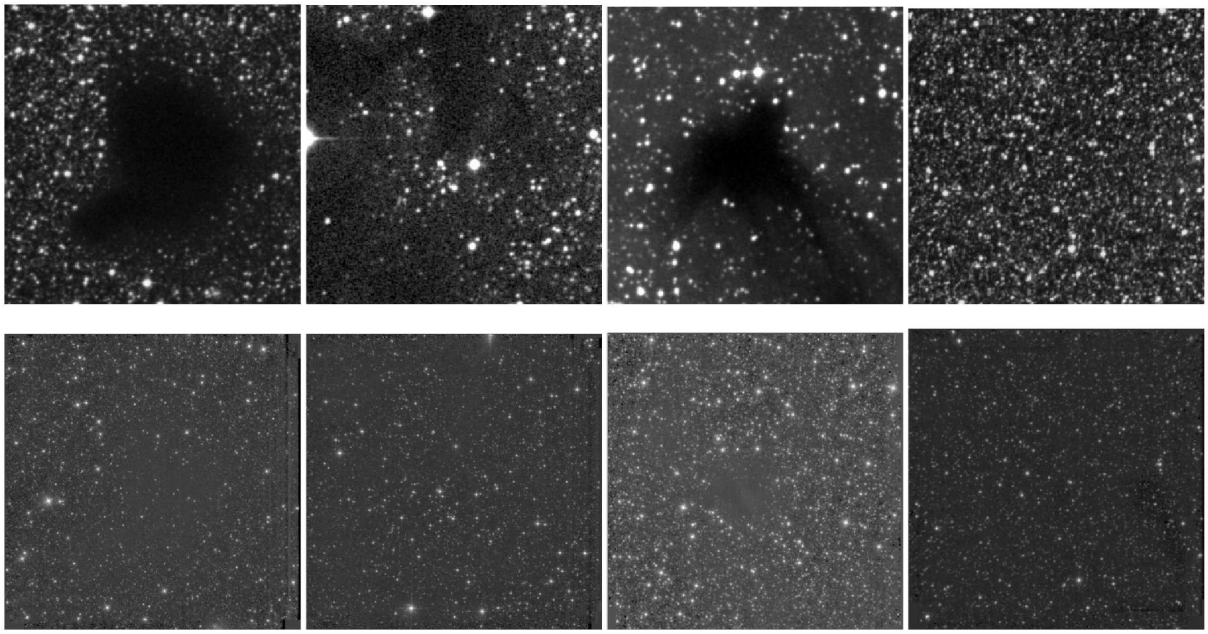

Figure 5.1: The 4 monitored fields, showing the structures of the nebulae and the background stellar densities. From left to right: B68, Circinus, bc131 and SMC. Up: images from the ESO-DSS2 in R. Down: our reference images (in K_S except for SMC that is in J).

- We chose fields with a significant fraction of stars which are not behind the nebulae to use them as control samples.

Our targets satisfy these requirements except Barnard 68 (hereafter B68) that does not match the second criterion, but instead, we benefit from large number of published studies on this nebula. A crowded field in the SMC is selected to increase the probability of scintillation detection induced by hidden halo gas (LMC was not observable at the observation epoch). The targets were observed in 4.92×4.92 Arcmin.^{2}-size fields in K_s (for the dark nebulae) and J (toward the SMC) bands.

Since through the dark nebulae, the light intensity is affected by dust extinction, we show that the flux fluctuation induced by absorption is negligible compared to the fluctuation induced by scintillation. Through the cores of the three selected nebulae B68, cb131 and circinus, we estimated gas column number density to be $N_l \sim 10^{22}$ cm^{-2}. Considering the phase delay induced by column density from equation (3.8) and substituting it in the phase structure function given by equations (3.27) and (3.26) we obtain the following relation between the column density fluctuation and the diffusion radius:

$$(\Delta N_l)^2 \;=\; \langle [N_l(x+x', y+y') - N_l(x', y')]^2 \rangle \;=\; (\frac{\lambda}{(2\pi)^2\alpha})^2\,(\frac{r}{R_{diff}})^{\beta-2}, \quad (5.1)$$

then, the mean column density variation within transversal separation $r = R_{diff}$ is:

$$\Delta N_l \;=\; 3.15 \times 10^{18}\,\mathrm{cm}^{-2}\,(\frac{\lambda}{1\mu\mathrm{m}})\,(\frac{\alpha}{\alpha_{H_2}})^{-1}, \tag{5.2}$$

which gives $\Delta N_l \sim 10^{19}$ cm^{-2} for molecular hydrogen in K_s band. Therefore, for the selected nebulae the relative gas column density variation is roughly estimated as $\Delta N_l/N_l \sim 10^{-3}$. This means that in strong scattering regime and for $R_s < R_{ref}$, such small density fluctuation can produce modulation index $\Delta I/I > 0.06$ (see figure 4.18) where I is the light flux. This gives the magnitude[4] variation $\Delta m > 0.06$.

The corresponding variation in magnitude induced by dust extinction is $\Delta m = \Delta A$ where A is the absorption factor (in magnitude). This factor is proportional to the column density, $A \sim N_l$. Thus, $\Delta m = \Delta N_l/N_l\ A$. For instance, in K_s band we have $A(K_s) \simeq 4$ toward the core of B68. For a column density fluctuation of $\Delta N_l/N_l \sim 10^{-3}$, we obtain $\Delta m < 0.004$ for the whole cloud. This value is negligible compared to the flux fluctuations induced by optical diffraction and hence *the scintillation should not be confused with dust extinction*.

5.1.1 Galactic Cool Flow

According to cosmological simulation in ΛCDM framework, the accretion of cool atomic hydrogen should exist in galactic halos. Through this accretion the gas is deposited in galactic disk and fuel star formation [Dekel & Birnboim (2006)]. Although such flow is yet to observe, we use the simulation results and show that they produce negligible scintillation.

In 2011, Kyle and his colleagues simulated the halo orbiting gas for Milky Way-like halos with different merger histories [Stewart et al. (2011)]. They performed a mock observation along different sightlines to determine the HI column density for different gas orbiting velocity. They removed the galactic rotation from gas velocities and plot the column density against the gas residual velocity according to figure 5.2. The gas with 90% of its velocity larger than the galactic rotation velocity (which is set to zero in the figure) is accepted to be accreting about the galaxy (left panel). They could distinguish between the co-orbiting gas and anti-orbiting gas with respect to galactic rotation. The non-orbiting flows can be distinguished from accreting gas if their velocities distributed around galactic rotation velocity (around zero in right panel).

Though such hypothesised flows consist of atomic hydrogen and can be detected through their absorption lines or 21 cm emission, we estimate their maximum diffusion radius. From figure 5.2, the maximum column density is $\sim 10^{18}$ cm^{-2}. Considering such column

[4] $m = m_0$ - 2.5 log$I$ where m_0 is a constant.

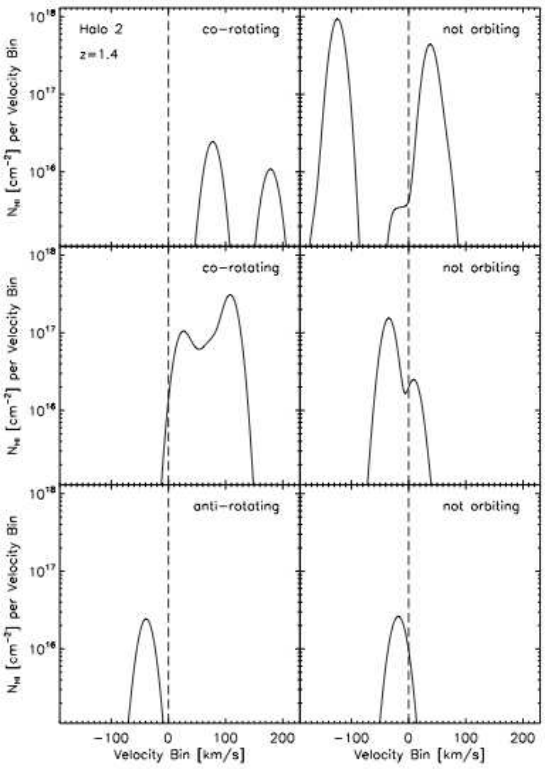

Figure 5.2: Mock observation of HI column density as a function of gas orbital velocity. The galactic rotation is subtracted. Left: Sightlines that show orbiting gas with respect to galactic rotation. The top and middle plot are co-rotating with respect to galactic rotation curve while the lower panel shows gas with counter rotation. Right: Sightlines that show not-orbiting gas with respect to galactic rotation [Stewart et al. (2011)].

density belongs to clouds with size of $\sim$ 10 A.U. at λ = 1 μm, the lower limit on diffusion radius is $R_{diff} > 10^8$ km which is larger than 100 times of R_F for flows extended in halo to 100 kpc.

5.2 IR Observation with the NTT

The NTT[5] owned by ESO is a 3.6 m alt-azimuth telescope located at La Silla observatory, Chile (70° 43'54.272" W -29° 15'18.440 " S). It benefits from active optics which corrects the defects and deformations of the telescope and mirror and has two Nasmyth focus platforms to mount two sets of instruments simultaneously. These platforms can be switched to each other by rotating the 45-degree third flat mirror by 180 degrees. Figure 5.3 shows a schematic view of the NTT. Compared to the classical telescopes, NTT has a

[5]New Technology Telescope

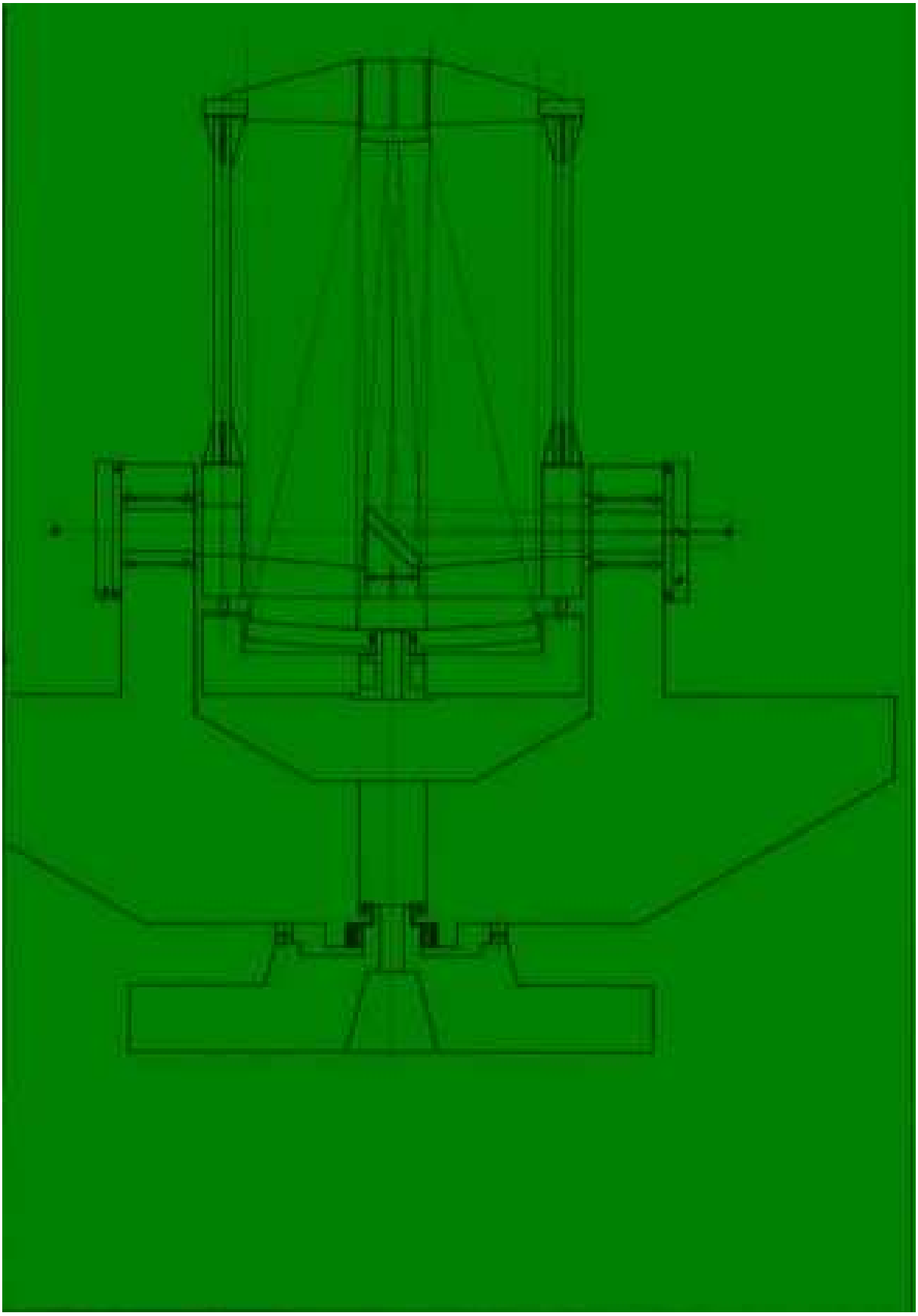

Figure 5.3: A schematic view of the NTT. [Wilson (1982)]

reduced weight of primary mirror and telescope structure. This results in a very accurate pointing of 1.5" r.m.s. over most of the sky, but, degradation occurs close to the zenith and at zenith angle larger than 60 degrees [NTT Overview, ESO].

From the Earth, IR observations, for wavelengths shorter than 2.3 μm, is affected by emission lines produced by O_2 molecules and OH radicals which are non-thermal sources. OH radicals are created from ozone and atomic hydrogen interactions in a layer of 6-10 km depth at an altitude of about 87 km. They produce emission lines from 0.61 μm to 2.62 μm. The absolute intensities of these emission lines strongly vary with time within a few minutes time scale. Since their fluxes are greater than the other IR sources of the sky, they are the dominant source of background [Rousselot et al (2000)]. Figure 5.4 shows the OH emission lines in near IR wavelengths. For wavelengths longer than 2.3 μm, the main source of background are the sky radiation and telescope's dome heat. Since K_s passband overlaps this wavelength, the background through this filter can vary by a factor of two between summer and winter, but is more stable than J passband at the minute time scale. This background also depends on the cleanliness of the primary mirror. Images through K_s filter contains 600-700 ADU/s of background, strongly dependent on the temperature and the humidity.

Beside of these emission and thermal backgrounds, there are atmospheric absorptions which reduce or even completely annihilate the star fluxes in some intervals of IR wavelengths. These absorptions are mainly due to water vapour and carbon dioxide in the atmosphere. Absorptions are time-varying and depend non-linearly on the airmass. Figure 5.6 shows the variation of water vapour absorption with the wavelength.

During two nights, we took 4749 consecutive exposures of T_{exp}=10 s. All four targets were observed both nights. The images were taken by the infrared large field objective[6] SOFI camera of NTT.

5.2.1 SOFI Camera

SOFI camera is mounted on the Nasmyth A platform focus of the telescope. After reflecting from the tertiary mirror of the telescope, the light enters the front window (see figure 5.5). Immediately after crossing the window, at the telescope focus, there is a cooled mask wheel. This wheel contains different masks for imaging objectives, long slit spectroscopes and polarimeters. The mask wheel is followed by a collimator lens to focus the instrument. There are two filter wheels. The first one contains the standard broad-band near IR filters (which we used), several narrow band filters, two order sorting filters for low resolution spectroscopy, an open and a fully closed positions. The second filter wheel has narrower band filters, a focus pyramid and also an open and a fully closed positions.

[6] with pixel size of 0.288 arcsec.

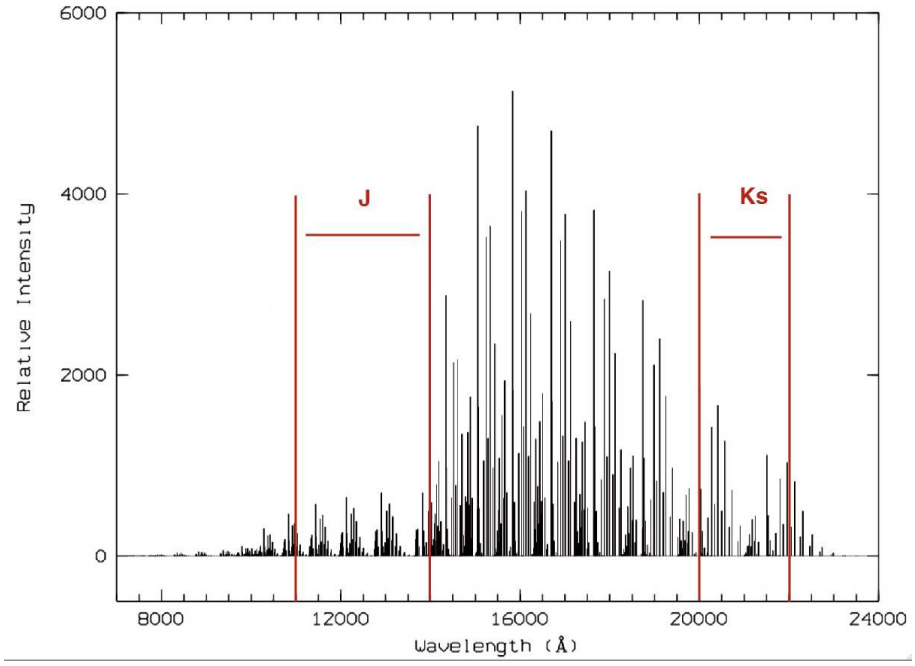

Figure 5.4: OH emission spectrum of the night sky. [Rousselot et al (2000)]

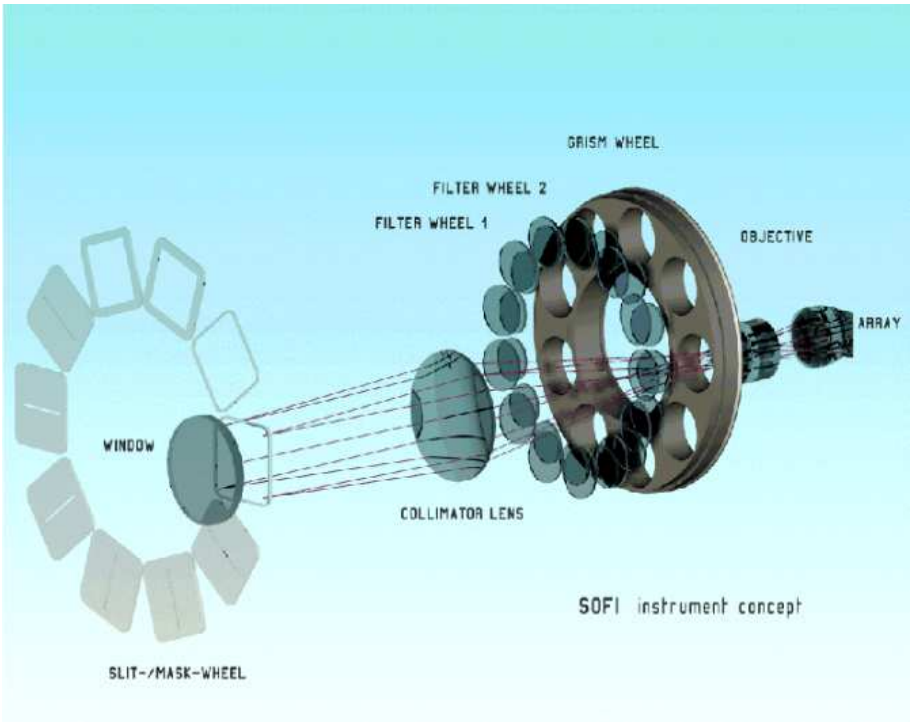

Figure 5.5: Optical layout of SOFI camera. [SOFI manual (2006)]

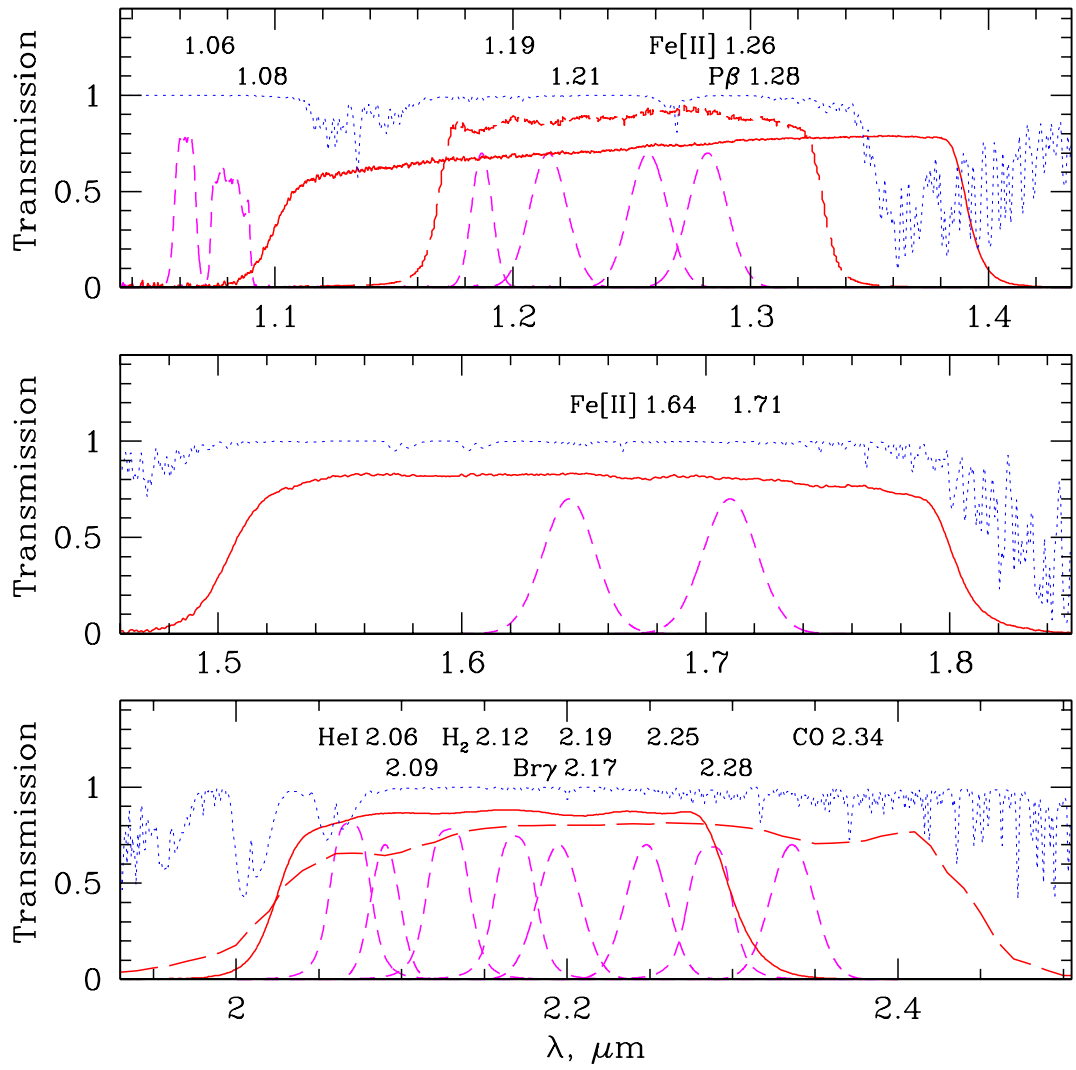

Figure 5.6: SOFI filters from [SOFI manual (2006)]. Solid red lines are broad-band J (top panel), H and K_s (down panel). The dashed magenta lines are narrower filters. The red dashed lines are J_s and K broad-bands. The dotted blue lines are the atmospheric transmission model for airmass=1.0, assuming 1 mm column of water vapour for Mauna Kea (Lord, S.D. 1992, NASA Technical Memor. 103957; courtesy of Gemini Observatory)

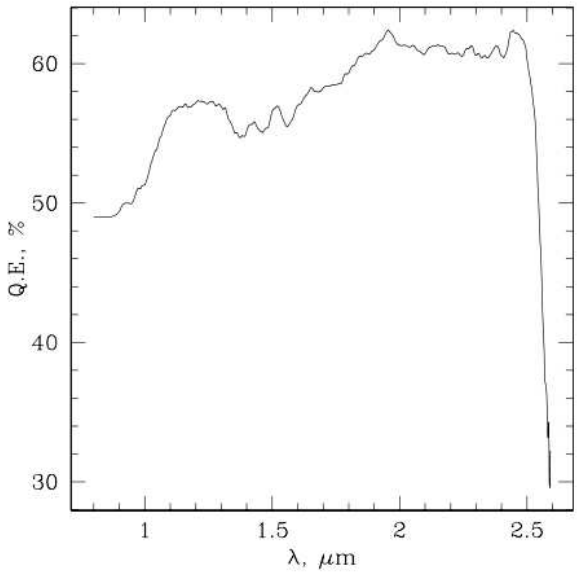

Figure 5.7: Average Quantum Efficiency of the SOFI detector at T = 78 K as a function of the wavelength. The peak is at 1.970μm, and the long wavelength cut-off is at 2.579μm. [SOFI manual (2006)]

After the filters, there is grism wheel containing grisms for long slit spectroscopy, imaging polarimetry and an open and a fully closed positions. We aimed to do star photometry and thus used the imaging mask and the open positions of the second filter wheel and the grism wheel. The imaging can be done through J, J_s , H, K_s and Z broadband filters. The central wavelengths for J and K_s filters are 1.247 μm and 2.162 μm with widths at half maximum of 0.290 μm and 0.275 μm respectively. Figure 5.6 shows the SOFI passbands in near IR with the corresponding atmospheric water vapour transmissions. The objective wheel contains two objectives for imaging at 0.288" (large field) and 0.144" (small field) per pixel. We used the objective with the largest field.

The IR detector used by SOFI camera is a Rockwell Hg:Cd:Te 1024 $\times$1024 Hawaii array with 18.5 μm pixels which corresponds to 0.288" on the sky for the large field objective. In normal imaging with SOFI, the North and the East are to the left and the bottom of the image respectively. The array is read out in four quadrants. One of the differences between the IR array and the CCD is the read-out mode which can be faster for IR array. In an IR array, unlike a CCD, the charges are not moved from pixel to pixel during the read-out process. They are read directly from the pixel. The average Quantum Efficiency of pixels is 65$\%$ for J and K_s bands. Figure 5.7 shows the variation of Q.E. with wavelength. Even with no incoming light, the thermal fluctuations create charges in the array which generate dark current. This current can be reduced by lowering the array temperature. For SOFI's detector, dark current is very low, about 20 e^-/hour and the readout

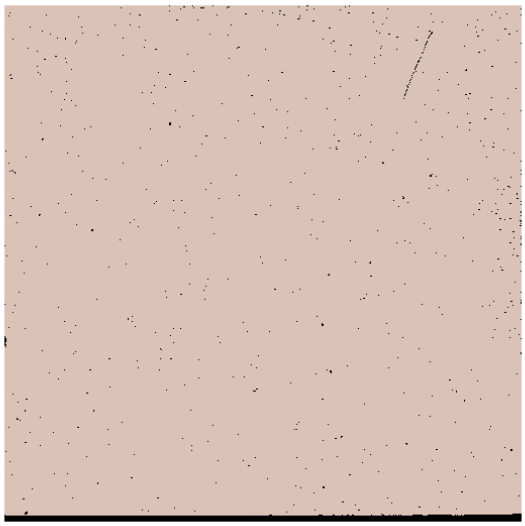

Figure 5.8: Bad pixels of the SOFI IR array are shown in black.[SOFI Overview, ESO]

noise is 12 e^-. This latter noise comes from two sources: the conversion of an analog signal to a digital number is not completely repeatable, and the electronics of the detector and the amplifying process can increase the uncertainties of the signal. The contributions of dark current and read-out noise are negligible compared to the statistical fluctuations of the incoming flux, and we will ignore them through data reduction process.

About 0.1% of the pixels are bad (figure 5.8). The bad pixels include dead and emitting pixels. Dead pixels can be detected on the images from a flat field illumination image and the emitting pixels can be distinguished in dark imaging. Flat field image is taken by closing the telescope's dome and illuminatinf it with uniform light emission.

The well depth of the array is 170,000 e^- which corresponds to 32,000 ADU for array gain of $\sim$5.4 e^-/ADU (Figure 5.9). The array response linearity is better than 1.5% for the signals up to 10,000 ADU and it is recommended to choose short-enough exposure time to maintain the background lower than 6,000 ADU, to avoid linearity deviations above this value. For stars $\sim$10 mag one should use the minimum detector integration time of 1.183 s to avoid saturation in K_s filter. For 12-15 mag stars, this value is 12 and 6 seconds for J and K_s filters. For fainter stars one can use safely 30 and 10 seconds for J and K_s filters. Figure 5.10 summarises the specifications of the IR detector of SOFI camera.

Due to an alignment defect of the large field objective, the images are radially elongated in the left (north) part of the field as shown in figure 5.11. This elongation affects a verti-

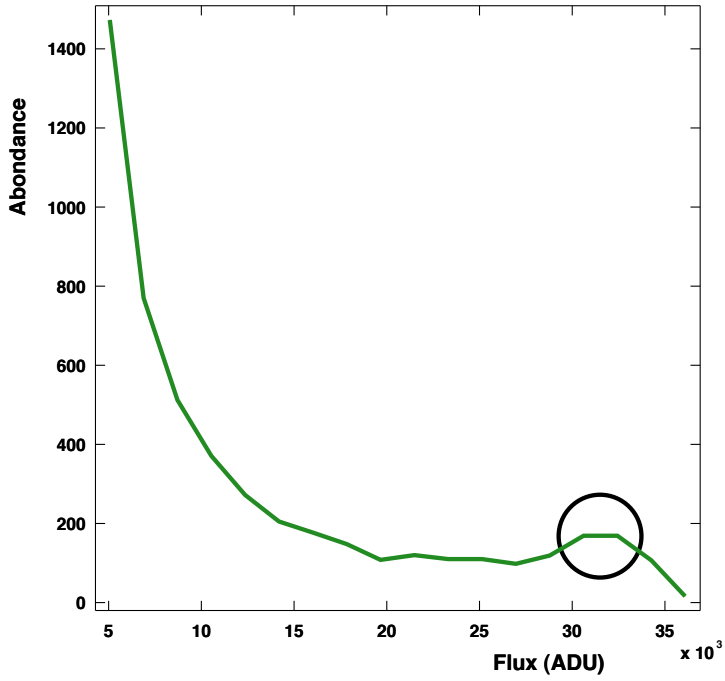

Figure 5.9: Distribution of pixels' contents toward one of our targets. Saturation occurs from $\sim$ 30,000 ADU

Array Format	Hawaii HgCdTe 1024x1024
Pixel Size	18.5 µ
Q.E.	65%
Gain	~ 5.4 e/ADU
RON	~ 2.1 ADU
Bad Pixels	About 1000
Non-Linearity	< 1.5% over 0 to 10000 ADU
Dark Current	< 0.1 e/s

Figure 5.10: Some facts about SOFI IR array. [SOFI Overview, ESO]

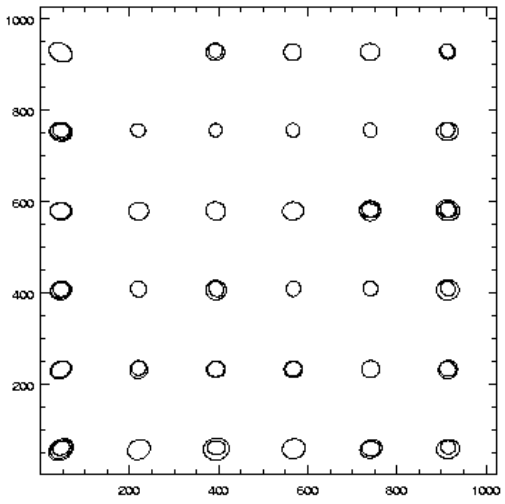

Figure 5.11: Objects are elongated at the border of large field images. [SOFI Overview, ESO]

cal strip of about 150 pixels and smoothly disappears when moving toward the centre of the field [SOFI Overview, ESO].

5.2.2 Observation Strategy

The observations were done at nights of 25-26 and 26-27 of June 2006. The observation sequence was optimised to observe each object at the time of minimum airmass[7], to minimise the atmospheric absorption and benefit from the best photometric precision. Following this strategy for both nights, as shown in figure 5.12, the observations began with Circinus with the airmass ~ 1.3; after reaching it's minimum airmass, the observations started toward B68 and continued for ~ 4 hours. Then, we observed cb131 until airmass ~ 1.6, and ended observations with the SMC.

5.2.3 The Database

Table 5.1 shows the coordinates of the selected targets and the total number of images per target. The longest sequence corresponds to B68 (about 10 hours) and the shortest series belongs to cb131 (about 4 hours).

[7] Airmass by definition is the inverse of cosine of the angle between the object and the zenith.

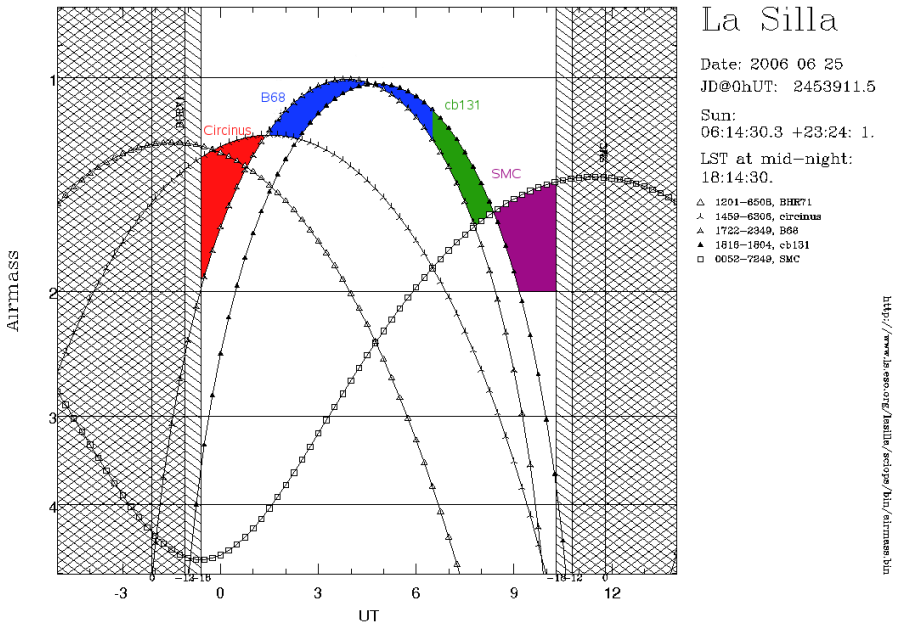

Figure 5.12: Airmass of the 4 targets as a function of the Universal Time. The objects were observed while their airmasses were around their minima.

	SMC	B68	cb131	Circinus
α (J2000)	00:52:41.3	17:22:40.7	18:16:59.4	14:59:28.9
δ (J2000)	-72:49:14.3	-23:49:47.2	-18.01:53.2	-63:06:10.1
J measurements	988	-	-	-
K_S measurements	-	2221	637	898
duration, night 1 (hours)	2.18	4.77	1.25	1.84
duration, night 2 (hours)	2.63	5.07	1.74	2.16

Table 5.1: The observations results.

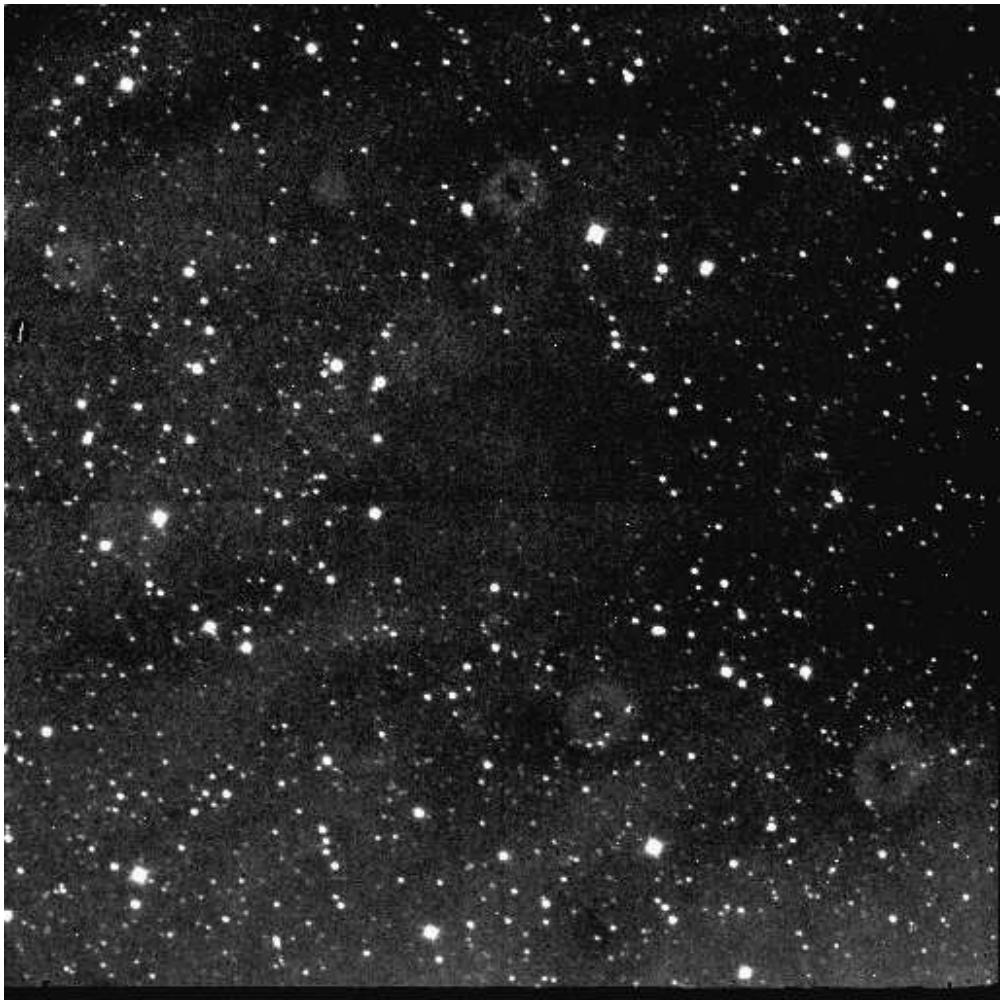

Figure 5.13: A raw image from nebula cb131.

5.3 Data Reduction

Compared to visual band, IR observation has stronger background because of sky emission. A standard way to reduce this effect is to subtract a science image from an image of the uniform sky. The sky images are usually taken after target images from a clear part of sky next to the target field with the same exposure time [SOFI manual (2006)]. We did not use this procedure as we determined the local background from equation (5.6) through the photometry process explained in section 5.3.2.

5.3.1 From Raw to Reduced Images

Unlike the CCDs, for IR arrays it is not possible to have a zero second exposure (bias) image[8]. This means we do not have direct access to the constant electronic offsets of the array's pixels. Therefore, bias contributions are indistinguishable in any image including dark current images. Beside the usual electron/hole generations of dark current, there are other dark components in IR imaging: shading, the variation of dark current with exposure time and incident flux intensity, heat from read-out amplifiers (amplifier glow). As the dark current appears to be stable during the observation [SOFI manual (2006)], it can be considered as the background emission and is computed through PSF photometry. Figure 5.13 shows an example of a raw image. The low spatial frequency variations due to array sensitivity can be seen in this figure.

Because of difference in pixels Q.E. of the array, the response to a uniform light emission (flat-field emission) is not homogeneous. To have this response, a flat-field image is produced from series of images obtained alternatively from uniformly illuminated and dark dome panel. The flat-field image is constructed from the subtraction of two images and divided by the average value. Figure 5.14 shows the flat-field images in J and K_s bands. To take into account the array response, the raw image is divided by the flat-field image pixel by pixel. If F is the flux (in ADU) of a pixel in a raw image and $F_{flat-field}$ is the flat-field value of the same pixel, the reduced flux $F_{reduced}$ is computed as:

$$F_{reduced} = \frac{F}{F_{flat-field}} \langle F_{flat-field} \rangle, \tag{5.3}$$

where $\langle F_{flat-filed} \rangle$ is the mean value of flat-field. Figure 5.15 shows the reduced image of figure 5.13. The brighter patterns on the left and the bottom of the raw image were due to the edge to edge long-scale variations of the array (varies between 1 to 3 percent) depending on the filter and the objective. Flat-field also is useful to correct the vignetting effect. The precision of the flat-field images varies with time. The illumination of the dome panel can change in time due to intensity variation of the illuminating lamp or variations in dome temperature. Figure 5.16 shows the distribution of the relative difference

[8] With CCD detectors the bias image is taken with shutter closed.

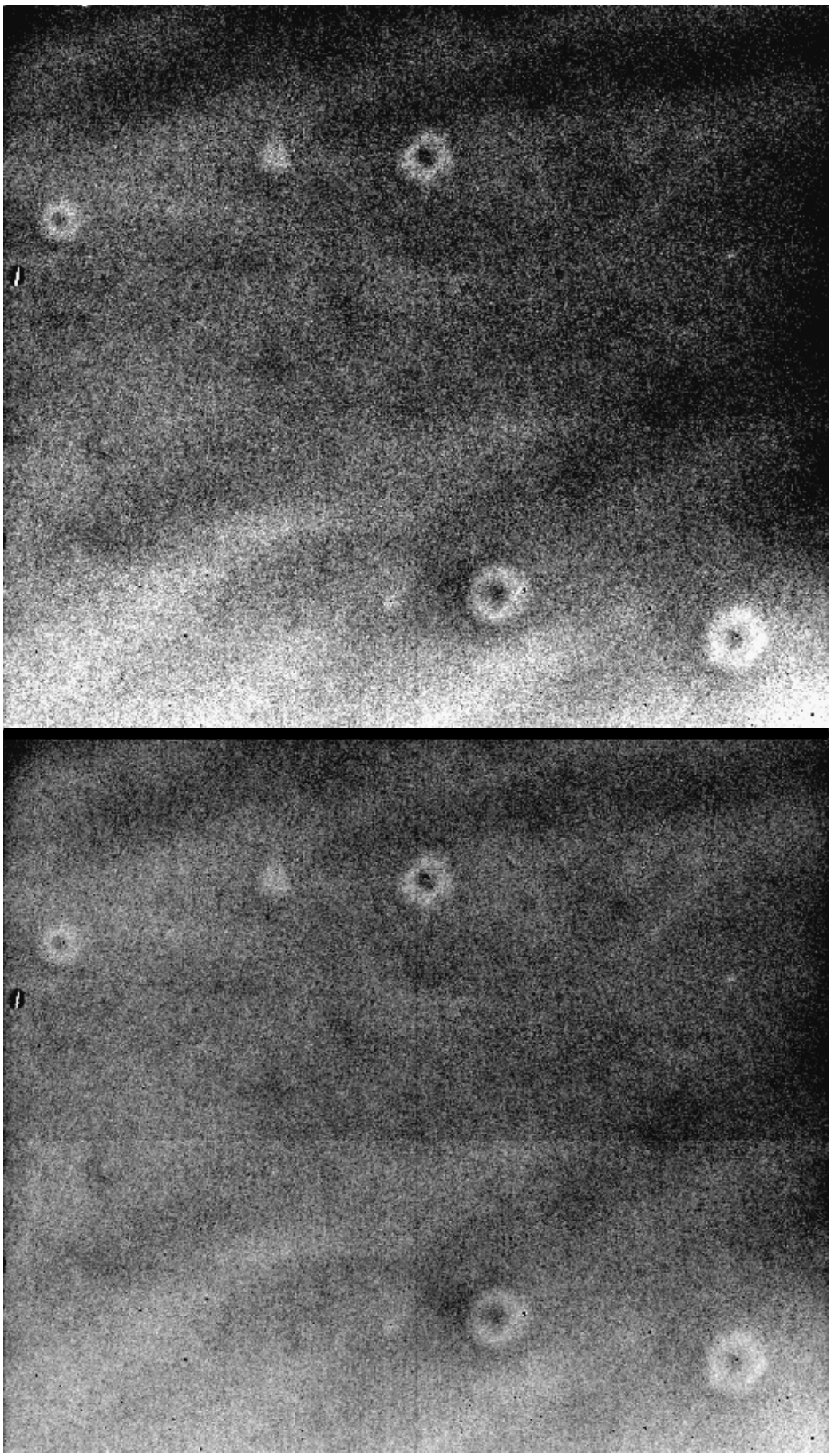

Figure 5.14: The pixels have different responses to a uniform light emission. Top: flat-field image in J band. Bottom: flat-field image in K_S band.

Figure 5.15: Reduced image of the figure 5.13. The patterns due to the different responses of array are flat-fielded. The residual rings are due to local fluctuations of the background induced by the telescope optics.

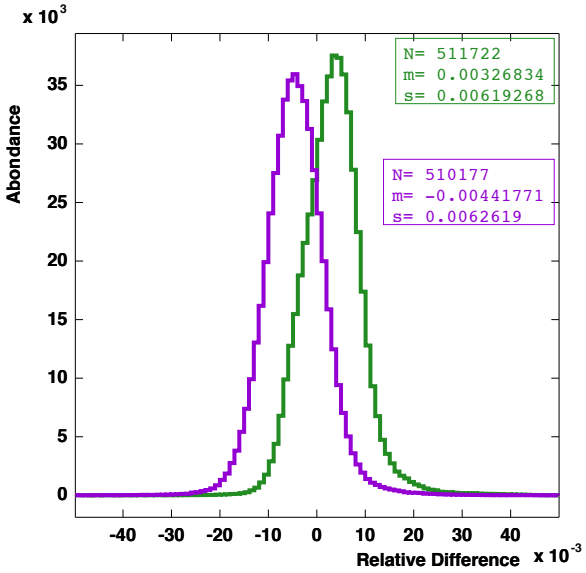

Figure 5.16: Distribution of the relative pixel to pixel difference of flat-field images taken 50 days apart. Green and violet curves are the distributions for J and K_S broad-bands respectively. The fluctuations in flat field measurement are given by the dispersion $0.6/\sqrt{2}$ = 0.4% for both bands.

of flat-field images taken 50 days apart. For both J and K_s bands a mean variation of about 0.6% is observed. This tiny variation, as we will see in section 5.3.3, can affect the photometric precision of the stars when observed with strong background (like in K_s band).

5.3.2 From Reduced Images to Light Curves

The stellar light curves are the series of photometric measurements extracted for all stars of each target image by image. We first produce a high signal to noise reference image for each target (called reference image). This image is used to detect stars and produce a reference catalog. The catalog contains the coordinates of the detected stars on the reference image and the reference fluxes are used to align the fluxes measured with the other images (hereafter current images). Stars detected on the current images are associated to the reference catalog stars through the geometrical alignment determined with the EROS software.

Reference Catalog

The reference image is constructed by co-adding a series of current images for the given field. Ten images (except for the SMC for which we selected 13 images) with consecutive

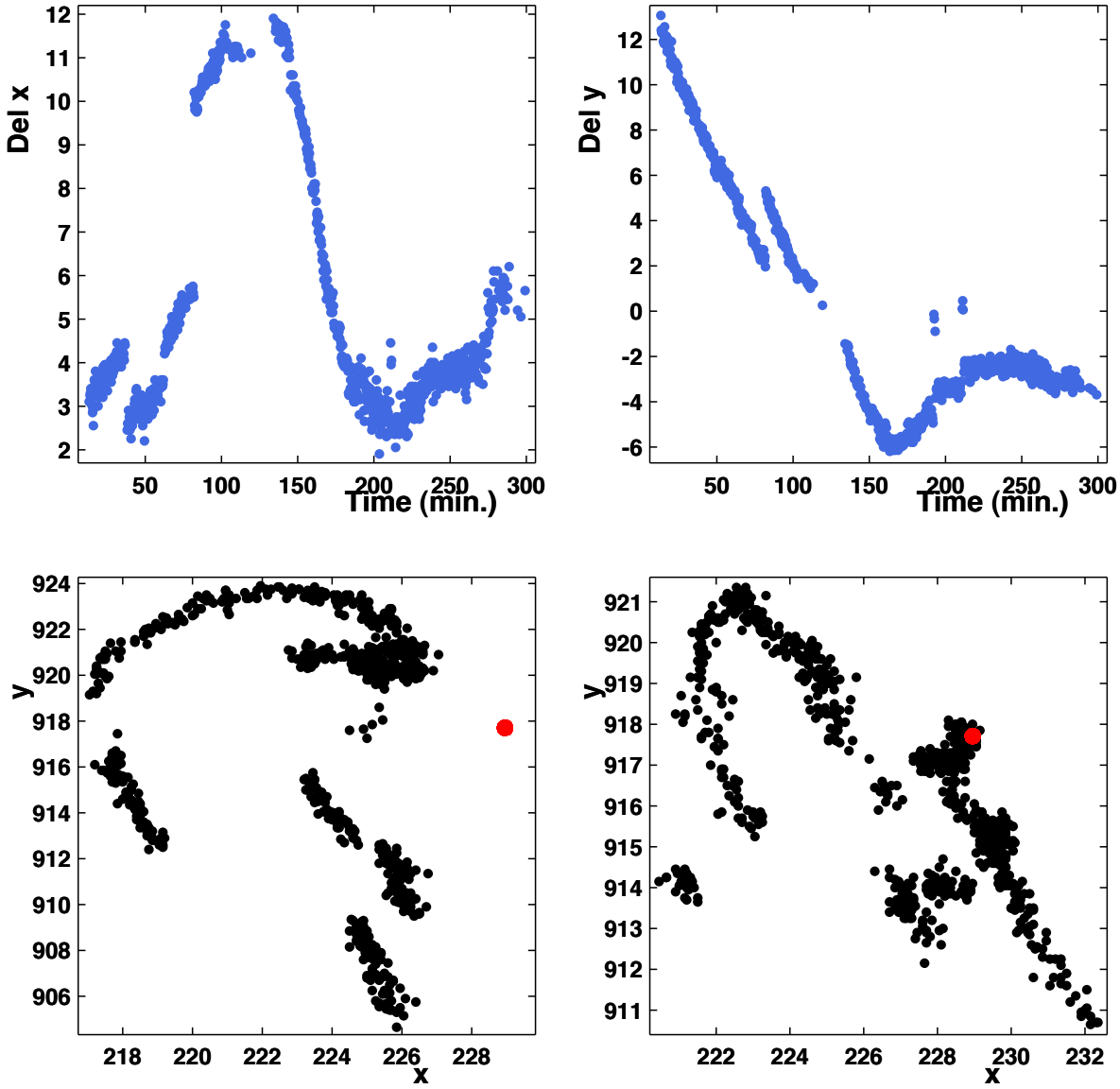

Figure 5.17: Top: Δx and Δy evolution as a function of time for current images in B68 field. Bottom: red points show the reference coordinate of a given star, black points are its coordinates on the current image frame. Left and right plots belong to first and second nights of observation respectively.

	SMC	B68	cb131	Circinus
Atmospheric seeing	0.87”	0.43”	1.17”	0.45”
Airmass at start	1.524	1.187	1.470	1.288

Table 5.2: The mean seeing and airmass of the selected images for the production of reference images.

	SMC	B68	cb131	Circinus
number of detected stars	5042	9599	9084	5249

Table 5.3: Number of detected stars in each field given from the catalog constructed from the corresponding reference images.

time spacing of about 1 minute were selected and added up. The selected images are chosen with a good seeing to optimise the signal to noise ratio. Table 5.2 shows the seeing and the airmass of the selected images for each field. Before co-adding the selected images, they are geometrically aligned. This alignment includes small translations and rotations which are entered in relation:

$$\begin{aligned} X &= \Delta x + x\,cos\theta + y\,sin\theta, \\ Y &= \Delta y - x\,sin\theta + y\,cos\theta, \end{aligned} \tag{5.4}$$

where x and y are the pixel coordinates on the first image and X and Y are the corresponding coordinates in the other image. θ, Δx and Δy are the rotation angle and translation parameters that give the best coincidence between two images. It is sufficient to align three bright stars from two images and find the transform parameters. All other stars will be aligned with same parameters. The constructed reference images of the four fields are shown on top of figure 5.1 at the beginning of this chapter.

Table 5.3 gives the number of detected stars in each field from the reference catalogs. Stars on current images are located through the geometrical alignment between reference and current images by using the same procedure explained above. The evolutions of translation parameters between reference and current images for a typical star in B68 field are illustrated at top of figure 5.17. At bottom of the same figure, the variations of the coordinates of the same star are shown.

For each star we assign a reference flux which is the average flux of the star calculated from the images entering the reference image. This reference flux is used to photometrically align the star flux of each current image.

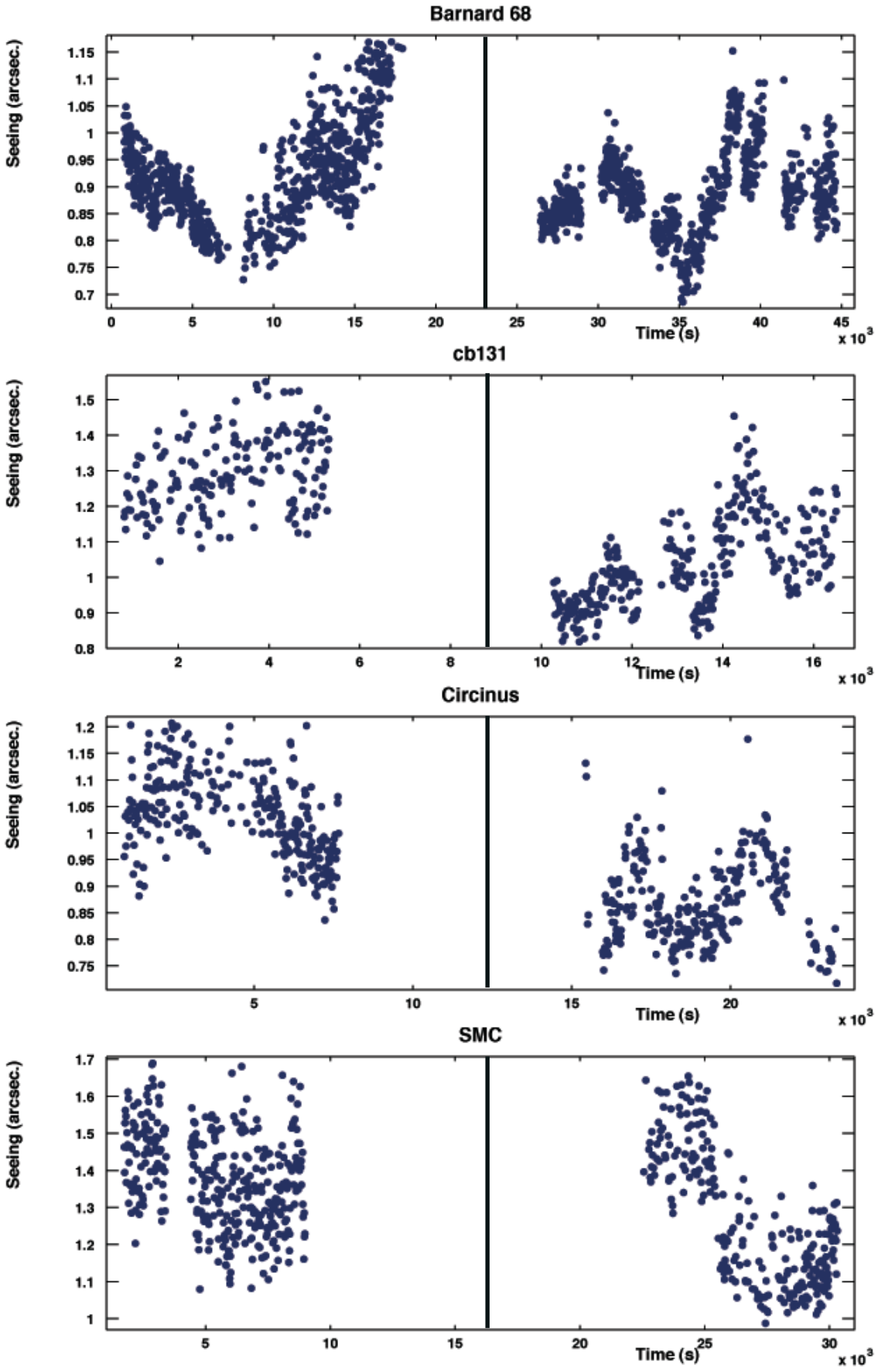

Figure 5.18: Seeing variations during the two nights for all fields. Times for the second night are shifted for easier visualisation.

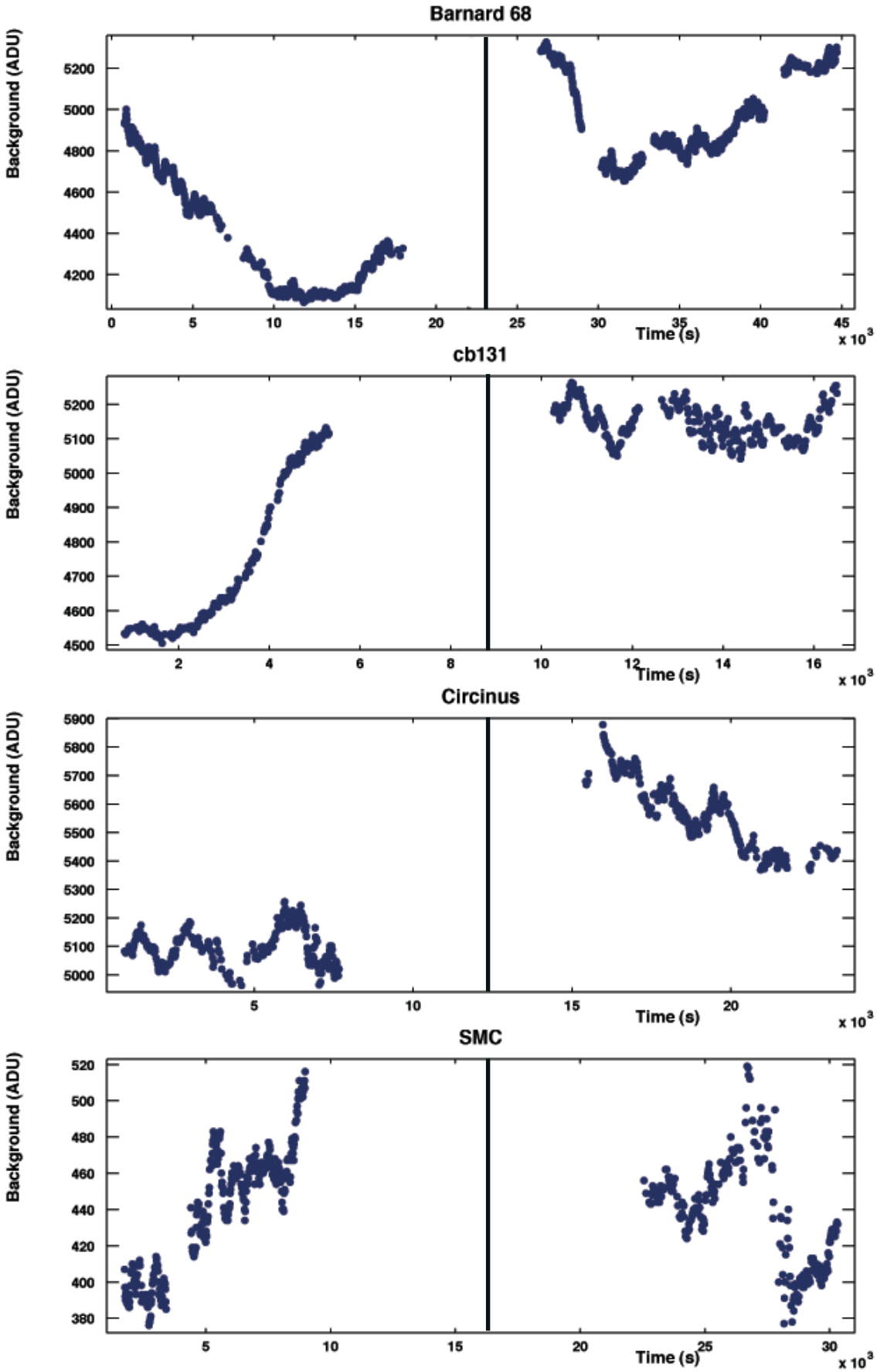

Figure 5.19: Background variations under a typical star during the two nights. The shape of variation is the same for all stars.Times for the second night are shifted for easier visualisation.

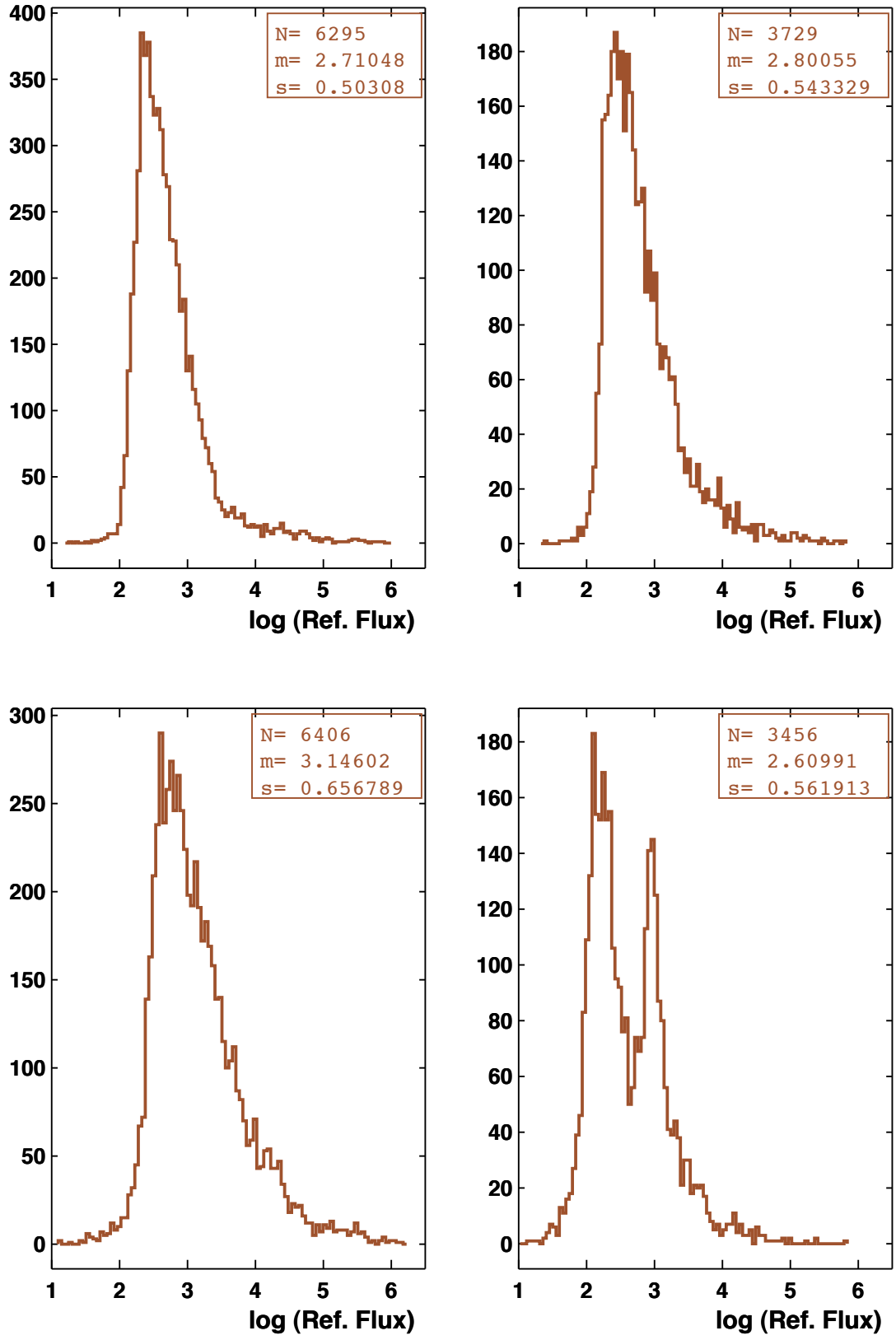

Figure 5.20: Distribution of the reference flux for the 4 observed fields. Top left: B68, Top right: Circinus, Bottom left: cb131, Bottom right: toward the SMC. The two stellar populations in the SMC belong to main sequence stars and red giants respectively. Reference flux is given in ADU (in 10s exposure).

Photometry with PEIDA

Photometry and light curve generation are obtained by a custom-designed fast photometry program named PEIDA, which stands for Programme pour l'Étude d'Image Destinées à l'Astrophysique [Ansari (1996)]. The Point Spread Function (PSF) of the star is assumed to be a Gaussian with an oblique elliptical section defined by seeing parameters σ_x, σ_y and ρ in pixel unit:

$$\psi(x,y) \;=\; exp\{-\frac{1}{2}\,(\frac{(x-x_0)^2}{\sigma_x^2}+\frac{(y-y_0)^2}{\sigma_y^2}-\rho\frac{(x-x_0)(y-y_0)}{\sigma_x\,\sigma_y})\}, \qquad (5.5)$$

where x_0 and y_0 are the star centre (PSF peak) coordinates. Seeing parameters are computed for the *entire* image by fitting the PSF to the brightest isolated stars. Then, the computed parameters are used to fit the luminosity of each star of the image. Figure 5.18 shows the seeing variations of the observed fields calculated from the PSF fit to the bright stars. Here, the seeing is the full width at half maximum (FWHM) of the PSF.

The content of a pixel consists of three components: the local sky background level, the flux contribution of the star (the signal) and the flux contribution of the neighbouring star(s). Since the PSF parameters are fixed, a linear fit is performed to the following function:

$$F_{total}(i,j) \;=\; B + A_0\,\psi(i,j) + \sum_{neighbours} A_k\,\psi(i,j), \qquad (5.6)$$

where (i,j) represents a pixel in a 13×13 pixel domain centred on the target star. B is the local sky background. The typical variations of a local background is shown in figure 5.19 for the four fields. A_0 is the flux assigned to the star. It is called either *raw flux* if the star belongs to one of the current images or reference flux if the image is the reference one. A_k is the contribution of the neighbouring star(s). This flux, A_k, is not to be considered as the definitive flux of the neighbouring star(s) since the background should be derived for each star separately and the impact of all first neighbours should be also included. Figure 5.20 shows the distribution of the reference fluxes for the observed fields.

Photometric Alignment

All the images taken from a given field have variable photometric conditions. The sky condition varies in time: variation of airmass or cirrus clouds affect the *absorption coefficient* of the sky. Therefore, we should calibrate the star flux with the reference flux to avoid flux fluctuations induced by variation in sky condition. For this purpose, we plot the reference fluxes of stars of each image versus their raw fluxes and fit a linear function. The slope of the line is the global absorption coefficient of the image. The distribution

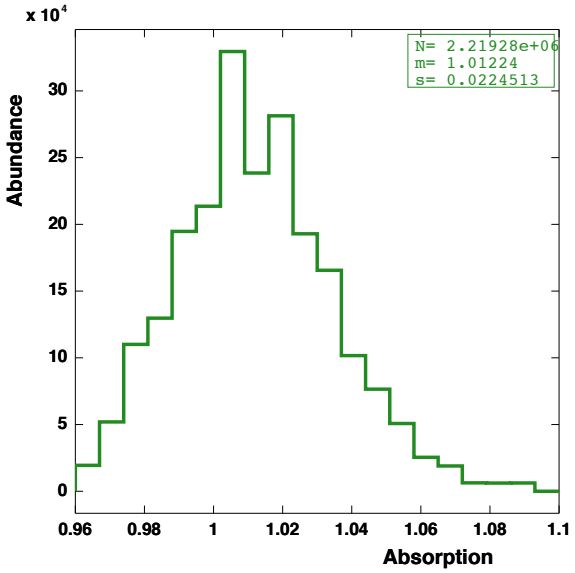

Figure 5.21: Distribution of the sky absorption relative to the reference image, for the second night observation of cb131.

of the absorption coefficient is represented in Figure 5.21. Usually absorption does not deviate largely from one. The calibrated flux, F_{cal}, is computed as:

$$F_{cal} \quad = \quad a\, F_{raw} + b, \tag{5.7}$$

where a is the absorption coefficient. b is the flux shift constant of the fit and has a small value as it is expected. After constructing the reference catalog and the reference fluxes, PEIDA performs the flux calibration and generates the light curves.

Magnitude Calibration

The photometric calibration is done by using the stars from the 2MASS catalog in our fields [Skrutskie et al. (2006)]. Such stars were found only in the SMC and B68 fields. As all our fields were observed during the same nights with stable atmospheric conditions, we extrapolated the calibration in K_s band from B68 to cb131 and Circinus, after checking that the airmass differences of the three reference images are smaller than 0.1, which could not induce flux variations larger than 0.1 magnitude. Figure 5.22 shows the calibration stars extracted from 2MASS and the corresponding fitted linear functions. The line m = C_i - 2.5 log F is fitted to magnitude-flux diagram, where m is the magnitude from the catalog, F is the reference flux and C_i is the calibration constant given by the fit. For J and K_s bands we find C_J = 25.29 and C_{K_s} = 24.63 respectively.

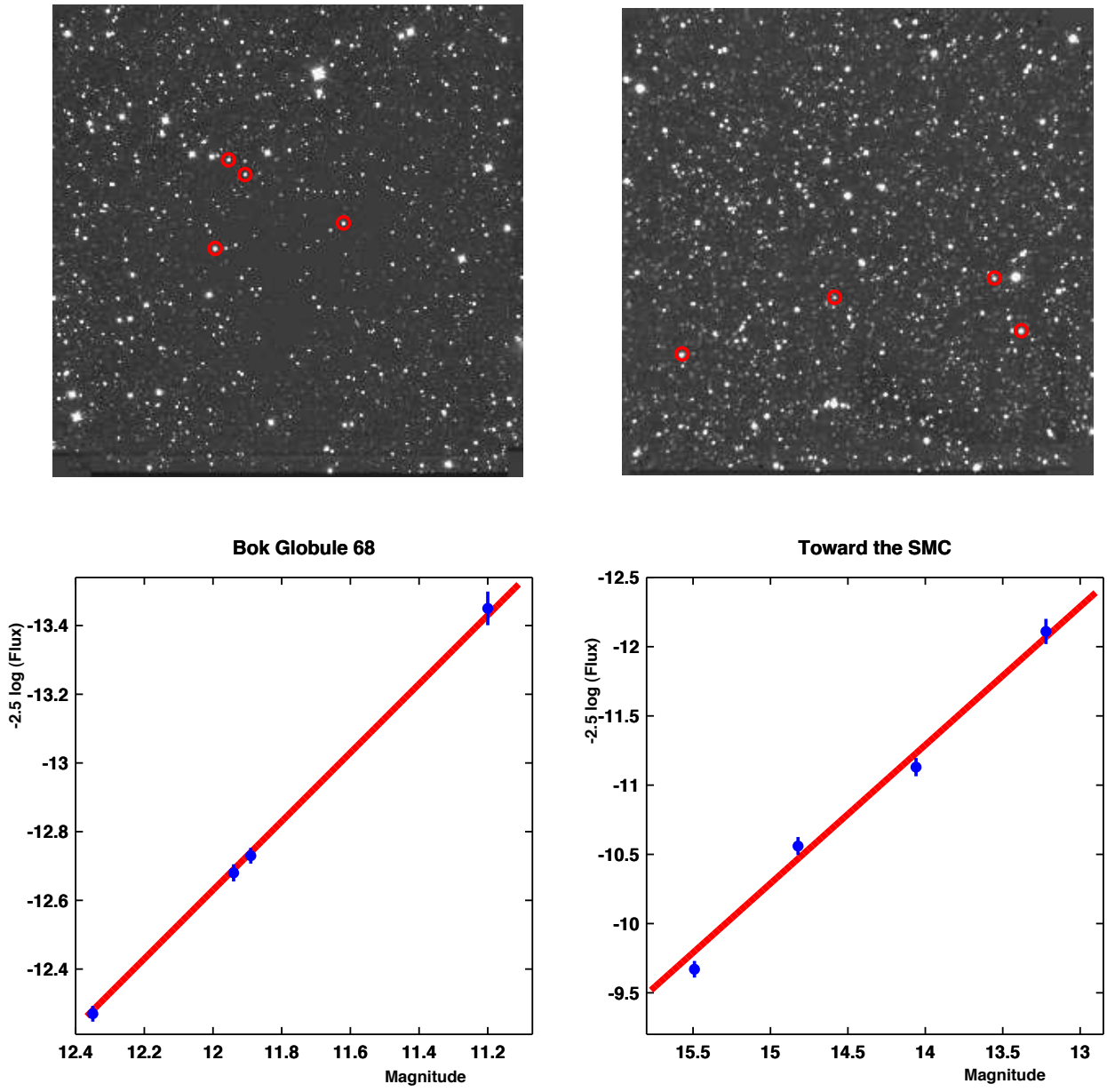

Figure 5.22: Flux-Magnitude calibration for K_s (left) and J (right) bands. Red circles on the images show the reference stars with measured magnitudes from 2MASS catalog. The calibration constants are $C_{K_s} = 24.63$ and $C_J = 25.29$.

5.3.3 Photometric Precision

To compute the flux of each star for each image, we use a fit of the pixels values $f(i,j)$ around the star by function (5.6) and compute the χ^2 as:

$$\chi^2 = \sum_{i,j} \left[\frac{f(i,j) - F_{total}(i,j)}{\sigma(i,j)} \right]^2, \quad (5.8)$$

where $\sigma(i,j)$ is the uncertainty on the flux measurement for pixel (i,j). We assume that the uncertainty in flux measurement is essentially due to *shot noise*, hence, if $n(i,j)$ is the number of photo electrons[9] in pixel (i,j) it is given by the relation $\sigma(i,j) = \sqrt{n(i,j)}/g$. The goodness of the fit is measured by the ratio between χ^2 and number of degree of freedom[10] χ^2 / n.d.f. Since the fitting region around the star is a zone always larger than 10 pix $\times$ 10 pix, the n.d.f. is usually larger than 100 and for a good fit we expect the peak of chi-square distribution to be at χ^2 / n.d.f. = 1. Figure 5.23 shows the chi-square distribution of star flux-fits for all measurements toward the SMC. The peak is clearly shifted from 1 to 1.4. The same behaviour happens for the three other fields. We propose two possible explanations:

1. The PSF may deviate from Gaussianity.

2. There are systematic photometric errors, which have to be added to the Poissonian noise.

As our exposure time is only 10 seconds it may not be long enough to have a Gaussian profile on detecting array. Figure 5.24 shows the variation of χ^2 as a function of seeing within different flux intervals for stars toward B68. Chi-squares are always better (smaller) for larger values of seeing. This can be explained by the fact that for small seeing, the shape of the narrow-width atmospheric PSF (which is Gaussian) can be perturbed through the convolution with instrumental PSF induced by the optics of the telescope. This can cause the non-Gaussianity of the final PSF. One can see a general increase in χ^2 with augmenting the stellar flux. This is due to systematic errors discussed below. We also calculated aperture photometry instead of PSF photometry with no improvement for the χ^2 distribution.

As we have included only the shot noises in expression 5.8, the existence of systematic uncertainties makes $\sigma(i,j)$ underestimated, explaining the increase of χ^2. To reconstruct the behaviour of measurement uncertainties, we compared the relative photometric precision of pure shot noise to the precision curve computed from PSF photometry. Figure 5.25 shows the comparison. Each red point shows the expected mean Poissonian pre-

[9] The pixel values are in ADU and should be multiplied by the gain (g) to give the number of photo-electrons: $n(i,j) = g\ f(i,j)$

[10] n.d.f. is the total number of pixels used in chi-square expansion minus the number of parameters to be fitted.

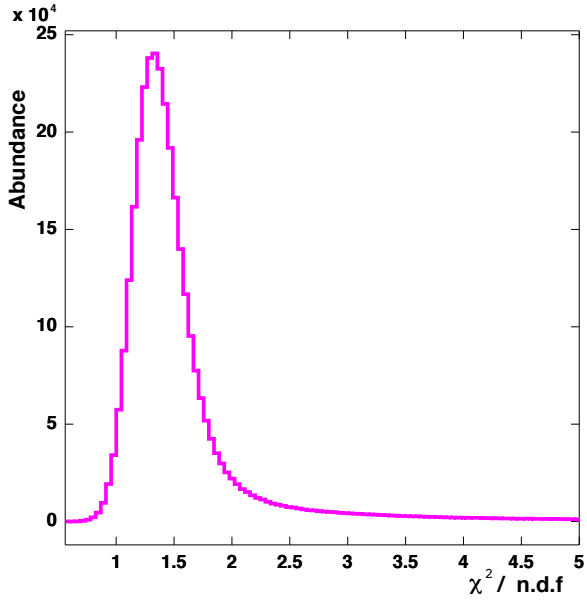

Figure 5.23: Distribution of chi-square divided by number of degrees of freedom computed from PSF fit for all measurements of star fluxes toward the SMC. The peak is located at χ^2 / n.d.f > 1.

cision δ_p of a stellar flux along a light curve as a function of the mean flux of the star: $\delta_p = \langle \frac{\sigma_p}{N_s} \rangle$ where N_s = g F is the star flux (signal) in number of photoelectrons and $\sigma_p = \sqrt{N_b + N_s}$ is the Poissonian uncertainty of the flux measurement. N_b is the total number of photoelectrons produced by background emission within the PSF. The average is done for all measurements of a star. Blue points show $\delta_F = \frac{\sigma_F}{<F>}$ where σ_F is the observed flux dispersion of the star through the light curve. As shown in the figure, δ_p decreases with mean flux because for the bright stars the major counts of $N_b + N_s$ belongs to the signal rather than the background. Therefore δ_p decreases approximately as $1/\sqrt{N_s}$ because of the high signal to noise ratio. According to the figure 5.25, if we just take into account the Poisson noise as the source of the uncertainties, the photometric precision should be better than 1% for the bright stars which is not confirmed by the dispersion computed from light curves (blue points).

We found two sources of systematic uncertainties. The first one is the uncertainty induced by the variation in flat field response. As shown in figure 5.16 the response of the IR array to flat field emission varies slowly with time for both J and K_s bands. Since we have used the flat field image produced monthly by NTT staff, it is probable that the array response is a bit different from the image we used. Although the variation is small ($\sim 0.4\ \%$) it is not correlated from pixel to pixel and its contribution can be noticeable for bright stars.

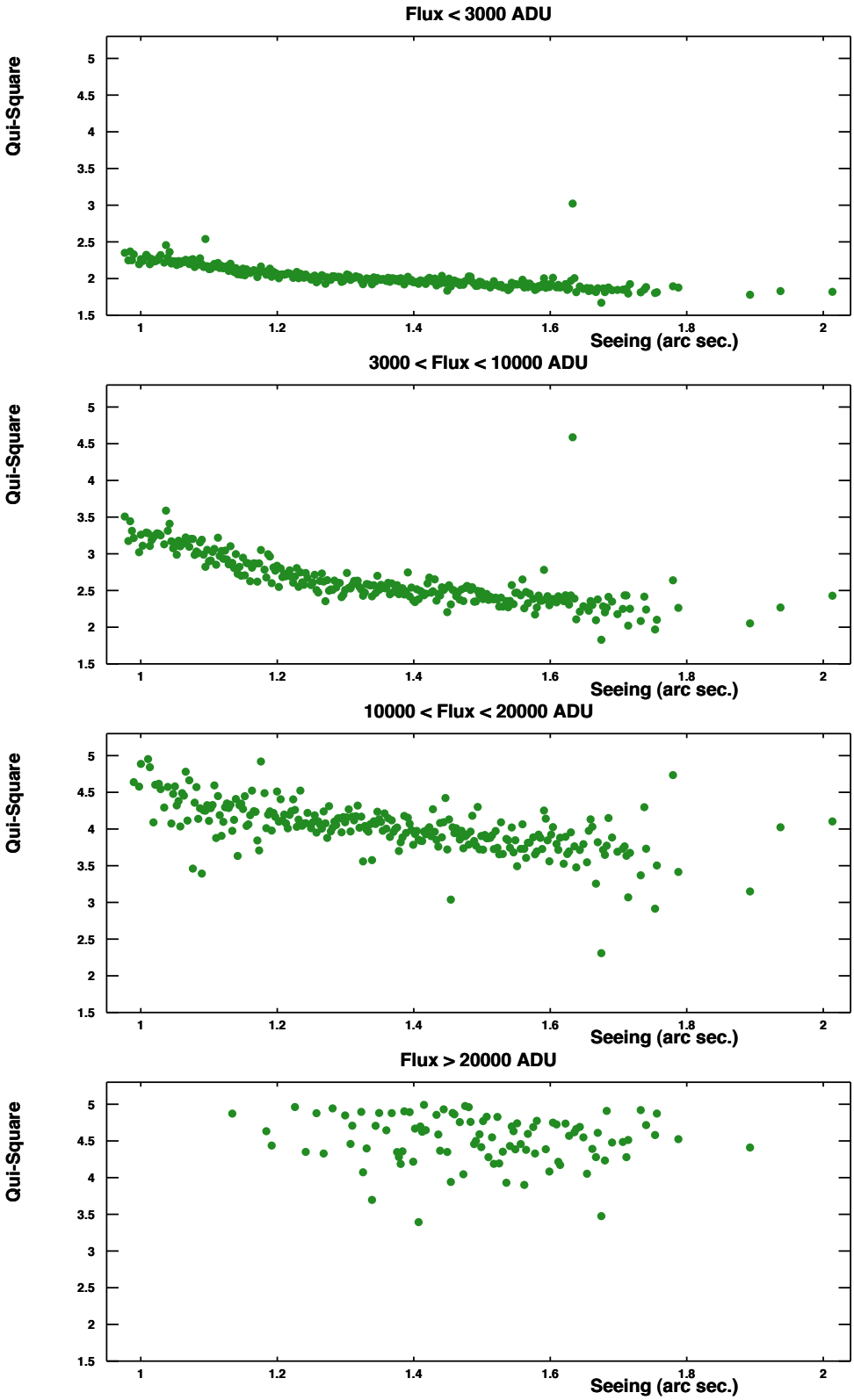

Figure 5.24: Variation of the chi-square of the PSF fit versus seeing for different flux intervals. The chisquare is always larger for the smaller seeings. The general increase of χ^2 with the flux is due to systematic errors uncertainties in the pixel flux.

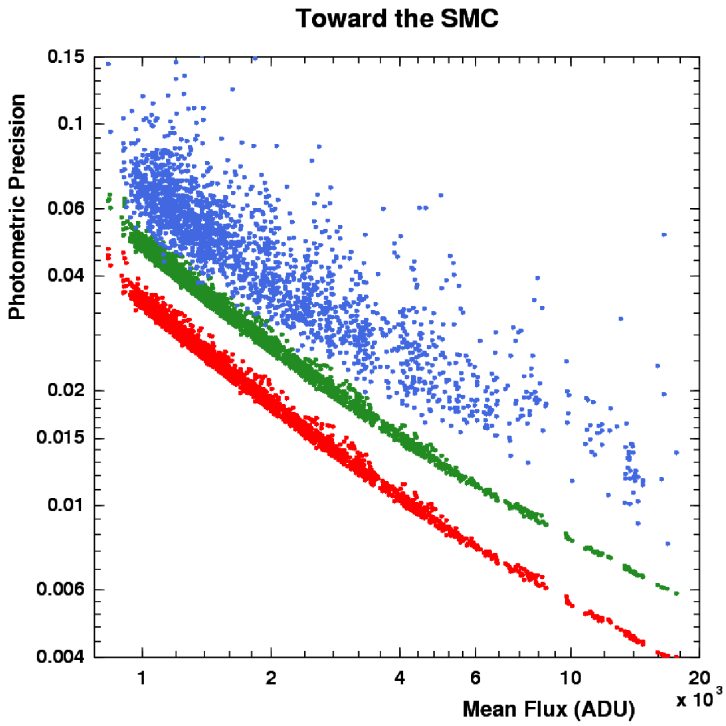

Figure 5.25: Precision curves for different uncertainty estimations. Red points represent precisions expected from pure Poissonian noise (δ_p). Blue points show dispersion along light curves (δ_f). Green points show precisions including systematic errors.

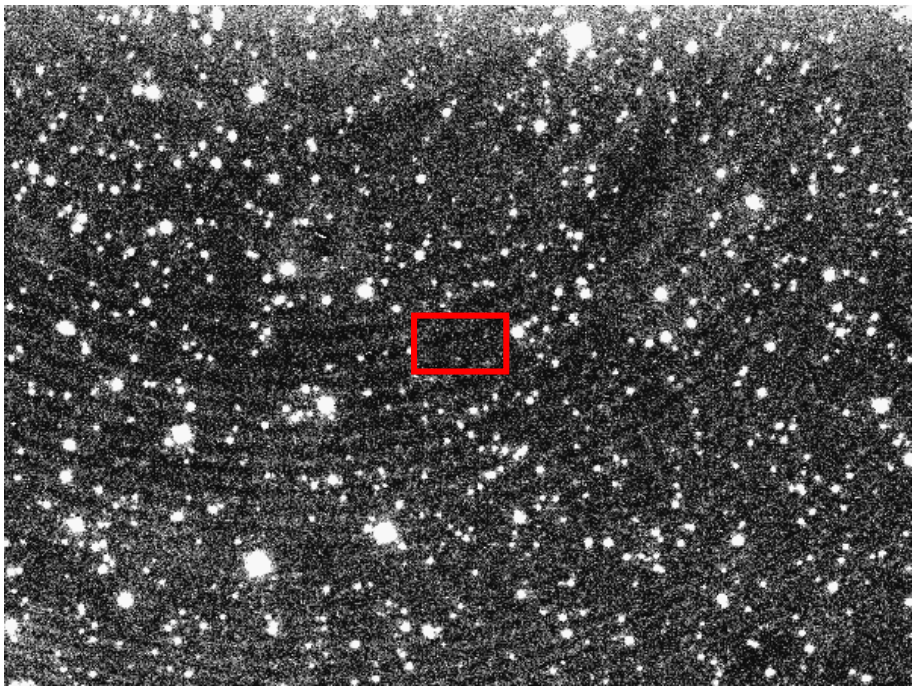

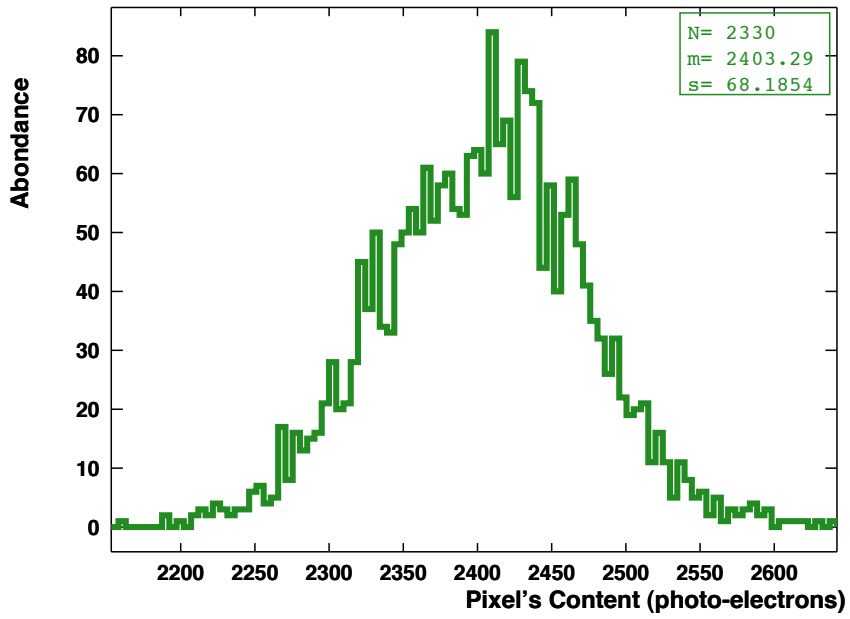

Figure 5.26: Fringing effect in J band. The arcs of fringing can bee seen from one of our images taken toward the SMC (top). The red rectangle shows a zone with no star to isolate the fringes. At bottom, we have plotted the distribution of photoelectron content of the zone's pixels. The expected Poissonian fluctuation is $\sim \sqrt{2400} \approx 49$ while the dispersion of the distribution is ~ 68 which exceeds by 40% the dispersion from Poissonian noise.

We found the fringing effect as the second source of systematics in J band. Figure 5.26 shows the fringing arcs at top panel in a current image taken toward the SMC. The consecutive light reflections within the thickness of the detector surface layer produce the fringing pattern. This effect depends on the thickness of the detector, the passband and the wavelength. It is less visible for wider passbands and longer wavelengths. To quantify the fringing effect, we have extracted a zone from an isolated star-free part of the image shown by the red rectangle at top of figure 5.26. We plotted the distribution of photoelectron count of the pixels (lower panel) of this zone. The dispersion of the distribution is about 40% larger than Poissonian fluctuation.

Taking into account these sources of systematic errors, we constructed a more realistic precision curve presented in figure 5.25 with green points. The residual difference should be due to PSF deviation from Guassianity.

5.4 Analysis

Before starting to analyse the light curves we checked the reliability of the fluxes. Any measurement with any kind of anomaly is removed through the *data cleaning* process. Firstly, we apply some general cleaning to all measurements and light curves as it is explained in the following subsection. Then, after light curve analysis and detection of variable light curves, we study each light curve individually to search for any residual anomaly or artefact.

5.4.1 Data Cleaning

To avoid anomalies due to low quality images, bad-measured stars, light curves with small number of measurements etc. We have systematically required some general criteria on different parameters that have effective contribution on flux measurement. There are more types of artefacts such as emitting or dead pixels, egret contamination from a bright neighbour, blending effect, gamma ray crosses etc. which will be considered after applying the general criteria.

Figure 5.27 shows the flux dispersions along the light curves for K_s and J bands. Each point shows the flux dispersion divided by mean flux along a light curve $\sigma_F/\langle F\rangle$. One can see abnormal effects such as stars with zero flux dispersions and lots of relatively faint stars as well as very bright stars with large dispersions. Since the vast majority of stars are stable stars with uniform fluxes, systematically large (or abnormal) flux dispersions are due to bad measurements which should be considered as parasitic effects. To select the measurements with the best qualities, we apply a general cleaning process as described below.

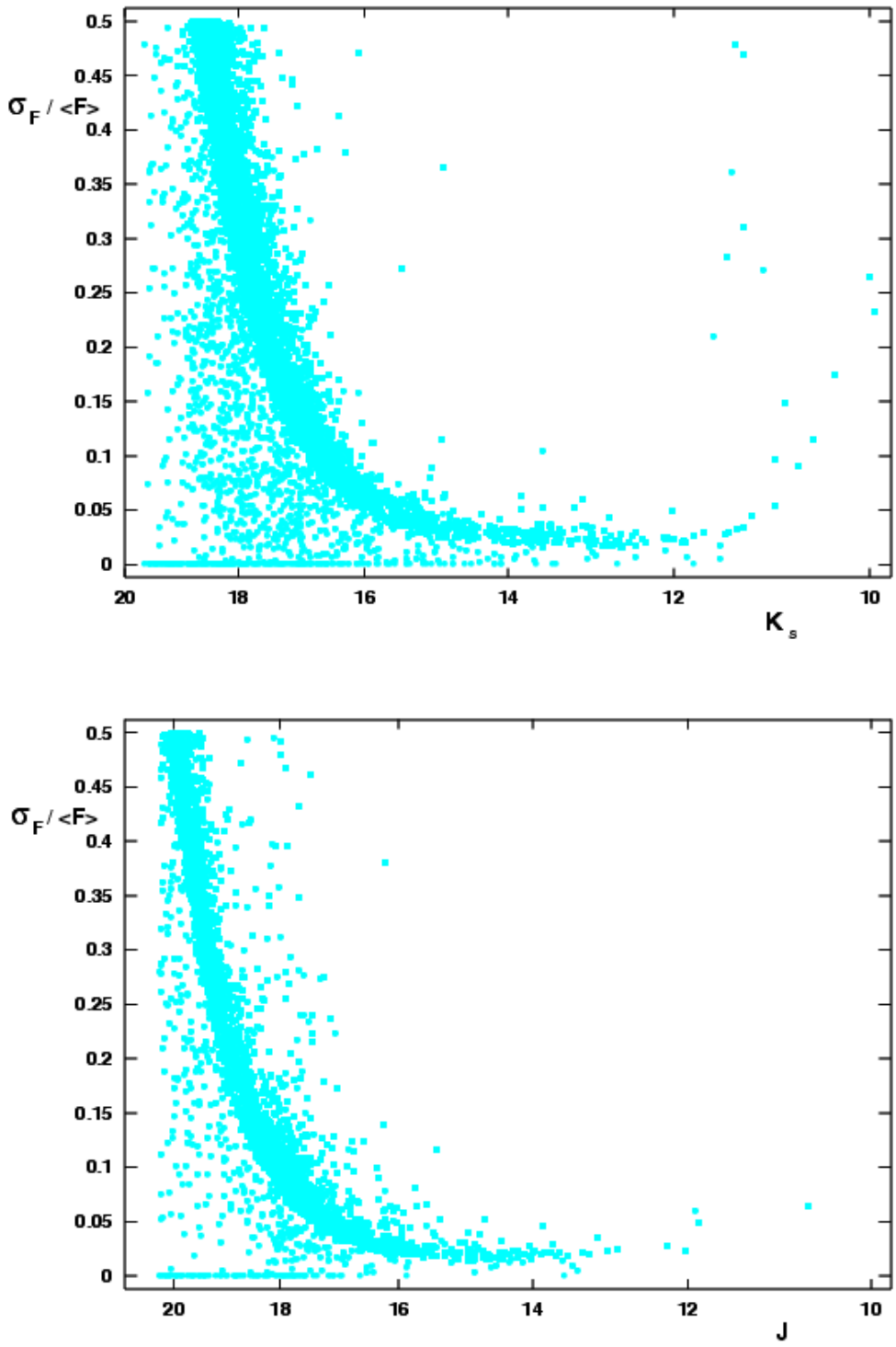

Figure 5.27: The flux dispersion σ_F, divided by the mean flux $\langle F \rangle$, along the light curves as a function of magnitude in K_s (top: B68) and J (bottom: SMC) bands. Each point represents the light curve of a star (before data cleaning).

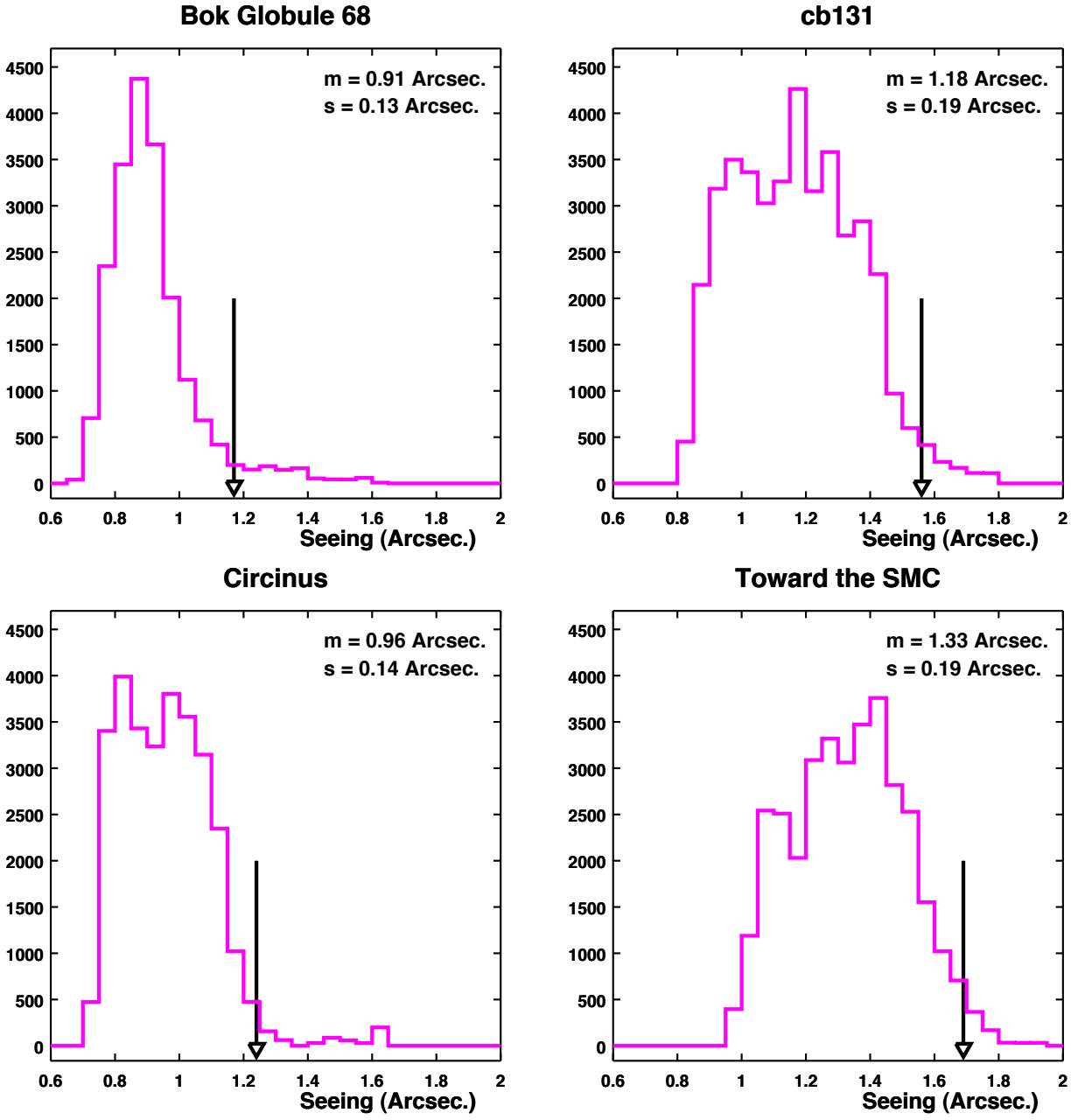

Figure 5.28: Filtering the best seeings. "m" and "s" are the mean value and dispersion of seeing distributions. The images with seeing larger than "m + 2s" are discarded from analysing process. The black arrows show the upper limit for each observed field.

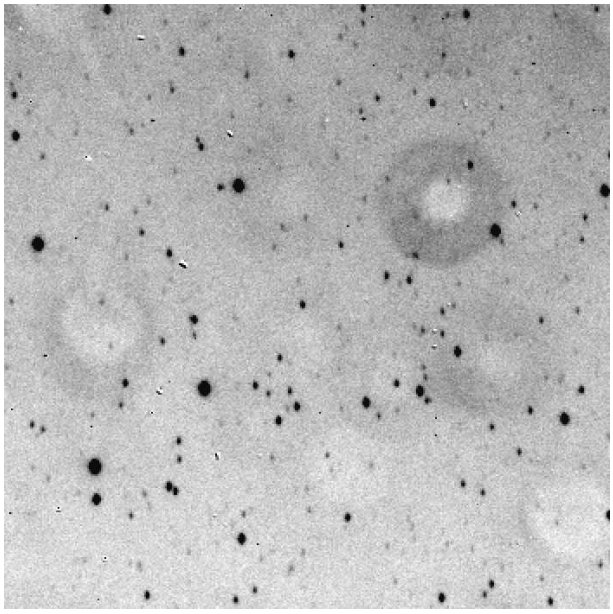

Figure 5.29: Stellar profiles are elongated vertically in this image. Such images are discarded.

Low Quality Images

One of the most important indicators of the image quality is the seeing parameter. With good (small) seeing conditions, the flux of the star is concentrated in few pixels, providing high signal to noise ratio per pixel. Inversely, in the case of poor seeing, we loose photometric precision since the flux is distributed in larger number of pixels, increasing the relative Poissonian fluctuation per pixel. The seeing distributions of both nights for all observed fields are represented in figure 5.28. The seeing conditions were better for B68 and Circinus. We discarded images with seeing exceeding the mean seeing by more than 2 standard deviations.

The software PEIDA that we used has the capability to produce synthesised images by reconstructing the stars PSF using the measured fluxes and PSF parameters. By subtracting a current image from such a synthesised image, we found that the images with elongated PSF are not measured properly. Figure 5.29 shows one of the images of Circinus with eccentricity 0.7. As the eccentricity is one of the PSF parameters, we discarded images with eccentricity larger than 0.55 for all fields as shown in figure 5.30.

Low Quality Measurements

We consider the variation of χ^2 with flux as shown in figure 5.31. Blue dots represent chi-squares of all measurements toward Circinus. We clearly see the increase of χ^2 for high fluxes. Besides, there is a χ^2-flux cross-correlation for flux > 5000 ADU. The correlation

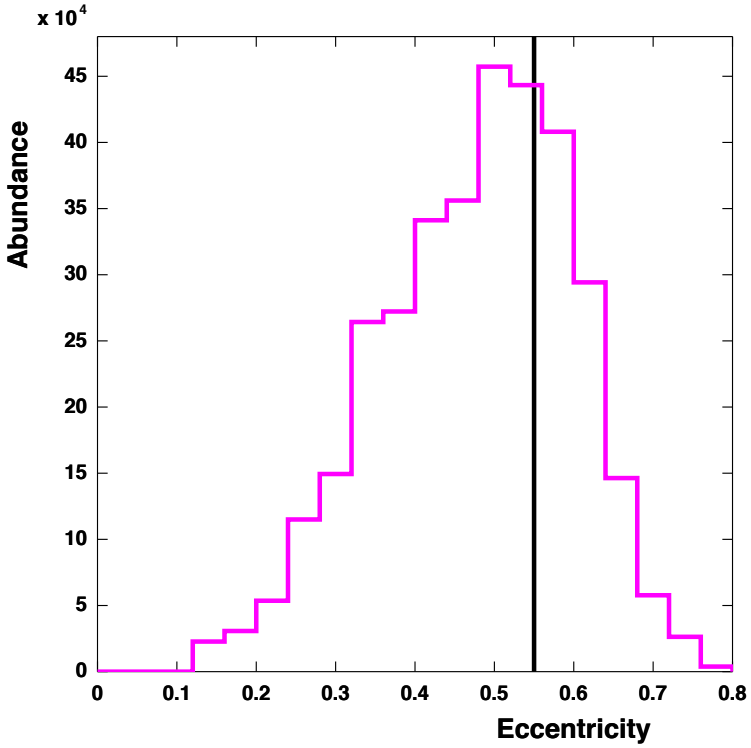

Figure 5.30: Distribution of the PSF eccentricity for all images taken from Circinus. Images with PSF elongation larger than 0.55 are discarded from analysing process.

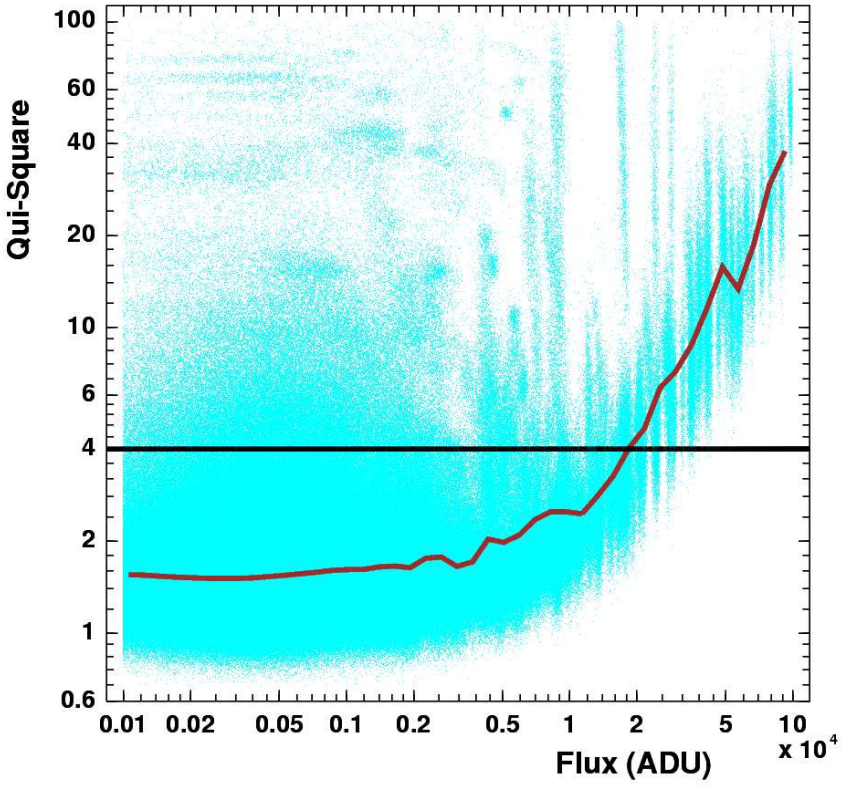

Figure 5.31: Blue dots show chi-square vs. flux for stars toward Circinus. Brown line shows the mean value of χ^2s. The upper limit on χ^2 is shown by the black line. Measurements with $\chi^2 > 4$ are discarded.

is probably due to the underestimated uncertainties in the χ^2 expression. As explained in previous section, systematic errors become dominant at higher fluxes. We discarded all flux measurements with $\chi^2 > 4$ for all directions.

Unusable Stars

All images have anomalies and distortions at borders. We defined a fiducial zone with margins of 100 pixels from the borders. By discarding stars located out of the fiducial zone, the edge distortions were avoided. As it is shown in figure 5.32, there are stars that cross the red line of the fiducial zone in different images and lose flux measurements. We keep the stars with a total number of measurements (within Fiducial zone) larger than 10 per night for the light curve analysis.

From figure 5.27 we decided to select stars with mean flux > 1000 ADU (corresponding to $J < 17.8$ and $K_s < 17.1$) to maintain a photometric precision better than $\sim 20\%$ in K_s band and $\sim 10\%$ in J band.

Flux Corrections

The PSF deviation from Gaussian induces flux versus seeing and flux versus background correlations for some light curves. We decided to apply flux corrections for light curves with large cross correlations. The correlation between flux and seeing is shown in figure 5.33 for all star fluxes of the SMC in different flux intervals. The flux is more correlated with seeing for fainter stars than for the brighter ones. The correlation tends to disappear for fluxes larger than 10000 ADU. To correct the fluxes of a light curve let's suppose F_i is the unbiased (or corrected) flux; according to figure 5.33, we assume the cross correlations are statistically linear and the correlated flux f_i is computed as:

$$f_i = F_i + a_s S_i + a_b B_i + c, \tag{5.9}$$

where S_i and B_i are the measured seeing and background repectively. a_s, a_b and c are constants. By applying the condition $\langle F \rangle = \langle f \rangle$ to the equation above we find the relation:

$$a_s \langle S \rangle + a_b \langle B \rangle + c = 0, \tag{5.10}$$

where $\langle S \rangle$ and $\langle B \rangle$ are the mean seeing and background along the light curve. We re-write the corrected flux as:

$$F_i = f_i - a_s(S_i - \langle S \rangle) - a_b(B_i - \langle B \rangle). \tag{5.11}$$

To compute a_s and a_b we consider that in an unbiased flux measurement, the flux has no cross correlation neither with the seeing nor the background. The cross-correlations

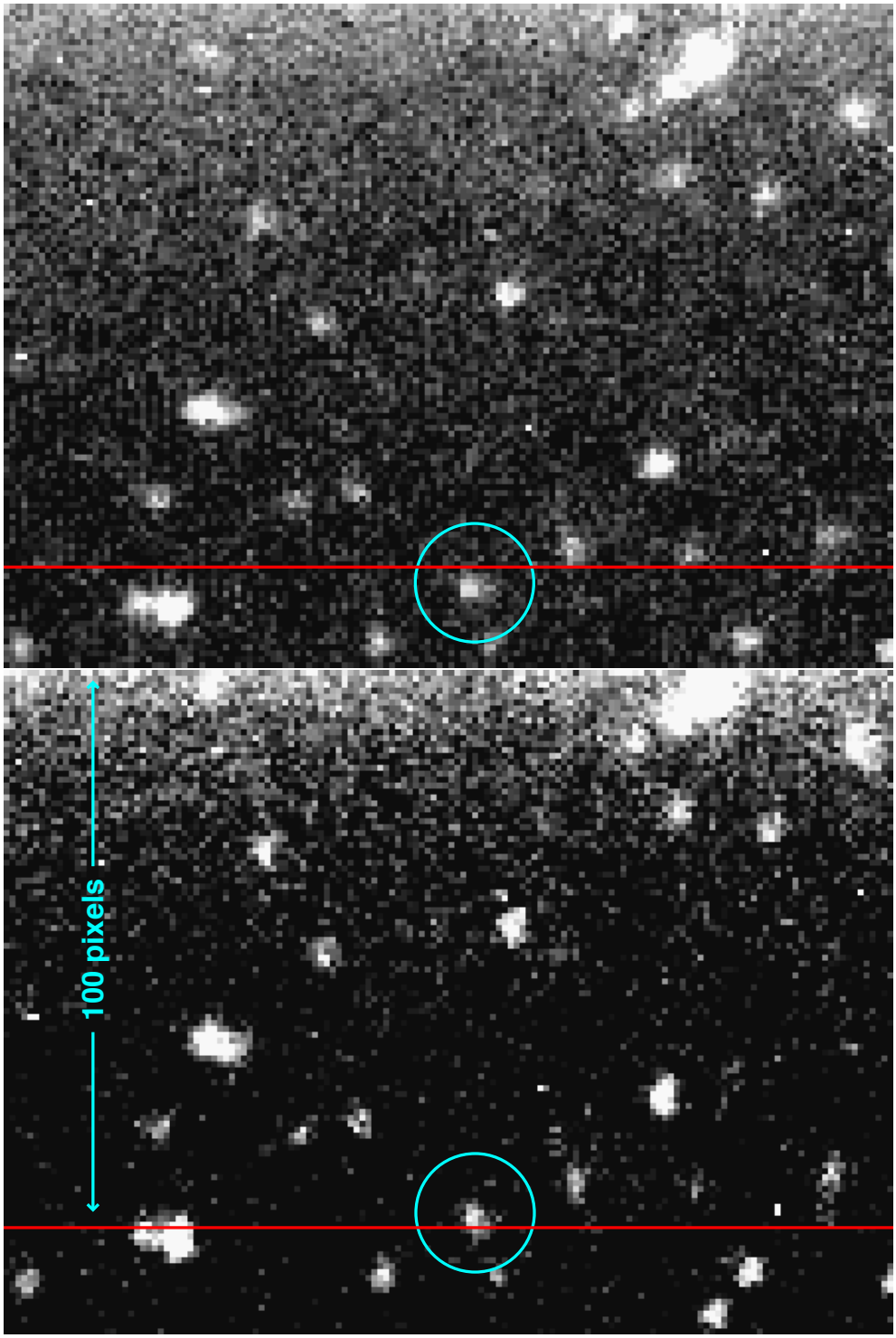

Figure 5.32: Some stars cross the Fiducial limits in some images. The Fiducial limit is given by the red line which is 100 pixels away from the image border. The figure shows the top part of two different images. The indicated star is located within the Fiducial zone at top panel and out of it at lower panel.

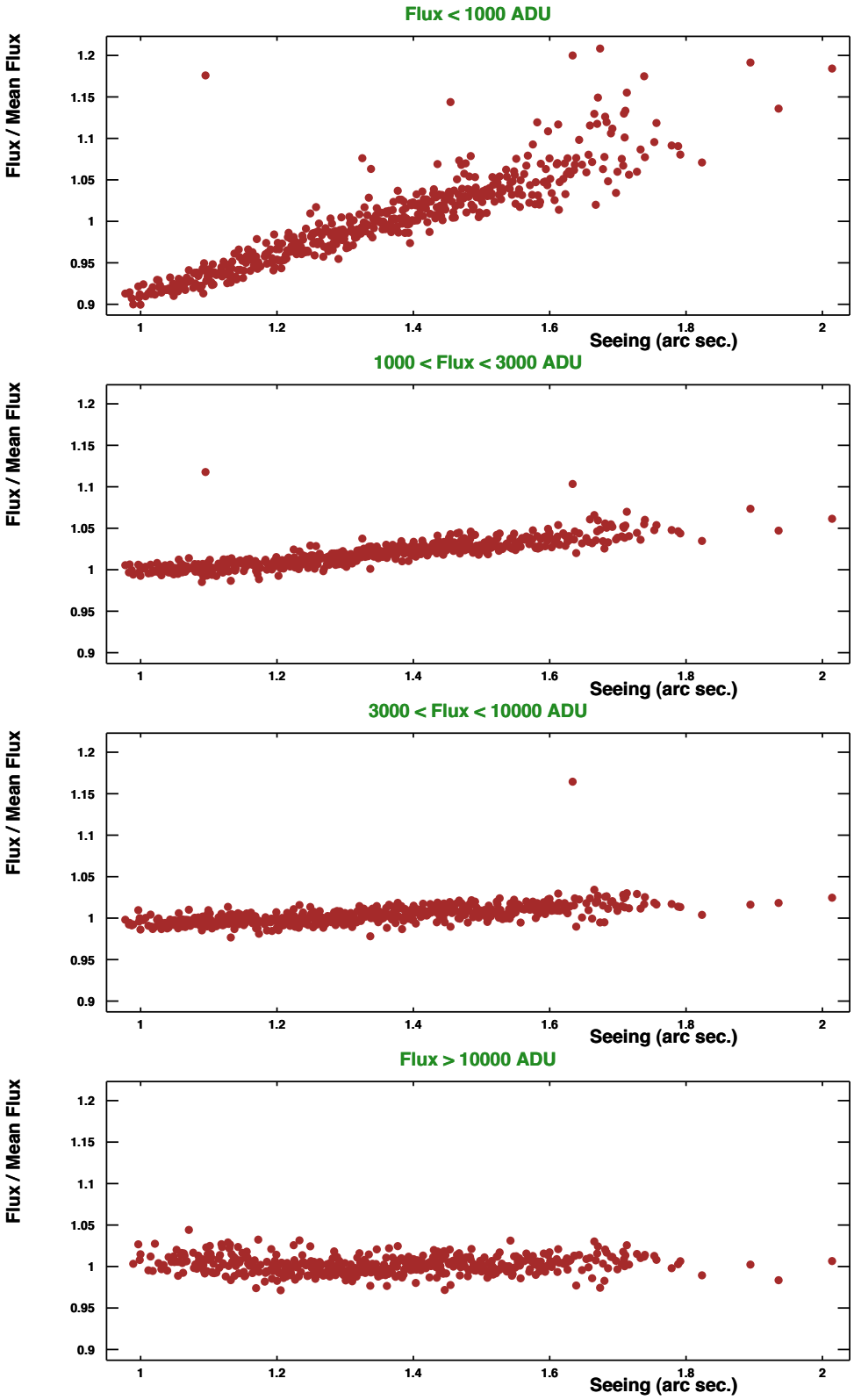

Figure 5.33: Profile of flux versus seeing for stars of the SMC. Each point is the average Flux / Mean Flux of stars within a given seeing bin of the profile. Flux of fainter stars show more correlation with seeing than brighter stars.

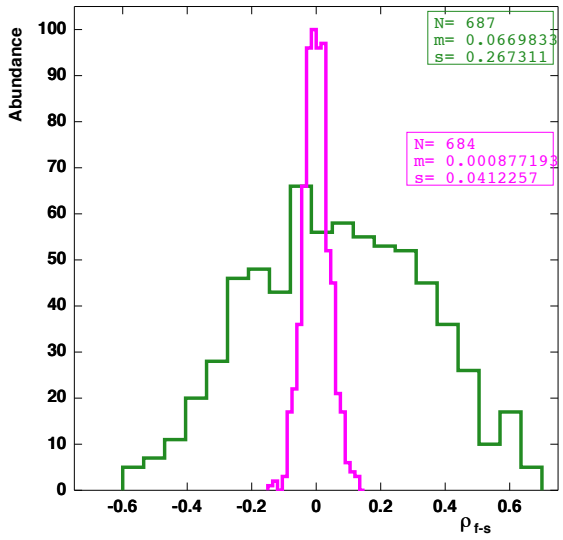

Figure 5.34: Cross-correlation of flux and seeing for stars of the SMC. The green curve belongs to the observed light curves. The magenta belongs to the corresponding simulated light curves (with no cross-correlations).

for the corrected flux versus seeing ρ_{F-s}, and corrected flux versus background ρ_{F-b} are given by:

$$\begin{aligned} \rho_{F-s} &= \frac{\langle (F_i - \langle F \rangle)\,(S_i - \langle S \rangle) \rangle}{\sigma_F\,\sigma_s}, \\ \rho_{F-b} &= \frac{\langle (F_i - \langle F \rangle)\,(B_i - \langle B \rangle) \rangle}{\sigma_F\,\sigma_b}, \end{aligned} \tag{5.12}$$

where σ_F, σ_s and σ_b are the dispersions of the corrected flux, the seeing and the background respectively. Requiring no cross correlations for the corrected flux gives:

$$\begin{aligned} \rho_{F-s} &= 0, \\ \rho_{F-b} &= 0. \end{aligned} \tag{5.13}$$

We substitute relation (5.11) to equations (5.12) and derive the constants which depend on the initial flux dispersion σ_f:

$$\begin{aligned} a_s &= \frac{\sigma_f}{\sigma_s}\,\rho_{f-s}, \\ a_b &= \frac{\sigma_f}{\sigma_b}\,\rho_{f-b}. \end{aligned} \tag{5.14}$$

We derive the corrected flux from expression (5.11). We do not correct every light curves; for each star we generated a uniform light curve with the same flux average and dispersion

	SMC	B68	cb131	Circinus
central gas density	-	$2.61 \times 10^5 cm^{-3}$	$1.8 \times 10^5 cm^{-3}$	
centre-to-edge density contrast	-	16.5	140.	
central column density N_l	-	$2.59 \times 10^{22} cm^{-2}$	$5.8 \times 10^{22} cm^{-2}$	
distance of nebula	-	80 pc	190 pc	170 pc
Fresnel Radius $R_F = \sqrt{\lambda z_0 / 2\pi}$	-	926 km	1420 km	1340 km
minor axis of nebula	-	17000 AU	24000 AU	complex
distance of the sources	62 kpc	$\sim 8\ kpc$	$\sim 7\ kpc$	$\sim 7\ kpc$
number of detected stars	5042	9599	9084	5249
number of monitored stars	691	1114	2779	913
fraction of monitored stars	14%	12%	31%	17%
magnitude of monitored stars	$J < 17.8$	$K_s < 17.1$	$K_s < 17.1$	$K_s < 17.1$
fraction of stars behind dust	0%	46%	64%	-
mean number of measurements/star	980	2013	629	888
accepted light curves with R	< 1.4	< 1.6	< 1.6	< 1.6

Table 5.4: Information on the targets and data reduction results. The data on the nebulae are taken from [Hotzel et al. (2002)] for B68 and from [Bacmann et al. (2000)] for cb131. The typical distance of the sources in the Galactic plane are taken from [Georgelin et al. (1994)] and [Russeil et al. (1998)].

as the observed light curve. We computed the cross correlations between the seeing (and background) and the *simulated* light curves (figure 5.34). The star by star distribution of this correlation is shown by the pink curve in figure 5.34. The green curve shows the correlation distribution of the *observed* flux and seeing (ρ_{f-s}). The flux correction is applied for a light curve if its absolute value of ρ_{f-s} (or ρ_{f-b}) exceeds that of the simulated curve (pink curve) by more than one standard deviation.

5.4.2 Selecting the Most Variable Light Curves

Table 5.4 shows the results of the general data cleaning. Apart from cb131, less than 17% of stars with sufficient number of measurements satisfied the quality requirements. The observations in K_s band are performed toward dark nebulae. In general, we can clearly decide if a star is located behind the nebula or not. We use the latter stars as the control stars (located in control region). Their light is not affected by gaseous medium and no scintillation is expected. We could define such a control region in B68 and cb131 as shown in figure 5.35. Circinus is a diffuse filamentary nebula for which we could not clearly separate the two regions

After the cleaning and quality selection procedures, we re-plot the relative dispersion vs. magnitude diagram in two bands as illustrated in figure 5.36. Top panel shows the stars

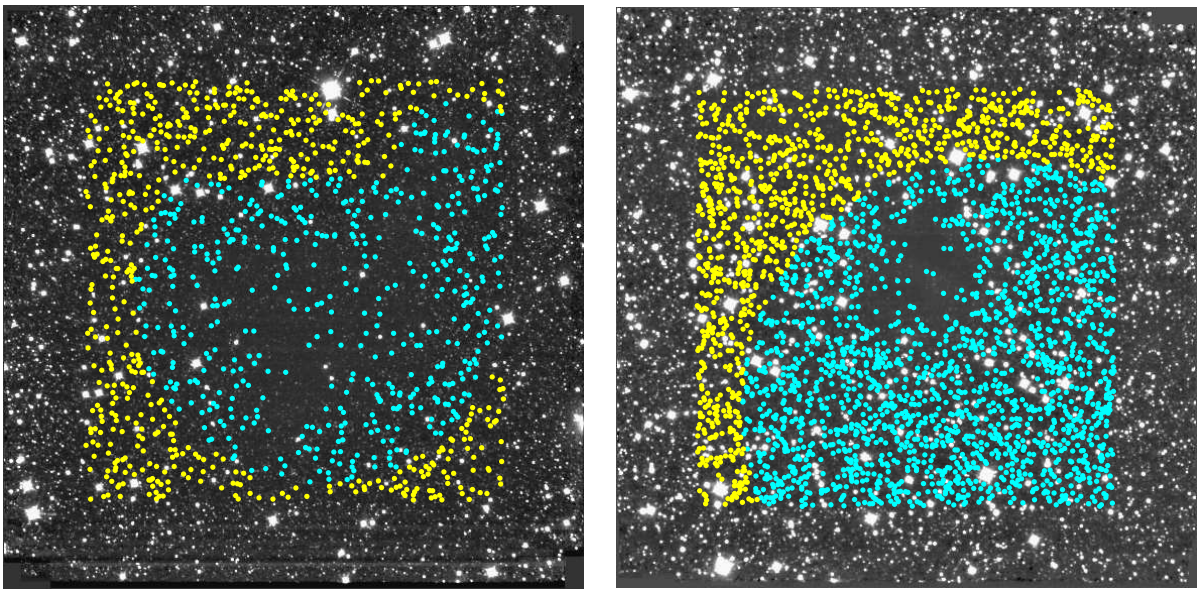

Figure 5.35: The control regions (yellow dots) and the search regions (blue dots) towards B68 (left) and cb131 (right).

toward B68 in the control region (black) and for stars located behind the cloud (blue). Most of the anomalies are removed and the precision on the flux measurement for a given (apparent) magnitude is not affected by the absorption. We consider the lower envelope of each distribution as the best precision we can achieve.

We used a simple statistical criterion to select the most variable light curves. The method, described in the following section, is sensitive to any kind of fluctuations whether it is intrinsic, due to light propagation in space or produced by artefacts.

Internal Dispersion

The time interval between two successive measurements is $\sim$ 15 seconds. Any fluctuation happening with time scale less than 15 seconds is impossible to detect by our observation and is smoothed in data[11]. What we can investigate is comparing the global variation of the light curve (flux dispersion σ_F) to the point to point flux variation of the light curve. We characterise the latter type of variation by the internal dispersion, σ_{int}, computed from the difference between a flux and the interpolation of its previous and next fluxes as

[11] Anyway, we do not expect to detect scintillation by such short time scale according to the simulation results.

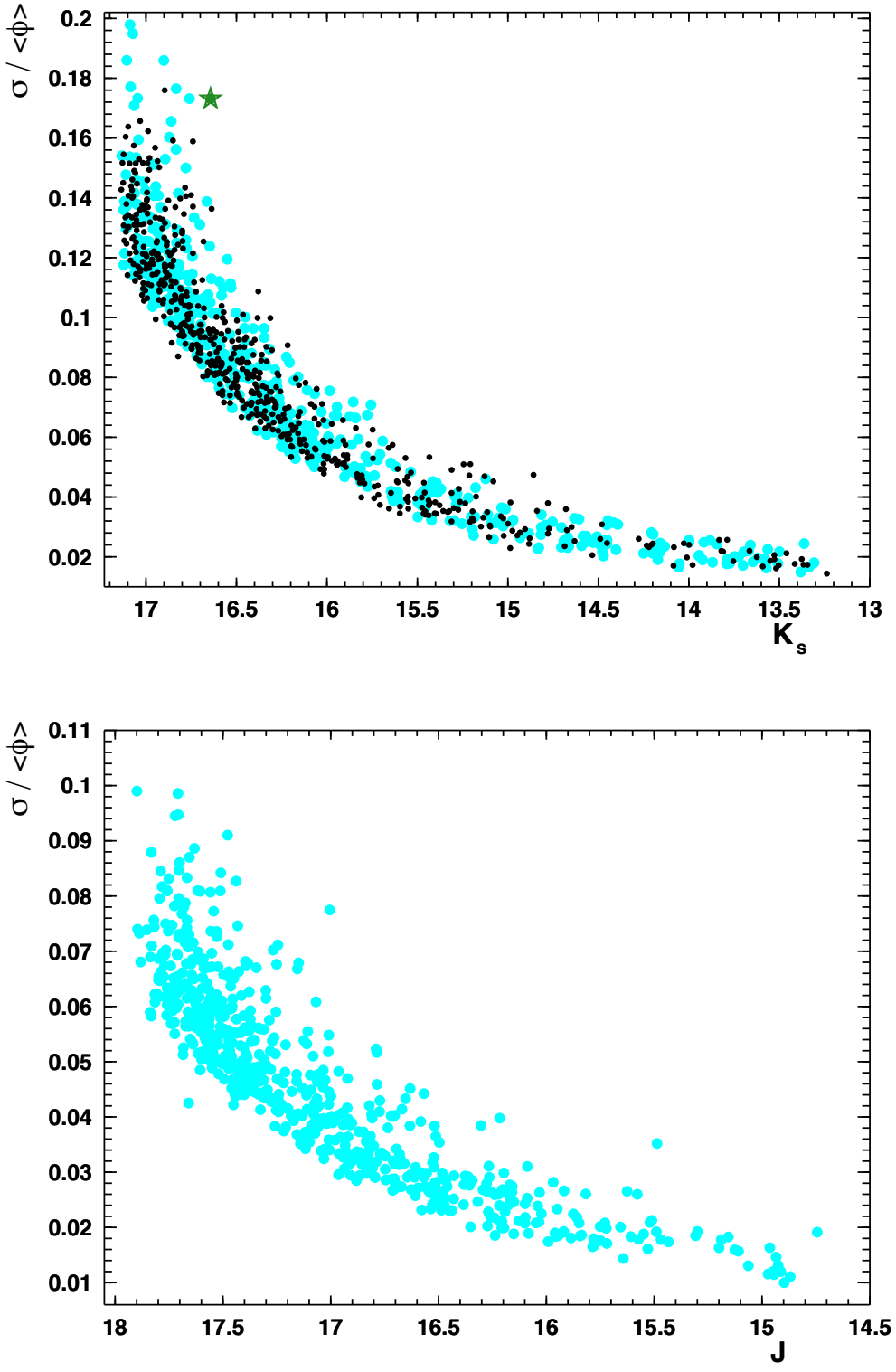

Figure 5.36: The precision diagram after data cleaning. This figure is the same as figure 5.27 after removing the low quality measurements and the faint stars. Blue points at top panel are stars located behind the B68 nebula and black dots are the control stars. The green star is our candidate to scintillation. The diagrams toward cb131 and Circinus have similar behaviour. The lower panel is the precision diagram of stars toward the SMC.

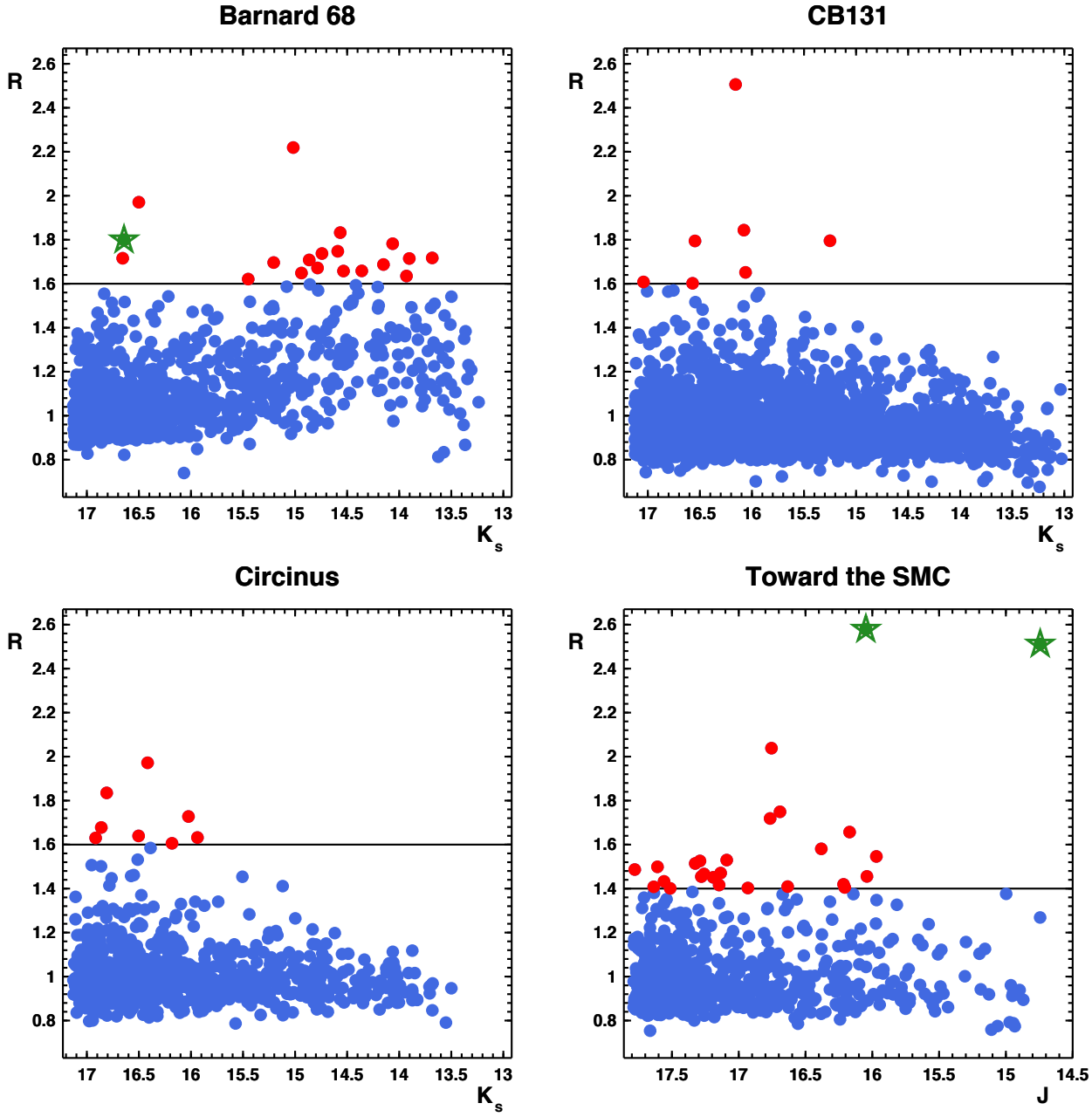

Figure 5.37: $R = \sigma_F/\sigma_{int}$ versus magnitude of the light curves of the monitored stars. The red dots correspond to the most variable light curves. The green stars indicate two detected periodic variable objects toward SMC and our scintillation candidate toward B68.

follows:

$$\sigma_{int} = \sqrt{\frac{1}{N-2}\sum_{i=2}^{N-1}\left[F(t_i) - \left(F(t_{i-1}) + [F(t_{i+1}) - F(t_{i-1})]\,\frac{t_i - t_{i-1}}{t_{i+1} - t_{i-1}}\right)\right]^2}, \quad (5.15)$$

where N is the number of flux measurements for the given light curve. $F(t_i)$ is the flux measured at time t_i. For a simulated uniform light curve (constant flux) $F(t_i)$ is randomly generated from a Gaussian distribution with mean value $\langle F \rangle$ and dispersion σ_F; as a rough estimate, the expression under summation in equation (5.15), which represents the mean point to point variation is of order of $\sqrt{2}\sigma_F$. This gives a typical ratio $R = \sigma_F/\sigma_{int} \simeq 0.7$ for uniform light curves. In contrast, the mean point to point variation is expected to be small compared to the global variation for a light curve with fluctuations longer than a few minutes, giving a typical $R > 1$.

Figure 5.37 shows R versus magnitude for the light curves of the four observed fields. Many stars have ratio R larger than 0.7-0.8 but it does not infer necessarily that they are variable. Other statistical or systematical uncertainties cause larger R than simulated from uniform light curves. Let's $F^{sim}(t_i)$ be the simulated flux from a stable star at time t_i. To take into account the true point to point variations of the observed light curve into the simulated ones, we construct $h^{sim}(t_i)$ as:

$$h^{sim}(t_i) \;=\; F^{sim}(t_i) + F(t_i) - \langle F \rangle. \quad (5.16)$$

Through this relation, we enter all the fluctuations of the observed flux (induced by systematic errors) to the simulated flux. $h^{sim}(t_i)$ will have the same auto-correlation as the observed light curve, $F(t_i)$. The computed R values for $F^{sim}(t_i)$, $h^{sim}(t_i)$ and $F(t_i)$ are shown in figure 5.38 for the SMC. The simulated distribution obtained with h^{sim} (red circles) looks closer to the real distribution (black dots). However, there are still light curves with larger R showing significant deviations from the simulated stable stars which should be studied in details to discriminate between real variabilities and the artefacts.

5.4.3 Detection of the Cataloged Variable Stars

We considered the variable light curves with $R > 1.6$ for the nebulae and $R > 1.4$ for the SMC. To check the relevance of the criterion we used (based on the ratio $R = \sigma_F/\sigma_{int}$), we have searched for the existing variable stars in our observed fields. There are no cataloged variable objects in the nebulae fields, but the CDS and EROS catalogs [Tisserand et al. (2007)] contain two cepheids toward the SMC that are selected by our analysis. They are represented in figure 5.37 by two green star markers.

The light curve of one of those detected variables in EROS is plotted in figure 5.39. The

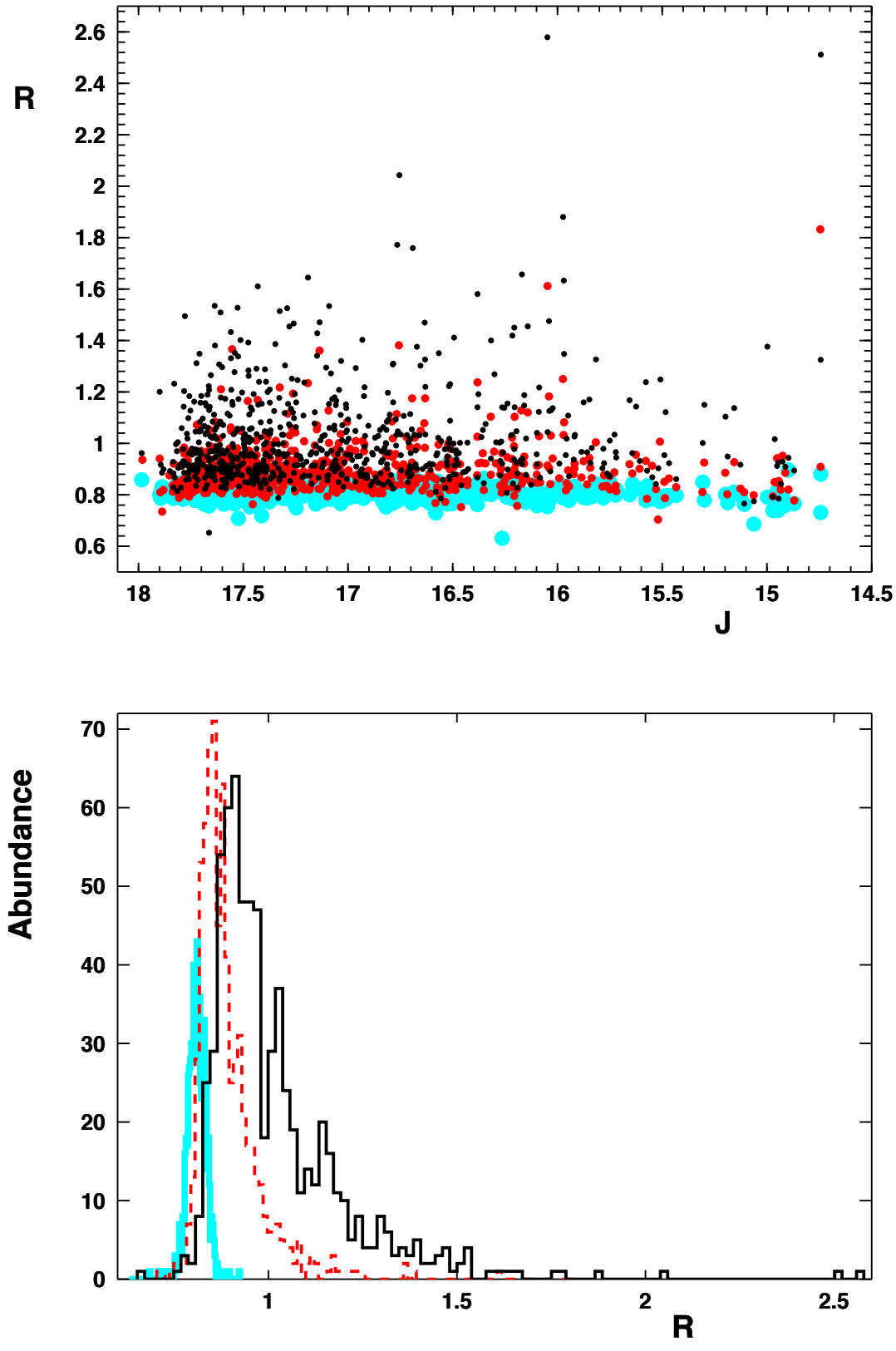

Figure 5.38: Top: R values for randomly generated uniform light curves (blue), for simulated light curves taking into account the observed point to point variations (red) and observed light curves (black). Bottom: the corresponding R distributions. Mean values are $0.8, 0.9$ and 1 respectively.

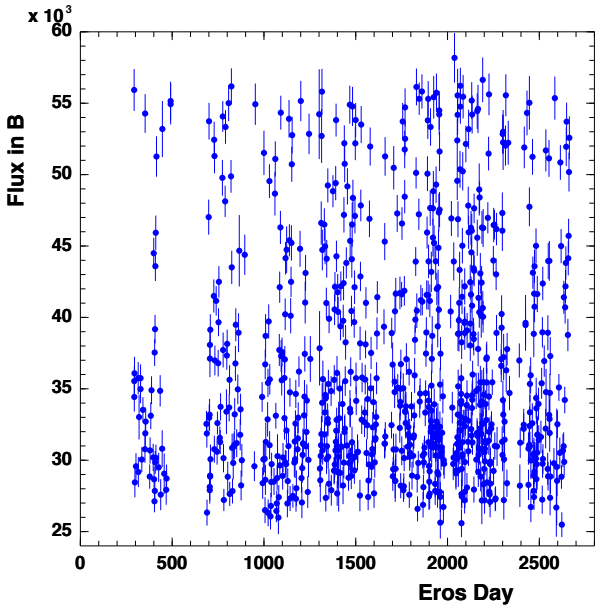

Figure 5.39: Light curve of a cepheid from EROS SMC database. The data should be folded according to the period to obtain the shape of variation within the complete period (phase diagram).

light curve has been measured in EROS during more than five years. To show the variation in a complete period (phase diagram) we fold the light curve according to period T of the cepheid by using the relation:

$$t_{fold} = t_{obs} - \left[\frac{t_{obs}}{T}\right] T, \tag{5.17}$$

where t_{fold} and t_{obs} are the folded time and the observation time respectively. $[\,]$ takes the integer part of the argument. To compare our data with these phase diagrams, we fold our light curves according to the period. This requires a careful synchronisation of the NTT and EROS observation times. The origin of EROS observation was on 2447892.5 Julian day and observation with NTT started on 2453912.85109 Julian day.

The first detected cepheid shown on figure 5.40 is $HV1562$ (α =13.1550°, δ = -72.8272° J2000) with mean magnitude J = 14.7 and periodicity of 4.3882 days. The red and blue points are folded light curves from the EROS SMC database in red and blue passbands respectively ([Tisserand et al. (2007)], [Hamadache et al. (2006)], [Rahal 2009]). The black points are our folded light curve in IR. Our measurements were precise enough to detect the rapidly ascending phase of $HV1562$ during the second night.

The second detected cepheid is the EROS object (α = 13.2250°, δ = -72.7951° J2000)

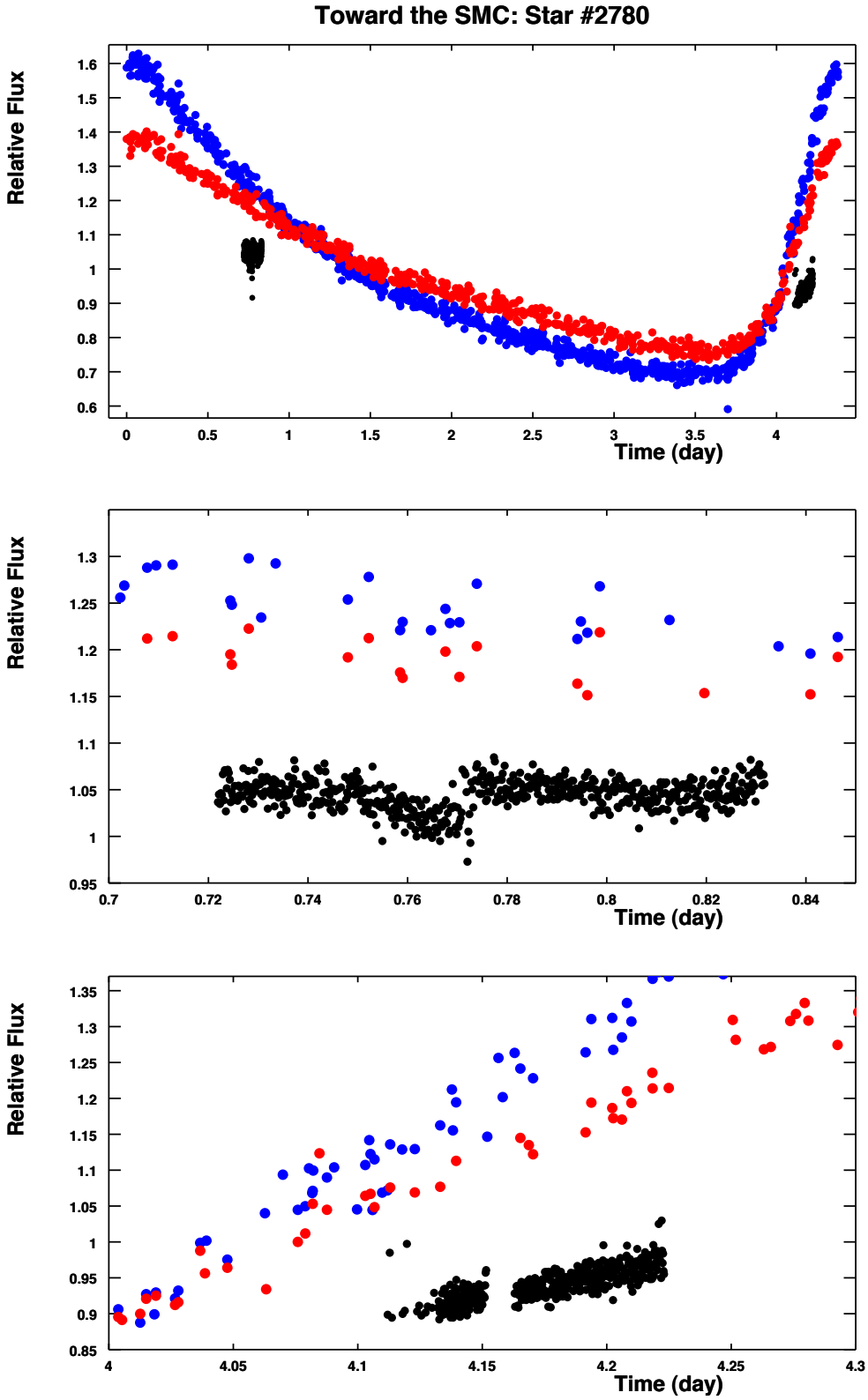

Figure 5.40: The EROS phase diagram of cepheid HV1562 in B_{EROS} and R_{EROS} passbands combined with our NTT observation in J band (black dots). The two lower panels show details of the phase diagram around our observation time.

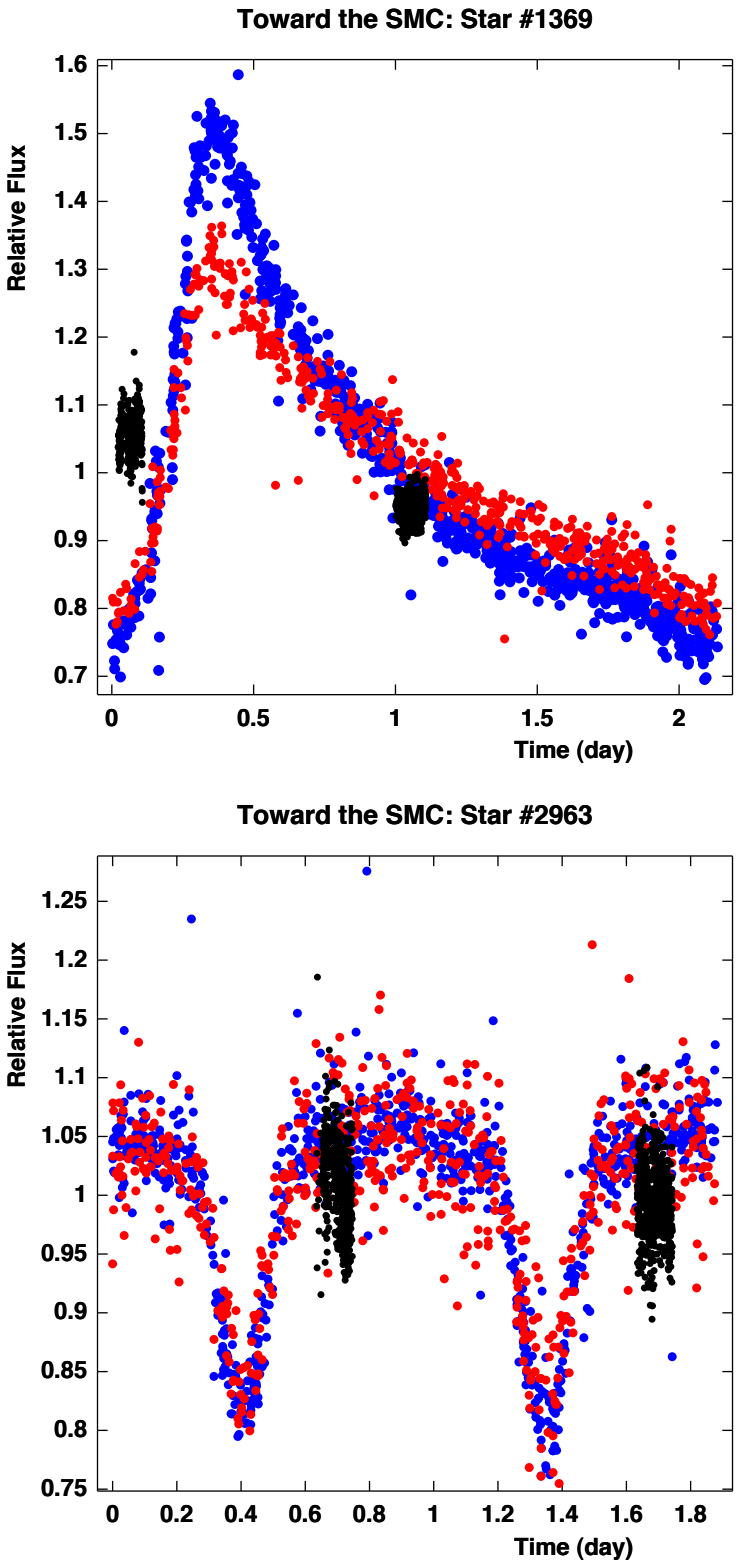

Figure 5.41: The phase diagram of the EROS object $(13.2250°, -72.7951°)$ (top) and the eclipsing binary OGLE SMC-SC6 148139 (Bottom) in B_{EROS} and R_{EROS} passbands combined with our NTT observations in J (black dots).

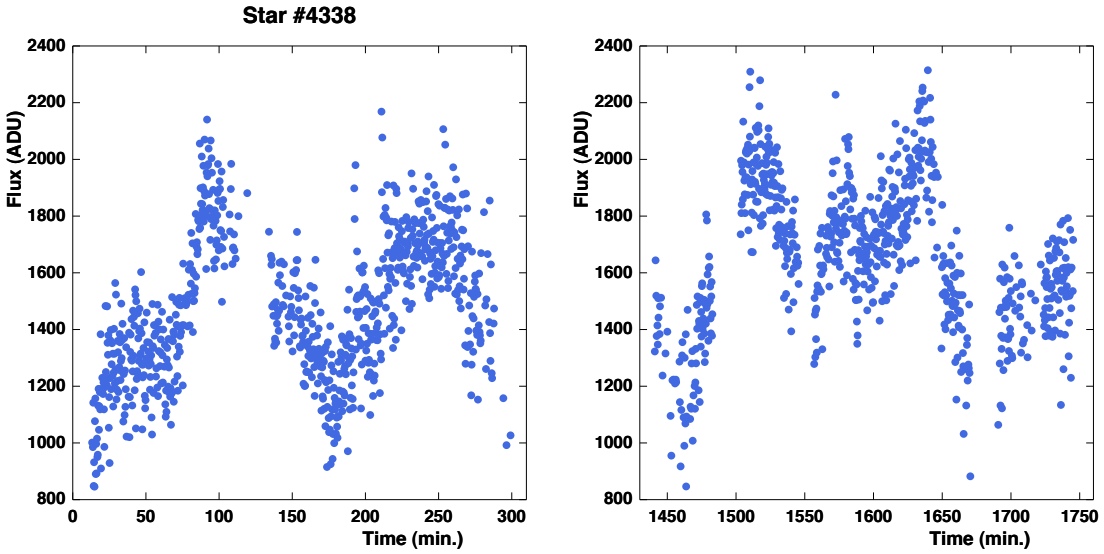

Figure 5.42: Light curve of the scintillation candidate. The dispersion to mean flux ratio (modulation index) is 0.17. The mean flux during both nights is 1566 ADU equivalent to K_s = 16.6 magnitude. Since the star is behind the cloud, its light is obscured by dust.

with mean magnitude J = 16.03 and periodicity 2.13581 day. (figure 5.41 up). The OGLE variable star catalog contained a third variable star in the SMC, an eclipsing binary, which has not been detected by our algorithm. It is OGLE SMC-SC6 148139 (α = 13.1446°, δ = -72.8333°, J2000) with mean magnitude B = 16.5 (figure 5.41 down). According to the figure, our observation were done during the plateau of the light curve and therefore could not be detected as a variable object.

One difference between the light curves of any variable star and the scintillation effect is that scintillation effect shows stochastic variations characterised by a time scale which depends on the wavelength. By doing multi-wavelength observations one should be able to distinguish scintillation effects from other variability causes.

5.4.4 A Scintillating Star?

After checking the sensitivity to variable light curves, we go back to variable R plotted in figure 5.37 to search for scintillation effects. We have checked all the light curves corresponding to the red points individually[12]. We found many similar anomalies. We explain some of them for each field.

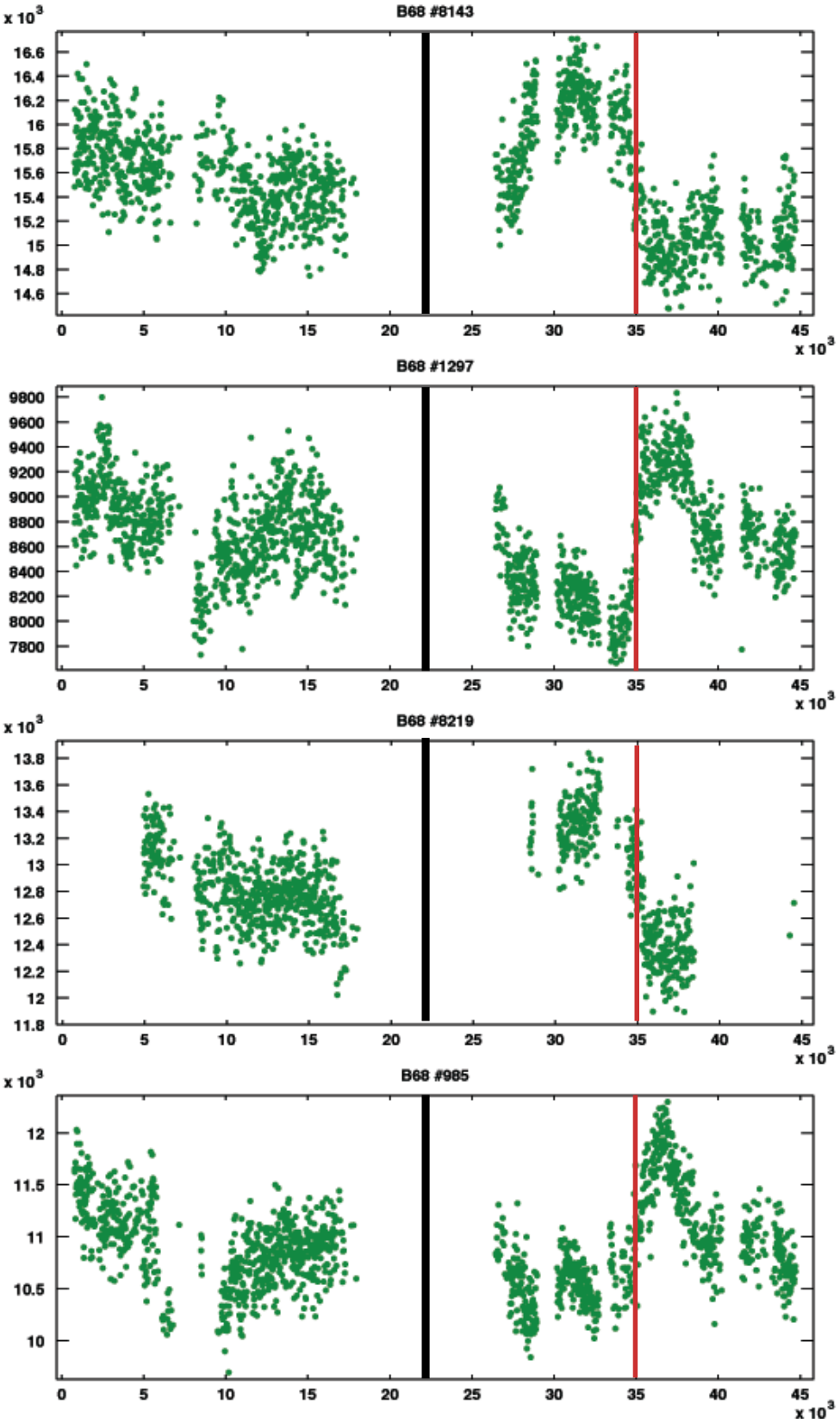

Figure 5.43: Light curves of four stars observed toward Barnard 68 nebulae. Vertical and horizontal axes are flux (ADU) and time (s). The fast drop/rise of flux at the second night (around the red line) is correlated with the meridian transition of the nebulae occurring around 35000 s. Times are shifted in the second night for better visualisation.

B68

- We found similar fluctuation patterns especially at the second night for many of the fluctuating light curves of B68. In figure 5.43 we show four typical light curves. Large variations are induced by sudden drop or rise of flux at the same time for all light curves at the second night. We found that this happened during the meridian transit. Therefore, the large flux dispersions for these kinds of light curves are probably due to the mechanics of the telescope that impacts the optical system. 12 of the selected top 19 light curves from 1114 stars shown in figure 5.37 suffer from this problem.

- The flux of 2 other were correlated with the chi-square of the PSF fit.

- 2 stars have very near neighbours causing blending effect, one star has a flux peak caused by the perturbation of an emitting pixel located within the star PSF.

- One star did not contain enough measurements.

Only one star remains with unexplained significant fluctuations. It is located behind the cloud and its light curve is shown in figure 5.42. It shows relative variations of more than 50% during both nights, which is significant. Fluctuations happen in scale of order of 100 min. (about 2 hours). Two images taken at the time of the star minimum and maximum fluxes are shown in figure 5.44. The variation of light intensity is clearly visible in these images.

cb131

From 2779 monitored stars toward cb131, we also visually inspected the 27 top light curves of figure 5.37. 23 of these variable light curves reveal the same variation pattern during the first night observation. Their typical behaviour is shown in figure 5.45. The main contribution to the flux dispersion is due to the first night curves. We found that the fluxes were systematically correlated to background variation, despite the corrections applied to the flux. These residual correlations are not linear (figure 5.48), and could not be corrected by the procedure discussed in section 5.4.1.

- Two light curves also show residual non-linear correlations with seeing at second night.

- Another one has a dead pixel within the star PSF.

- The last one did not show significant variation during the nights, but only a flux step from the first to the second night. It may be a variable object which is not cataloged yet, but it is not compatible with a scintillation signal.

[12]For cb131 and Circinus we extended this visual inspection to light curves with $R > 1.4$.

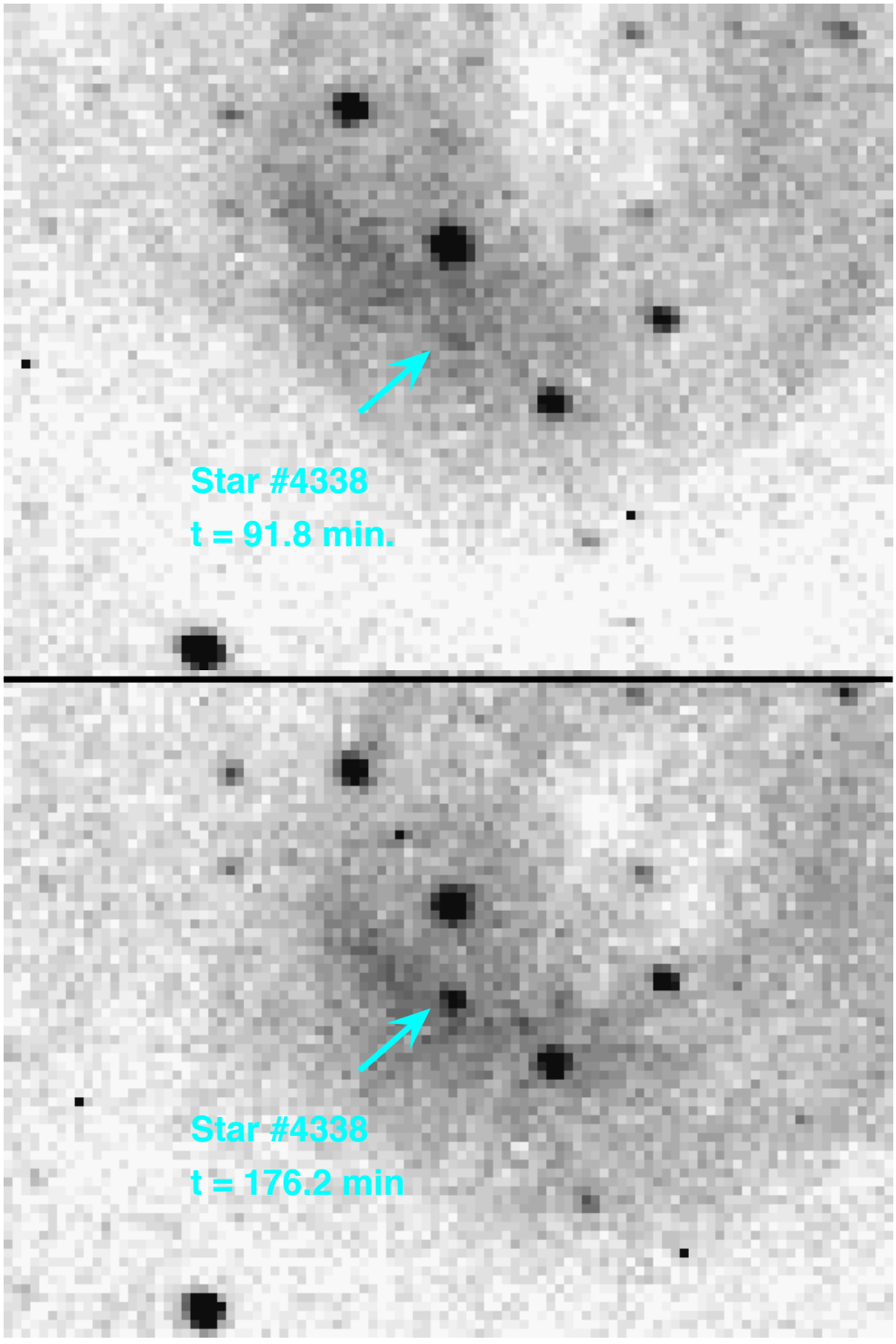

Figure 5.44: Light intensity fluctuation for the scintillation candidate. The star at its minimum and maximum intensities are shown at top and bottom images. To improve the visibility, five images around the minimum and five around the maximum have been co-added.

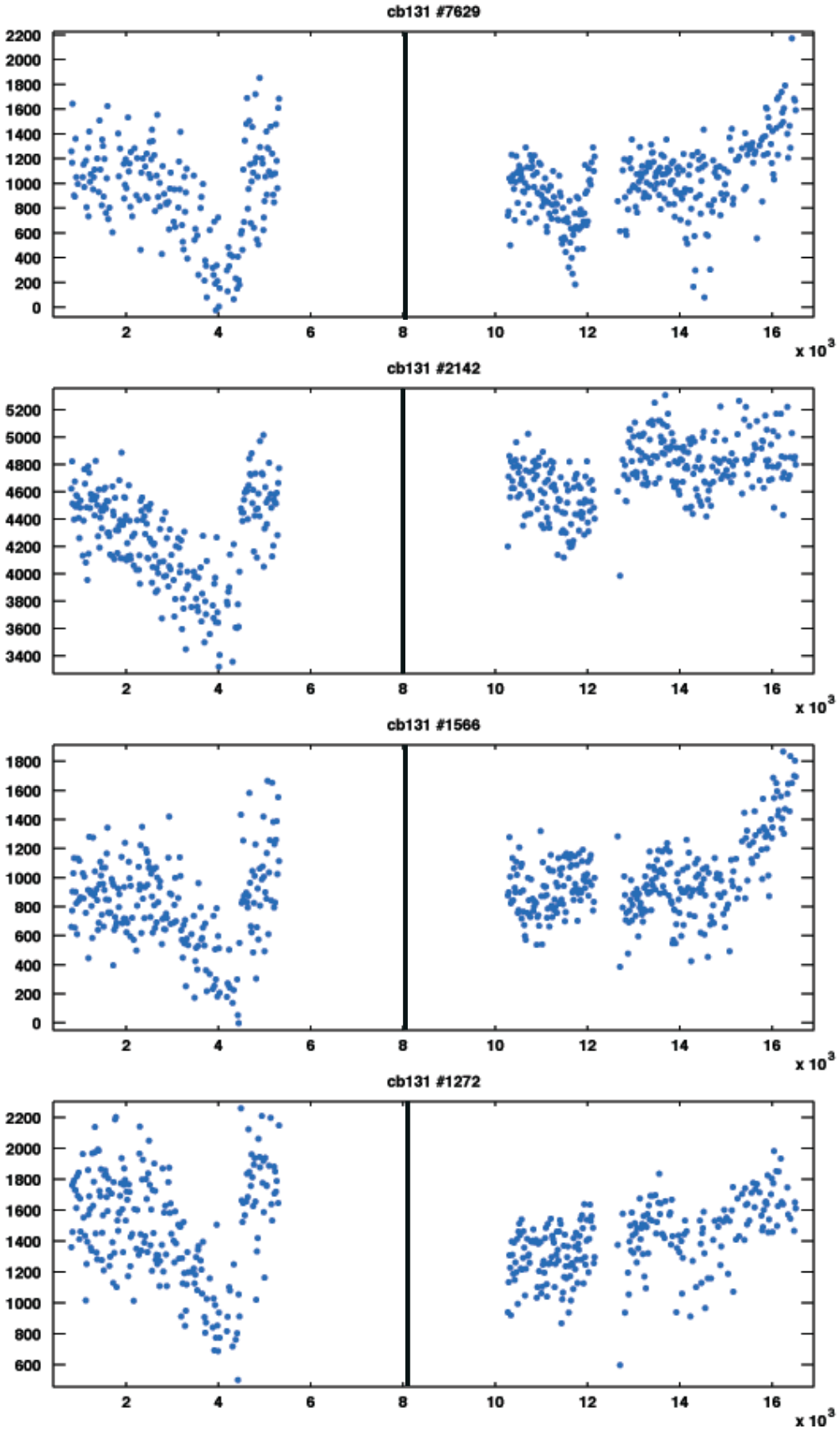

Figure 5.45: Four light curves of cb131. Flux is non-linearly correlated to the background at first night. Times are shifted in the second night for better visualisation.

Circinus

From 913 monitored star of Circinus, we selected the first 15 most variables.

- 8 light curves were blended[13] with the flux of close neighbours.
- 3 light curves were disturbed by light emitting pixels.
- 4 light curves suffered from residual flux-background or flux-seeing non-linear correlations.

Some light curves are shown in figure 5.46. The effect of the emitting pixel is shown in figure 5.47.

SMC

691 stars satisfied the cleaning filters. We selected the 15 most variable from figure 5.37. Apart from the two detected cepheids,

- 8 light curves are correlated with seeing (see figure 5.49).
- 2 light curves are correlated with the background.
- Another couple are affected by blending effect (see figure 5.50 and light curves of figure 5.51).
- The last one has flux vs. chi-square correlation.

Summary

We found the cataloged variable stars plus only one star located behind the nebula B68 as a candidate for scintillation effect. For all the other stars, the observed fluctuations in the light curves are due to flux correlation with other PSF parameters, blending or defects on IR detector.

A definitive conclusion on the scintillation candidate would need complementary multi-epoch and multicolour observations, but the hypothetic turbulent structure possibly responsible for scintillation has probably moved from the line of sight since the time of observations, considering its typical size. Nevertheless, re-observing this object would allow one to check for any type of known variability. Considering the small time scale (less than three hours) and the large amplitude fluctuations, a flaring or eruptive star may be suspected, but probably not a spotted star or an effect of astroseismology. An important result comes from the rarity of such fluctuating objects: There is no significant population of variable stars that can mimic scintillation effects, and the future searches should not be overwhelmed by background of fakes.

[13] Blending happens when the angular separations of neighbouring stars are so small that stellar lights are mixed through photometry procedure.

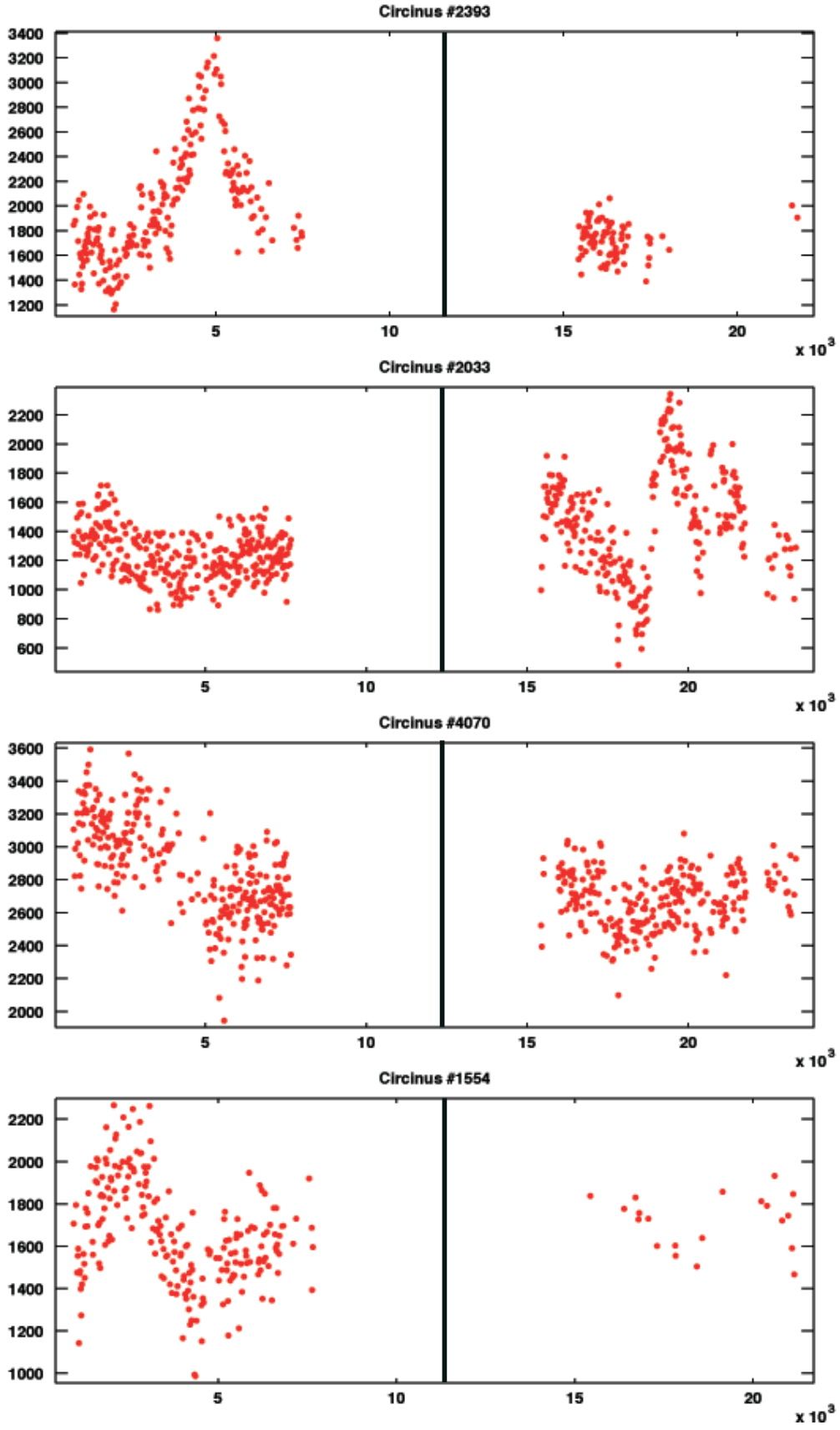

Figure 5.46: From top: first, second and forth light curves are contaminated by light emitting pixels. The third light curve is affected by the flux of a neighbouring star at second night. Vertical and horizontal axes are flux(ADU) and time(s). Times are shifted in the second night for better visualisation.

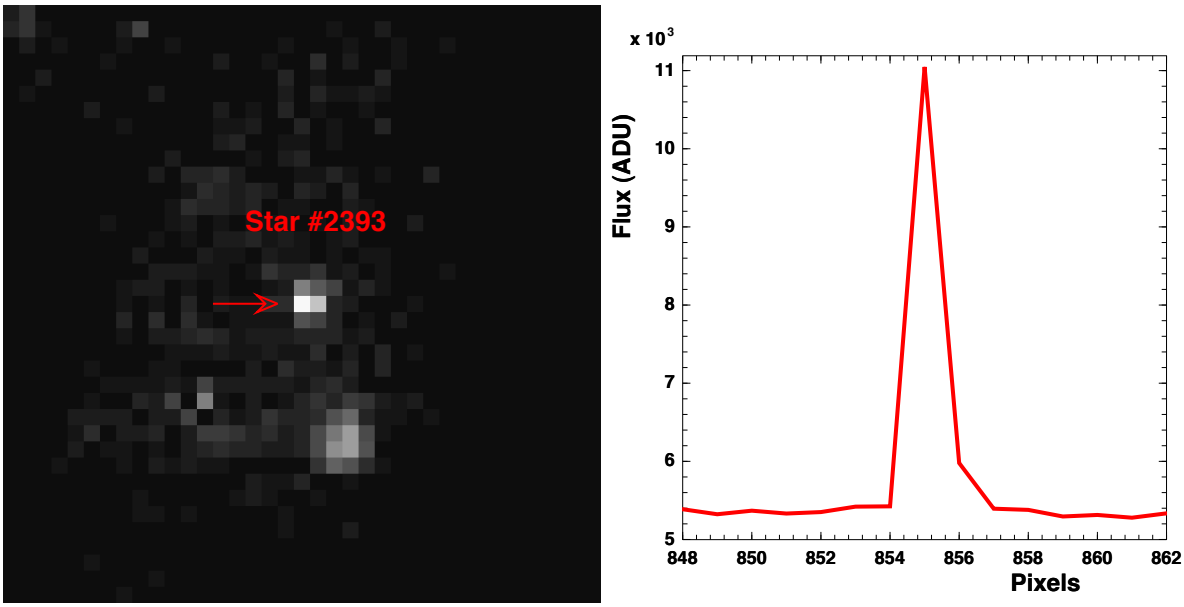

Figure 5.47: Left: a light emitting pixel inside the star PSF. Right: high rise in flux is artificially induced by the hot pixel.

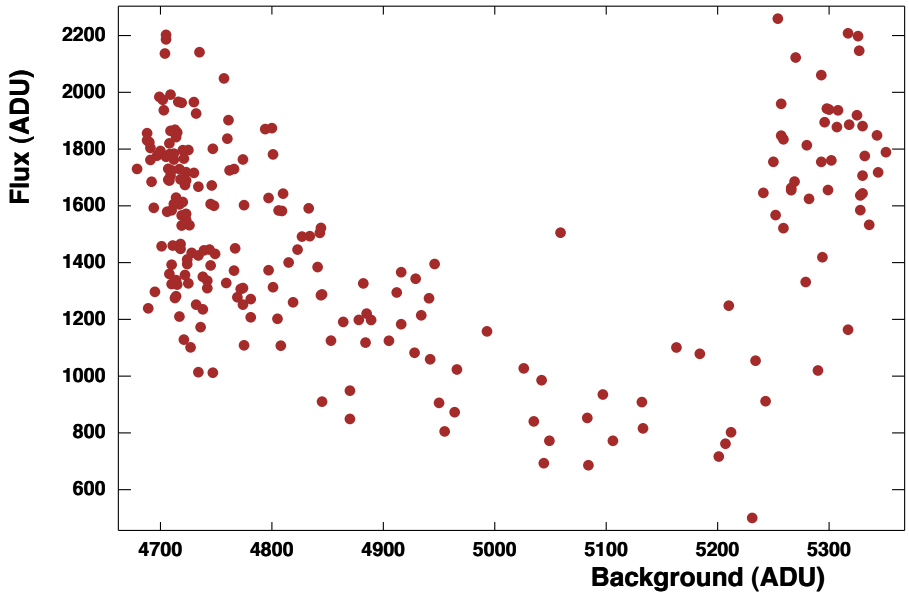

Figure 5.48: A typical non-linear flux-background correlation for a light curve from cb131.

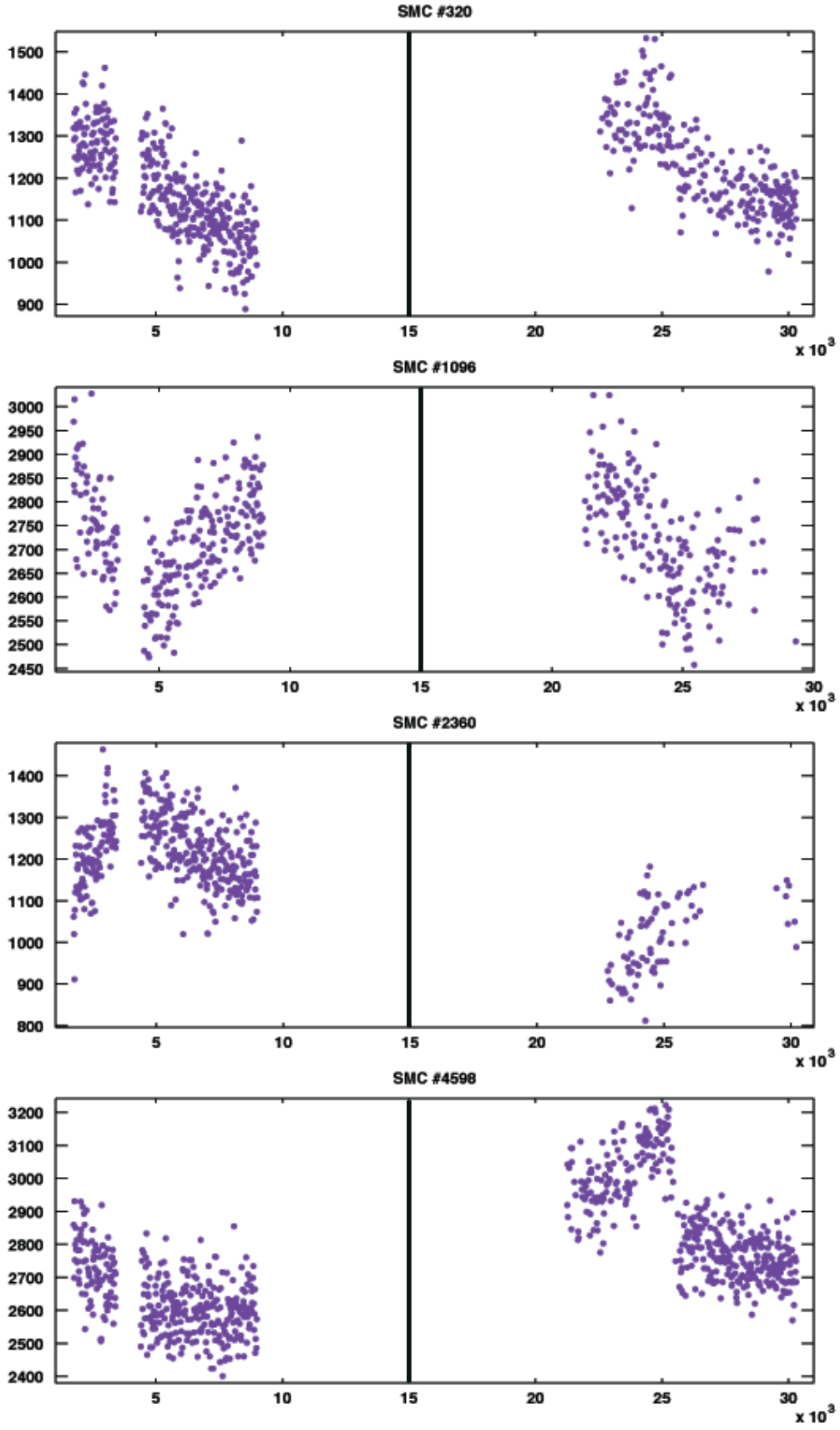

Figure 5.49: Some SMC light curves with variations induced by artefacts. Vertical and horizontal axes are flux(ADU) and time(s). From top: flux-seeing correlation (see figure 5.18), blending with undetected neighbour (see figure 5.50), blending with a detected neighbour (see figure 5.51), flux-seeing correlation at both nights. Times are shifted in the second night for better visualisation.

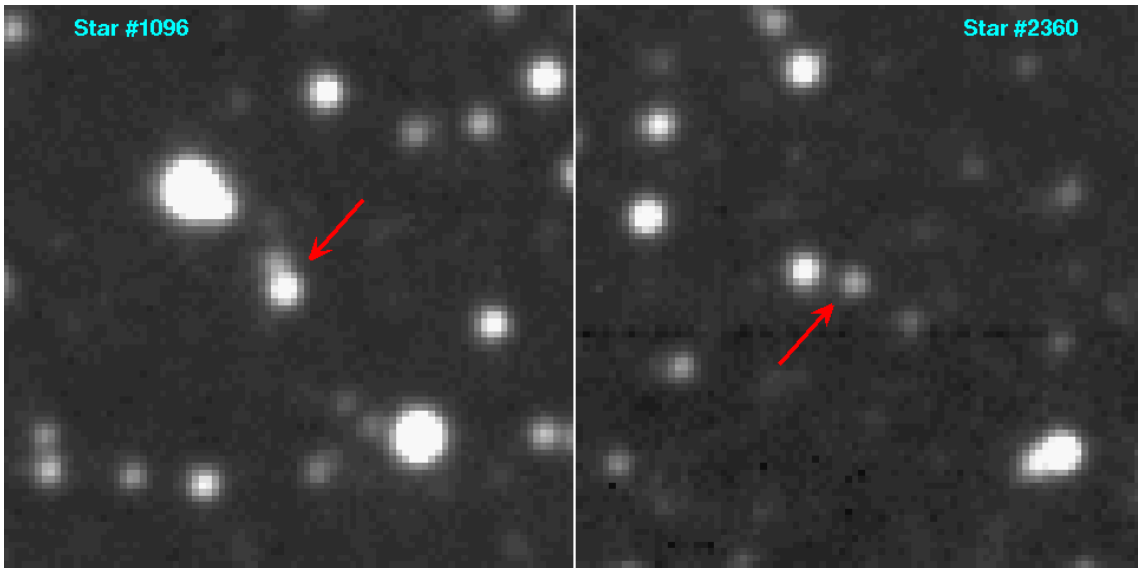

Figure 5.50: Left: star flux is blended by the flux of its unresolved neighbour. Right: the star flux is blended by the flux of its brighter neighbour.

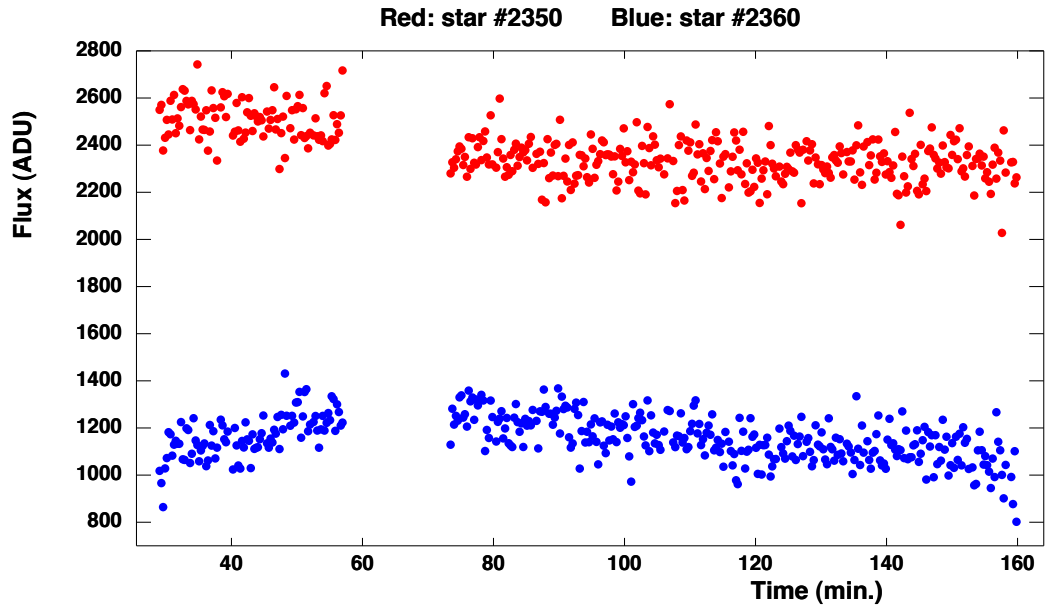

Figure 5.51: At the beginning of observation, blending induced anti-correlation between the flux variations of the two neighbour stars of figure 5.50 right.

5.5 A "Zero Signal" Analysis

From table 5.4, the Fresnel radius of the nebulae is $\sim$ 1000 km which means that the diffusion radius has to be smaller than 1000 km to allow a strong regime of scintillation. Considering the entire cloud as a turbulent bubble ($L_{out} = L_z$), and using relation (3.38), the minimum value of R_{diff} can be estimated for the parameters of the table for B68 and cb131. By using the corresponding wavelength (λ), clouds sizes (L_z) and density fluctuations (σ_{3n}), the diffusion radius is estimated $\sim$ 10 million kilometres for both nebulae which is larger than Fresnel radius by orders of magnitudes. Hence, we do not expect such single cloud to produce a detectable scintillation. However, we can consider *local* turbulences (with turbulence outer scale $L_{out} < L_z$ and diffusion radius given from relation (3.39)) being able to develop large density dispersion that induces scintillation on background stars along the line of sight. Through this effect, it is possible to study the local sub-structures of the nebulae.

Although the flux fluctuations of the monitored stars are dominated by effects other than scintillation, we can use the measured modulation indices of the monitored stars to set a lower limit on the local diffusion radii (R^{min}_{diff}) of gas (visible or hypothetical) on the line of sight. From the R^{min}_{diff} distribution for the observed line of sights (stars) for each target, we infer the maximum optical depth for each target as a function of the minimum diffusion radius.

5.5.1 Establishing Limits on the Turbulent Gas

According to figure 4.18, for a given x (= R_s/R_{ref}), the scintillation modulation index, $m_{scint} = \sigma_F^{scint}/\langle F \rangle$, is confined between the following limits:

$$F_{min}(x) < m_{scint} < F_{max}(x), \tag{5.18}$$

where relations for $F_{min}(x)$ and$F_{max}(x)$ are given in figure 4.18. The observed modulation index ($m_{obs} = \sigma_F^{obs}/\langle F \rangle$) of a monitored star, given from figure 5.36, are always larger than m_{scint} because there are effects other than scintillation that increase the dispersion of the light curves. Therefore, we can wrire: $F_{min}(x) = 0.17\ \mathrm{e}^{-1.2x} < m_{obs}$, then:

$$x \;=\; \frac{R_s}{R_{ref}} \;>\; 0.83\ \ln(\frac{0.17}{m_{obs}}). \tag{5.19}$$

Using equation (4.25) we derive a lower limit for R_{diff} corresponding to the observed modulation index:

$$R_{diff} > R^{min}_{diff} \simeq 370\,km \left[\frac{\lambda}{1\mu\mathrm{m}}\right] \left[\frac{r_s/R_\odot}{z_1/10\,kpc}\right]^{-1} \ln\left[\frac{0.17}{m_{obs}}\right]. \tag{5.20}$$

the source-observer distance is z_1+z_0 which for the case $z_1 \gg z_0$ can be approximated by z_1. This approximation is reasonable for the corresponding distances of our observed

fields[14]. The ratio $r_s/z_1 = \theta_s$ is the angular radius of the source as observed from the earth. To compute R_{diff}^{min} in equation (5.20), we know λ and m_{obs} values directly from the observations. θ_s value is estimated as follows:

A star with bolometric luminosity L located at distance z_1 from the observer has an apparent bolometric magnitude given by:

$$m_{bol} \;=\; M_{bol\,\odot} \,-\, 2.5\,\log\frac{L/z_1^2}{L_\odot/(10pc)^2}, \tag{5.21}$$

where $M_{bol\,\odot}$ and $L_\odot$ are the absolute bolometric magnitude and the bolometric luminosity of the sun. According to Stephan-Boltzmann law the luminosity is a function of the source radius r_s and temperature T:

$$L \;=\; 4\pi\,\sigma\,r_s^2\,T^4, \tag{5.22}$$

where $\sigma = 5.6704 \times 10^{-8}$ kg s^{-3} K^{-4} is the Stephan-Boltzmann constant. By substituting this equation in relation (5.21) we obtain:

$$m_{bol} \;=\; M_{bol\,\odot} \,-\, 5\,\log\frac{r_s/R_\odot}{z_1/10pc} \,-\, 10\,\log\frac{T}{T_\odot}. \tag{5.23}$$

m_{bol} is related to the visual magnitude V through the relation $m_{bol} = V + BC$, where BC is the bolometric correction[15]. It comes:

$$\log\frac{\theta_s}{R_\odot/10kpc} \;=\; 3 - \frac{V}{5} + \frac{M_{bol\,\odot} - BC}{5} \,-\, 2\,\log\frac{T}{T_\odot}. \tag{5.24}$$

$M_{bol\,\odot} = 4.47$ and $T_\odot = 5777$ K is the sun temperature [Cox (2000)].

To compute θ_s we need the magnitude V and the stellar type to estimate the temperature and the BC factor. Since the observations were done in wavelengths other than visual band V, we re-write the equation (5.24):

$$\log\frac{\theta_s}{R_\odot/10kpc} \;=\; 3 - \frac{m_\lambda}{5} \,-\, \frac{V - m_\lambda}{5} + \frac{M_{bol\,\odot} - BC}{5} - 2\,\log\frac{T}{T_\odot}. \tag{5.25}$$

Here, m_λ is the observed apparent magnitude in the given passband and $V - m_\lambda$ is the colour index of the star.

In this equation, these magnitudes and colour index are supposed to be free from extinction. As the stars are observed through a dark nebula, we need a correction which is described in the following section.

[14]For dark nebulae, $z_0 \sim 100$ pc and $z_1 \sim 10$ kpc.

[15]Bolometric correction is the difference between the source magnitude in visual band and its bolometric magnitude. BC is always a negative value and depends on the stellar type.

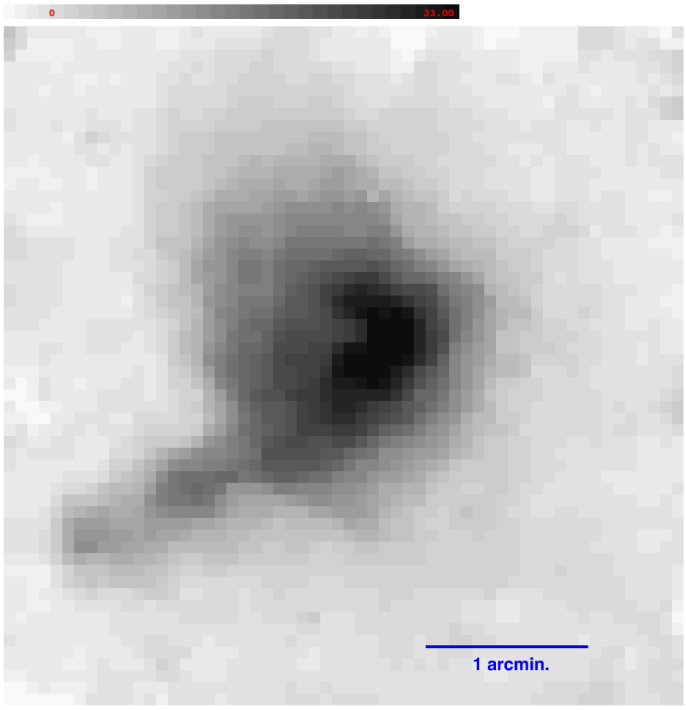

Figure 5.52: Absorption map of Barnard 68 in visual band. The cloud absorption reaches 33 magnitude in the core ($\sim$ 3.9 magnitude in K_s band) corresponding to $\sim 10^{22}$ H_2 / cm^2. Grey scale indicates the absorption magnitude and spans 0 to 33. The map is kindly provided by J. Alves [Alves et al. (2001)].

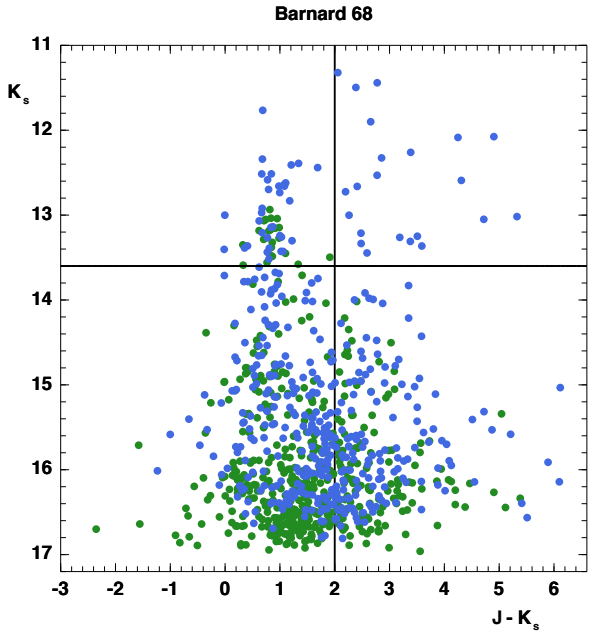

Figure 5.53: Dereddened colour-magnitude diagram for stars toward Barnard 68 field. Blue and green dots are stars located behind the cloud and control stars respectively. Stars with colour index $J - K_s > 2$ and $K_s < 13.6$ are assumed to be red giants.

5.5.2 Limits on the Gas Structuration of the Nebulae

Dust absorbs and scatters the light. Thus, the stars behind the dusty nebulae appear to be fainter and redder than what they really are. We need to correct the observed magnitudes according to dust models in K_s band.

In 2001, Alves and his colleagues published a high-accuracy absorption map of B68 in visual band. Barnard 68 is located in the direction of Galaxy centre above the Galactic plane with rich star field of the Galactic bulge at background. The authors used SOFI camera of NTT to observe the background stars in J (1.25 μm), H (1.65 μm) and K_s (2.16 μm) bands. To build the extinction map, they took the stars in unobscured part of the field as control stars and considered their average colour (H-K_s) as the intrinsic colour of all bulge stars in the field. Using reddening laws, they computed the corresponding absorptions in visual band [Alves et al. (2001)]. Prof. Alves kindly provided us with the absorption map which is shown in figure 5.52.

We also used an extinction model to obtain the absorption for any desired wavelength, $A(\lambda)$ from the visual absorption $A(V)$. Cardelli et al. [Cardelli et al. (1989)] proposed a

linear relation to parametrize the average value of $A(\lambda)/A(V)$:

$$\langle \frac{A(\lambda)}{A(V)} \rangle \;=\; a(x) \,+\, \frac{b(x)}{R_V}, \tag{5.26}$$

Where $x = 1/\lambda\ \mu\mathrm{m}^{-1}$, $R_V \equiv \frac{A(V)}{E(B-V)}$ is the characteristic value for dust extinction and is about 3.1 for diffuse nebulae and $E(B-V) = A(B) - A(V)$ is the colour excess due to extinction. The coefficients are determined for near IR band from the following relations:

$$\begin{aligned} a(x) &= 0.574\, x^{1.61}, \\ b(x) &= -0.527\, x^{1.61}. \end{aligned} \tag{5.27}$$

We use $R_V = 3.1$ as standard interstellar reddening law for B68 and derived the extinctions for J and K_s bands:

$$\frac{A(K_s)}{A(V)} \;=\; 0.117, \tag{5.28}$$

$$\frac{A(J)}{A(V)} \;=\; 0.282. \tag{5.29}$$

We determine the dereddened magnitude of stars behind the dust from their position, by using the absorption map and relation (5.28). If m_λ is the observed magnitude in a given passband, the dereddened magnitude m_λ^0 is given by:

$$m_\lambda^0 \;=\; m_\lambda \,-\, A(\lambda). \tag{5.30}$$

This is the corrected magnitude that we will use in equation (5.25). This correction was only possible for B68. For the two other dark nebulae no extinction maps is available.

To calculate the stellar apparent radius from relation (5.25), the temperature and V magnitude are also needed. Although we do not have spectral information on the stars, we could estimate or constrain the stellar types as follows: For B68 we have observation in J band obtained in 2004. We dereddened the measured magnitudes according to relations (5.28) and (5.29) and plotted the colour-magnitude diagram shown in figure 5.53. The redder and brighter stars of the figure are red giants which are located behind the cloud. We chose $K_s - J > 2$ and $K_s < 13.6$, to distinguish giants from the main sequence stars.

Our sensitivity is limited by the apparent size of the star θ_s. To be conservative, for each star (with magnitude K_s), we chose among the stellar types the one that maximises θ_s assuming the star is further than 4 kpc. The result of this procedure is summarised in tables 5.5 and 5.6.

In figure 5.54, θ_s^{max} is given as well as the corresponding stellar type as a function of

K_s	11	12	13	14	15	16	17
$\theta_s^{max}/(R_\odot/10kpc)$	14.82	10.20	7.30	4.92	4.00	2.84	1.86

Table 5.5: θ_s^{max} for main sequence stars behind B68.

K_s	11	11.5	12	12.5	13	13.5
$\theta_s^{max}/(R_\odot/10kpc)$	39.6	31.5	20.6	15.5	12.5	9.4

Table 5.6: θ_s^{max} for red giants behind B68.

	Stellar Type	T (K)	B.C.	M_V
Main Sequence	K0	5150	-0.31	+5.90
	F8	6250	-0.16	+4.00
	F0	7300	-0.09	+2.70
	A0	9790	-0.30	+0.65
	B2	20900	-2.35	-2.45
Giants	G5	5050	-0.34	+0.9
	K2	4390	-0.61	+0.5

Table 5.7: Stellar spectral types.

K_s. Some stellar type properties are given in table 5.7. We discarded the light curves that have been identified as artefacts and computed the maximum angular radius for each monitored star from figure 5.37. In the case of B68, K_s and J measurements allowed us to distinguish between main sequence stars and red giants.

Since the absorptions are not measured towards Circinus and cb131 and because they are observed only in K_s bands, we can not know the dereddened magnitude nor the colours; to be conservative, we attribute the largest angular radius value $\theta_s^{max}/(R_\odot/10kpc) = 35$ for all monitored stars for these two fields.

From θ_s^{max} estimate, we determine R_{diff}^{min} from equation (5.20) for the stars of the three nebulae. Figure 5.55 shows the distribution of R_{diff}^{min} for the light curves measured towards the nebulae. For B68 and cb131 the distributions are plotted for the monitored stars located behind the clouds. For Circinus, as mentioned before, it was not possible isolate a control region free from absorption, therefore, we included all stars of the field.

We used these diffusion radii limits to constrain the turbulence of the gas along the line of sight. In this purpose, we considered a cumulative distribution of variable R_{diff}^{min} , that

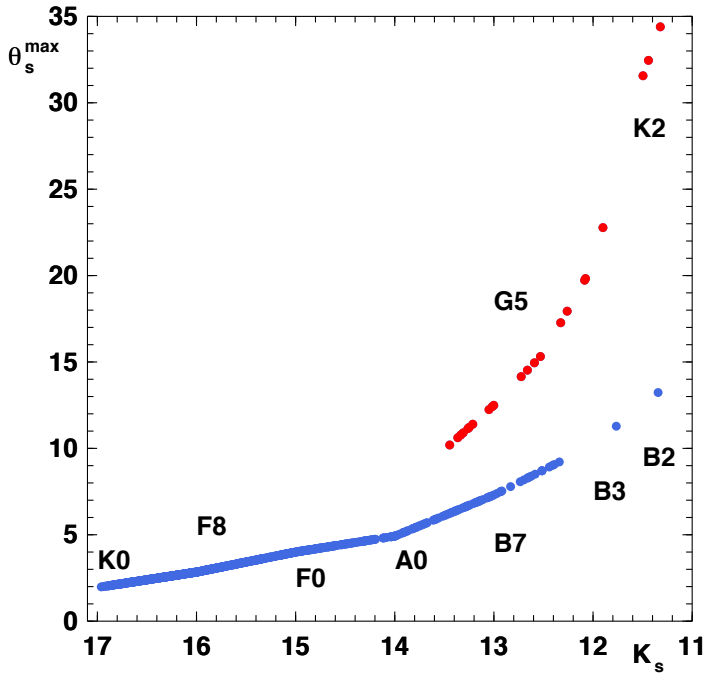

Figure 5.54: Maximum angular radius θ_s^{max} and corresponding stellar types for B68 as a function of K_s. Blue points represent the main sequence stars. Red giants are shown by red points.

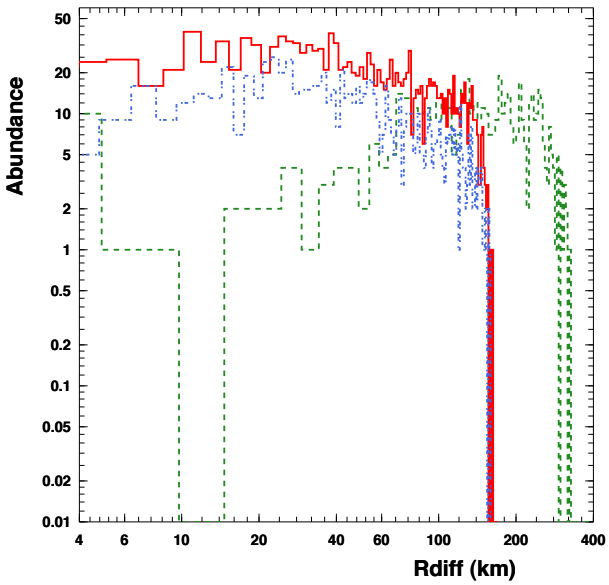

Figure 5.55: Distribution of R_{diff}^{min}. Green line: B68. Red line: cb131. Blue line: Circinus. Numbers of l.o.s with R_{diff}^{min} < 4 km (under flows) are 12 for B68, 33 for cb131 and 178 for Circinus.

is $N_\star(R_d)$, the number of stars whose line of sight do not cross a gaseous structure with $R_{diff} < R_d$. Top panel of figure 5.56 shows this cumulative distribution for the obscured regions of B68 and cb131 (see figure 5.35), and over the complete field of the Circinus nebula, which has indistinct boundaries. The best limits are naturally obtained towards B68, as a consequence of the better knowledge of the stellar sizes.

From the distribution of $N_\star(R_d)$, one can infer limits on the scintillation optical depth $\tau_{1.25\mu m}(R_d)$. Indeed $N_\star(R_d)$ is the number of lines of sights (l.o.s.) that do not cross structures with $R_{diff} < R_d$. Defining N_{behind} as the total number of monitored l.o.s. through the nebula (the stars behind the gas or all the monitored stars toward the SMC as we are searching for invisible gas), the upper limit on the optical depth $\tau_{1.25\mu m}(R_d)$ is the upper limit on the ratio p = $\frac{N_{behind}-N_\star(R_d)}{N_{behind}}$. The 95% statistical upper limit on p is given by the classical confidence interval [Ventsel (1973)]:

- if $N_*(R_d)$ and $(N_{behind} - N_*(R_d))$ are both larger than 4:

$$\tau_\lambda(R_d) < p + 1.643\sqrt{\frac{p(1-p)}{N_{behind}}}, \tag{5.31}$$

where the second term at right of the inequality is the 95% upper limit computed from binomial probability distribution.

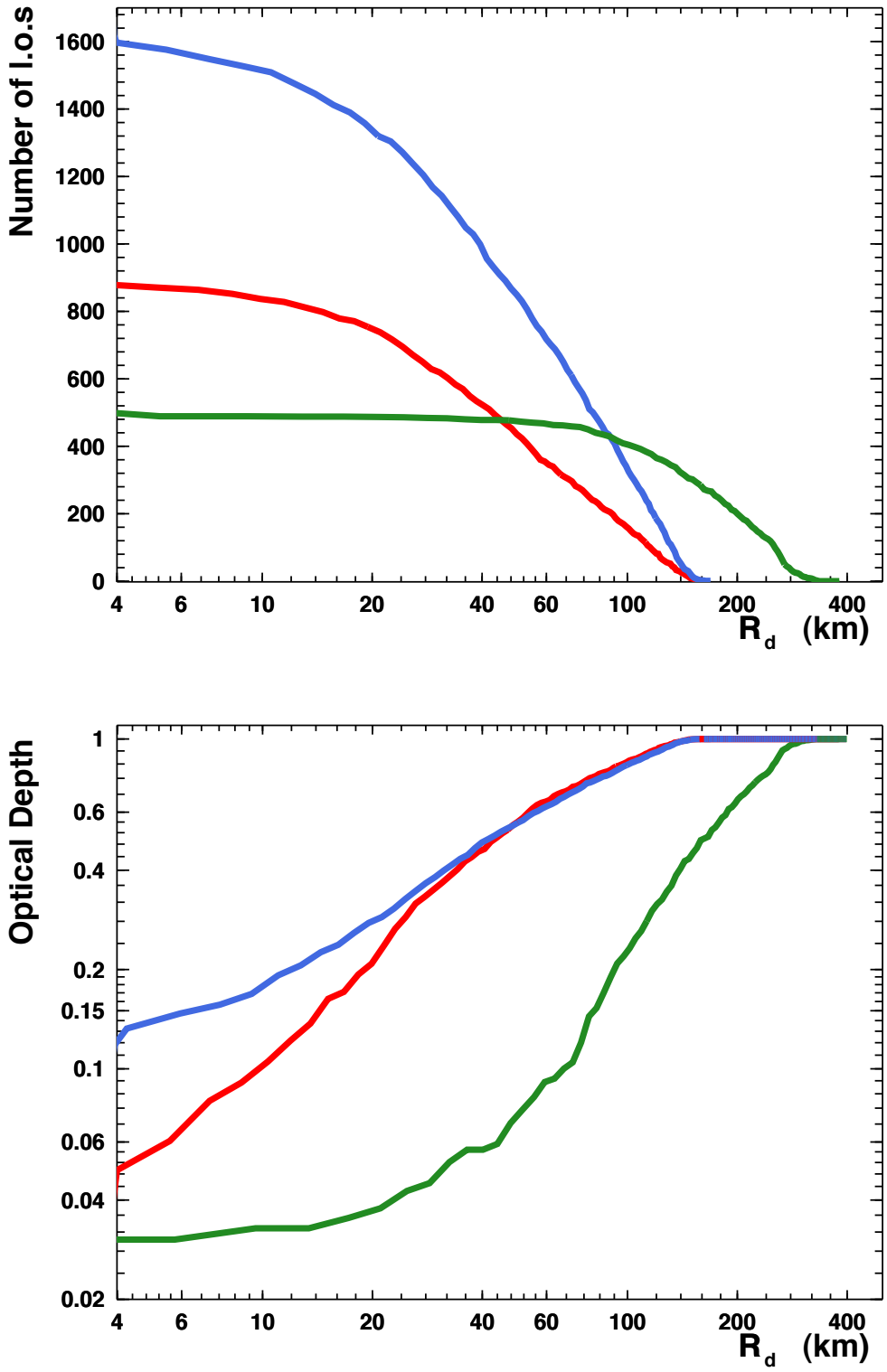

Figure 5.56: Top: $N_\star(R_d)$, the number of directions with no turbulent structure with $R_{diff}(2.16\mu m) < R_d$ along the line of sight toward the obscured regions of B68 (green), cb131 (blue) and towards Circinus (red). Bottom: The upper limit of optical depth of structures with $R_{diff}(2.16\mu m) < R_d$. Total number of stars behind the nebulae N_{behind} (including under flows l.o.s): 512 for B68, 1778 for cb131 and 913 for Circinus.

- if $N_*(R_d) \leq 4$:
$$\tau_\lambda(R_d) < (N_{behind} - N_{95\%}(R_d))/N_{behind}, \quad (5.32)$$
where $N_{95\%}(R_d)$ is the $95\%C.L.$ Poissonian lower limit on $N_*(R_d)$;

- if $(N_{behind} - N_*(R_d)) \leq 4$:
$$\tau_\lambda(R_d) < (N_{behind} - N_*(R_d))_{95\%}/N_{behind}, \quad (5.33)$$
where $(N_{behind} - N_*(R_d))_{95\%}$ is the $95\%C.L.$ Poissonian upper limit on $(N_{behind} - N_*(R_d))$.

The upper limit of the optical depth is shown at bottom of figure 5.56 for the three nebulae. As an example, for B68, the upper limit on the optical depth for structures with $R_{diff} < 100$ km is obtained as follows: from green curve at top plot of figure 5.56 we read the value of $N_\star(100\,\text{km}) \sim 400$; since $N_{behind} = 500$, by using expression (5.31) it comes $\tau_{2.16\mu m}(100\,\text{km}) < 0.22$. This is the number given in the lower plot of figure 5.56.

The Impact of the Candidate

The mean magnitudes of the scintillation candidate star are K_s = 16.6 and J = 20.4. The star is located at α = 260.6762°, δ = -23.8159° (J2000) and according to the absorption map $A(V)$ = 13.21, corresponding to $A(K_s)$ = 1.54 magnitude. It is a main sequence star with possible type ranging from A0 at 9.6 kpc (r_s = 2.4 $R_\odot$) to A5 at 6.1 kpc (r_s = 1.7 $R_\odot$) or from F0 at 5.0 kpc (r_s = 1.6 $R_\odot$) to F5 at 4.0 kpc (r_s = 1.4 $R_\odot$). Consequently, it can be a star small enough to experience observable scintillation ($r_s/d > 2.5\ R_\odot$/10kpc). Although the observed modulation index, m = 0.17, is quite high, it is compatible with scintillation as shown by the simulation results in figure 4.18. From this figure we infer that $R_s/R_{ref} < 0.25$ if we suppose the modulation (m_{scint} = 0.17) is completely produced by scintillation. Expression (4.25) gives the upper limit on diffusion radius of the candidate, $R_{diff} < 96$ km. The limit on density fluctuations of the turbulent structure responsible for such scintillation is deduced from equation (3.39), where the cloud size is taken as L_z = 17000 AU:

$$\sigma_{3n} \quad < \quad 7.18 \times 10^9 \, [\frac{L_{out}}{10 A.U.}]^{\frac{1}{3}} \ \text{cm}^{-3}. \quad (5.34)$$

5.5.3 Limits on Turbulent Hidden Gas Toward the SMC

Looking through the halo toward the small magelanic cloud, we can probe the existence of turbulent clouds made of molecular hydrogen with no dust. Although the observations are done only in J band, we produce the colour-magnitude diagram by using EROS data in B_{EROS} and R_{EROS} bands ([Tisserand et al. (2007)], [Hamadache et al. (2006)] and [Rahal 2009]) as is shown in figure 5.57. We distinguish main sequence stars from giants qualitatively at colour $B_{EROS} - R_{EROS} = -0.7$ as shown by the red line in the

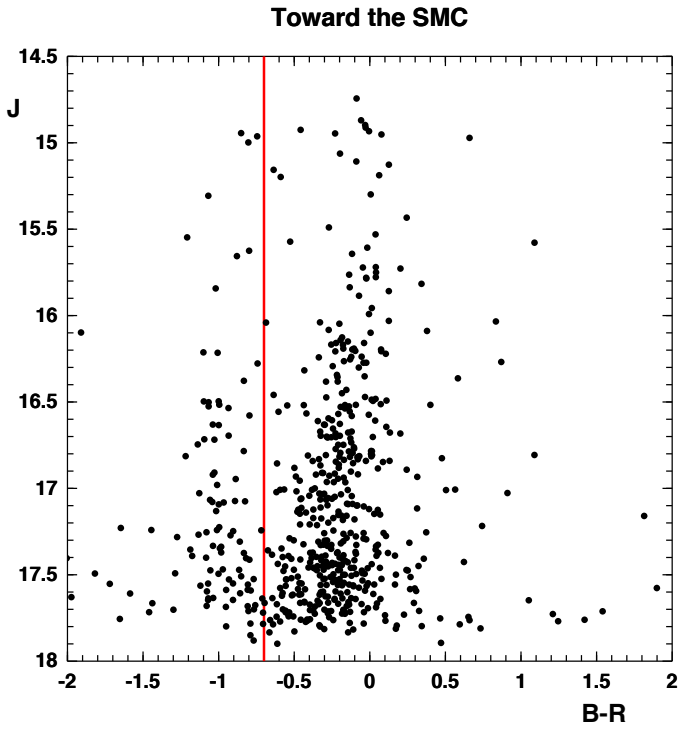

Figure 5.57: HR diagram for the stars of the SMC field. We have used data from EROS database. The main sequence stars and red giants are separated by the red line. The majority of stars are red giants.

J	14.00	15.20	15.67	17.07	18.12
$\theta_s/(R_\odot/10kpc)$	2.82	1.51	1.42	0.99	0.70

Table 5.8: θ_s for main sequence stars in SMC.

J	13.63	15.29	15.75	16.46	17.60	17.96	18.21
$\theta_s/(R_\odot/10kpc)$	14.93	10.52	7.45	4.22	2.59	1.99	1.73

Table 5.9: θ_s for red giants in SMC.

figure. In contrast with the stars towards the nebulae, we know the distance of SMC stars ($d = 62.23$ kpc [Szewczyk et al. (2006)]). Since the distance is known, we obtained directly the θ_s versus J relation for the different stellar types. Tables 5.8 and 5.9 show θ_s for each magnitude. The variation of apparent radius versus magnitude is drawn in figure 5.58 for our monitored stars of the SMC. We have used the tables to interpolate θ_s for any value of J.

R_{diff}^{min} is obtained from expression (5.20) by using θ_s and the measured modulation index (m_{obs}) of the light curve (see the distribution figure 5.59). Our observation is not sensitive to structures with $R_{diff} > 800$ km. Like the other directions, we determine the number of lines of sights, $N_\star(R_d)$, containing no turbulent structure with diffusion radius smaller than R_d (top panel of figure 5.60). The upper limit on the optical depth is also shown in figure 5.60.

The grey zone in the figure indicates the possible values for the halo clumpuscules according to [Pfenniger & Combes (1994)]. To compute the maximum optical depth for the clumpuscules we consider that the Galaxy contains a gaseous mass of $M_G \sim 10^{12}$ $M_\odot$ within radius of $R_G \sim 80$ kpc [Gnedin et al. (2010)]. From equation (2.6) we take clumpuscules mass $M_\bullet \sim 10^{-3}$ $M_\odot$ with a maximum size of $R_\bullet \sim 50$ A.U. If the halo is maximally filled by N_{clump} of clumpuscules, we have:

$$N_{clump} = \frac{M_G}{M_\bullet}, \tag{5.35}$$

and the maximum clumpuscule sky coverage is:

$$\tau_{clump} < \frac{N_{clump} R_\bullet^2}{R_G^2}, \tag{5.36}$$

substituting the corresponding values to the relation above we find:

$$\tau_{clump} < 10^{-2}. \tag{5.37}$$

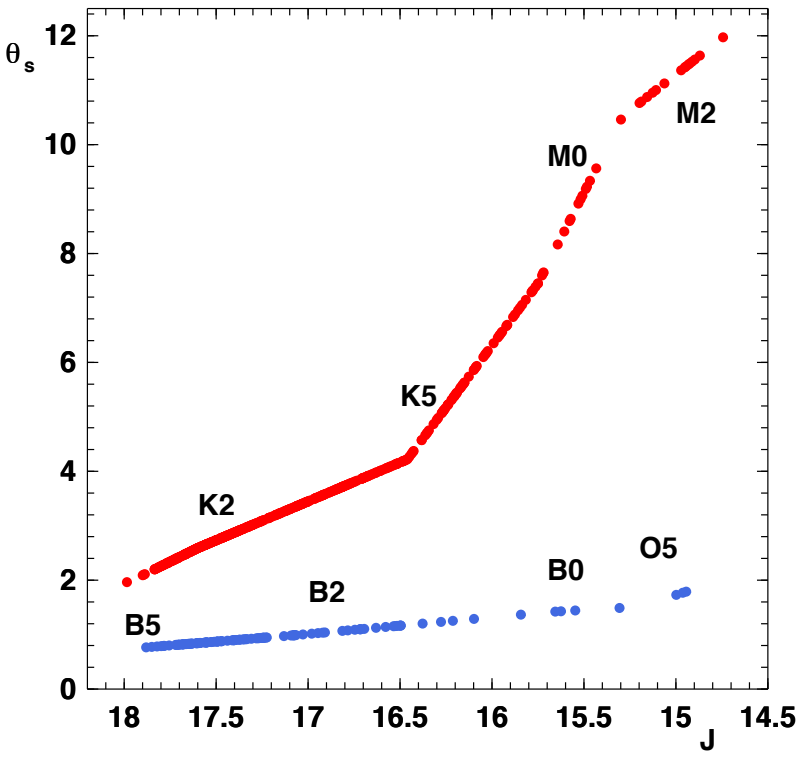

Figure 5.58: θ_s vs. J for the observed main sequence stars (blue) and red giants (red) of the SMC.

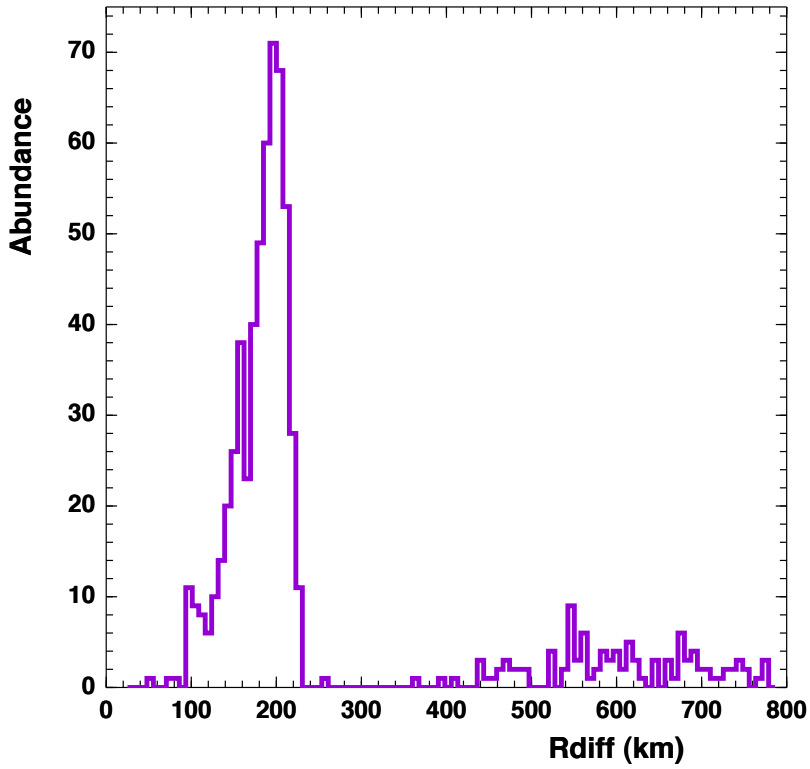

Figure 5.59: Distribution of the minimum diffusion radius compatible with observed modulation indices toward the SMC.

The sudden rise on the estimated optical depth upper limit (or the sudden fall in $N_\star(R_d)$) is due to the prominence of red giants in the SMC field. Since red giants have large apparent radii, only the small diffusion radii can produce detectable modulations.

We can conclude that our sensitivity is not yet sufficient to establish a significant limit on the halo fraction made of clumpuscules.

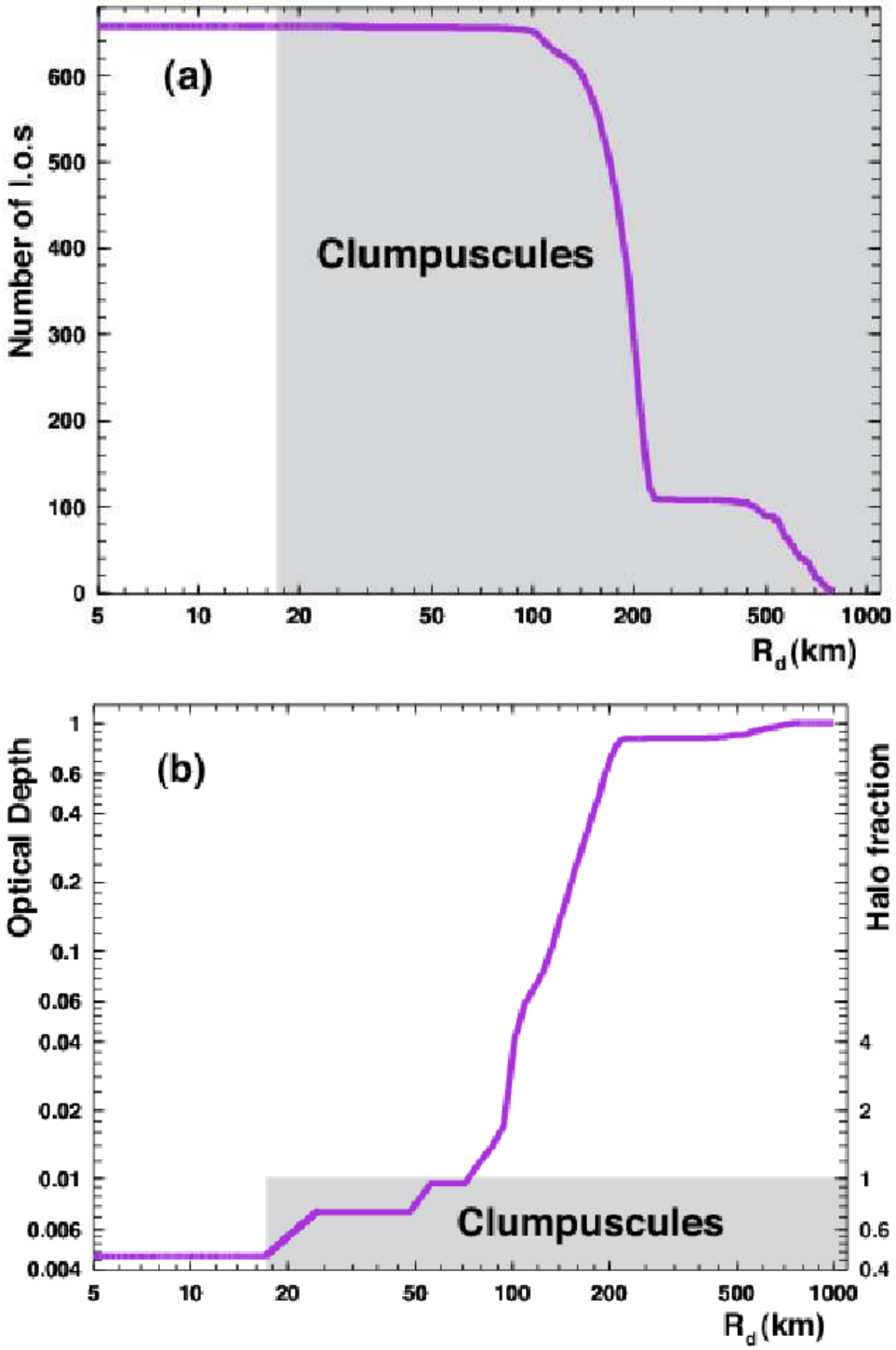

Figure 5.60: Top: $N_\star(R_d)$, the number of directions toward the SMC with no turbulent structure with $R_{diff}(1.25\mu m) < R_d$ along the line of sight. Bottom: The upper limit of optical depth of structures with $R_{diff}(1.25\mu m) < R_d$. The grey zone is the permitted domain for the halo clumpuscules. The minimum diffusion radius computed for clumpuscules corresponds to the maximum density dispersion of 10^{10} cm^{-3}.

Chapter 6

Conclusions and Perspectives

This thesis can be considered as the first attempt to use scintillation effect as a tool to probe the molecular media in IR or visual band. The detection of this effect would have a major impact on the search for the hidden baryons of the Galactic halo. Moreover, this technique can be used to study the turbulent sub-structures of the ISM. We have developed a complete simulation of the turbulent medium and of the light propagation. Through this simulation we can connect the turbulence parameters to the observables. The data analysis tools are now available for future searches. We were lucky enough to find a candidate with a modulation index compatible with simulation. Since it is located behind a relatively laminar nebula, multicolour and multi-epoch observations are needed to discard or find a convincing signature of the effect.

One of the crucial tasks of the future analysis is to exploit the temporal features of the light curves. This would enable us to extract typical time scales. We need a specific Fourier analysis technique for irregularly sampled light curves and compute the time power spectra. It would be helpful to acquire data with different passbands simultaneously. As time scales of scintillation depend on the wavelength, this would help to distinguish the scintillation effect from other types of variabilities. Furthermore, multi-wavelength observation would be helpful to determine the stellar type of the candidates.

According to relation (3.59), the refraction time for a typical star at Galactic disc is ~ 5 minutes. This would be somewhat larger for LMC or SMC stars. For future observations we can take longer exposure time (~ 30 s) with the shortest possible read-out time to have better signal to noise ratio. This strategy would also reduce the systematics due to PSF shape. As we need a sensitivity of a few percent on flux fluctuations, the photometric precision is at outmost importance. Telescopes with diameter larger than 4 meter with large field of view would be adequate. To benefit from the maximum emission, future searches should also use visible light; observing wide crowded fields with long exposures ($\sim 10^6$ star $\times$ hour) with such a large telescope will allow us to increase the chance of detection with a good determination of the modulation index and the time scales. According to our

derived optical depth for clumpuscules toward the SMC (figure 5.60b), we at least need 100 times more exposure than what we has in our test-data to significantly constrain the clumpuscules contribution to the halo.

We can also emphasise that two light curves extracted/observed from a given 2D illumination pattern, which are sufficiently separated from each other, contain the same time scales but their flux fluctuations are not correlated. Therefore, a more ambiguous observational strategy would be to use at least two synchronised distant telescopes observing the same target.

Bibliography

[Alcock et al. (1997)] Alcock et al. (MACHO) The MACHO Project Large Magellanic Cloud Microlensing Results from the First Two Years and the Nature of the Galactic Dark Halo 1997, ApJ, 486, 697

[Alves et al. (2001)] Alvez, J., Lada, C. J., Lada, E. A., 2001, Nature, 409, 159

[Ansari (1996)] Ansari, R. Photometric Reconstruction and Data Analysis Softwares in the EROS Experiment (EROS Collaboration) Vistas in Astronomy, 40:519

[Bacmann et al. (2000)] Bacmann, A., André, P., Puget, J.-L., *et al*., 2000, A&A 361, 555

[Bosma (1981)] Bosma, A., Astronomical Journal, Volume 86, Number 12, 1981

[Bohlin et al. (1978)] Bohli, R.C., Savage, B.D., Drake, j. F., 1978 ApJ 224:132

[Cardelli et al. (1989)] Cardelli, A. J., Clayton, G. C., Mathis, J. S., ApJ, 345: 245-256

[Coc et al (2004)] Coc, A.; Vangioni-Flam, E.; Descouvemont, P.; Adahchour, A.; Angulo, C. Astrophys.J. 600 (2004) 544-552

[Coles & Lucchin (2002)] Coles, P.; Lucchin, F. Cosmology John Wiley & Sons, Ltd 2002

[Cox (2000)] Cox, A.N., Allen's Astrophysical Quantities, 4th ed., 2000, Springer

[CRC (1998-99)] CRC: Handbook of Chemistry and Physics, 1998-99

[Dekel & Birnboim (2006)] Dekel, A., Birnboim, Y., 2006 MNRAS 368, 2

[Dunkley et al. (2009)] Dunkley, J. et al. Five-Year Wilkinson Microwave Anisotropy Probe (WMAP) Observations: Likelihoods and Parameters from the WMAP data, Astrophys.J.Suppl.180:306-329, 2009

[Elmegreen (1992)] Elmgreen, B.G., 1992, in: The Galactic Interstellar Medium, Saas-fee Advanced Course 21, D.Pfenniger, P.Bartholdi (eds.), Springer-Velarg, Berlin, p. 157

[Freedman et al. (2001)] Freedman, W. L., et al. 2001, ApJ, 553, 47

[Georgelin et al. (1994)] Georgelin, Y.M., Amram, P., Georgelin, Y.P. *et al*., 1994, A$AS, 108, 513

[Giodini et al. (2009)] Giodini, S., et al. 2009, ApJ, 703, 982

[Gnedin et al. (2010)] Gnedin, O. Y., Brown, W. R., Geller, M., J., Kenyon, S. J., 2010, ApJ, 720, L108

[Hamadache et al. (2006)] Hamadache C., Le Guillou L., Tisserand P. *et al*., 2006, A&A, 454, 185

[Hamidouche (2003)] Hamidouche, M.; Ph.D. thesis: Simulation de la Scintillation Interstellaire de Pulsars.

[Hosford et al. (2009)] Hosford, A.; Ryan, S. G.; Garcia Perez, A. E.; Norris, J. E.; Olive, K. A. Astronomy and Astrophysics, Volume 493, Issue 2, 2009, pp.601-612

[Hotzel et al. (2002)] Hotzel S., Harju J., Juvela M. *et al*., 2002, A&A 391, 275

[Hoyle (1954)] Hoyle, F., 1953, ApJ 118, 513

[Komatsu et al. (2009)] Komatsu, E. Five-Year Wilkinson Microwave Anisotropy Probe Observations: Cosmological Interpretation. 2009 ApJS, 180..330K

[Landau & Lifshitz (1971)] Landau L., Lifshitz E., 1971, Fluid Mechanics, Mir, Moscow

[Larson (1981)] Larson R. B. MNRAS (1981) 194, 809-826

[Lasserre et al. (2000)] Lasserre, T. et al. (EROS) Not enough stellar mass Machos in the Galactic halo 2000 A&A 355L 39L

[Liddle (2003)] Liddle, A. An Introduction to Modern Cosmology John Wiley & Sons, Ltd 2003

[Lovelace (1970)] Lovelace, R. E. V., Ph.D. thesis, Cornell University, 1970

[McGaugh et al. (2000)] McGaugh, S. S., Schombert, J. M., Bothun, G. D., and De Blok, W. G. ApJ 533: L99-L102, 2000

[McGaugh (2005)] McGaugh, S. S. 2005, ApJ, 632, 859

[McGaugh et al. (2010)] McGaugh, S. S., Schombert, De Block, W. J. G. and Zagursky, M. J., ApJ, 708: L14-L17, 2010

[Melendez & Ramirez (2004)] Melendez, J. & Ramirez, I. Reappraising the Spite Lithium Plateau: Extremely Thin and Marginally Consistent with WMAP Data. 2004 ApJ, 615L..33M

[Moniez (2003)] Moniez, M., A&A 412, 105-120, 2003

[Moniez (2008)] IDM2008 - identification of dark matter 2008, Stockholm : Suède (2008)

[Narayan (1992)] Narayan,R. Phil. Trans. R. Soc. Lond. A (1992) 341, 151-165

[Nissen & Schuster (1997)] Nissen, P.E. & Schuster, W.J. 1997, A&A, 326, 751

[NTT Overview, ESO] http://www.eso.org/sci/facilities/lasilla/telescopes/ntt/overview/index.html

[O'Meara et al. (2006)] O'Meara, J.M.; Burles, S.; Prochaska, J.X.; Prochter, G.E.; Bernstein, R.A.; Burgess, K.M. 2006, ApJ, 649L..61O

[Ostriker et al. (1974)] Ostriker, J. P, Peebles, P. J. E. and Yahil, A., 1974 ApJ 193, L1

[Ostriker (2007)] Triggerd Star Formation in a Turbulent ISM, Proceedings IAU Symposium No. 237, 2006

[Palanque-Delabrouille (1997)] Palanque-Delabrouille, N. Research on Galactic Dark Matter Implied by Gravitational Microlensing, Ph.D. thesis 1997

[Peimbert et al. (2007)] Peimbert, M., Luridiana, V., & Peimbert, A. 2007, ApJ, 666, 636

[Peimbert (2008)] Peimbert, M. The Primordial Helium Abundance. arXiv:0811.2980

[Pfenniger & Combes (1994)] Pfenniger, D., Combes, F. Is dark matter in spiral galaxies cold gas? II. Fractal models and star non-formation. 1994, A&A 285, 94-118

[Pfenniger & Revaz (2005)] Pfenniger, D., Revaz, Y. A&A 431,511-516 2005

[Rahal 2009] Rahal Y. R., 2009, A&A 500, 1027

[Rogerson et al. (1973)] Rogerson, J.G. & York D.G. 1973 ApJL, 186, L95+

[Romani et al. (1986)] Romani, R. W., Narayan, R. and Blandford, R. Mon. Not. R. astr. Soc (1986) 220, 19-49

[Rousselot et al (2000)] Rousselot1 P., Lidman C., Cuby J. G., Moreels G., and Monnet G. 2000, A&A 354, 1134

[Russeil et al. (1998)] Russeil, D., Amram, P., Georgelin, Y.P. *et al*. 1998, A&AS, 130, 119

[Rubin et al. (1980)] Rubin, V. C., Ford, W. K., Thonnard, N., ApJ, 238:471-487, 1980

[Savage et al. (1977)] Savage, B.D., Bohli, R.C., Drake, j. F., Budich, W., 1977 ApJ, 216:291-307

[Skrutskie et al. (2006)] Skrutskie, M.F., Cutri, R.M., Stiening, R. et al. 2006, the Astronomical Journal, 131, 1163

[SOFI Overview, ESO] http://www.eso.org/sci/facilities/lasilla/instruments/sofi/ index.html

[SOFI manual (2006)] SOFI User's Manual, Doc. No. LSO-MAN-ESO-40100-0004 Issue 2.0

[Spite & Spite (1982)] Spite, F. & Spite, M. 1982, A&A, 115, 357

[Stark et al. (2009)] Stark, D. V., McGaugh, S. S. & Swaters, R. A. 2009, AJ, 138, 392

[Trachternach et al. (2009)] Trachternach, C., de Blok, W. J. G., McGaugh, S. S., van der Hulst, J., M. & Dettmar, R. J., 2009, A&A, 505, 577

[Steigman (2006)] Steigman, G. Primordial Nucleosynthesis: successes and challenges. Int. J. Mod. Phys E 2006; 15: 1-35

[Steigman (2006)] Steigman, G. The cosmological evolution of the average massper baryon. J.Cosmol.Astropart.Phys.2006; 10: 16-20

[Stewart et al. (2011)] Stewart K. R. et al. Orbiting Circum-galactic gas as a Signature of Cosmological Accretion 2011 ApJ...738...39S

[Szewczyk et al. (2006)] Szewczyk, O., Pietrzynski, G., Gieren, W. et al. 2009, the Astronomical Journal, 131, 1163

[Tatarski (1961)] Tatarski, V. Wave Propagation in a Turbulent Medium, 1961

[Tisserand et al. (2007)] Tisserand, P. *et al*., 2007, A&A, 469, 387

[Tully & Fisher (1977)] Tully, R., B. and Fisher, J., R. A&A 54, 661-673 1977

[van Albada et al. (1985)] van Albada, T. S., Bahcall, J. N., Begeman, K. and Sancisi, R., 1985, ApJ 295, 305-13

[Ventsel (1973)] Ventsel, H. 1973, Théorie des probabilités (Moscou: Mir)

[Walker et al. (2009)] Walker, M. G., Mateo, M., Olszewski, E. W., Penarrubia, J., Wyn Evans, N., & Gilmore, G. 2009, ApJ, 704, 1274

[Wheelon (2001)] Wheelon, A. D. Electromagnetic Scintillation I.Geometric Optics, Cambridge University Press, 2001

[Wilson (1982)] Wilson, R. The Messenger No. 29 - September 1982

[Zwicky (1937)] Zwicky, F., 1937, ApJ, vol. 86, p.217